The 750 keV RFQ INJECTOR UPGRADE

C.Y. Tan, D.S. Bollinger, K.L. Duel, P.R. Karns, M.J. Kucera, J.R. Lackey, J.F. Larson, W.A. Pellico, E.A. Peoples-Evans, V.E. Scarpine, C.W. Schmidt, B.A. Schupbach, R.E. Tomlin & A.K. Triplett

Date: November 10, 2012

Version: 11/10/12 08:32 AM

Table of Contents

Abstract..... 1
1.Introduction..... 2
2.The Plan..... 2
3.Analysis of Present Operations..... 2
3.1. Injector Downtime..... 3
3.2. Maintenance and Failures..... 5
3.3. Operating Costs..... 5
3.3.1. Power consumption..... 7
3.4. Future Expenditures..... 7
4.The New Injector Design..... 9
4.1. The H- Source..... 10
4.1.1. Extraction..... 12
4.1.2. FNAL source design..... 14
4.1.3. Testing the source in the test stand..... 16
4.1.3.a. Perveance measurement..... 16
4.2. The LEBT..... 18
4.2.1. Focusing with gas..... 18
4.2.1.a. Demonstration of gas focusing..... 19
4.2.2. LEBT optics with 2 H- sources..... 20
4.2.3. The Solenoids..... 22
4.2.3.a. The measurements..... 22
4.2.3.b. Magnetic stripping of H- 23
4.2.3.c. Emittance measurements at the end of the LEBT..... 26
4.2.4. Chopper..... 28
4.2.4.a. The Einzel lens modulation technique..... 30
4.2.4.b. The push-pull circuit test results..... 32
4.2.4.c. The Einzel lens..... 33
4.2.4.d. Einzel lens chopper experiments..... 36
4.2.5. LEBT Dipole Correctors..... 40
4.3. The RFQ..... 41
4.3.1. Tuner..... 48
4.3.2. Power Coupler..... 51
4.3.3. Power requirements of thick versus thin rods..... 52
4.3.4. Field flatness..... 52
4.3.4.a. Effect of field flatness and capture efficiency..... 55
4.3.5. Beam tests..... 57
4.3.5.a. Beam transmission efficiency measurements..... 57
4.3.5.b. Beam transmission as function of input power..... 60
4.3.5.c. Bunching as a function of input power..... 61
4.3.5.d. Transverse emittance..... 64
4.3.5.e. Energy..... 66
4.3.5.e.i. Energy spectrometer..... 67
4.3.5.f. Longitudinal Emittance..... 69

4.3.5.g. LEBT vacuum pressure and its effect on beam capture efficiency and current distribution..... 72
4.4. The MEBT.....73
4.4.1. MEBT Lattice.....75
4.4.2. Buncher..... 80
4.4.2.a. Buncher drawings and photographs.....81
4.4.2.b. Correcting transit time factor with grids..... 82
4.4.2.c. Low power RF measurements..... 83
4.4.3. Quadrupoles with embedded corrector dipoles.....86
4.4.3.a. Doublets..... 88
4.4.3.b. Higher order harmonics.....90
4.4.3.c. Strength of the embedded dipoles.....92
4.4.3.d. Sextupole components..... 93
4.4.3.e. Coupling..... 95
4.4.4. Beam measurements..... 96
4.4.4.a. Emittance of "flat" beam.....96
4.4.4.b. Emittance of "round" beam..... 98
4.5. Layout..... 99
5.Controls, Interlocks and Safety.....103
5.1. Controls..... 103
5.1.1. PLC..... 103
5.1.2. HRM..... 104
5.1.3. Motor Controls..... 104
5.1.4. PC-104.....104
5.2. Electrical Safety..... 104
5.3. RFQ Driver PA System Controls.....105
5.3.1. ACNET..... 105
5.3.1.a. Hardware setup.....105
5.3.1.b. ACNET devices..... 105
5.3.1.c. Analog readbacks.....105
5.3.1.d. Digital status.....105
5.3.1.e. Controls system response.....107
5.3.2. Hardware and device protection.....107
5.3.2.a. High level block diagram.....107
5.3.2.b. Driver PA.....108
5.3.2.c. RFQ..... 108
5.3.2.d. Summary..... 109
5.4. Critical Devices..... 109
6.Vacuum (Deprecated)..... 110
6.1. Source Vacuum..... 110
6.1.1. LEBT vacuum gauges..... 111
6.1.2. LEBT vacuum valves.....112
6.2. RFQ Vacuum..... 112
6.3. MEBT Vacuum..... 112
6.4. Vacuum Controls..... 112
7.Performance Goals.....114

7.1. Beam Current Definitions.....115
8.Cost Estimate..... 116
9.Pictures of the installed RFQ injector..... 118
10.Conclusion.....121
11.Acknowledgments.....121
11.1. People.....122
A.The RFQ.IN4 File..... 123
B.The BNL Injector..... 125
B.1 The BNL Injector (1982-1989).....125
B.2The BNL Injector (1989-present)..... 125
C.RFQ Problems..... 128
C.1Incorrect Energy..... 128
C.1.1Source of the problem.....128
C.2Poor Capture Efficiency and High Power Requirements.....132
C.3Power Coupler Sensitivity..... 134
C.4Unstraight Rods..... 135
References..... 137

Abstract

The present FNAL H- injector has been operational since 1978 and consists of a magnetron H- source and a 750 keV Cockcroft-Walton Accelerator. The upgrade of this injector consists of replacing it with a slit aperture and Cockcroft-Walton with a new magnetron with a round aperture and a 200 MHz RFQ. Operational experience from BNL (Brookhaven National Laboratory) has shown that a similar upgraded source and RFQ design will be more reliable and require less manpower to maintain than the present system.

1. Introduction

The present FNAL injector has been operational since 1978 and has been a reliable source of H- beams for the Fermilab program. At present there are two Cockcroft-Walton injectors, each with a magnetron H- source with a slit aperture [1]. Normally one source and Cockcroft-Walton is operational at any one time, with the other on stand by and ready to take over if there is a failure. With two sources in operation, the injector has a reliability of better than 97%. However, issues with maintenance, equipment obsolescence, and retirement of critical personnel, have made it more difficult for the continued reliable running of the H- injector. The recent past has also seen an increase in both downtime and source output issues. With these problems and others looming on the horizon, a new 750 keV injector is being built to replace the present system. The new system will be very similar to the one at BNL (Brookhaven National Laboratory) which has a similar magnetron source with a round aperture and a 200 MHz RFQ. This combination has been shown to operate extremely reliably [2].

2. The Plan

Based upon the experience at BNL and research/testing done at FNAL (HINS and source upgrade design studies) the plan is to replace the present injector with a round (dimpled) magnetron 35 keV source followed by a 750 keV RFQ. The design uses conventional technology such as solenoids, buncher cavity, quadrupoles and steering elements to match into the present drift tube linac (DTL). For a small additional cost of adding a second magnetron, solenoid and steering elements, uninterrupted maintenance and repair can be carried out. The design intends to reuse as much of the present power sources, beam line hardware and infrastructure in order to keep cost at a minimum. New items which are required are a buncher cavity, three solenoids and a 1 to 1.5 m long RFQ and RF amplifier (beam pipe and the associated hardware will require mechanical labor), and four quadrupoles. This design uses two magnetrons (and their respective focusing solenoids) mounted on a slide, followed by a chopper, RFQ and buncher (diagnostics and miscellaneous hardware). The following paper will describe the present injector and its operations and cost followed by sections that will describe in detail the design, physics and cost of the upgrade. For a comparison, the BNL pre-injector system is discussed in Appendix B.

3. Analysis of Present Operations

The current Cockcroft-Walton accelerators have been a reliable source of protons to the FNAL complex for over 40 years. This reliability has been attained because of the combination of the two Cockcroft-Walton accelerators and a group of skilled technicians who have maintained the systems over the years. Continued improvements have been made over time, but the basic system has remained the same.

There has been extensive preventive maintenance done to reduce the chance of having an equipment related failure. Also the ion source and high voltage regulation have taken a fair amount of tuning, typically on a daily basis. All these efforts have added up to a large number of “man

hours" to keep the systems running at an acceptable level. Figure 3.1 shows the beam output from the H- and I- sources in 2009. It can be seen from the histograms that the variations are large and thus continuous tuning is required to meet the beam demands for the downstream machines. The scale of the variation can be related to Booster turns where in this plot each bin is equivalent to approximately one Booster turn. For the rest of the analysis, the downtime logger, hand written log books, and the long time experience of the skilled technicians have been taken into account.

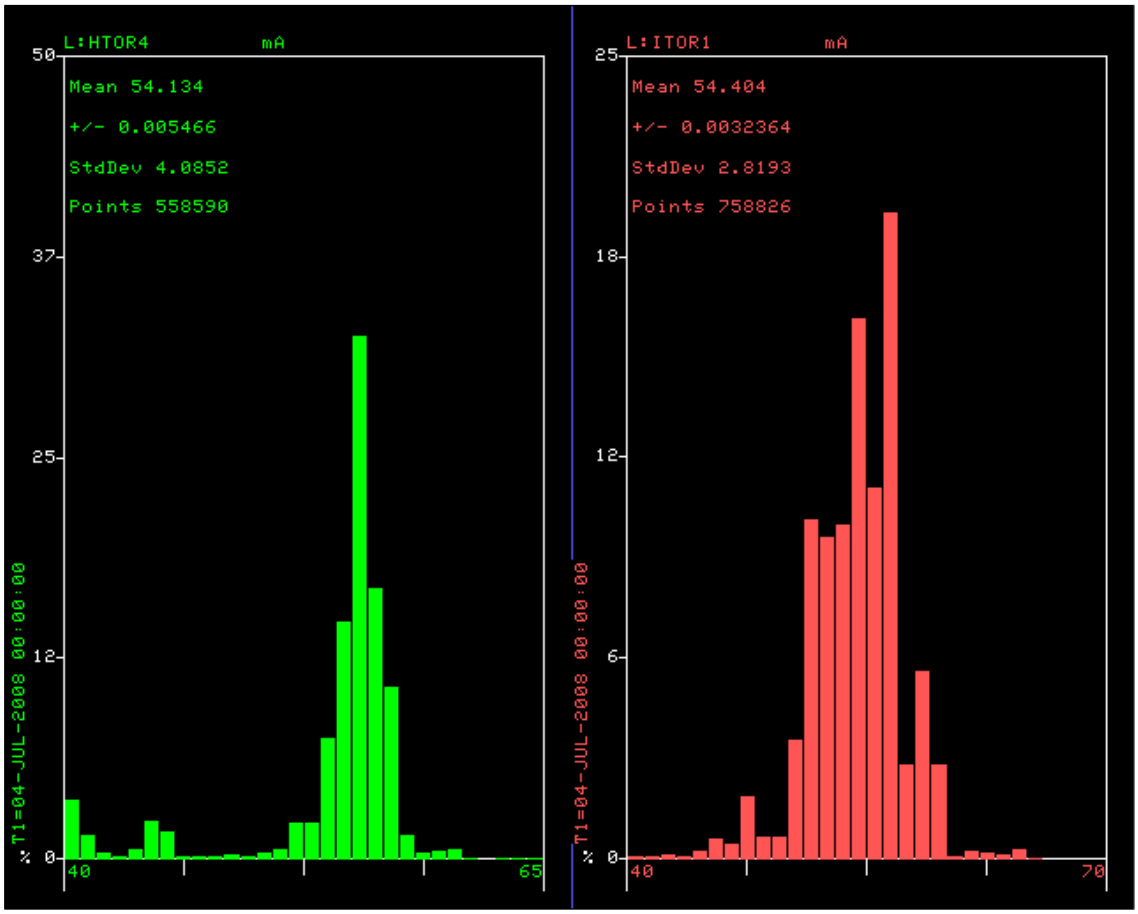

***Figure 3.1**: The variation in the H- (green) and the I- (red) sources over the past year. The large variation in intensity affects operations.*

3.1. Injector Downtime

The injector systems are crucial for the operation of the accelerator complex. They supply all of the particles used for neutron therapy, p-bar and neutrino production, and Tevatron collider operations. When there is an equipment problem this leads to downtime for the entire complex. The downtime is logged by operations and this log has been searched for injector downtime.

The total downtime for the injector over the past 9 years is about 300 hours. Figure 3.2 shows how the downtime is distributed over the injector systems.

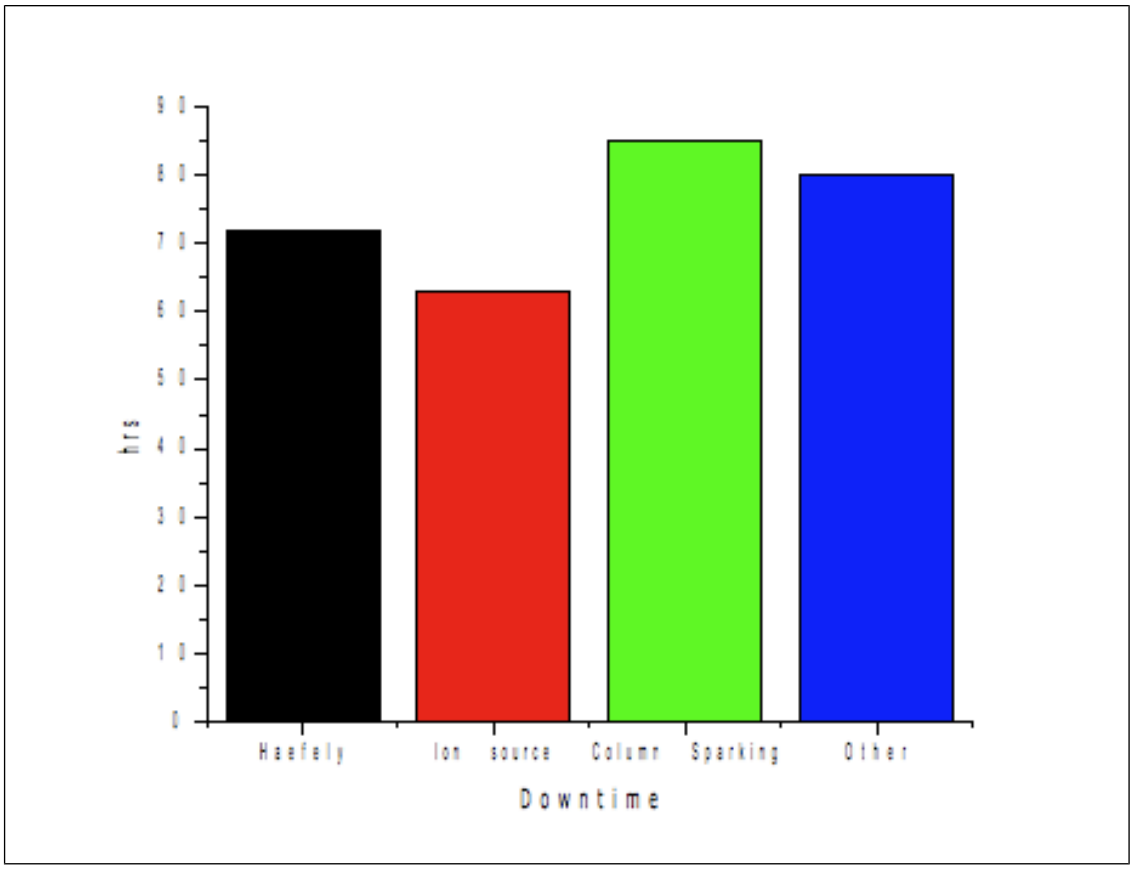

***Figure 3.2**: Downtime data in hours from Jan 2000 to the present.*

The downtimes can be broken down in order of largest downtime first:

(a) Column This presents the largest amount of down time because of sparking in the Cockcroft-Walton accelerating columns which results in missed beam pulses during the spark and afterwards for the high voltage to recover.

(b) Other These downtimes contain all the vacuum trips, repairs to elements in the 750 keV line, switching to the backup H- source and other small problems.

(c) Haefely The Haefely downtimes include the Haefely high voltage and its controls.

(d) Source The ion source downtime is specific to the H- magnetron and associated electronics.

Since the Cockcroft-Walton consists of the Haefely and accelerating column they can be combined and shown as a percent of downtime. When this is done, the Cockcroft-Walton dominates and takes up about 52% of the total injector downtime. The breakdown of the downtimes in percent is shown in Figure 3.3.

Many of the failures associated with downtimes also lead to a loss of redundancy. This puts the injector at risk of not being able to deliver beam when needed.

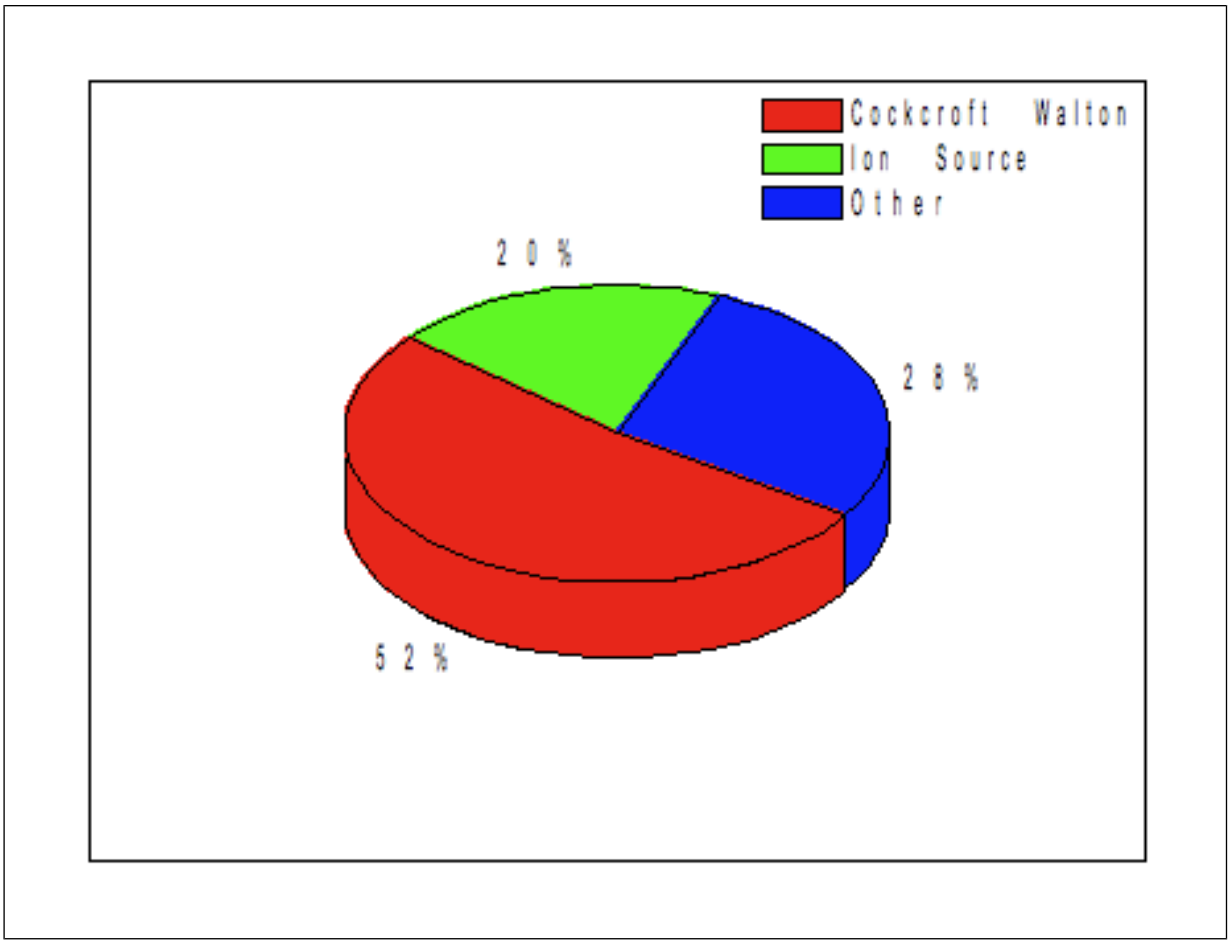

***Figure 3.3**: Percent of downtime by system. It is dominated by the Cockcroft-Walton.*

3.2. Maintenance and Failures

There are several complex tasks associated with the maintenance of the injector systems. These activities include electrical, mechanical and chemical systems that take a special skill set that takes years to acquire. Table 3.1 shows some of the normal maintenance that takes place in the injector. With the exception of the power and extractor tubes, the other items are preventive maintenance. There are many other tasks that are smaller and harder to quantify in a meaningful way.

3.3. Operating Costs

The actual cost of operating any system includes the number of man hours worked, cost of equipment, and power consumption among other factors. The Cockcroft-Walton accelerators require a large number of man hours coupled with a few high dollar maintenance items. The Pre-Acc group currently consists of 2 technicians, 2 Sr. Operations Specialists, and 2 Engineering Physicists. One of the Engineering Physicists is currently working on numerous other projects and will not be included in the following discussion. Figure 3.4 shows the percentage of man hours worked by full time employees on the injector systems and all other projects. The operations

specialists have retired and so the distribution of man hours will change in the near future.

There are numerous costs associated with the equipment itself. Some of the bigger material costs are listed in Table 3.2. The labor to perform these far outweighs the material costs. For example the ion pump rebuild requires about 120 man hours and the generator rebuild takes about 32 man hours to remove and reinstall.

Maintenance Item	Interval	Labor (man hours)
Generator Brushes		
Checking	Monthly	2
Replacing	Weekly	2
Water Resistor		
Flushing	Monthly	4
Changing	Annually	8
Ion Source		
Cleaning	Quarterly	16
Tuning	Daily	4
Cesium		
Change Boiler	Annually	8
Ion Pump		
Zapping	Quarterly	2
Change	Annually	80
Power Tubes	Biennially	4
Extractor Tubes	Annually	1
Interlock Testing	Annually	16
Clean Cold Box/Diaphragm	Annually	80

***Table 3.1**: Estimate of the man hours needed to keep the injector running.*

Work	Cost
Generator rebuild	$2.8k
Ion pump rebuild	$5k
Cockcroft-Walton pits cleanse	$5k

***Table 3.2**: The big material costs.*

3.3.1. Power consumption

Each Cockcroft-Walton consumes about 45 kW of electricity. There is also a significant heat load from the quad power supplies. The present operating parameters of the slit source+Cockcroft-Walton is summarized in Table 3.3.

Parameter	Value	Units
H- current	50 – 60	mA
Extraction voltage	18	kV
Arc voltage	140 – 160	V
Arc current	40 – 60	A
Repetition rate	15	Hz
Pulse width	80	μs
Duty factor	0.12	%
rms normalized emittance	ϵ_x=0.23, ϵ_y=0.27	π·mm·mrad
Cs consumption	0.5	mg/hr
Average power	$150\,\mathrm{V}\times 50\,\mathrm{A}\times 15\,\mathrm{Hz}\times 80\,\mu\mathrm{s}=9$	W

***Table 3.3**: Operating parameters of the present injector.*

3.4. Future Expenditures

Table 3.4 lists a set of possible future upgrades to the Haefely controls, ion source support electronics and the needed spares. The cost estimate for the ion source electronics upgrades are based on the HINS project designs.

With the retirement of the resident Cockcroft-Walton experts, there is a certain amount of risk that significant downtime will occur. Currently technicians are being trained to replace the experts, however the loss of 82 years of experience will take some time to recover.

Project	Cost
Haefely HV regulator	unknown
Spare anode power supply	$22k
Spare chopper power supply	$6k
Source heaters DC power supplies	$9k
Source extractor pulser	$6k
Ground vacuum turbo pump	~$30k

***Table 3.4**: Future cost to maintain the injector hardware.*

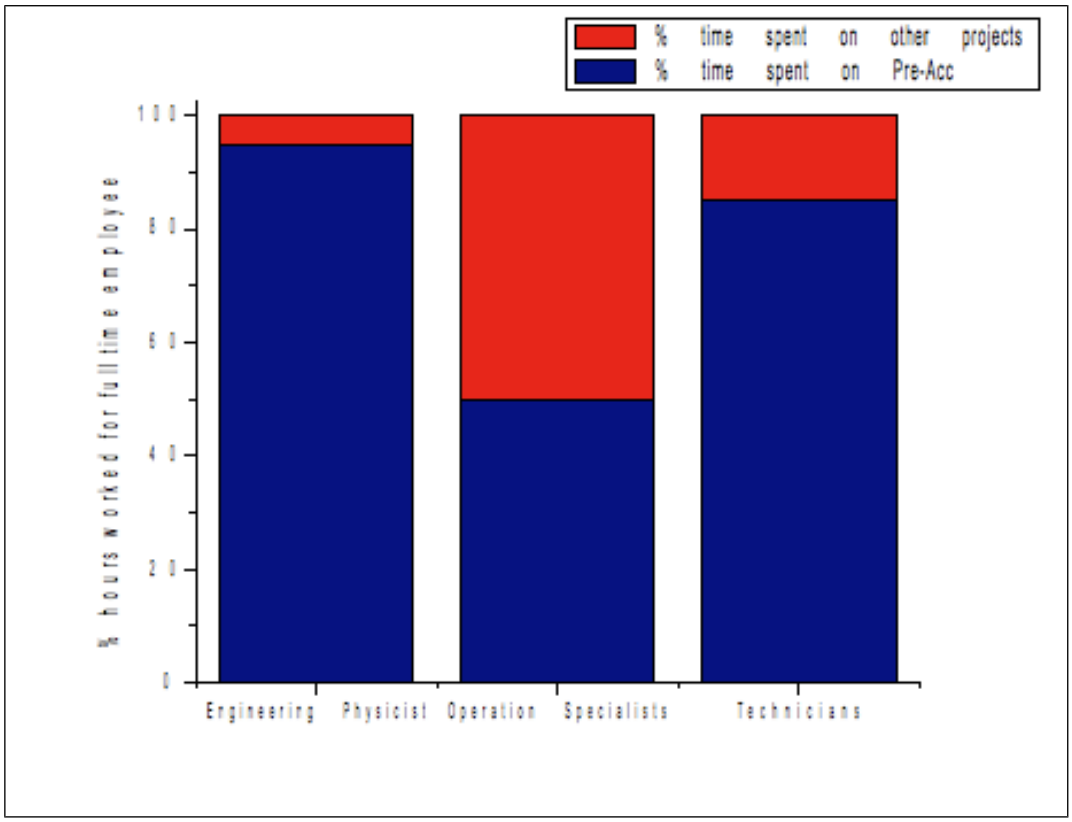

***Figure 3.4**: The breakdown of hours worked by the full time employees of the Pre-Acc group.*

4. The New Injector Design

The new design can be divided into two transport lines: the low energy beam transport (LEBT) and the medium energy beam transport (MEBT). The LEBT is the transport line before the RFQ and the MEBT is the transport line from the end of the RFQ to the beginning of the DTL. A preliminary drawing of the new injector is shown in Figure 4.1.

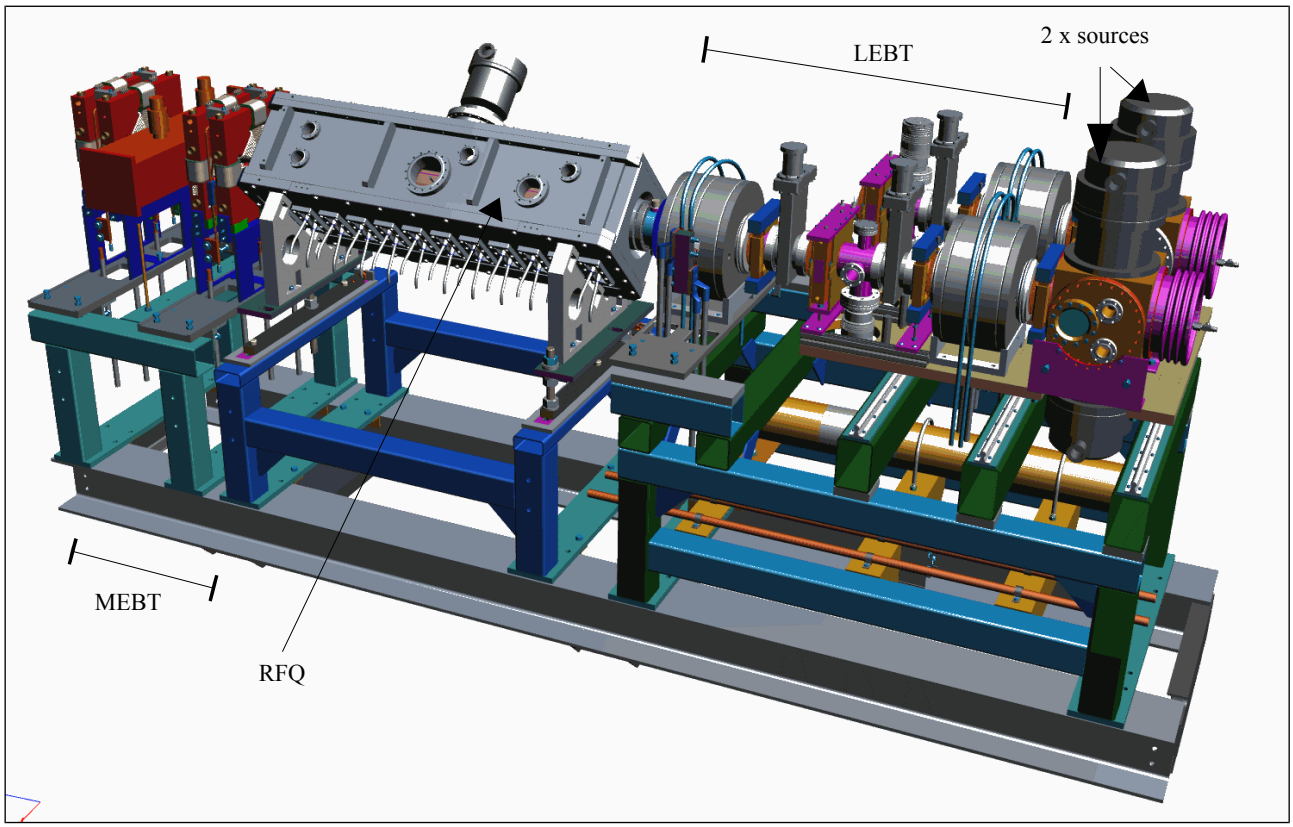

Figure 4.1: *A 3D drawing of the new injector. Shown here are the 2 H- sources for redundancy, a short LEBT, RFQ and a very short MEBT.*

For the LEBT, the proposed design will contain two H- magnetron sources for increased reliability. Each H- magnetron source will be the round type and will be mounted on a slide. (See Figures 4.1 and 4.14). The beam out of the source is at 35 keV and has been measured to be > 60 mA and thus space charge dominated. Therefore, it must be focused with a solenoid right out of the source to preserve its emittance. The paraxial beam is transported through a short beam line to one more solenoid which strongly focuses it into the small aperture (< 1 cm radius) at the entrance of the RFQ. Neutralization from the residual gas focusing of the H- beam because it has been shown on the test stand that a "not so good" vacuum (~3×10^{-6} Torr) helps focus the beam and increases transmission efficiency at the end of the RFQ. (Note: BNL uses Xe gas rather than residual gas because the cryo pumps that they use gives very good vacuum [3]. It may be necessary to use Xe gas in this injector at a later time.) An Einzel lens installed near the entrance of the RFQ will be used as the chopper because it is much easier to chop the beam at low energy and also there is insufficient space in the MEBT. It is necessary to place the chopper very close to the RFQ because a pure electrostatic kicker will de-neutralize the H- and any advantage of gas focusing will be lost during the chopping process [4].

The RFQ will focus, bunch and accelerate the H- beam from 35 keV to 750 keV. Once the

beam exits the RFQ it has a tendency to blow up both longitudinally and transversely and thus the MEBT must be short and must contain quadrupoles and a buncher for focusing. The proposed MEBT which is < 80 cm long consists of two doublets and one two gap buncher. Doublet focusing has been chosen because the beam exiting the RFQ is round. The buncher is nearly identical to the operational BNL buncher and is used to keep the beam from debunching longitudinally before Tank 1.

Using both empirical data and computer simulations, it is predicted that about 88% of the beam can be transported from the H- source to the end of the first DTL. If the source can produce 43.5 mA of H- beam (Note: the BNL source routinely produces 90 – 100 mA of H- beam [2]), it is predicted that 37.5 mA will be at the end of the first DTL. For a comparison, the present Cockcroft-Walton system transports 37.5 mA to the end of the first DTL for a source current of ~60 mA . See Figure 7.1.

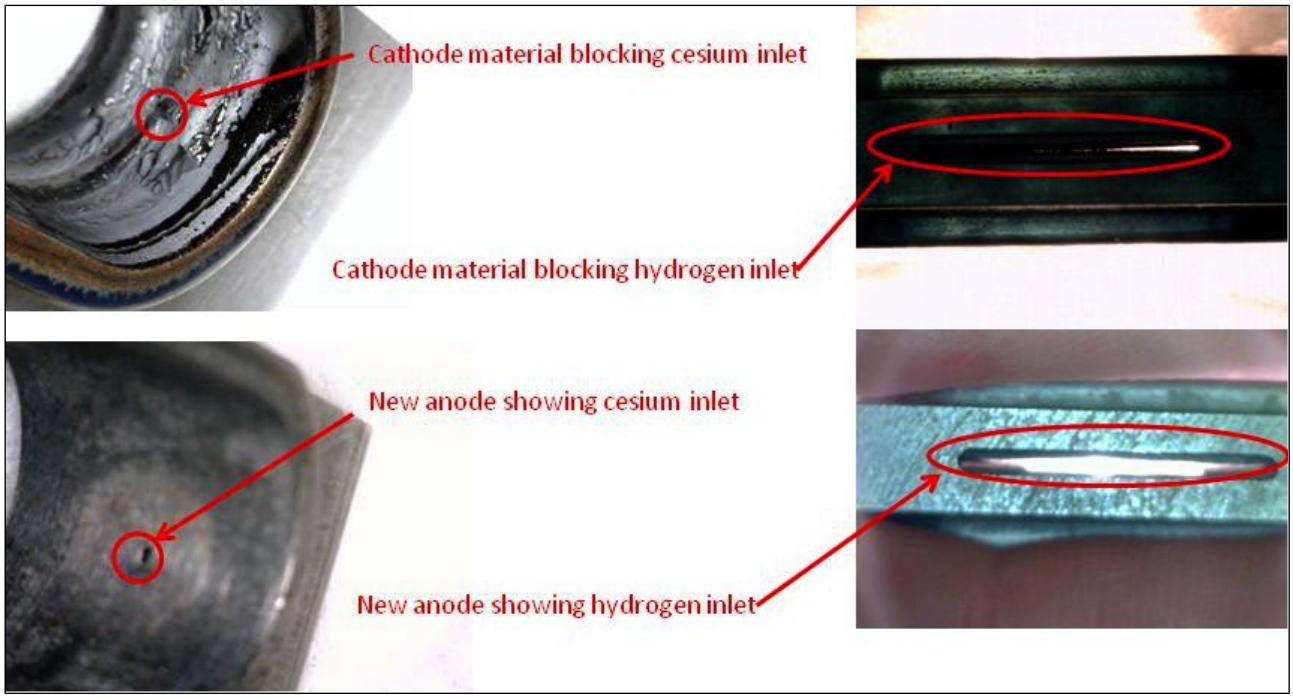

Figure 4.2: *This figure compares the postmortem of a broken source to a new source. High arc current operation causes the cathode to erode and to deposit some of it onto the anode which blocks the cesium inlet.*

4.1. The H- Source

FNAL has been using an H- magnetron ion source for ~34 years and as such has accumulated much experience and equipment associated with this source. Following the initial FNAL use, ANL (Argonne National Laboratory), DESY and BNL have also adopted this source design to produce H- beams for injection into their linacs. Originally, the source had a slit aperture producing a ribbon shaped beam which was transformed to an elliptically shaped beam which could be further accelerated, transported and injected into a linac. BNL improved it using a circular aperture to produce a round beam which could be more easily focused and injected into an RFQ. Recently, a source, very similar to the BNL source, was built and tested at FNAL for the HINS R&D program. The recent work to produce a circular-aperture direct-extraction H- source for the

HINS project is conveniently applicable as a source for this plan. Likewise, two sources which have been received from Argonne recently due to the dismantling of the Intense Pulsed Neutron Source (one was loaned to them many years ago and the second ANL built as a spare) has given many significant parts for assembling the sources needed for this plan. This will greatly reduce the effort, cost and time to have a working source for the RFQ tests and operation.

Like most accelerator equipment the H- source is operated at or near its maximum output and thus has a variable and limited lifetime. However, the evolution of the magnetron source at BNL from slit/flat groove geometry to the present circular/dimpled aperture geometry has vastly improved its lifetime. Table 4.1 summarizes the effects of these geometric changes. It can be seen from this table, that the important parameter which is crucial for the improved lifetime is the power efficiency. Presently, the BNL circular aperture source only requires 10 A of arc current to obtain 100 mA of H- beam which translates to 67 mA/kW. The present FNAL slit source, on the other hand, requires a much higher arc current of 50 A to obtain 50 mA of H- beam which translates to 8.3 mA/kW. This means that the BNL circular aperture source is 8× more efficient than the FNAL slit source which explains why the BNL source has a lifetime 2× to 3× longer than the present FNAL source. Postmortem examination of the FNAL source also shows that running at high arc current causes cathode erosion. Figure 4.2 shows cathode material (molybdenum) deposited and blocking the cesium inlet in the anode.

With the experience FNAL has had with magnetron sources and elsewhere it is a logical choice to use it for this plan. The low duty-factor (0.2%), modest intensity (50 to ~100 mA), pulsed (15 Hz) H- ion source of the magnetron surface-plasma type is suitably matched to the capabilities of the present FNAL Linac and Booster to meet the objectives of the FNAL program. It is not in the same league with the high current and high duty-factor modern H- sources which are used to produce intense secondary beams. Still, with proper attention and the manpower to maintain it, the magnetron source has and can continue to meet the capacity of the FNAL Linac and Booster.

The evolution of the BNL H- source					
Cathode	H- current (mA)	Arc current (A)	Arc voltage (V)	Power efficiency (mA/kW)	Lifetime (months)
slit/flat	50	150	150	2.2	-
slit/grooved	50	50	150	6.7	-
circular/dimpled	100	10	150	67	6 – 9
The FNAL H- source					
slit/flat	50	150	150	2.2	-
slit/grooved	50	50	120	8.3	3.5 (average)

Table 4.1: *The evolution of the magnetron source at BNL and FNAL.*

4.1.1. Extraction

The current operational sources are surface plasma magnetrons that have a slit aperture. The sources are mounted so that the aperture points down with a 90° bend magnet that helps sweep away electrons and shape the beam for injection into the accelerating column. See Figure 4.3.

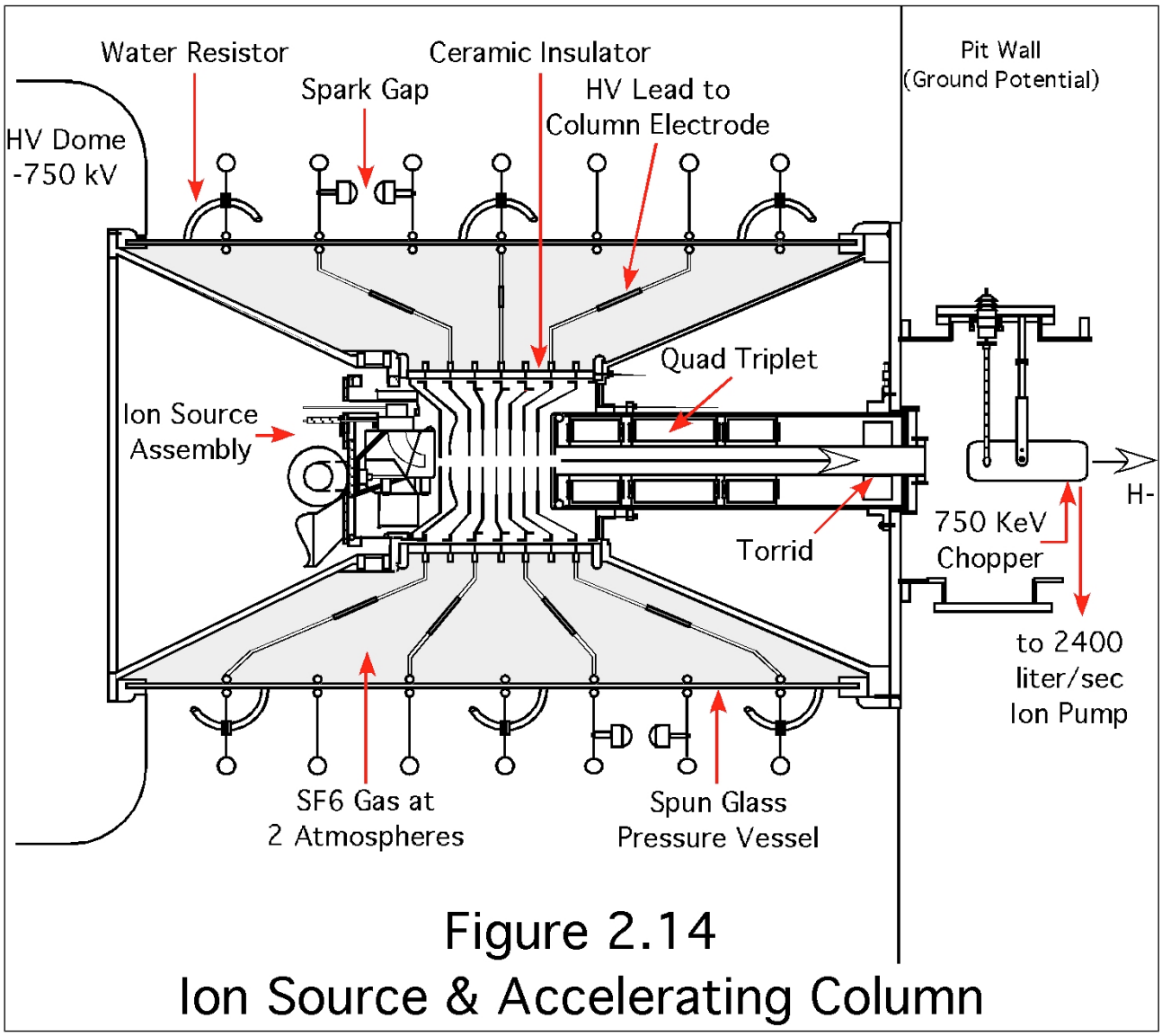

Figure 4.3: *H- ion source and Cockcroft-Walton assembly (from Linac Rookie Book).*

The H- ions are extracted through a slit opening in the anode cover plate by an H shaped extractor electrode with a positive potential of 12 kV to 20 kV. The extraction scheme is shown in Figure 4.4. With the source floating at 750 kV the H- ions are accelerated to ground potential.

The low extraction voltage requires the source to run with a high arc current to achieve the required H- beam current (See Table 4.1). With the high arc current and voltage, the power efficiency is on the order of 8 mA/kW. The high arc current and low power efficiency contribute to a source lifetime of 3 to 4 months. Typical aging of sources is caused by cathode erosion that deposits material on the anode which restricts the cesium and hydrogen inlets. Once a source is removed from operations it is cleaned and its worn out parts replaced.

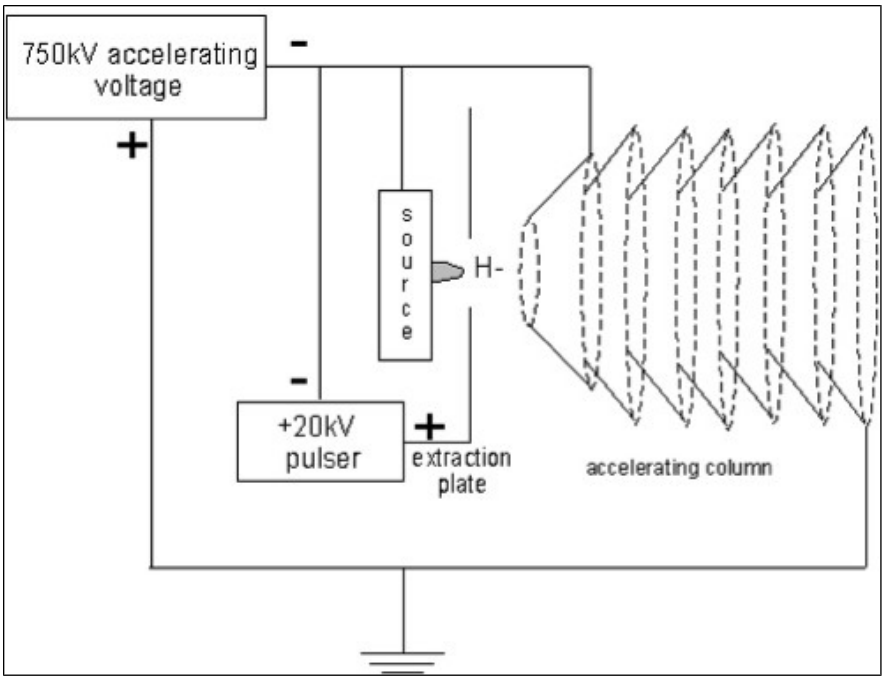

Figure 4.4: *The schematic of the Cockcroft-Walton extraction scheme.*

The new source extraction scheme is shown in Figure 4.5. It is different than the current operational system in that the extraction voltage is the acceleration voltage. The higher extraction voltage is more effective at pulling H- out of the source, which allows the source to run with a much lower arc current and thus better power efficiency. This contributes to its longer lifetime.

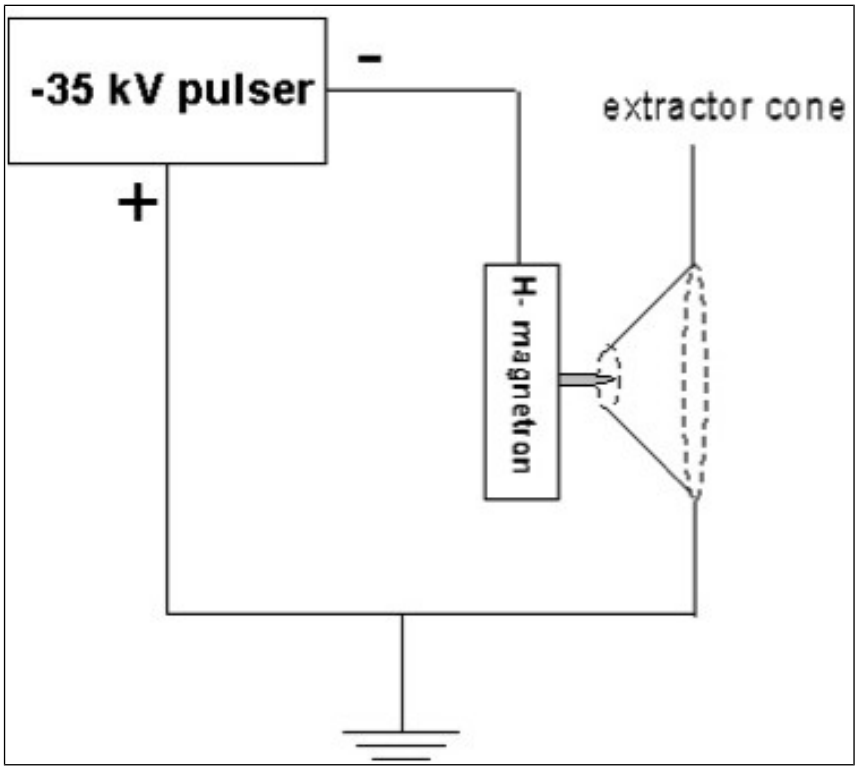

Figure 4.5: *BNL extraction scheme. The extraction voltage is the accelerating voltage.*

The negative 35 kV extraction pulser design is a modified version of the FNAL extractor and is similar to the one used at BNL. The pulser is capable of delivering –40 kV, 400 mA pulses at 15 Hz. It pulses a floating HV relay rack that contains source electronics and the hydrogen bottle, that are tied to the source body (anode), at –35 kV. This provides the potential difference for the extraction/accelerating voltage since the extractor cone is tied to ground.

4.1.2. FNAL source design

The new source design is a round aperture magnetron which was developed by BNL. The cathode has a spherical dimple that has a focal length of 0.101". The dimple is located behind the anode aperture and is used to focus the H- produced here for efficient extraction. The cathode design also has a smaller plasma region than previous magnetron designs. The cathode geometry is shown in Figure 4.6.

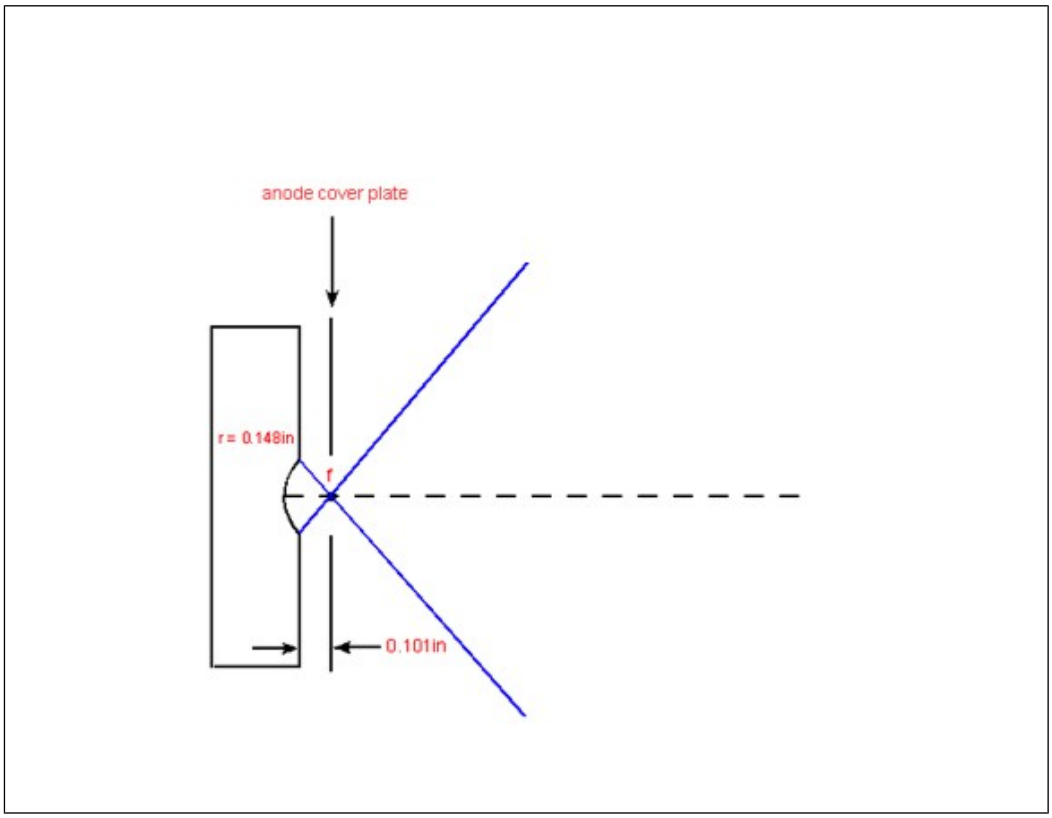

Figure 4.6: *Spherical cathode dimple geometry.*

The extractor cone shown in Figure 4.7 is similar to the one that BNL uses. It has an angle of 45° and an aperture of 0.26". The extraction gap, distance from the anode cover plate to the extraction cone is currently set to 0.095". This gap needs to be able to hold off 35 kV since it is the extraction and acceleration gap. The cone tip is made of molybdenium to minimize erosion due to co-extracted electrons. This gap and the aperture diameters will be optimized after the beam parameters required for the transport line are determined.

Figure 4.8 shows the source mounted in a reentrant manner in the vacuum chamber. The source mounting was designed for ease of assembly and disassembly. The extractor cone is connected to the vacuum chamber by a short set of bellows that provides a ground connection and a vacuum break from the rest of the LEBT. Since the source output is highly divergent due to space charge effects, the source is located 3/16" from the downstream aperture of the vacuum chamber.

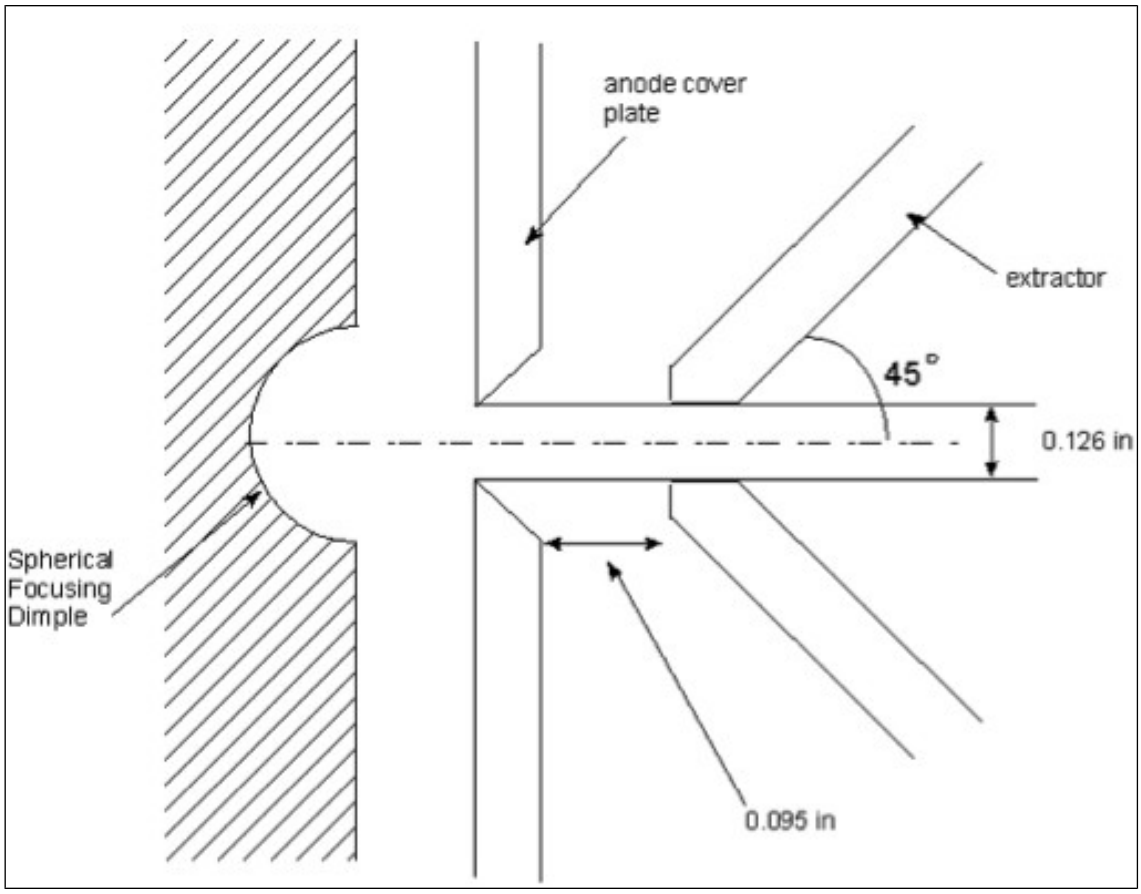

Figure 4.7: *Extraction region of the source.*

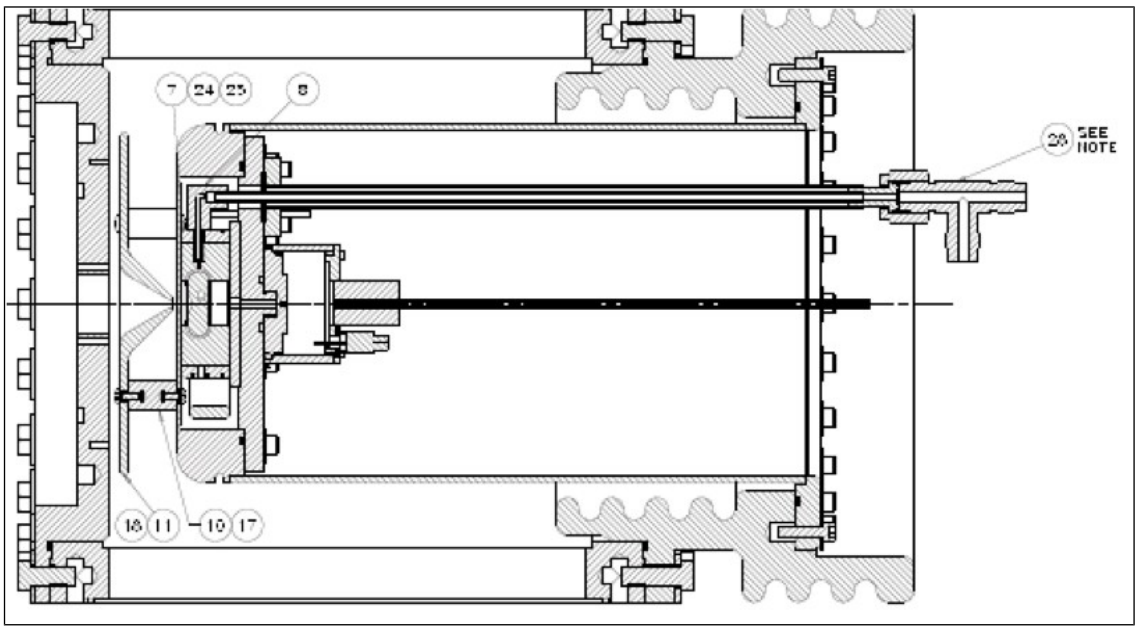

Figure 4.8: *The source chamber. Beam emerges from the left side of the chamber.*

4.1.3. Testing the source in the test stand

The new source is currently mounted on the test stand which has an Einzel lens for focusing, a toroid and a Faraday cup for measuring beam current and horizontal and vertical slit type emittance probes. Figure 4.9 shows a drawing of the test stand. The test stand was used for the development of the first generation of H- ion sources used at FNAL. The Einzel lens is sufficient for focusing low intensity beams (< 50mA) but does not have enough strength to focus higher intensity beams produced by the new source. For example, simulations using SIMION show the beam scraping in the Einzel lens when the beam current is 60 mA. See Figure 4.10. In order to measure the total beam coming out of the new source, the test stand was reconfigured so that the toroid is at the output of the source cube. Even though this is a better arrangement for measuring beam current coming out of the source, the beam current may still be higher than what is measured because the beam is very divergent due to space charge. A better measurement will come once the source is installed in the LEBT.

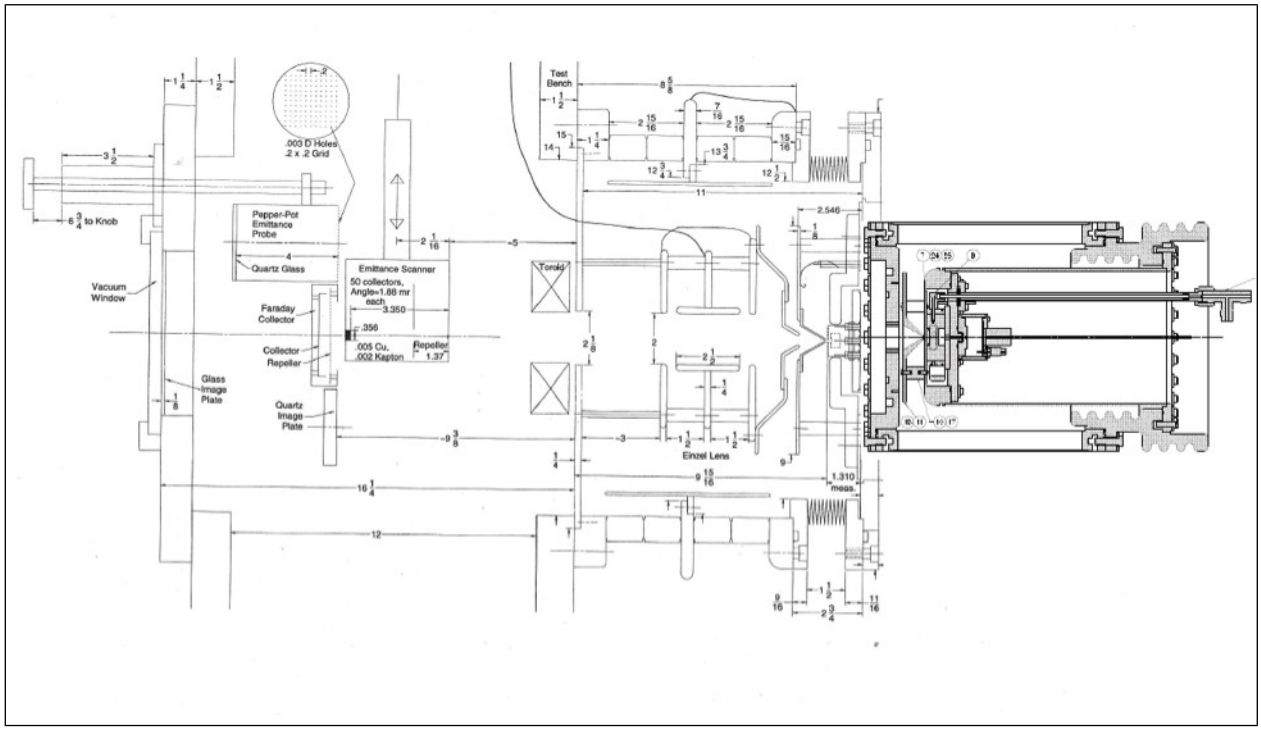

Figure 4.9: *A drawing of the test stand with the new H- source installed.*

4.1.3.a. *Perveance measurement*

With the toroid mounted at the source cube aperture the maximum beam current measured was 90 mA with 35 kV extraction. Figure 4.11 shows the perveance curve for the source with 15 A of arc current. Perveance is defined to be

$$I_{\text{H-}} \propto V_{\text{extract}}^{3/2} \tag{1}$$

where $I_{\text{H-}}$ is the H- current and V_{extract} is the extraction voltage.

The extracted beam current reaches saturation and starts to roll over at 35 kV because all of the available H- are extracted.

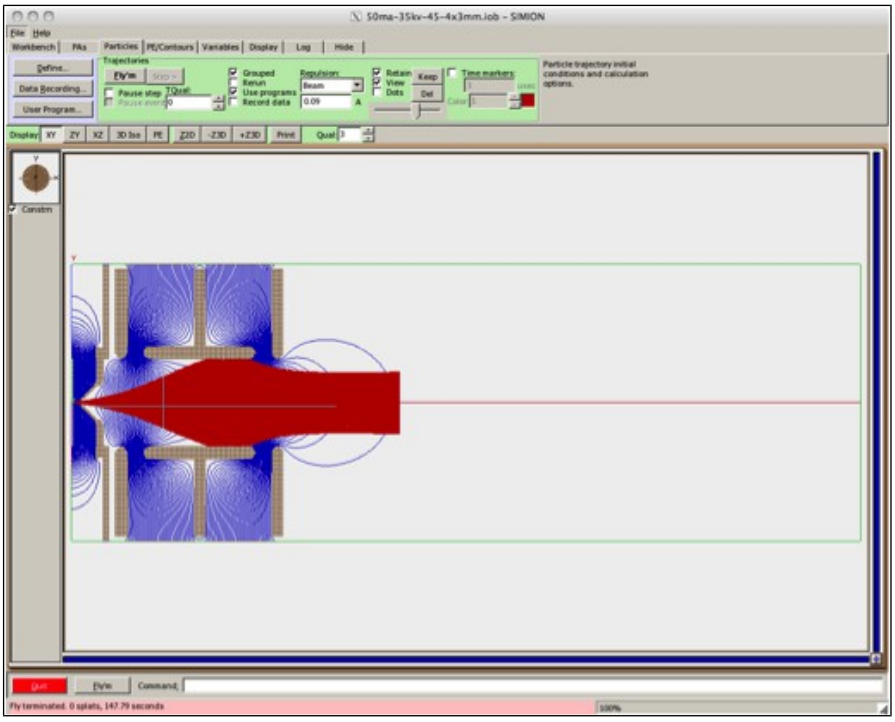

Figure 4.10: *SIMION simulations of the test stand optics with 60 mA H- beam. It is clear that the beam is scraping on the Einzel lens and therefore the entire beam does not make it to the toroid or the emittance probes.*

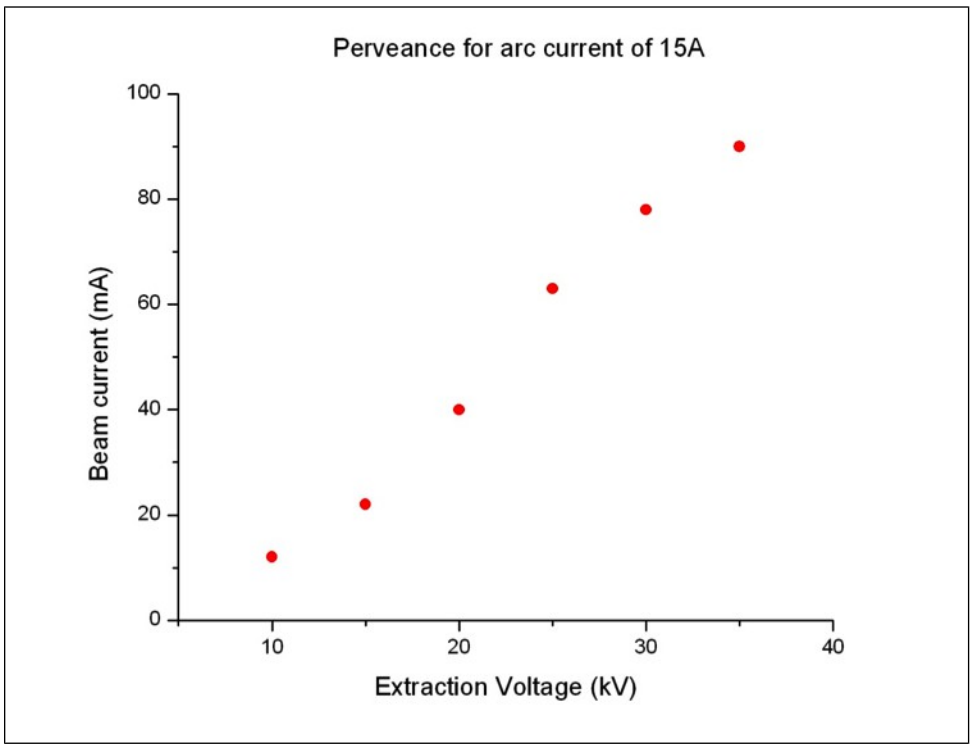

Figure 4.11: *Perveance curve of the new H- source with 15 A of arc current.*

4.2. The LEBT

The H- beam from the source is space charge dominated and at low energy its emittance will blow up if there is insufficient focusing. The combination of gas focusing and solenoid focusing will enable the transport of the H- beam with smaller losses to the entrance of the RFQ than without gas focusing. However, care must be used with gas focusing because if the gas pressure is too high or the transport length is too long, stripping of the H- ions will become a problem. Furthermore, if an electrostatic chopper is used for low energy chopping, the ions from residual gas focusing will be swept away by the electric field if it is turned on for too long. The solution to this problem is to place an Einzel lens as close as possible to the entrance of the RFQ. The use of the Einzel lens as a chopper is fully discussed in Section 4.2.4. A photograph of the LEBT line under test is shown in Figure 4.12.

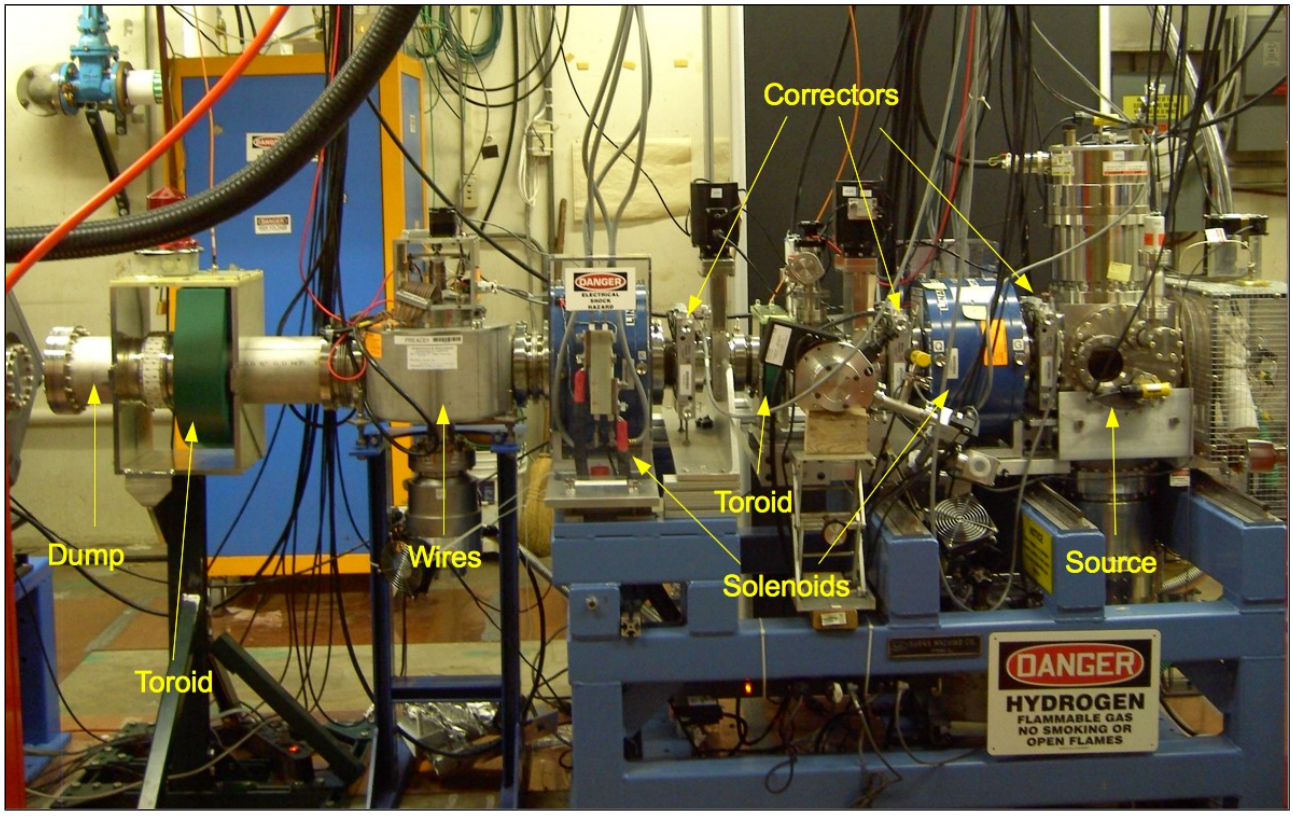

Figure 4.12: *The LEBT test line.*

4.2.1. Focusing with gas

The idea behind gas focusing is completely described by Reiser [5]. For example, when low pressure Xe gas is introduced, one or both electrons can be stripped from the H- ions to form either H0 or H+ ions, and Xe can form Xe+ ions and electrons. The electrons are repelled by the H- beam to the wall while the H+ and Xe+ ions are trapped in the H- beam region. The H+ and Xe+ ions attract and focus and neutralize the H- beam. The gas that is used is Xe because its high atomic mass (131.3 amu) keeps the escape velocity of the Xe+ ions low and so keeps the Xe+ ions trapped.

A crude calculation which assumes that when the H- is over-neutralized, the amount of focusing of H- from the Xe+ ions, independent of beam current, is (Eq. 4.308 of Reiser [5])

$$a = 1.74\times10^{5}\epsilon_n \frac{1}{(V_b V_i)^{1/4}} \tag{2}$$

where $\epsilon_n = (0.15\times10^{-5})\pi\,\mathrm{m\cdot rad}$ or $1.5\pi\,\mathrm{mm\cdot mrad}$ (using $5\times$ rms emittance, see Table 4.6) is approximately the output emittance of the H- source, $V_b = 35\,\mathrm{kV}$ is the potential difference applied to the H- beam, $V_i = 12.1\,\mathrm{V}$ is the ionization potential of Xe when the H- beam goes through Xe gas and a is the radius of the focused beam. Putting in these numbers, the radius of the focused H- beam is $a = 3.2\,\mathrm{cm}$ (1.25") and thus implies that the beam pipe must be at least 2.5" in diameter.

In fact, BNL has demonstrated that using low pressure Xe gas at 3.7×10^{-6} Torr the transmission efficiency of H- from the source to the entrance of the RFQ is improved by 30% over optics without the Xe gas [3]. Therefore, it is important to use some type of gas focusing in the FNAL LEBT. It turns out that the residual gas left in the LEBT is sufficient for this purpose. However, since the gas does strip some H-, some intensity will be lost. For example, the following is a simple formula which relates the fractional loss per unit length λ of H- to the molecular density ρ[m^{-3}] of Xe in the beam pipe and ionization cross section σ [m^2] of Xe:

$$\lambda = \rho\sigma_i \tag{3}$$

and for the proposed LEBT, at $\rho = n_x\times(3.7\times10^{-6})[\mathrm{Torr}] = 1.2\times10^{17}\ \mathrm{m}^{-3}$ 20°C[6][1] and for $\sigma_i = 3\times10^{-19}\ \mathrm{m}^2$, 35 keV H- ions impacting on Xe [7], the fractional number of H- lost per meter is $\lambda = 0.036$. The LEBT is about 1 m long, so about 3.5% of the H- will be lost from gas stripping. Note: BNL measured 32% of H- loss from Xe gas stripping (and 20% loss by using Eq. (3)) for their 4 m long LEBT [3]. Therefore, it can be expected that gas stripping for a 1 m long LEBT can be as high as 8%, i.e. a factor of two larger than the back of the envelope calculation shown above.

Another consideration is that it takes finite time for neutralization to take place. (Eq. 4.285 of Reiser [5]) gives the neutralization time τ_N to be

$$\tau_N = \frac{1}{\rho\sigma_i v} \tag{4}$$

where v is the speed of the H- ions in $\mathrm{m\cdot s^{-1}}$. Using the same numbers for calculating λ, $v = 0.00864c$ for 35 keV H- ions, the neutralization time is about 10 μs using Eq. (4). However, BNL has measured it to be about 40 μs, so the pulse length must be increased by this amount, i.e. if the pulse length is 120 μs, then only the last 80 μs is useable.

In practice, the LEBT vacuum is dominated by H_2 gas and the LEBT pressure is ~ 2.5×10^{-6} Torr even with 2 × 350 L/s turbos pumping in the LEBT when the source is running. Therefore, the LEBT vacuum is sufficiently poor that it is not deliberately spoiled with Xe. An analysis of the effect of H_2 neutralization is discussed in section 4.3.5.a and 4.3.5.g.

4.2.1.a. *Demonstration of gas focusing*

The H- test stand shown in Figure 4.32 has been used to demonstrate focusing with N_2. Figure 4.13 shows the result of introducing air into the test stand which spoils the vacuum. The beam currents shown here have been measured on the Faraday cup downstream from the Einzel lens. The Einzel lens has been adjusted to focus the beam into the Faraday cup. When the vacuum is

1 $n_x = 3.3\times10^{22}\,\mathrm{m}^{-3}/\mathrm{Torr}$ is the number density of gas per torr at 20°C calculated from Loschmidt's constant.

"good" at 10^{-6} Torr, the H- beam current is ragged and looks like it has hit a limiting aperture (probably the Einzel lens). When the vacuum is spoilt and is at 10^{-4} Torr, there is much better focusing of the beam because the current is very flat. H- stripping is also clearly evident here because the beam current is lower.

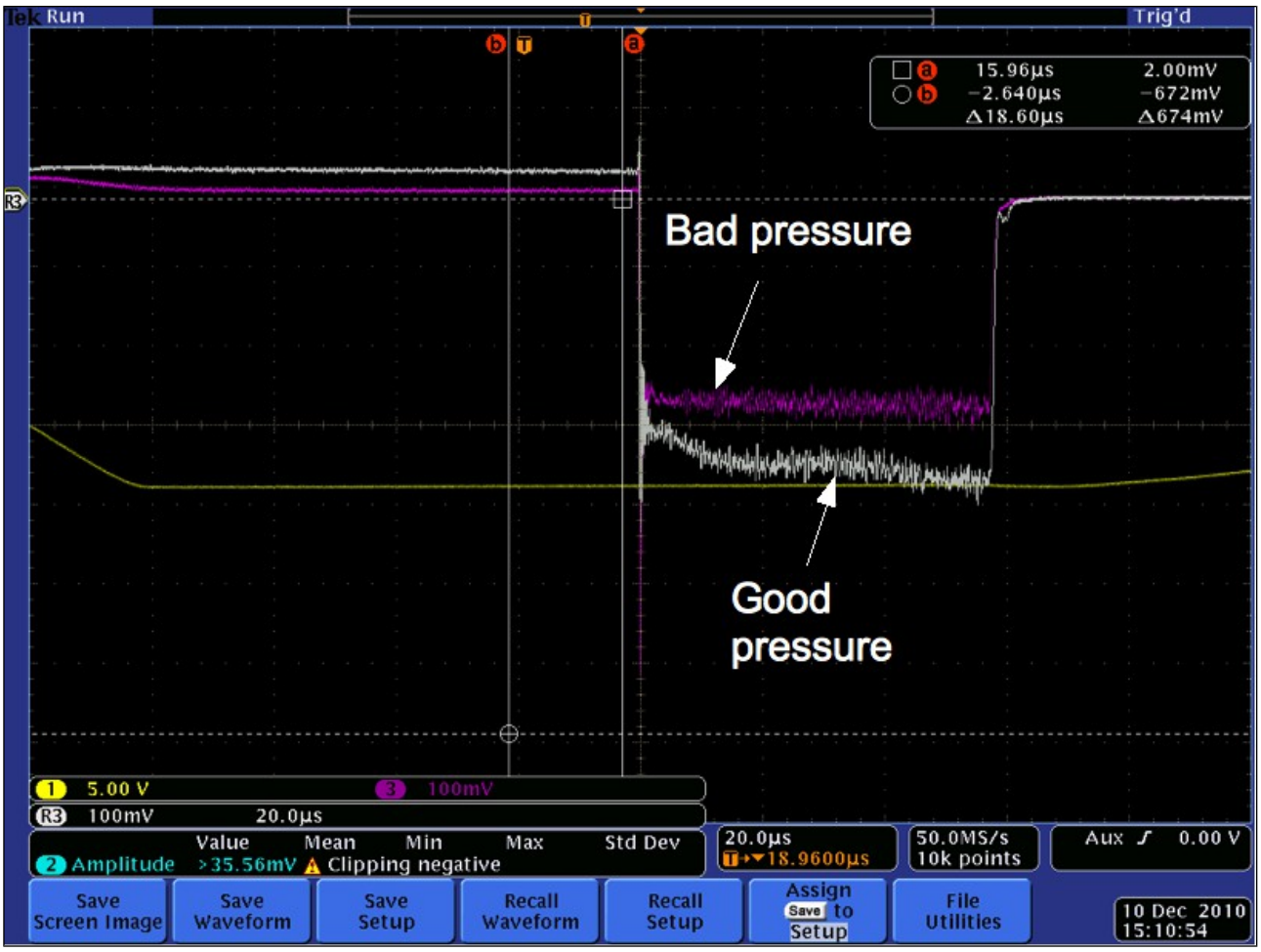

Figure 4.13: *When N_2 (air) is introduced into the test stand, the beam current measured on the Faraday cup becomes flat (magenta).*

4.2.2. LEBT optics with 2 H- sources

The LEBT has been designed with two H- sources to ensure high reliability. Figure 4.14 shows the proposed layout of the LEBT with source A as the operational source. Both source A and B are mounted on a slide so that either source can be slid into the injection line for operations.

The LEBT optics is a standard one where two solenoids are separated by a short distance so that the beam at the source and at the entrance of the RFQ are at the focal points of each solenoid. In the present design, the LEBT is about 1.2 m from the exit of the source to the entrance of the RFQ. From the BNL experience, an LEBT which is < 2 m (6 ft) is ideal. The strength of the solenoids have been calculated with Trace2D and the results are summarized in Table 4.2. Figure 4.15 is the Trace2D result which matches the output emittance of the source (BNL values have been used here because the proposed source will be similar to theirs) to the input emittance of the RFQ which has been provided by the manufacturer. (See Table 4.5 which has the RFQ parameters

provided by the manufacturer). For historical interest only, see section 4.2.3.c for measured emittance values.

Trace2D Element ID	Element Type	B_z (gauss)	Focal Length (cm)
2	Solenoid	2694	19.6
4	Solenoid	2658	20.1

Table 4.2 *Summary of the relevant parameters used to match a DC H- ion beam from the source to the entrance of the RFQ for source A and B configurations See Figure 4.15 for the Trace2D element ID. (For historical interest only).*

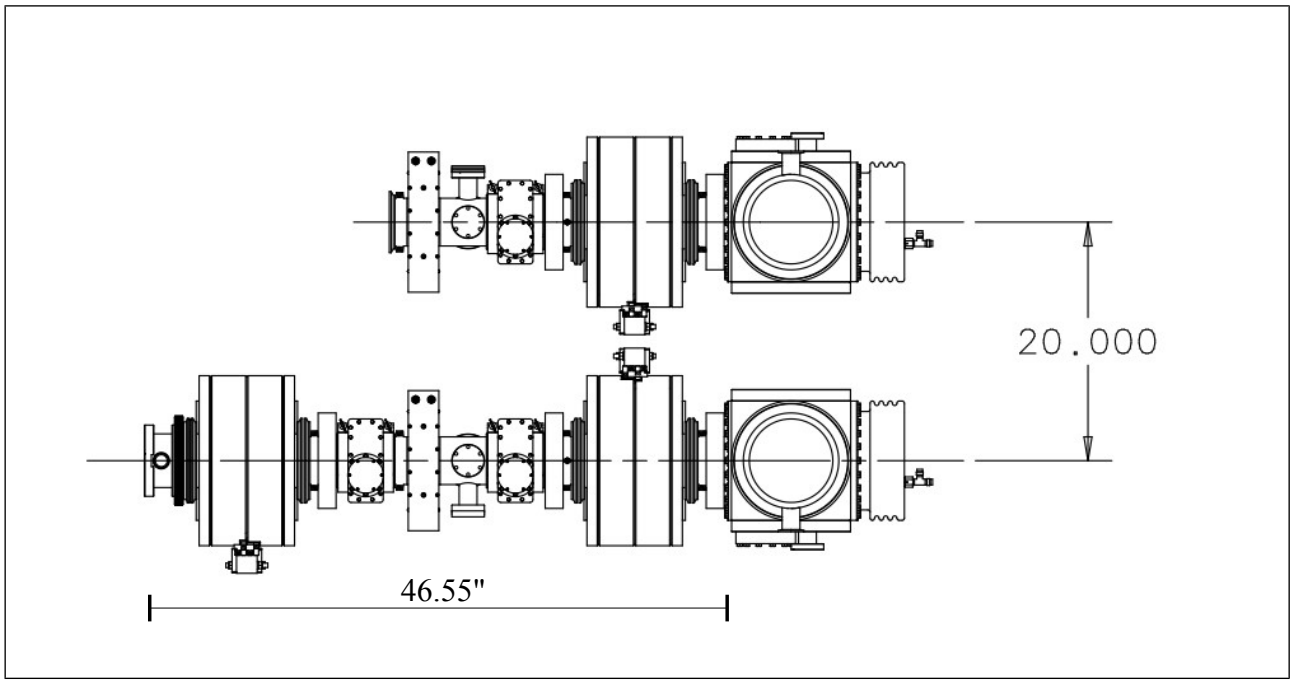

Figure 4.14: *The LEBT has 2 H- sources but only one is used at any given time. The two sources are mounted on a slide so that either source can be slid into operation. The length of the LEBT from the end of the source to the start of the RFQ is about 1.2 m.*

The focal length f_{sol} of each solenoid is shown in Table 4.2 and have been calculated using the well-known formula

$$f_{\text{sol}} = \frac{4(B\rho)^2}{\int_{L_{\text{sol}}} B_z^2 dz} = \frac{4(B\rho)}{B_z^2 L_{\text{sol}}} \tag{5}$$

for constant B_z in the solenoid, and $(B\rho)[\text{T m}] = 3.3357\, p[\text{GeV/c}]$ is the magnetic rigidity and for 35 keV H- ions p = 8.1 MeV/c, B_z is the longitudinal magnetic field of the solenoid and L_{sol} = 8" (= 20.3 cm) is the length of the solenoid.

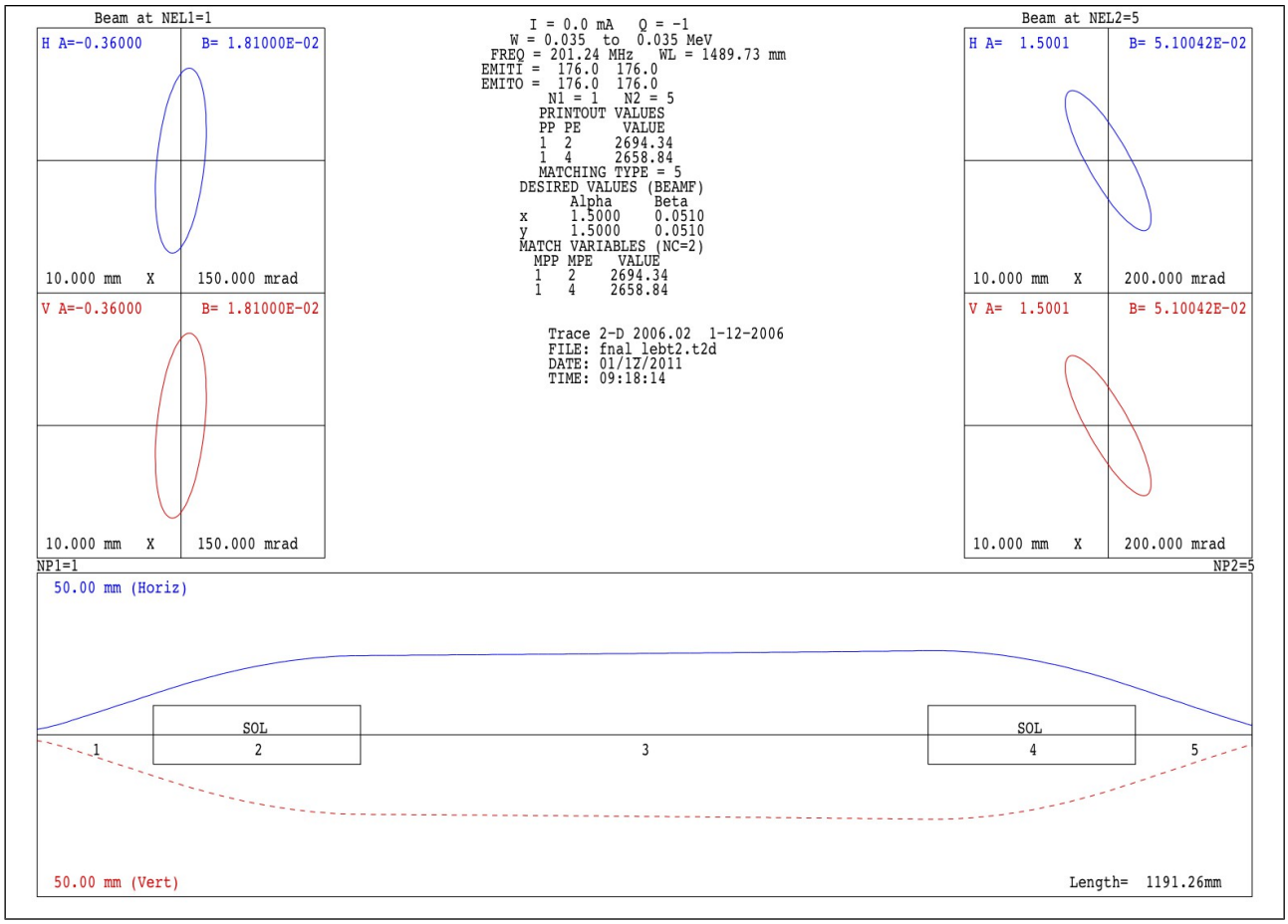

Figure 4.15: *The optics of the LEBT for zero current H- beam from the source to the entrance of the RFQ using the geometry shown in Figure 4.14.(For historical interest only).*

4.2.3. The Solenoids

The solenoids have been designed by V. Kashikhin which have been simulated to have magnetic properties compatible with the results of the optics simulations. A longitudinal view of the solenoid is shown in Figure 4.16 and pictures of the assembled solenoid are shown in Figure 4.17. Compared to the BNL solenoid, this solenoid is shorter by about 1.5" but keeps the same outer radius. The bore radius, however, has been increased from 4.255" to 4.75" so that there is space to align the axis of the 4" beam pipe to the magnetic axis of the solenoid.

4.2.3.a. *The measurements*

Three solenoids have been manufactured (as of 16 June 2011) and the B-field measurements done at 400 A are shown in Figure 4.18. The B^2 vs z results shown in this figure have been rescaled to 500 A in order to compare the calculated focal length to those in Table 4.2,

$$f_{\mathrm{sol}} = \frac{4(B\rho)^2}{\int_L B_z^2\,dz} = \frac{4\times 0.0269[\mathrm{T}^2\mathrm{m}^2]}{0.009919[\mathrm{T}^2\mathrm{m}]} = 0.18\,\mathrm{m} \tag{6}$$

Therefore at 500 A, the solenoid has the required focal length.

The magnetic axis of the solenoid has also been measured and shown in Figure 4.19. All three solenoids show that there is an excursion in the *x*-offset when the current is increased from 500 A to 600 A. However, both the position and angular changes are small compared to the transverse size of the beam and the strength of the correctors and so this should not be a problem. Note: there is no such excursion in the *y*-direction above 500 A.

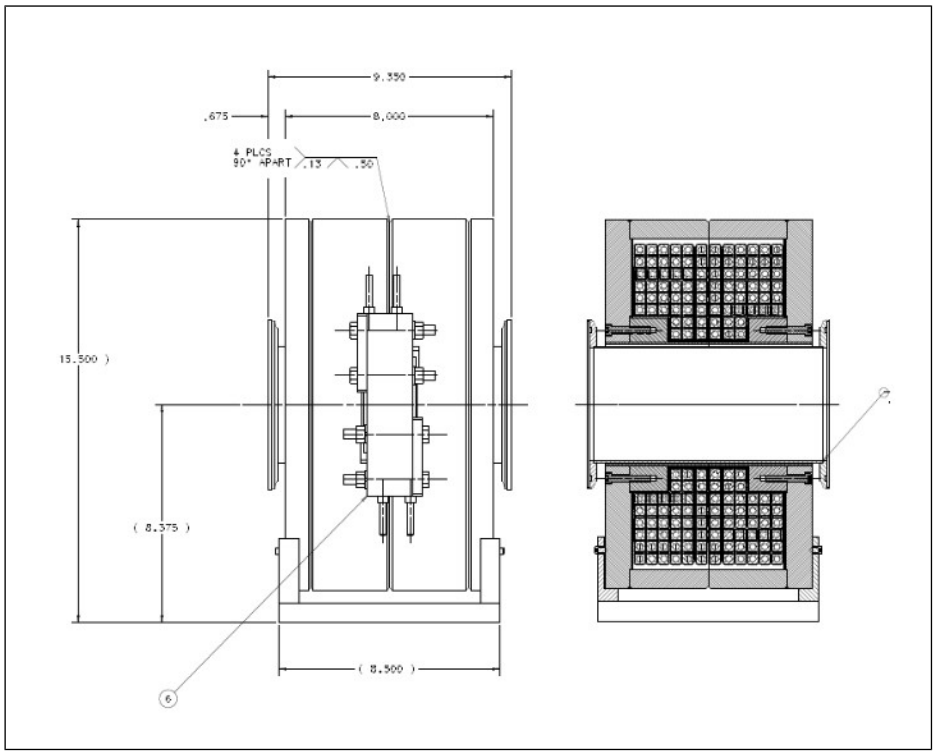

Figure 4.16: *A longitudinal view of the solenoid.*

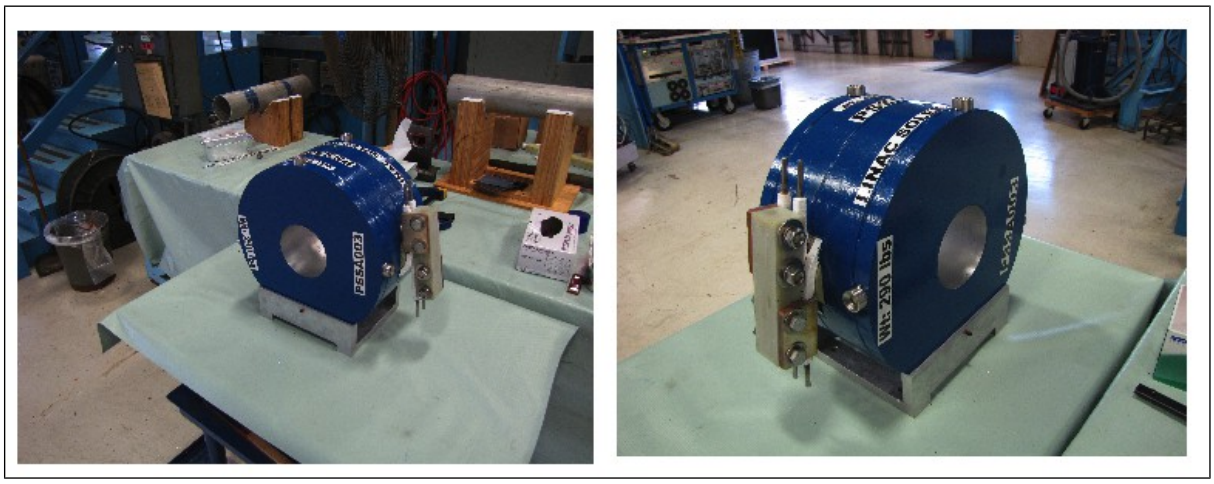

Figure 4.17: *An assembled solenoid. One of the four that has been built.*

4.2.3.b. *Magnetic stripping of H-*

B-fields can strip H- because the two electrons and the proton of the H- experience opposite Lorentz forces. The energy required to strip the loosely bound electron is only 0.75 eV, while in contrast it is 13.6 eV for the tightly bound one. However, for the magnetic fields and energy of the

H- in the LEBT magnetic stripping is irrelevant. A quick calculation below will show that this is indeed the case.

When the B-field in the laboratory frame is boosted to the frame of 35 keV H- ions, the H- ions will see an E-field $\vec{E}=\gamma(\vec{v}/c)\times\vec{B}$, which in more convenient units is

$$E[\mathrm{MV/cm}]=3.197\,p[\mathrm{GeV/c}]\,B[\mathrm{T}] \tag{7}$$

where p is the momentum of the H- in the laboratory frame. The only source of B-field in the LEBT are from the solenoids. The solenoidal field is about 0.25T in the LEBT design. For 35 keV H- ions, the momentum is p = 8.1 MeV/c, and by using Eq. (7), the E-field for B=0.2 T in the rest frame of the H- ion is $E=6.5\times10^{3}\,\mathrm{V/cm}\ll10^{6}\,\mathrm{V/cm}$ for the weakly bound electron to tunnel through the potential barrier [8]. In fact, the present H- source has a 90° bend which has a B-field of 0.25 T and there has been no noticeable H- loss. Therefore, the largest contributor to H- stripping is from the background gas (see section 4.2.1) and not from the magnetic field.

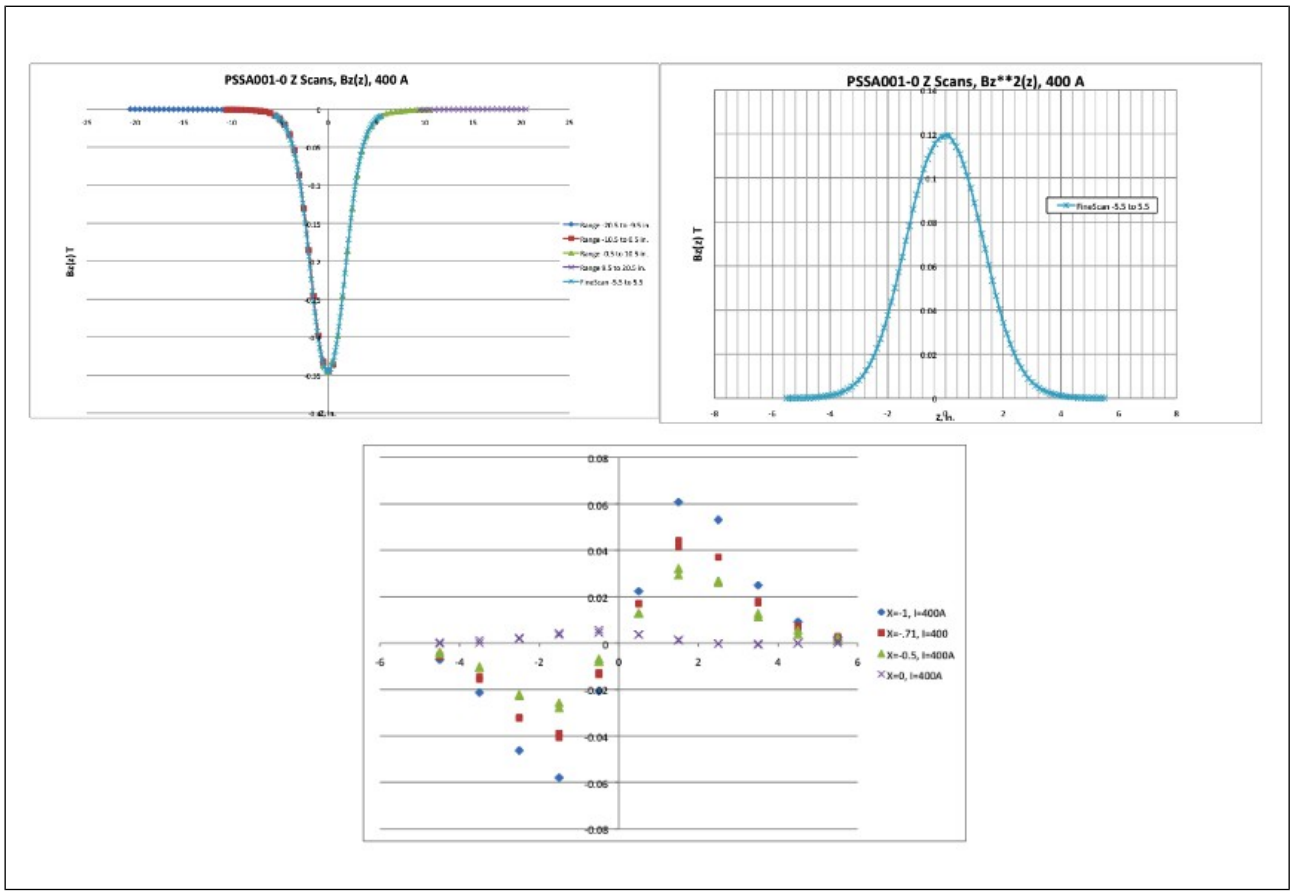

Figure 4.18: *The measured B-fields of PSSA001 at 400 A. The measured fields of PSSA002 and PSSA003 are nearly identical. Shown here are Bz, Bz^2 and Bx vs z.*

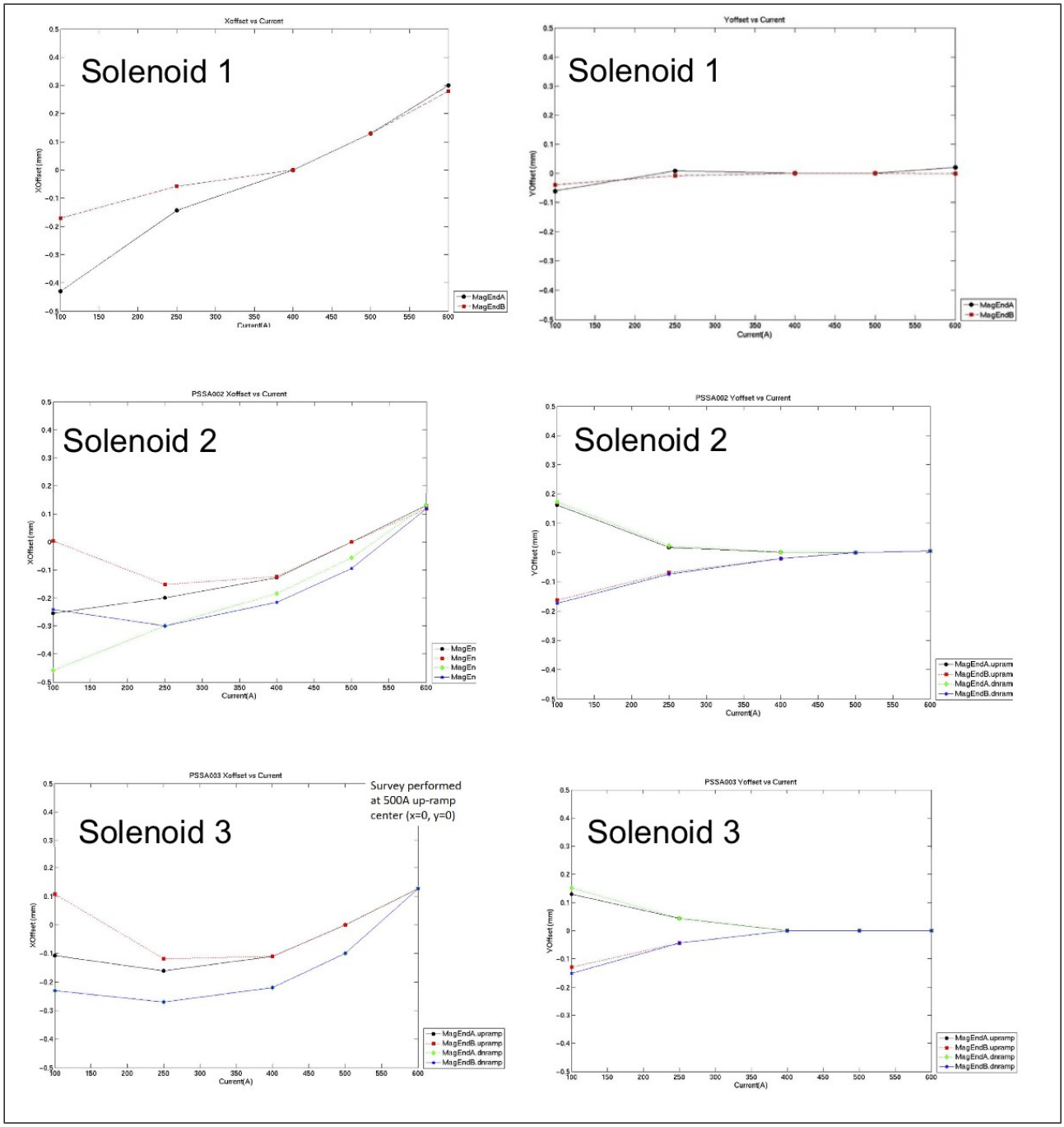

Figure 4.19: *These measurements show that there is a small x-offset in both position and angle when the current is changed. This is not a concern because the solenoids will operate above 500 A and so the x-offset is small compared to the beam size. There is no change in the y-offset for currents above 500 A.*

4.2.3.c. *Emittance measurements at the end of the LEBT*

The emittance probes are connected to the end of the LEBT. See Figure 4.20. This distance from the end of the downstream solenoid to the slits is 8". Examining the drawings of the RFQ and the LEBT, the distance between the downstream solenoid to the RFQ rods (Note: not the starting flange) is 6" and so the Twiss parameters can be calculated by back propagating the measured results back by 2". This has been done and is shown in Figure 4.21.

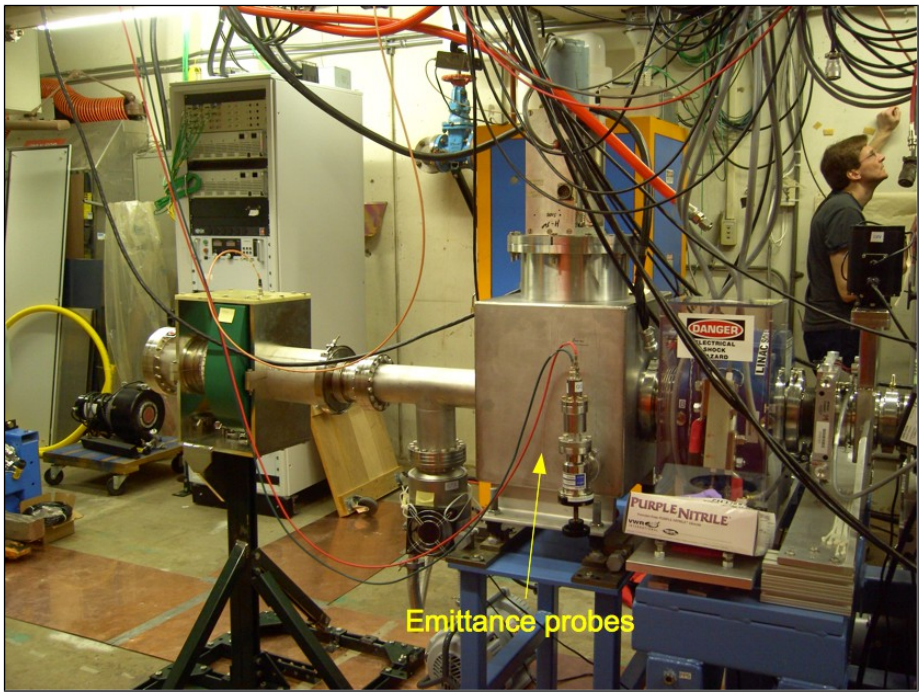

Figure 4.20: *The emittance probes are connected to the end of the LEBT. The distance from the end of the last downstream solenoid to the slits is 8".*

This data was taken at 3.2×10^{-6} Torr in the LEBT with nominal solenoid settings for RFQ injection. It is assumed that the H- beam is fully neutralized at this pressure. Table 4.3 summarizes the Twiss parameters at the rods of the RFQ.

Parameter	Horizontal	Vertical
α	–0.29	0.0
β (m)	0.16	0.01
ε (normalized, 1 sigma) (π mm mrad)	0.15	0.11

Table 4.3: *The Twiss parameters at the start of the rods of the RFQ.*

Notice that the emittances are asymmetric. This source of the asymmetry comes from the source magnetic field which breaks the symmetry of the beam.

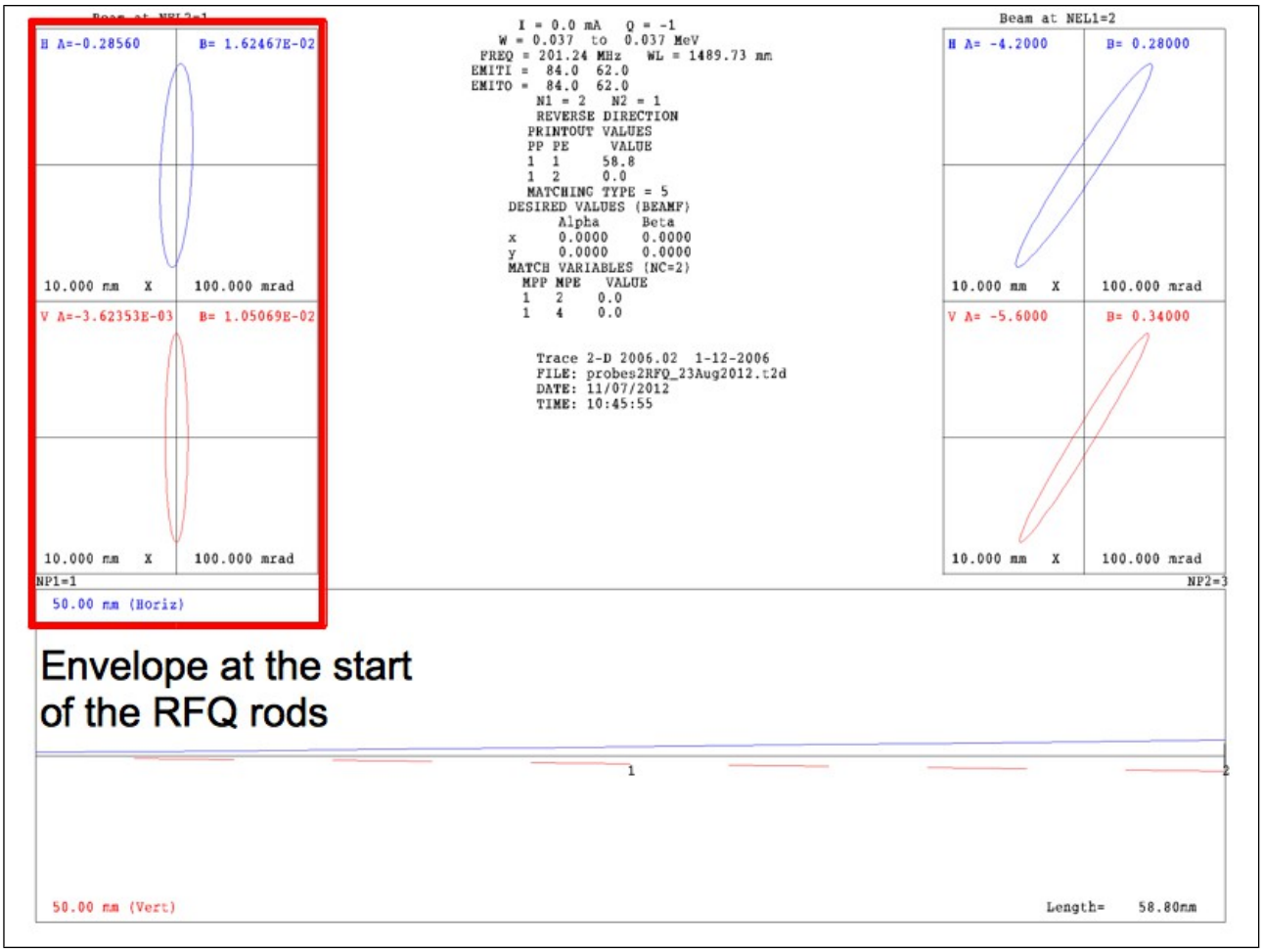

Figure 4.21: *Using Trace2D the measured Twiss parameters can be back propagated back to the start of the RFQ rods.*

4.2.4. Chopper

The chopper is in the low energy part of the injector and so some care must be taken in the design, operation and placement of the chopper based on the BNL experience. If electrostatic choppers (which use parallel plates) are used and the voltage on the plates is on for a long time ($\gg 1\ \mu s$), the H- emittance grows because the neutralizing gas ions are swept out of the H- beam. Fortunately, from studies done at BNL [4], de-neutralization is confined in the region between the chopper plates.

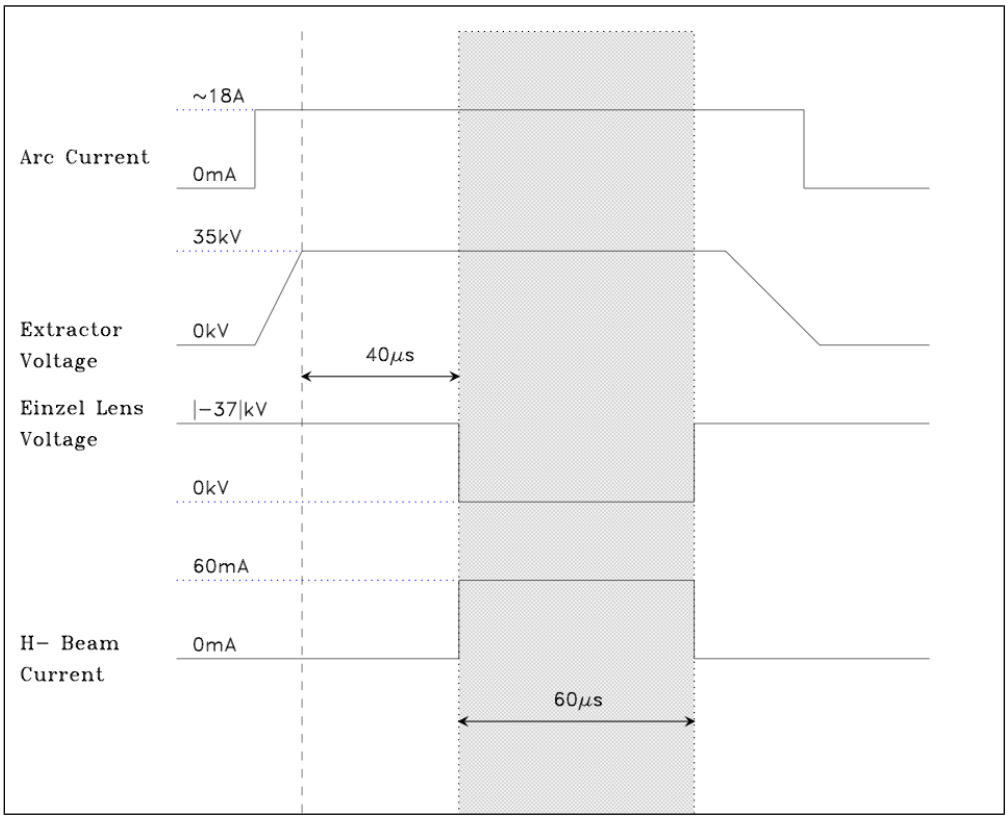

Figure 4.22: *The timing diagram for chopping. In this example, it is assumed that a Marx generator is able to short the Einzel lens to 0 kV for 60 μs. Figure 4.23 shows a more intuitive picture of how the chopping process works. Other ways to modulate the Einzel lens voltage are discussed in section 4.2.4.a*

A possible solution for the de-neutralization problem is to use an Einzel lens as a chopper because it can be placed very close to the entrance of the RFQ.[9] Furthermore, the H- beam is strongly focused by the solenoid here and thus neutralization should also be minimum as well.

Therefore, to create a chopper from an Einzel lens, its potential has to be set to $>|-35|$ kV. In this condition, the lens acts like a mirror and reflects the 35 keV H- ions from the entrance of the RFQ. When the lens is shorted to ground, the H- passes through the lens and enters the RFQ. The beam is stopped after the required H- pulse length by either powering up the lens again, or by turning off the arc current in the source.

For example, the chopping scheme for neutron therapy can proceed as follows (See Figure 4.23). It is assumed that a Marx generator can be used to power the lens and that setting the lens to

-38 kV is sufficient to stop the H- beam. See section 4.2.4.c

1. The Marx generator energizes the lens to -38 kV stop the first ~ 40 µs of the H- beam from entering the RFQ because it takes this amount of time for the H- beam to be fully neutralized in the LEBT.
2. The Marx generator shorts the lens voltage to ground and the H- beam goes into the RFQ for 60 µs which is the required bunch length for neutron therapy.
3. The Marx generator re-energizes the lens back to -38 kV to stop the H- beam.
4. The arc current is turned off.

The timing diagram for the entire chopping process is shown in Figure 4.22.

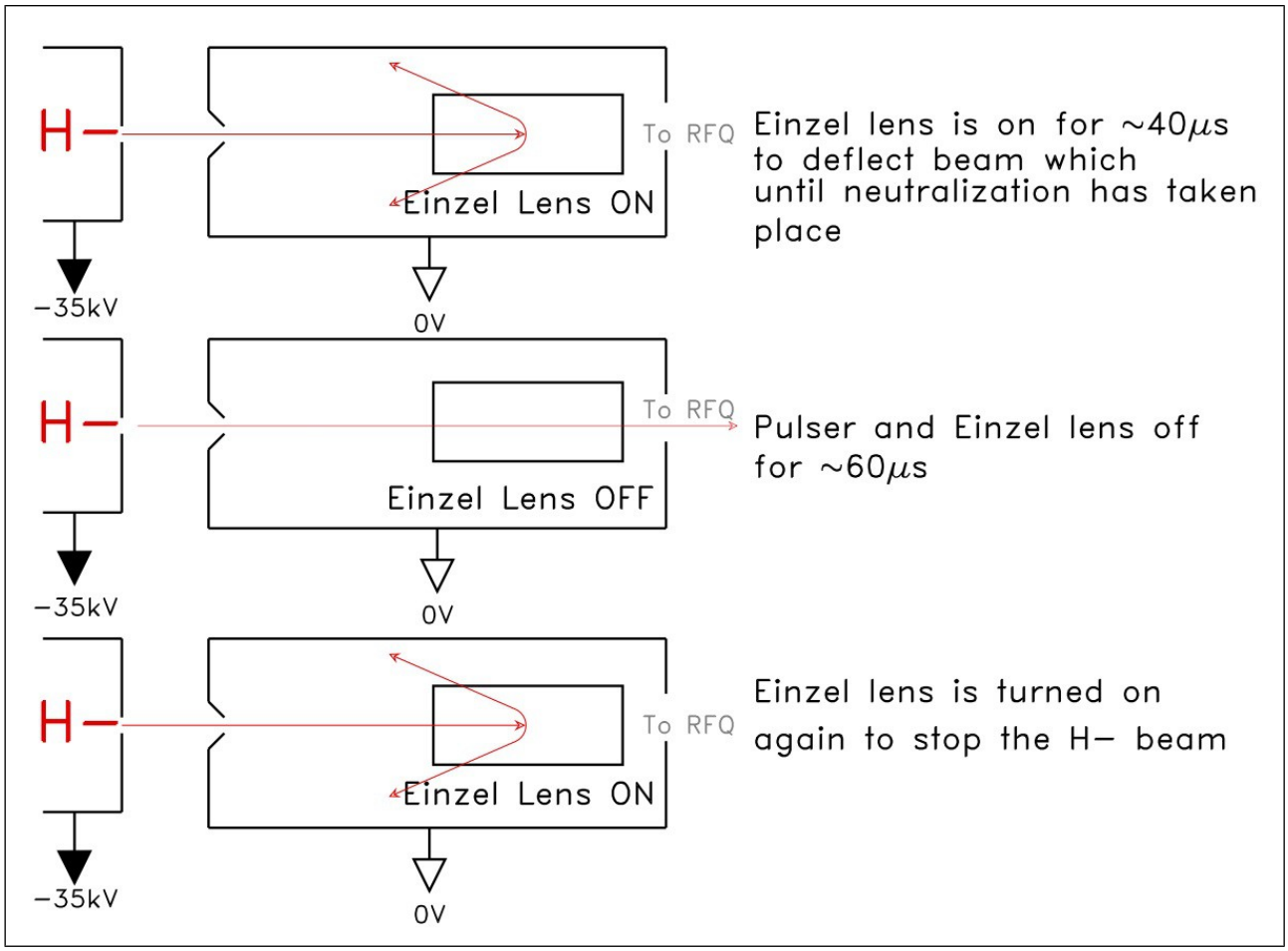

Figure 4.23: *In this example which is used for neutron therapy, the H- source is turned on and the first 40 µs of the H- beam is not transmitted into the RFQ because it takes this amount of time to neutralize the H- beam. Everything is off for the next 60 µs so that the neutralized beam is sent into the RFQ. After 60 µs the beam is turned off again by powering the Einzel lens. The cycle repeats after 1/15[Hz]=67 ms.*

4.2.4.a. *The Einzel lens modulation technique*

Although a Marx generator was used for modulation in the example in the previous section, the chopping specifications are outside the abilities of present day Marx generators. Therefore, another method has been devised.

The technique that will be pursued uses MOSFET switches that directly turns the voltage on the Einzel lens on and off. The push-pull switch circuit is shown in Figure 4.24. The rise and fall times of this circuit is determined by the time constant, $t_{RC} = Rs1 * Clens$ and it takes about $t_{\text{asym}} = 5 \times t_{RC}$ for the voltage to get very close to its asymptotic value. The MOSFET switches have been bought from Diversified Technologies and the test results are discussed in section Figure 4.25 shows the MOSFET switches and controller before assembly into the switching circuitry.

The circuit diagram of the switching circuit is shown in Figure 4.24. For example, if $Clens = 100$ pF (this value has been chosen for the design because from simulations, although the Einzel lens capacitance is <15 pF, the stray capacitance from the connecting cables is probably much larger) and $Rs1 = 500\,\Omega$ (this comes from the peak current limits of the HV switches) then $t_{RC} \sim 50$ ns .

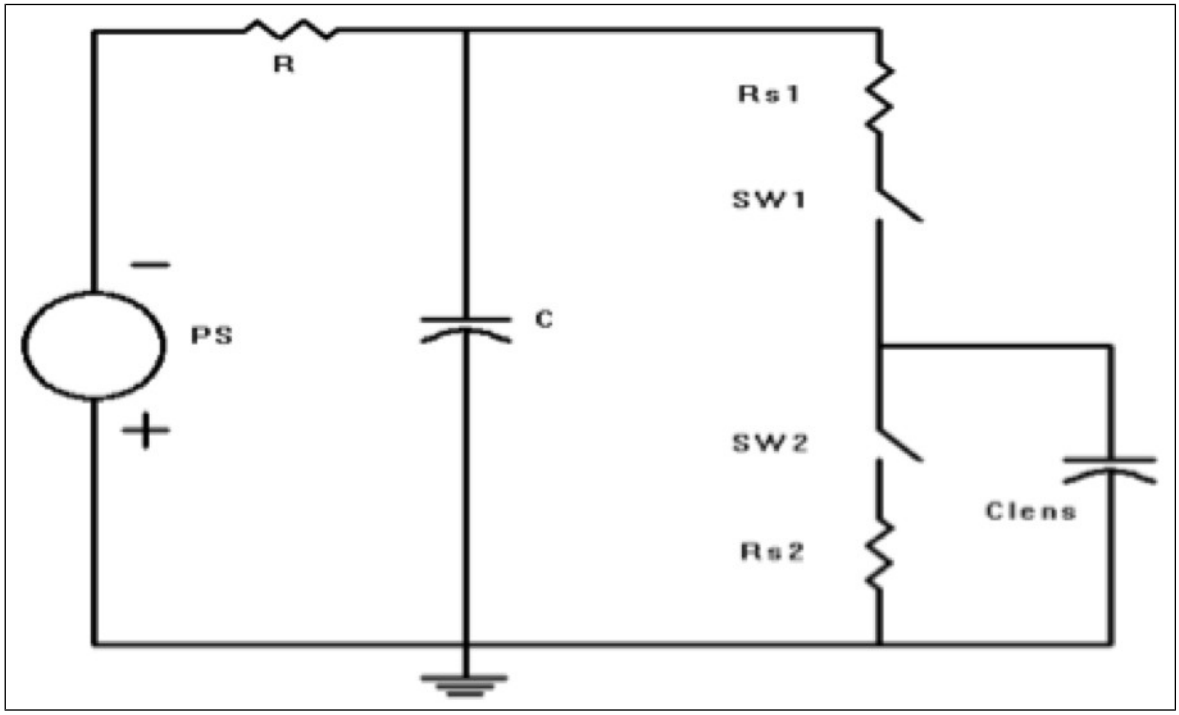

Figure 4.24: *This figure shows a push-pull switch scheme for modulating the voltage on the Einzel lens.*

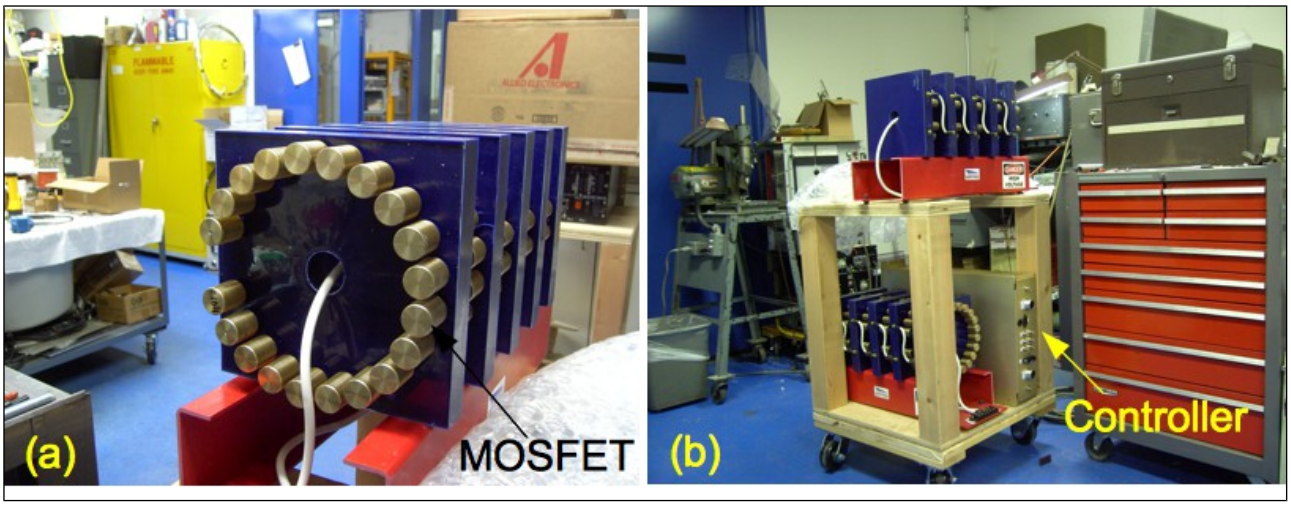

Figure 4.25: *The MOSFET switches. (a) Twenty MOSFETs (gold cylinders are the MOSFET heat sinks) are wired in series to form one pad. Five pads are stacked together to make one switch that is specified for 100A peak current, 50 kV operation. (b) shows two sets of switches and their controller before assembly into the push-pull switching scheme.*

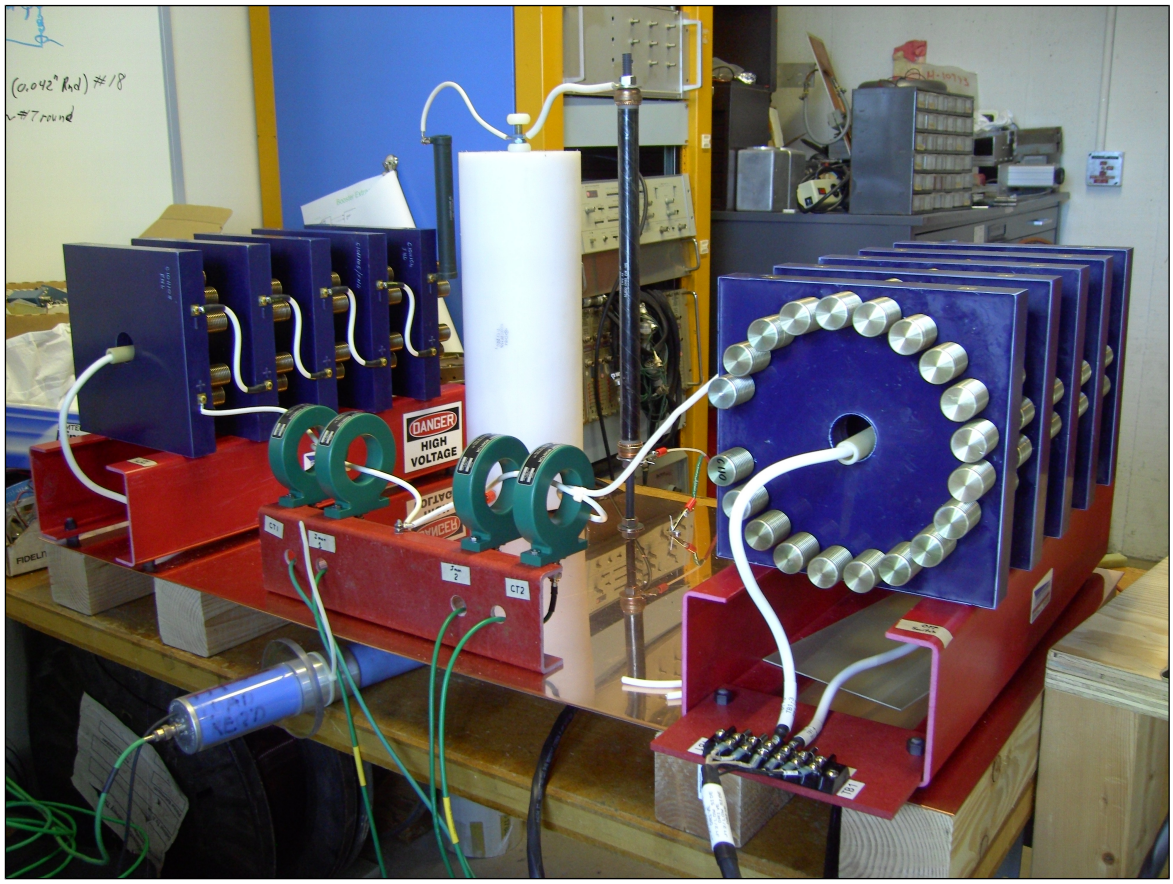

Figure 4.26: *The switching circuit under test.*

4.2.4.b. *The push-pull circuit test results*

Figure 4.26 shows the push-pull circuit used for the bench test. The results of switching 2 kV on the bench into a load capacitance of 15 pF are shown in Figures 4.27 and 4.28. The measured fall time from ~0 kV to –2 kV is about 214 ns. However, when the load capacitance is reduced to 10 pF, this time decreased to 204 ns. The "~0 kV" measured on the load is a probe error.

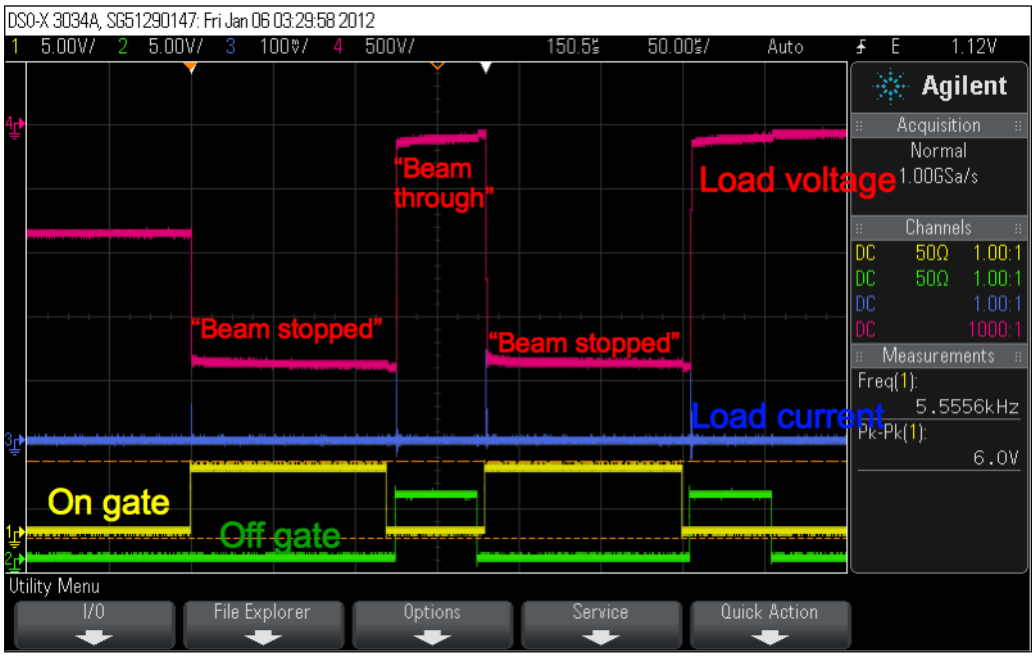

Figure 4.27: *This figure shows the switches turning on/off and the load voltage waveform which allows beam to get through for 50 μs when the load is shorted to ground.*

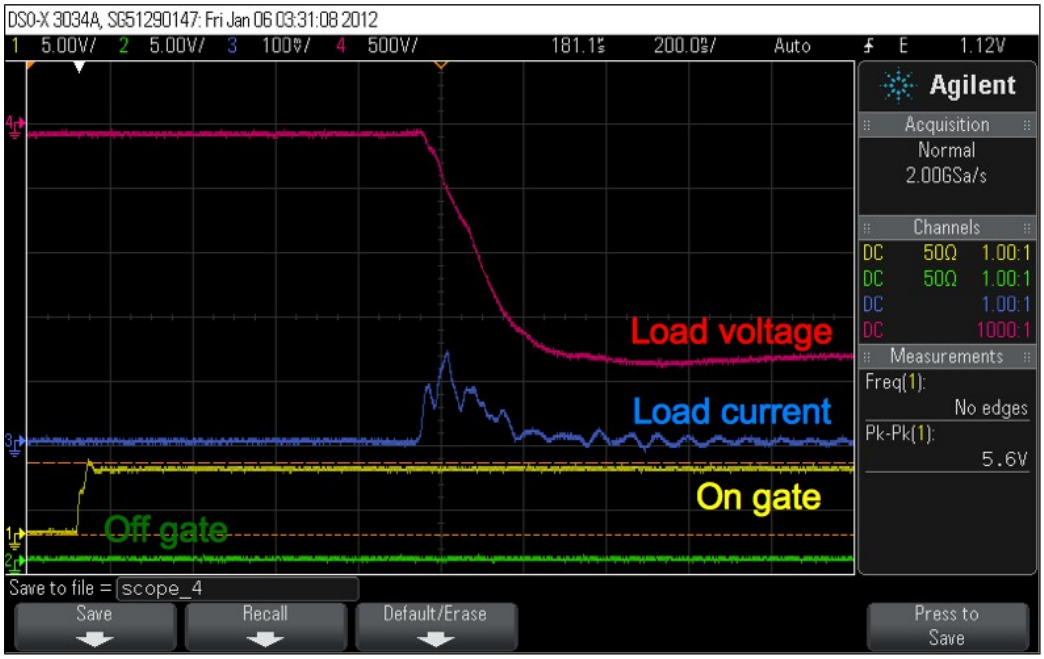

Figure 4.28: *Zoomed in view of the load voltage falling from ~0 kV to –2 kV in ~214 ns.*

4.2.4.c. *The Einzel lens*

The Einzel lens is placed as close as possible to the entrance of the RFQ in order to keep the de-neutralized region as small as possible when the Einzel lens is on. And note that because of the strong focusing from the solenoids, neutralization of the H- beam at this location should also be at a minimum.

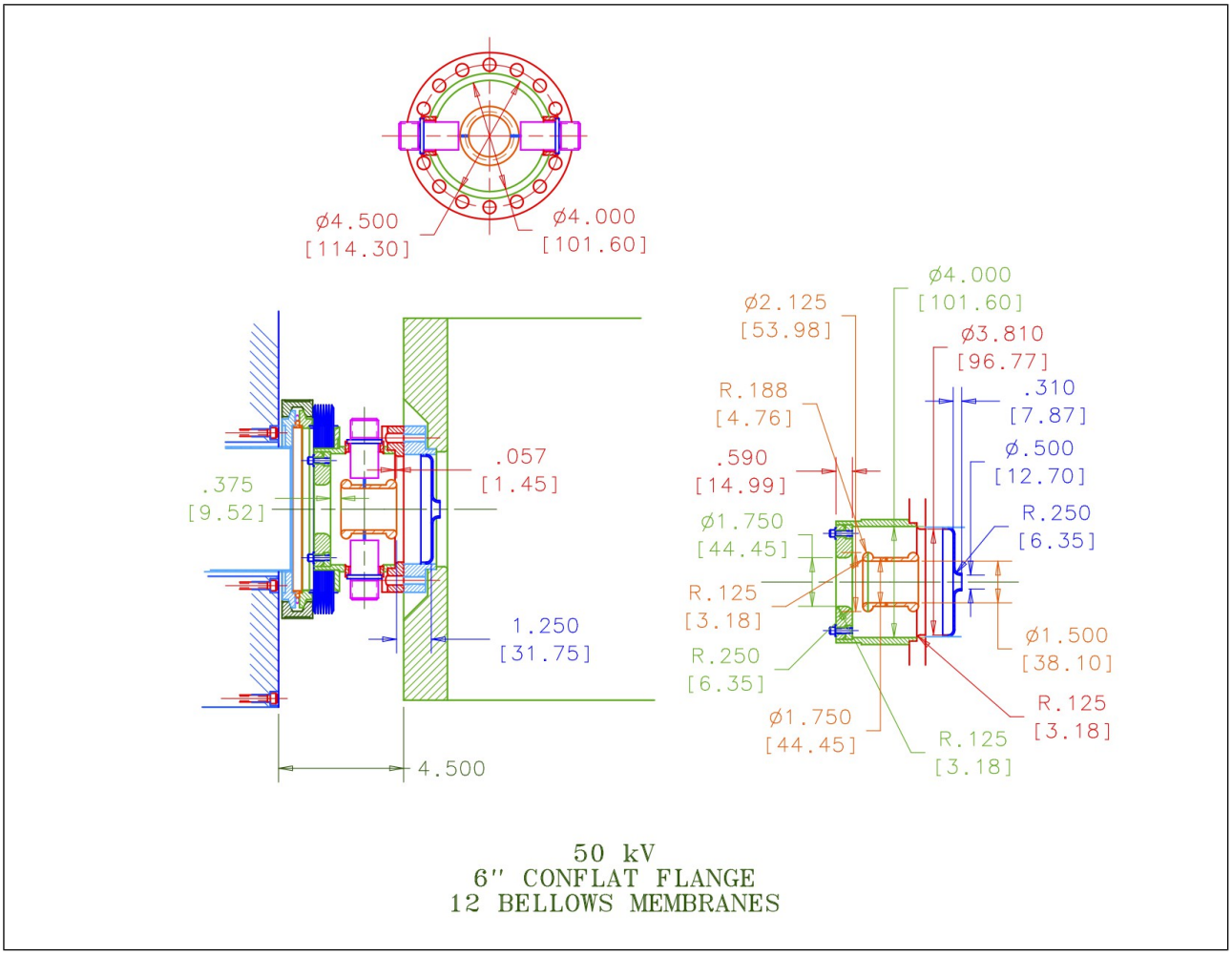

Figure 4.29: *The drawing of the Einzel lens (1.75" ID) and how it is attached to the end of the LEBT and to the entrance of the RFQ. Although shown here to be a 0.5" aperture at the entrance to the RFQ, the actual hole is 2 cm is diameter and is used for both vacuum isolation between the LEBT and the RFQ and the creation of electric boundary conditions. (Designed by A. Makarov)*

Figure 4.30: *The assembled Einzel lens. Two lenses have been made. One will be operational and the other will act as a spare.*

Computer simulations with SIMION show that for an Einzel lens that is 2" long and 1.75" in diameter, the potential difference needed to stop 35 keV beam is -38 kV. Figure 4.31 shows how the H- is reflected at the Einzel lens when the potential is on and transmitted when it is off. When the Einzel lens is on at -38 kV all the incident H- beam is reflected away from the entrance of the RFQ. When the Einzel lens is off, the H- beam is transmitted into the RFQ. The capacitance of the Einzel lens in the structure calculated with SIMION (and an independent calculation done by G. Romanov) shows that it is ~8 pF and so can be discharged very quickly in < 1 ns if the resistance of the discharge circuit < 50Ω. Therefore, the rise and fall time of the chopped beam is dominated by the pulser rise and fall times rather than the capacitance of the Einzel lens. Figure 4.29. shows the design of the mounting for the Einzel lens at the end of the LEBT and before the RFQ. Figure 4.30 shows the assembled lens.

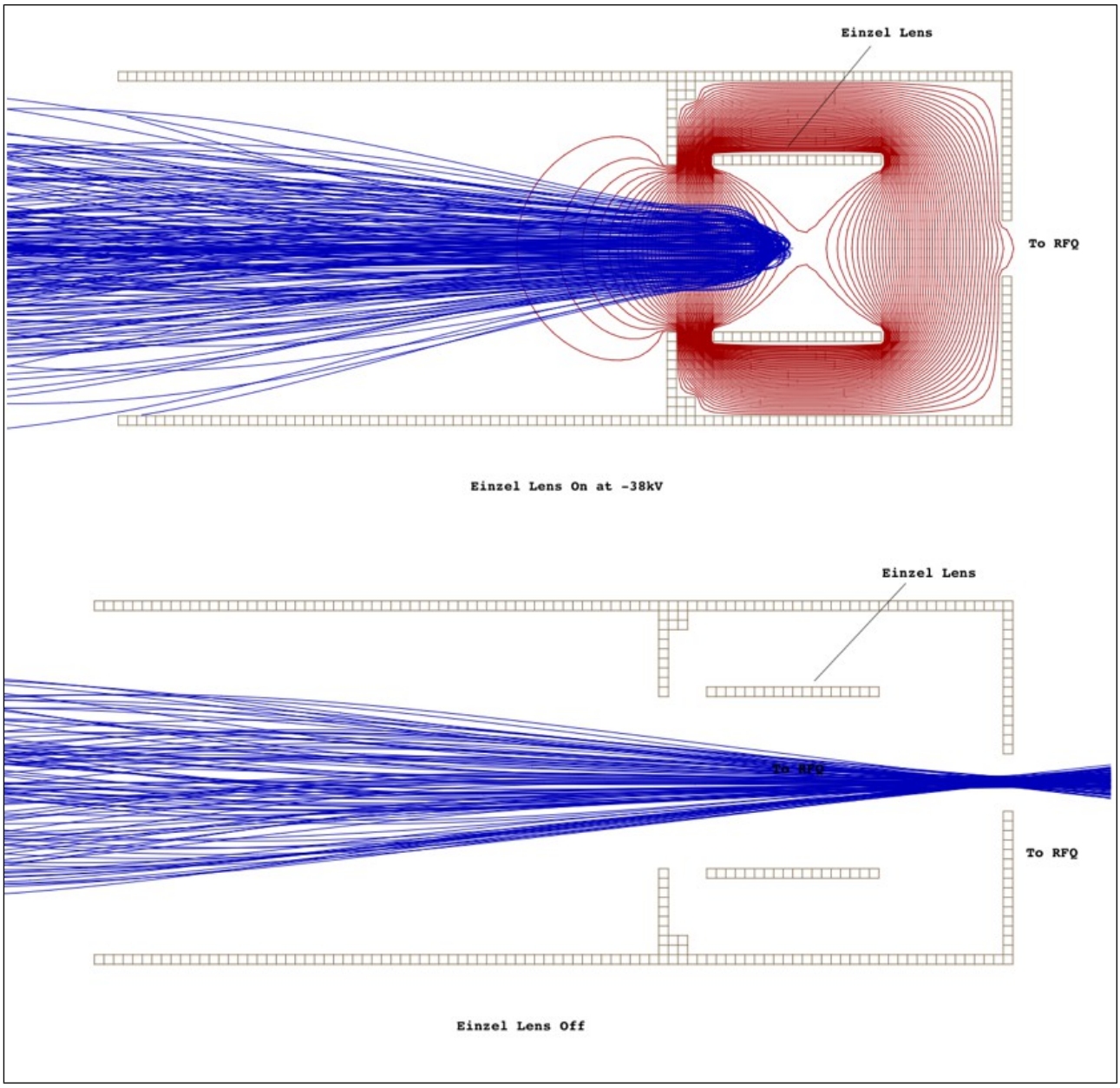

Figure 4.31: *The magnetic field from the solenoid (See Figure 4.29) focuses the beam into the entrance of the RFQ when the Einzel lens is off. When the Einzel lens is on, it acts like a mirror on the H- beam by reflecting the beam away from the RFQ.*

4.2.4.d. *Einzel lens chopper experiments*

The Einzel lens is mounted at the end of the LEBT and a fast Faraday cup [10] is attached 11" from the downstream end flange of the lens, and a toroid called Z:LTOR is mounted 50" from the lens. See Figure 4.32.

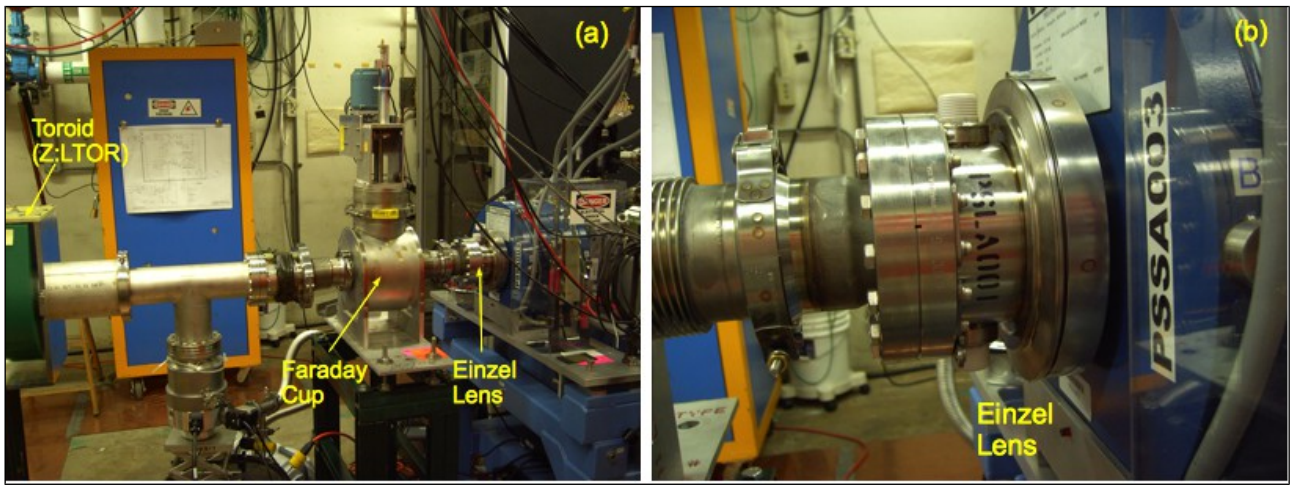

Figure 4.32: *(a) The test line used to demonstrate chopping consists of the Einzel lens connected to the end of the LEBT, a fast Faraday cup and a toroid. (b) A zoomed in view of the Einzel lens connected to the end of the LEBT.*

The Einzel lens is pulsed using the push-pull circuit discussed in section 4.2.4.b. The current measured on the toroid upstream of the Einzel lens (Z:ATOR), the downstream toroid (Z:LTOR) and the lens voltage pulse used in these experiments are shown in Figure 4.33.

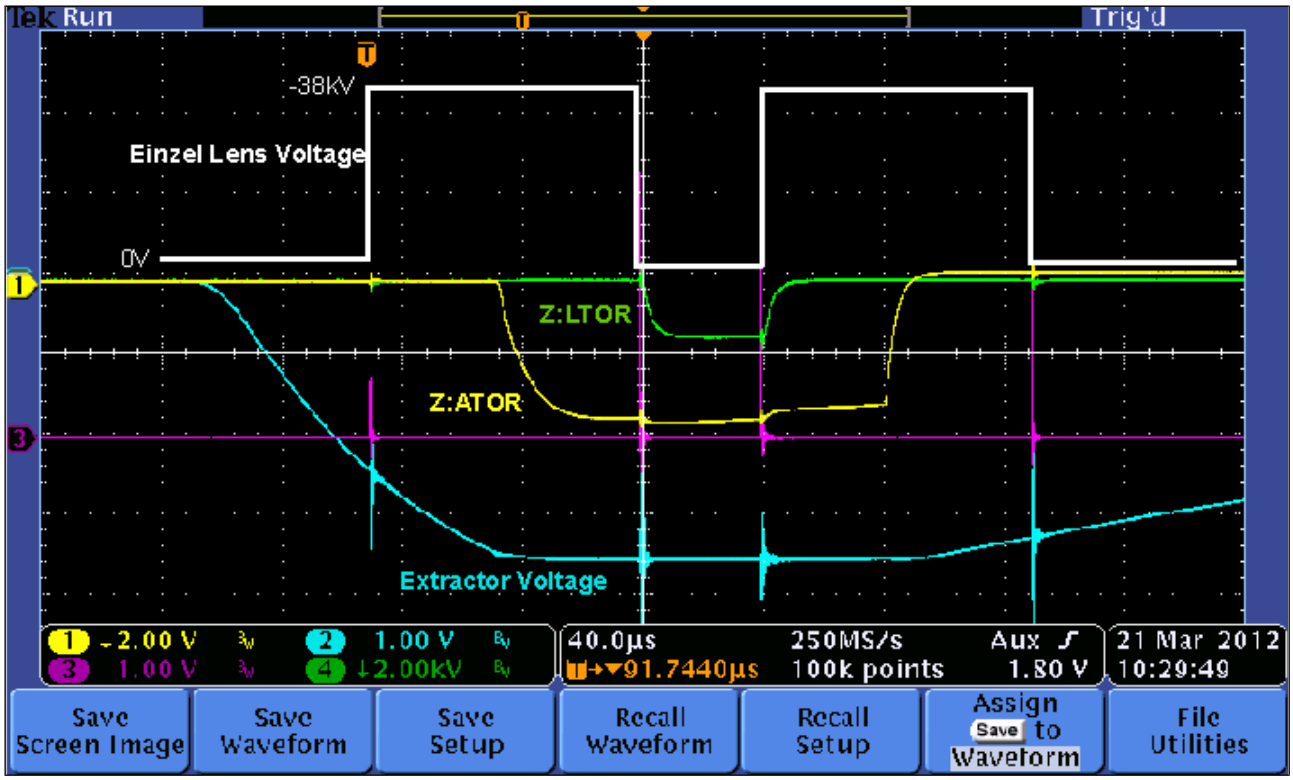

Figure 4.33: *The Einzel lens voltage and the toroid signals.*

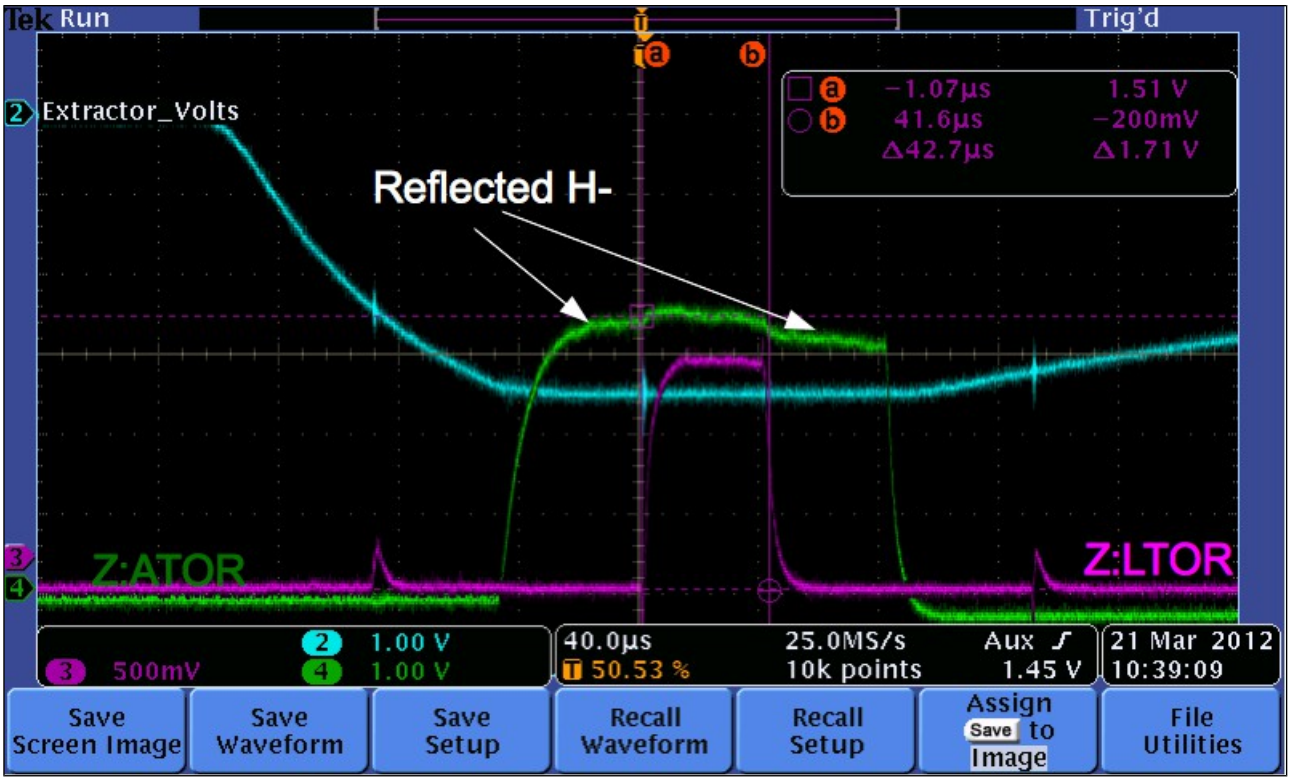

Figure 4.34: *The measurement on Z:LTOR clearly shows that the beam is chopped to a width of ~43 µs downstream of the Einzel lens. The current measured on Z:ATOR is smaller when the lens reflects the H- beam because toroids are sensitive to beam direction. The rolls in the toroid signals come from the low pass filters of the toroid amplifiers.*

The first experimental shows that the Einzel lens does function like a chopper when pulsed with the lens voltage shown in Figure 4.33. Figure 4.34 shows the chopped current signal measured on Z:LTOR. The initial H- pulse has been reduced from 120 µs to 42 µs in the chopping process. On the upstream toroid, Z:ATOR, when the H- beam is reflected backwards, the measured current is reduced because toroids are sensitive to the direction of the current. The roll of toroid currents come from the low pass filters used in the toroid amplifiers. For a good measurement of the rise and fall times of the H- beam, the fast Faraday cup is used and the experiment is discussed below.

The voltage required to stop 35 keV H- beam is between –38 kV and –39 kV. For the experiments the stopping voltage has been set to –38.5 kV. This number is very close to –38 kV calculated using SIMION discussed in section 4.2.4.c. Figure 4.35 shows that beam leaks out of the Einzel lens when the voltage is set to –38 kV, while at –39 kV, the beam is completely stopped.

The rise and fall times of the chopped H- beam are measured with the fast Faraday cup [10]. See Figure 4.36 for a photograph of the fast Faraday Cup. The measured rise time is ~138 ns and the fall time is ~81 ns. See Figure 4.37. The rise time is slower than the fall time because the stray capacitances are comparable in size to the load capacitance and the combination of the two is larger during discharge. The main contributors to the RC time constants which affect the rise/fall times are the resistance of the MOSFET switches and the capacitance of the system. Each pad contributes 150Ω and so for a stack of 5 pads, each stack contributes 750Ω. It is conceivable to short out one pad of each stack to reduce the rise/fall times, however, these times are already within the requirements for chopped beam.

The pressure in the LEBT is about 2.5×10^{-6} Torr for these experiments. The rise time of

Z:ATOR which should be dominated by the neutralization time is about 30 μs and is much shorter than the value expected for hydrogen dominated vacuum. See Eq. (12).

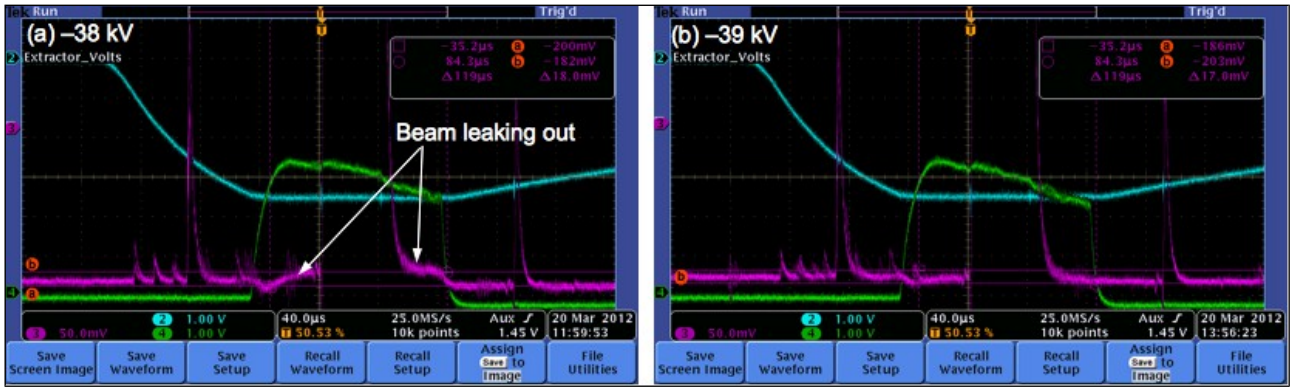

Figure 4.35: *The H- beam is stopped when the voltage on the Einzel lens is above |–38| kV.*

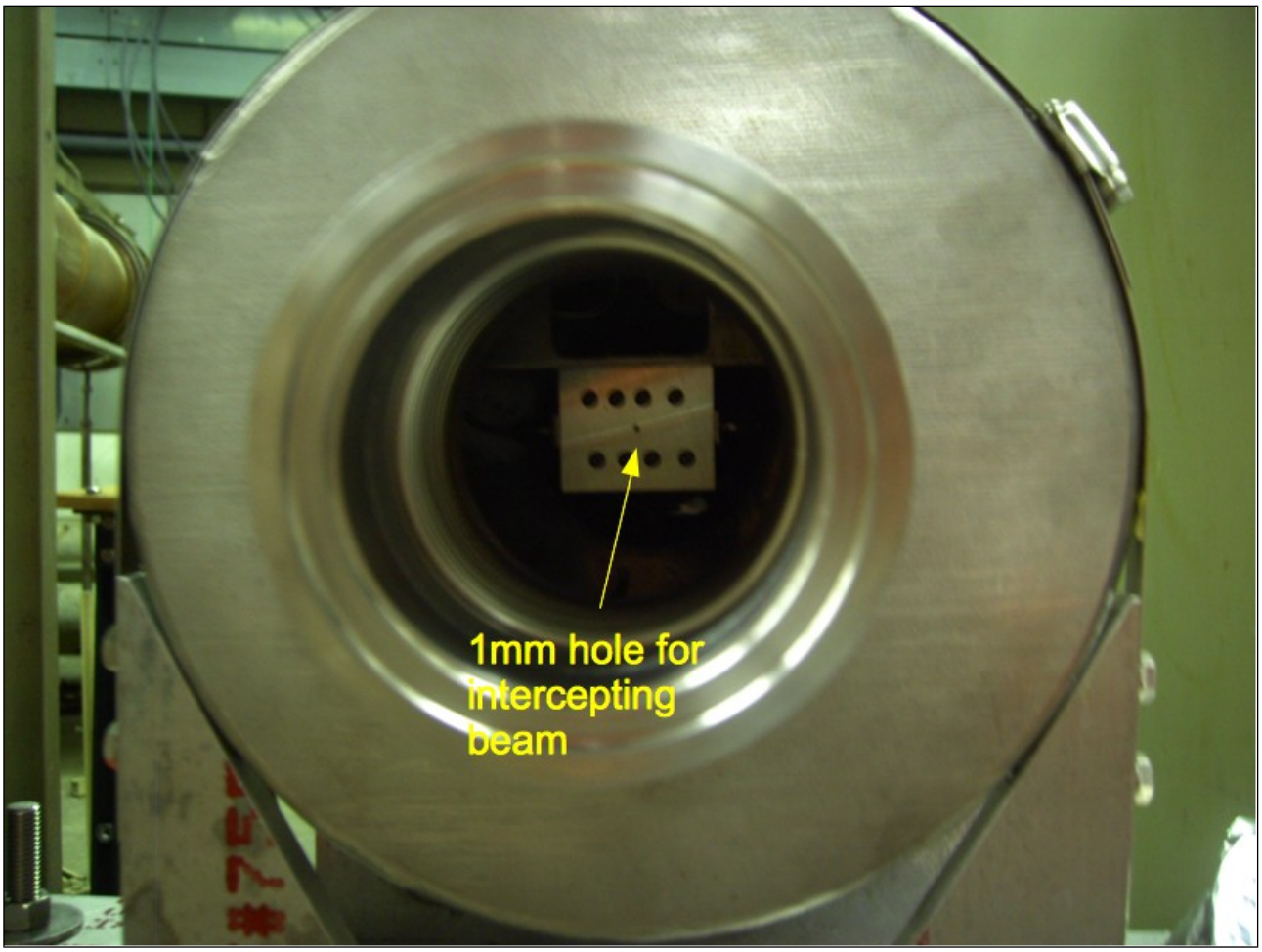

Figure 4.36: *This is a photograph of the intercepting end of the fast Faraday cup. The hole that interceptrs the beam is about 1 mm in diameter.*

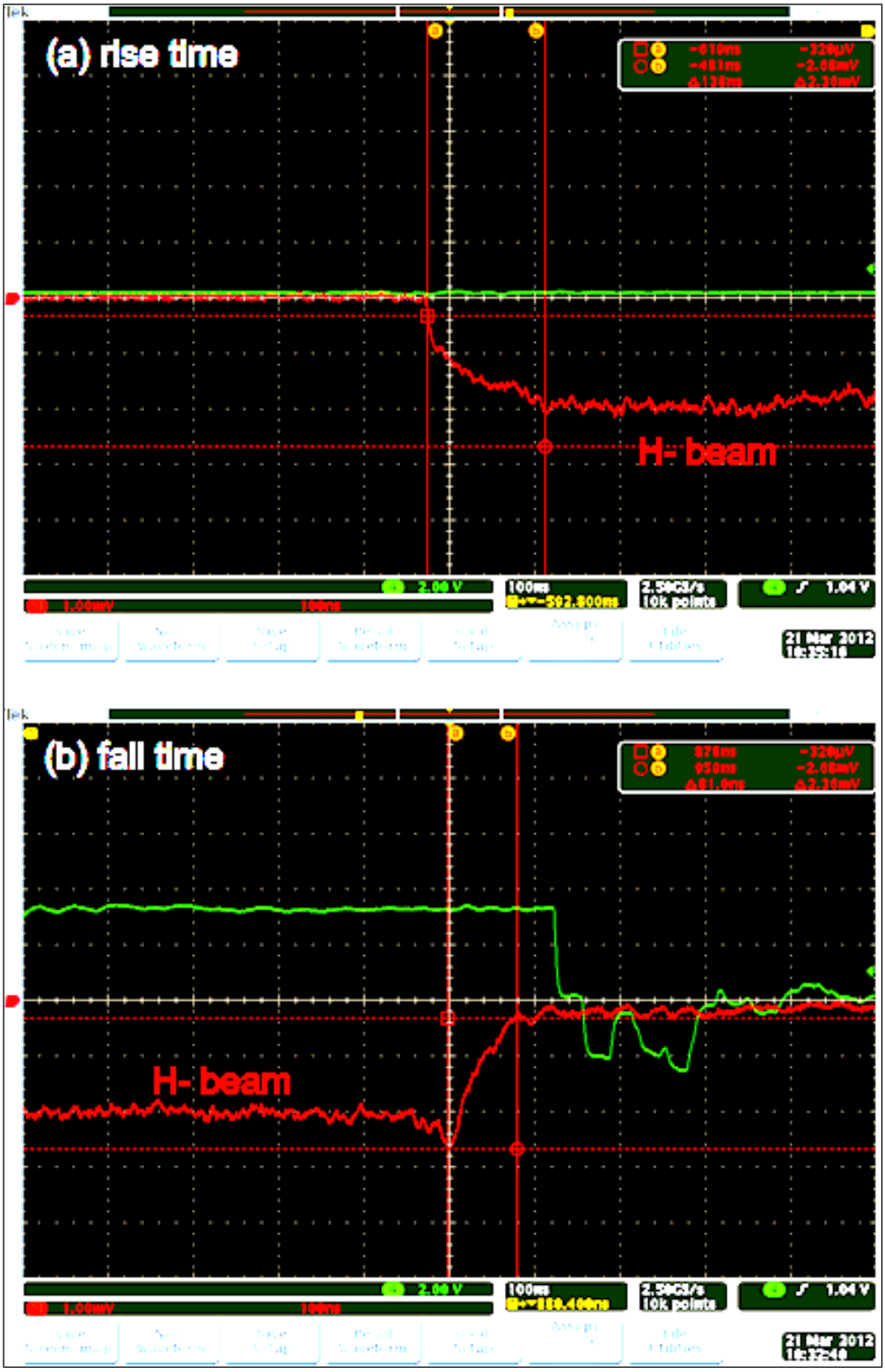

Figure 4.37: *The rise and fall times of the chopped H- beam. The traces have been averaged 16x and background subtracted.*

4.2.5. LEBT Dipole Correctors

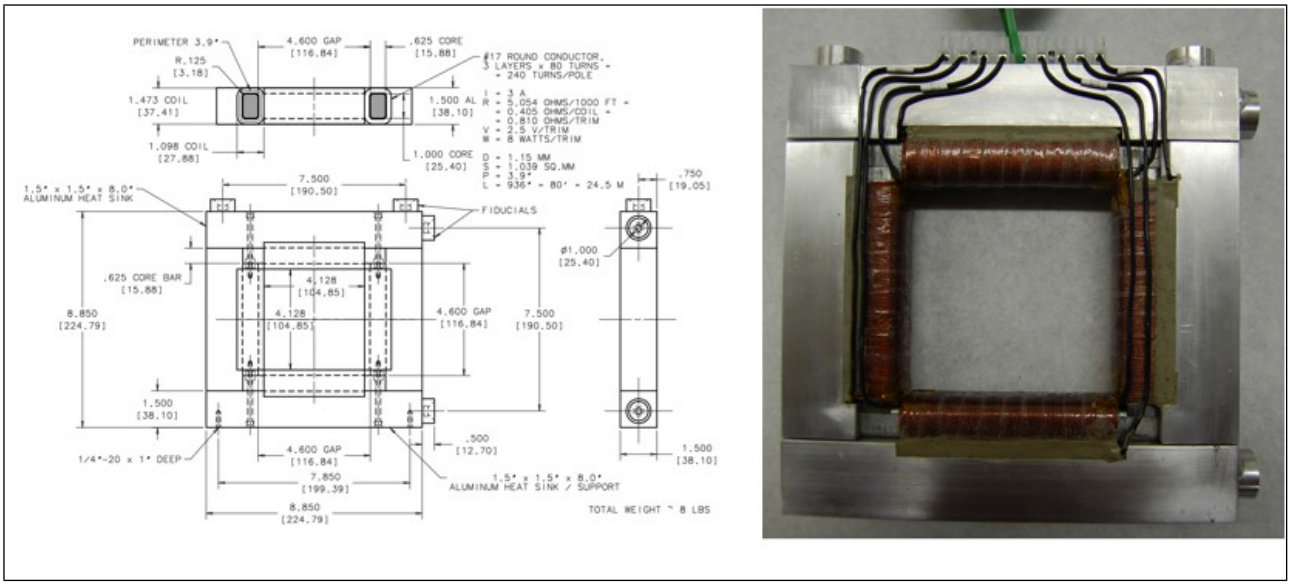

Figure 4.38: The LEBT dipole correctors are designed to correct ±1° in both planes in a package that is <1.5" long. (Designed by A. Makarov)

The LEBT correctors have been designed to fit over a 4" beam pipe and are as short as physically realizable. The placement of the correctors, especially the one closest to the exit of the source requires some thought because of the drop in integrated field *Bdl* when the corrector is placed close to the solenoid iron. V. Kashikhin has calculated that when the corrector design shown in Figure 4.38 is placed 2" (closest edge to closest edge) from the solenoid iron, *Bdl* is reduced by 28%. This integrated field drop can be compensated by increasing the current in the corrector but at the expense of increasing the temperature of the corrector. In order to adequately cool the correctors, aluminium heat sinks have been added to the design to keep the corrector temperature to below 50˚C when they are run at full current of 10 A. The dipole corrector in each plane has been specified have at least $Bdl = 5.1$ gauss·m at full current *far* from iron which corrects a maximum angle error of ±1º for 35 keV H- beam.

The as constructed dipoles have $Bdl = 8-9$ gauss·m in both planes at –2 A and $Bdl = 7-8$ gauss·m in both planes at +2 A *far* from iron. The asymmetry in the measurements are assumed to come from the residual magnetization of the iron in the correctors during the measurement. The reduction in field when the dipoles are close to iron should be about 28% which means that the dipole field is reduced to about |5.8| gauss·m near iron at ± 2 A. This value is within the specifications. Table 4.4 summarizes the measured *Bdl*'s for five sets of dipoles.

magnet	PSDC001		PSDC002		PSDC003		PSDC004		PSDC005	
	Horizontal *Bdl* (gauss·m)	Vertical *Bdl* (gauss·m)	Horizontal *Bdl* (gauss·m)	Vertical *Bdl* (gauss·m)	Horizontal *Bdl* (gauss·m)	Vertical *Bdl* (gauss·m)	Horizontal *Bdl* (gauss·m)	Vertical *Bdl* (gauss·m)	Horizontal *Bdl* (gauss·m)	Vertical *Bdl* (gauss·m)
@ –2 A	8.93	8.73	9.13	8.80	9.06	8.75	8.95	8.74	9.03	8.84
@+2 A	7.36	7.97	7.59	8.05	7.62	7.91	7.48	7.95	7.54	7.99

Table 4.4: *Summary of the measured Bdl for the five LEBT dipoles.*

4.3. The RFQ

The FNAL RFQ was ordered from A. Schempp on 19 May 2010 and delivered to FNAL on 04 Aug 2011. However, problems with its output energy, capture efficiency and power coupling plagued the delivered RFQ. Extensive fixes were required before the RFQ met enough of the specifications for final installation. See Appendix C for the summary of the problems and the fixes. The final fixes were:

1. Removal of the end plate of the RFQ to get the correct output energy. See Figure C.5. The effect on the output energy of the RFQ are discussed in Appendix C.1.
2. Replacement of the "thick" rods with "thin" rods for better power efficiency. See Figure 4.39 and section 4.3.3 for the discussion.

The RFQ is a rod-type RFQ and photographs of it is shown in Figure 4.40 and after it has been assembled in its vacuum tank in Figure 4.42. Its physical and operating specifications specified by FNAL and the manufacturer are summarized in Table 4.5. The RFQ has been tuned for field flatness and the results are shown in Figure 4.43 where it can be seen that the field variation is < 12%. This is certainly not ideal because field flatness does affect capture efficiency. There are also indications from CST MICROWAVE STUDIO simulations that the shape of the field flatness also affects capture efficiency. See section 4.3.4 for the discussion. Other measurements performed at FNAL are shown in Table 4.7.

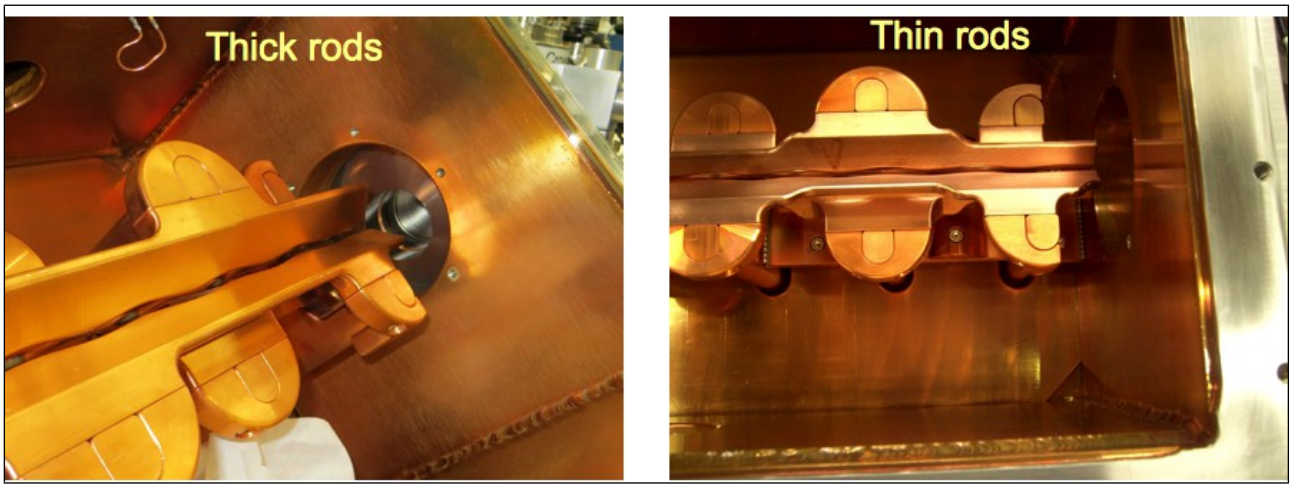

Figure 4.39: *One major repair of the RFQ is the replacement of the original thick rods with thin rods. The thinner rods have lower capacitance and thus higher impedance which may reduce power requirements.*

The RFQ PARI model [11] has been supplied by the manufacturer and is shown in Appendix A Using the PARI model[2], the RFQ design parameters from the model are shown in Figure 4.41. Using the input Twiss parameters shown in Table 4.6, FNAL has verified the transmission efficiency, output energy and output Twiss parameters with PARMTEQM. The FNAL PARMTEQM simulation shows that for 10^4 H- ions at 60 mA, < 2% of the H- ions are lost. Figure 4.44 shows the result of the transport through the RFQ and Figures 4.45, 4.46 and 4.47 show the phase space and real space distributions of the particles before and after they have gone through the RFQ. Note: the RFQ as delivered have the rods rotated by 45°, i.e. in the laboratory coordinate system, the RFQ

2 To match the manufacturer's results, PARI had to be set to "adjust modulation only" in order to produce the same acceleration efficiency as the 2-term potential.

quadrupoles are actually skew quadrupoles. Therefore, there must be some care in performing simulations downstream of the RFQ.

However, experimental results do not agree with PARMTEQM simulations and show that the capture efficiency is at best 70% at this time. See section 4.3.5 for the discussions about the experimental results. The transverse emittances and longitudinal beam sizes are discussed in sections 4.3.5.d and 4.3.5.e.i.

Parameter	Value	Units
Input energy	35	keV
Output energy	750	keV
Frequency	201.25	MHz
Number of cells	102	
Length	120	cm
Minimum radial aperture	0.3	cm
Maximum peak surface field	25.18	MV/m
Peak cavity power+beam power	~180[3]	kW
Duty factor (80 μs, 15 Hz)	0.12	%
Design current	60	mA
Modulation m	$1 \leq m \leq 1.95$	
Intervane voltage	72	kV
Transmission efficiency (PARMTEQM)	98	%
Transmission efficiency (measured)	< 70	%

Table 4.5 *The physical and operational characteristics of the FNAL RFQ.*

3 This is the measured power that is required for operations.

Twiss Parameter	*x*		*y*		*z*	
	Manufacturer	**FNAL**	**Manufacturer**	**FNAL**	**Manufacturer**	**FNAL**
Input α	1.5	-	1.5	-	-	-
Input β	5.1 cm/rad	-	5.1 cm/rad	-	-	-
Input ϵ (1× rms)	0.30 π mm mrad norm.	-	0.30 π mm mrad norm.	-	-	-
Output α	−0.18	−0.039	0.07	−0.0813	0.21	0.25
Output β	12.5 cm/rad	12.7 cm/rad	5.5 cm/rad	5.6 cm/rad	1170° MeV	1110° MeV
Output ϵ (1× rms)	0.37 π mm mrad norm.	0.38 π mm mrad norm.	0.35 π mm mrad norm.	0.36 π mm mrad norm.	0.14 MeV deg unnorm.	0.14 MeV deg unnorm.

Table 4.6: *The input parameters are supplied by the manufacturer. The output Twiss parameters supplied by the manufacturer are compared to the FNAL numbers calculated with* PARMTEQM*. Traditionally there is no π in longitudinal emittances.*

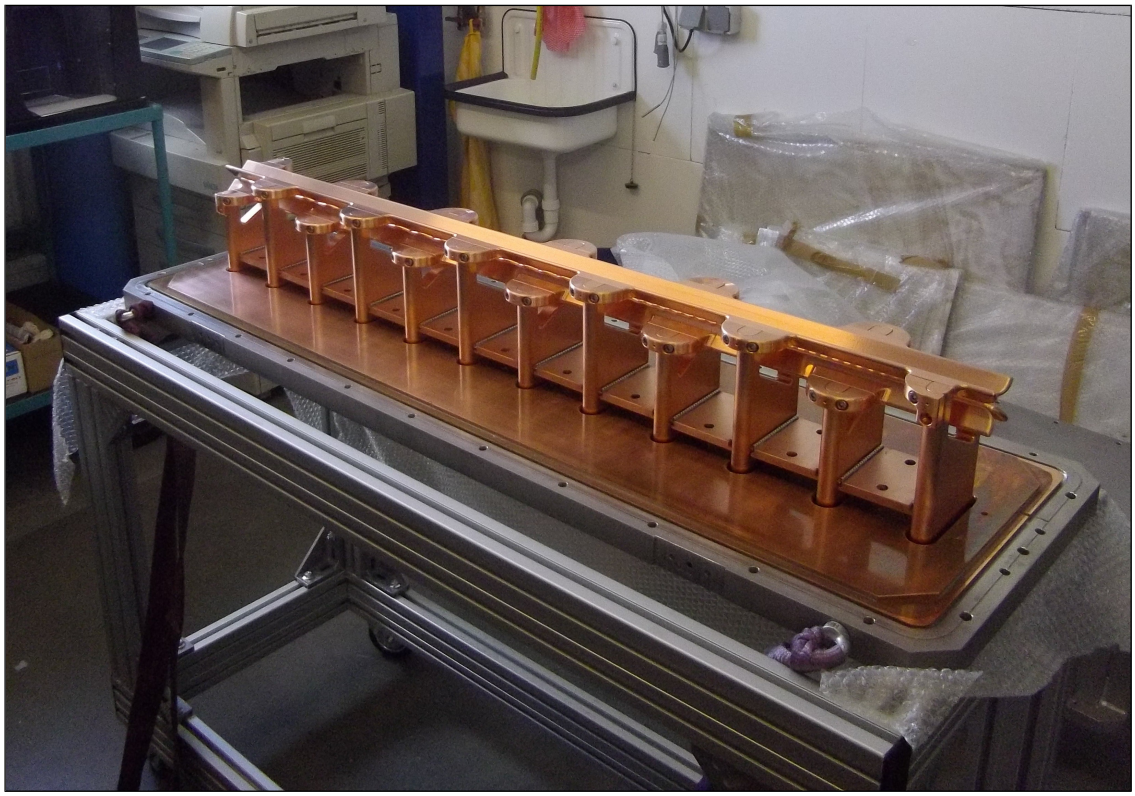

Figure 4.40: *The RFQ rods assembly.*

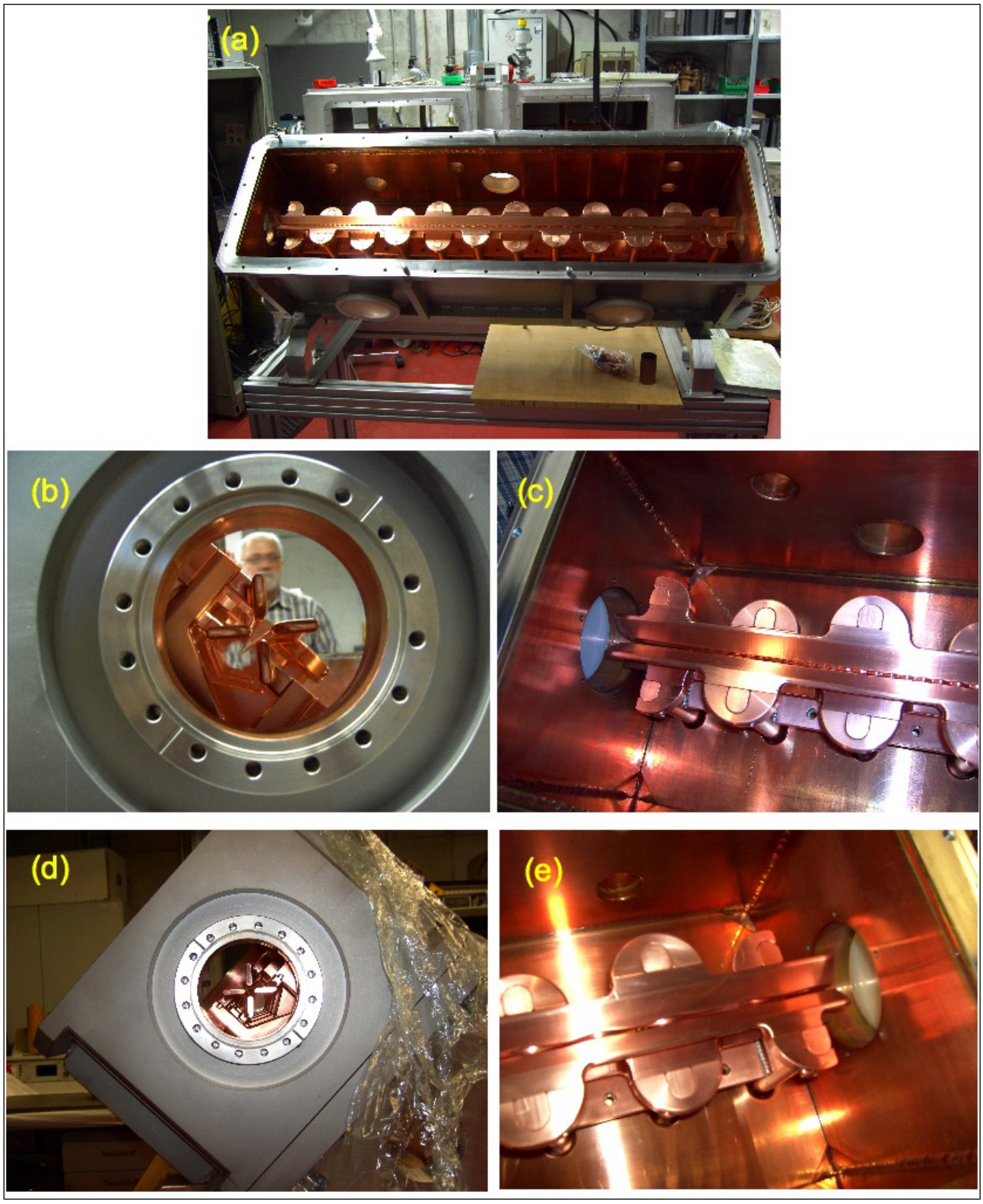

Figure 4.42: *Pictures of the RFQ after assembly but before tuning. (a) RFQ in the vacuum tank, (b,c) upstream end (Prof. Schempp, the RFQ designer is in the background), (d,e) downstream end. (Frankfurt, Germany, 26 May 2011).*

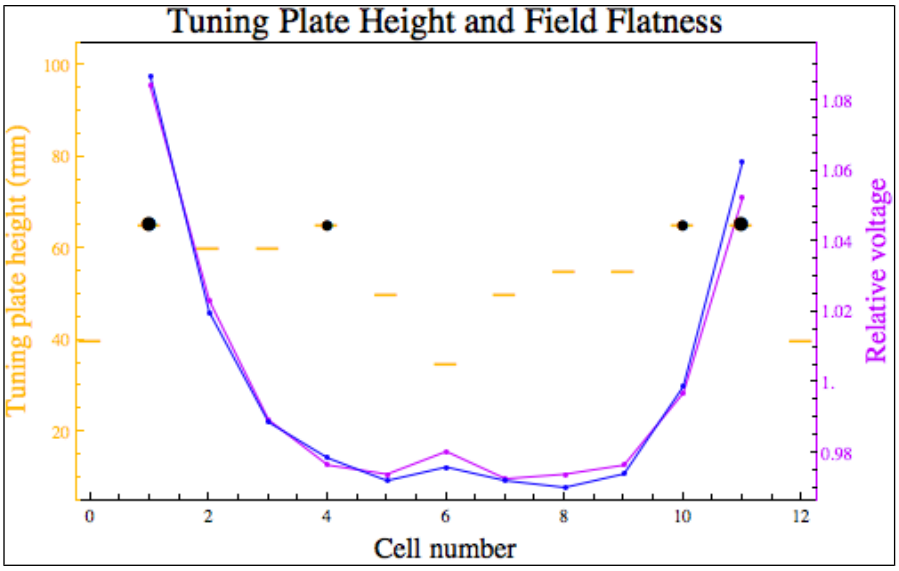

Figure 4.43: *Field flatness of the RFQ and the position of the tuning plates. The blue and magenta curves were taken at two different plunger positions @ 201.12 MHz and 201.06 MHz. The size of the circles show the location and size of the half moons used together with the tuning plates. A photograph of the tuning plates and half moons are shown in Figure 4.50. See section 4.3.4 for the definition of "Relative Voltage".*

Parameter	Value	Units
Resonant frequency	201.25	MHz @ 60°F in air
Q (unloaded)	2800	
Field flatness	< 12	%
Coupler s11	< – 20	dB @ 201.25 MHz in vacuum
Coupling of power port → upstream probe	– 27	dB @ 201.25 MHz in vacuum
Coupling of power port → downstream probe	– 25	dB @ 201.25 MHz in vacuum

Table 4.7: *The network analyzer measurements of the RFQ performed at Fermilab in air and the rods cooled to 60°F.*

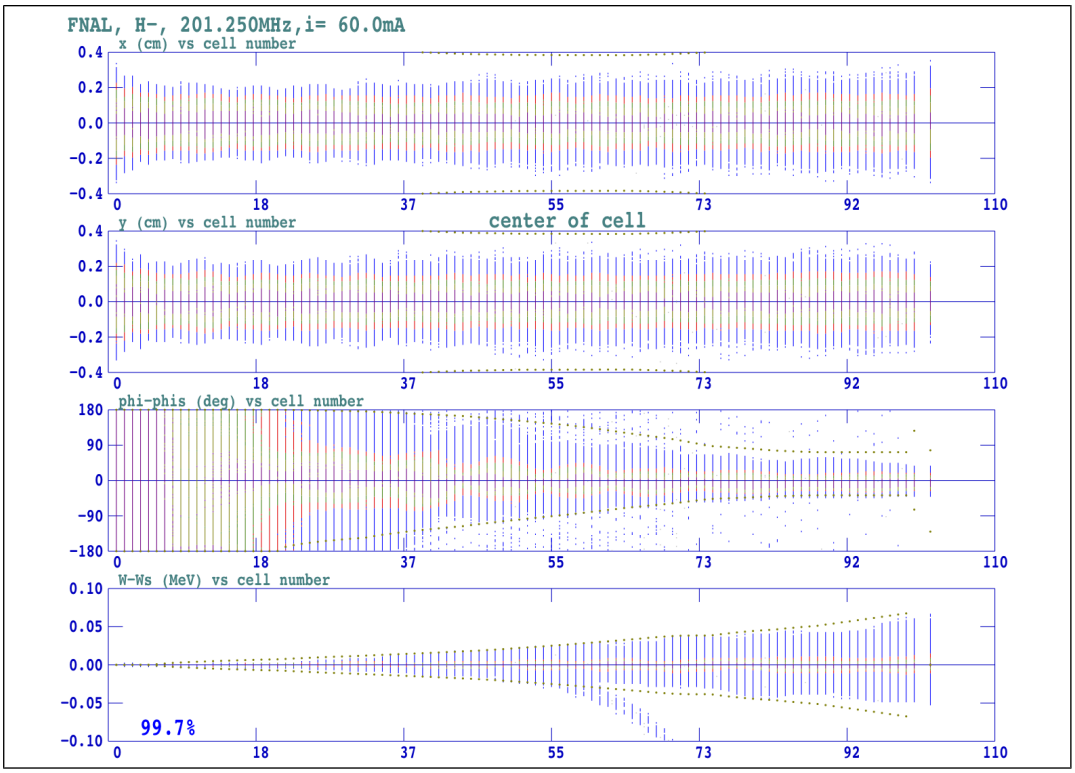

Figure 4.44: *This is a* PARMTEQM *simulation of 60 mA beam going through the RFQ. The transmission efficiency is >99%.*

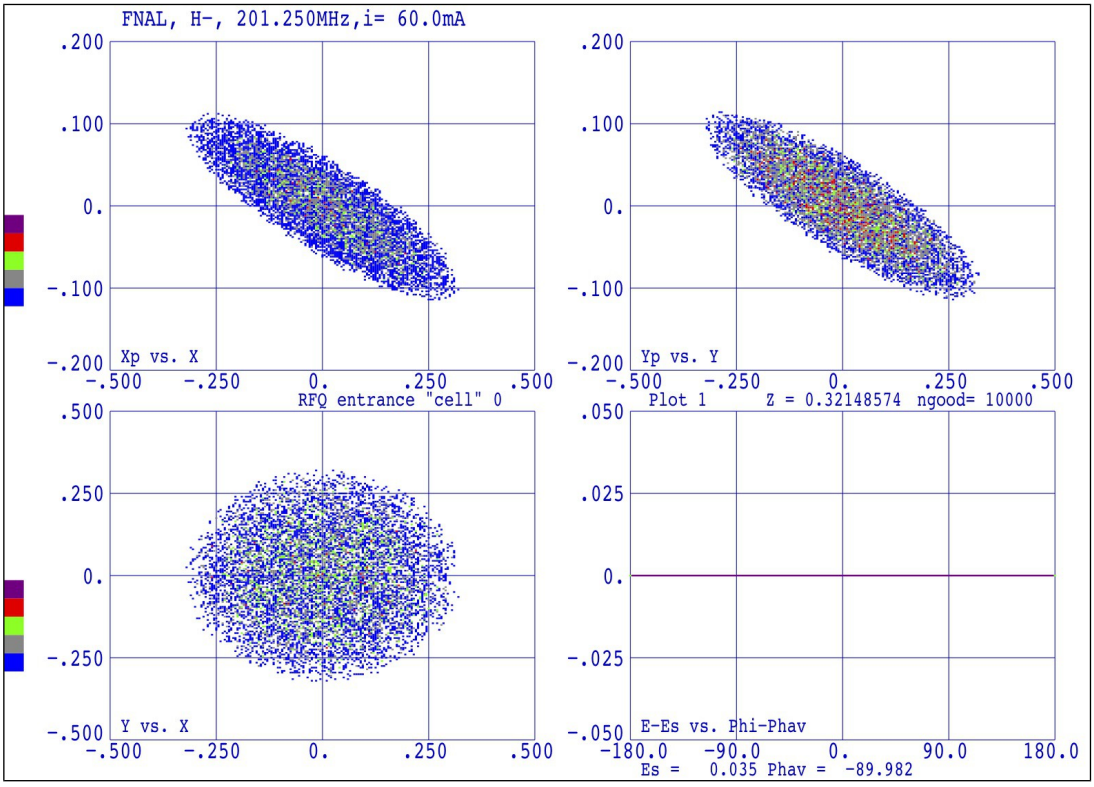

Figure 4.45: *The initial phase space distribution at the entrance of the RFQ.*

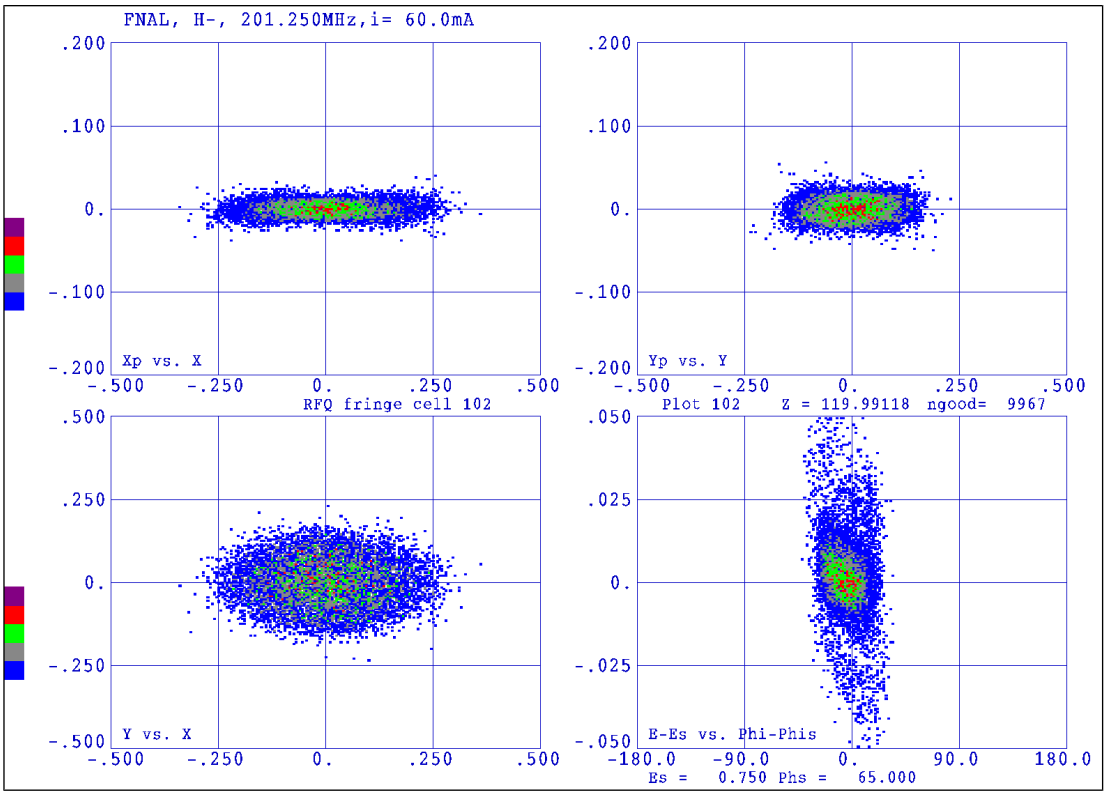

Figure 4.46: *The phase space distribution at the end of the RFQ.*

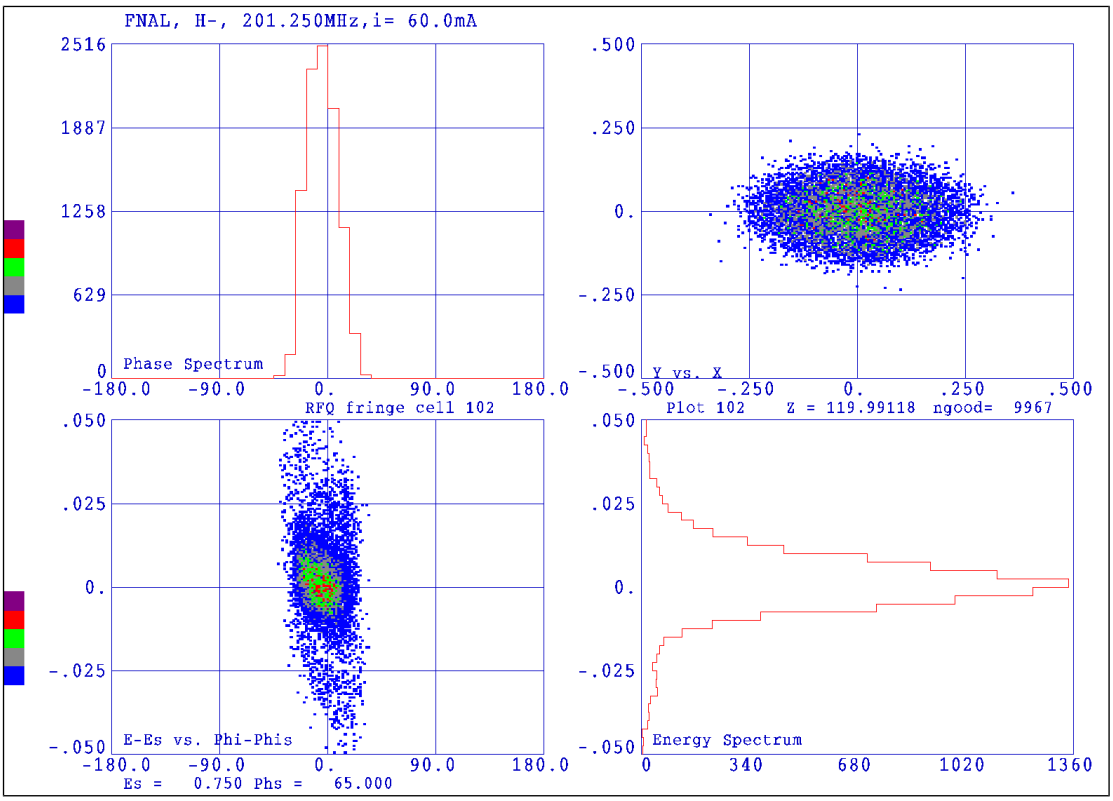

Figure 4.47: *The longitudinal distribution at the end of the RFQ. Note: spatial units are in cm, divergence units are in rad, phase coordinates are in deg, and energy in MeV.*

4.3.1. Tuner

The tuner is located in the middle of the RFQ structure. See Figure 4.48. The tuner is inserted between two copper walls which hold the rods and magnetically couples to the RFQ. The plunger mechanism changes the resonant frequency of the RFQ as it moves towards or away from the rods. When the plunger is closer to the rods, the resonant frequency is higher than when it is further away. See Figure 4.49. The measured frequency change as as function of plunger position is shown in Figure 4.51. The RFQ has been tuned so that when the plunger is near the end of its travel, the resonant frequency is 201.25 MHz at 60°F (temperature of the cooling water) under vacuum (< 10^{-6} torr). The reason for this is that when the RFQ warms up the plunger is pushed into the RFQ so that it is closer to the rods. In this particular set up the entire tuner range is ~220 kHz.

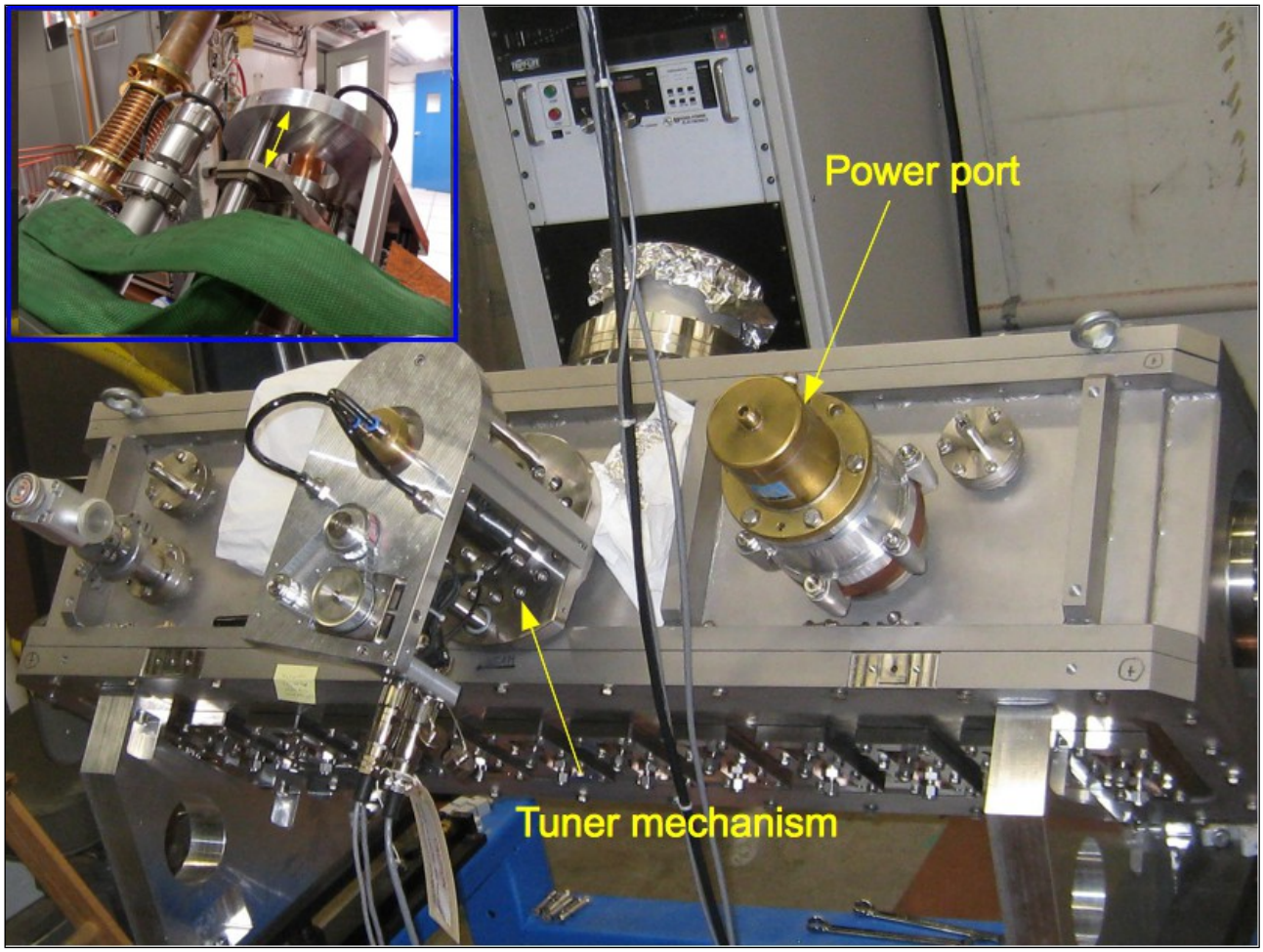

Figure 4.48: *The tuner mechanism is inserted into the middle of the RFQ structure.The inset shows the distance between jaws.*

A quadratic has been used to fit the data points to give the resonant frequency as a function of plunger position and it is

$$f_{\text{vac}} = 201.227 + 0.0143805\text{x} - 0.000237757x^2 \tag{8}$$

f_{vac} is the resonant frequency under vacuum in MHz for the plunger position x in mm. $x=0$ mm is defined to be position of the plunger when the tuner mechanism is fully pulled out of the RFQ, so that the distance between the jaws is 2.939". See Figure 4.48. This distance depends on where the

limit switches are set.

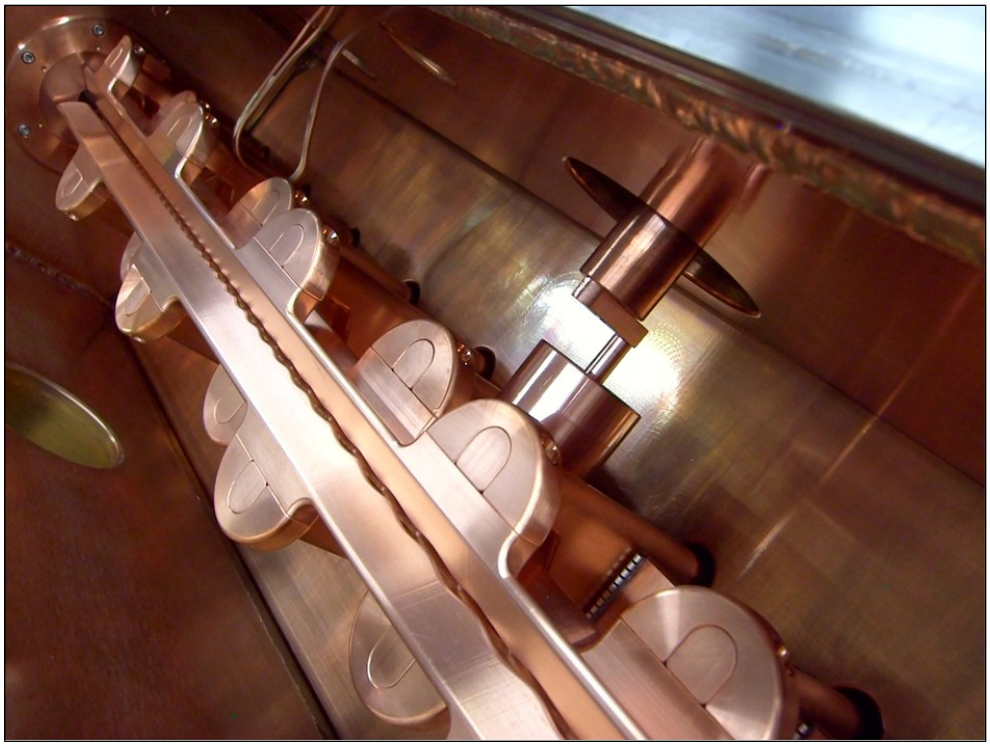

Figure 4.49: *The tuner mechanism inserted into the RFQ. The resonant frequency increases when the plunger gets closer to the rods.*

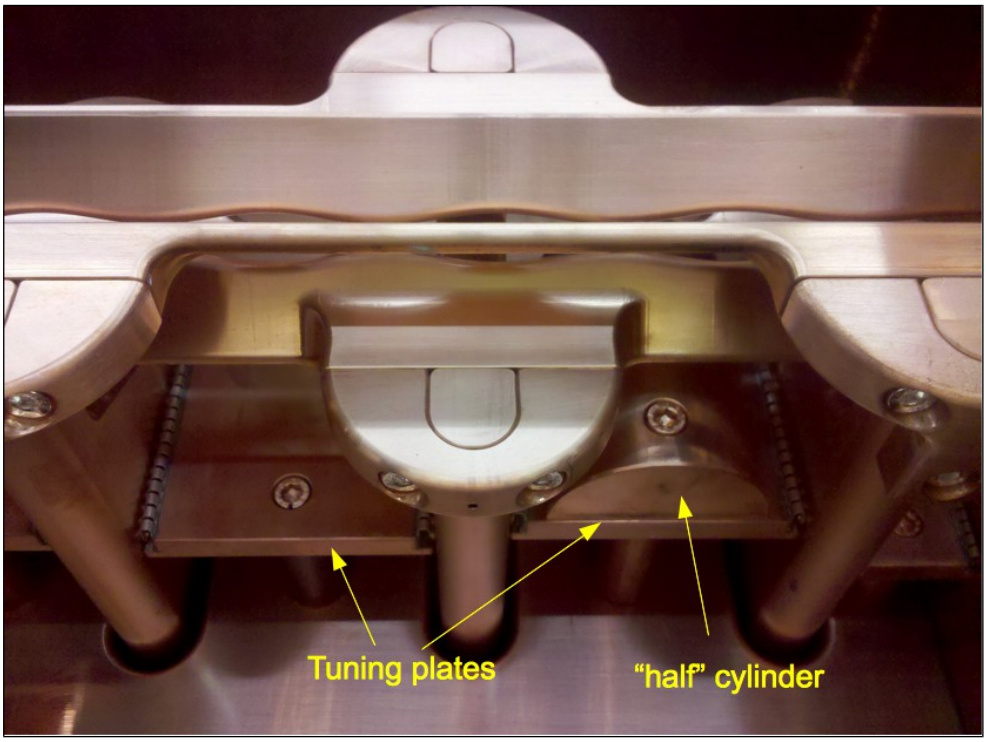

Figure 4.50: *Closeup showing the tuning plates and a "half moon" used to flatten the voltage in the rods.*

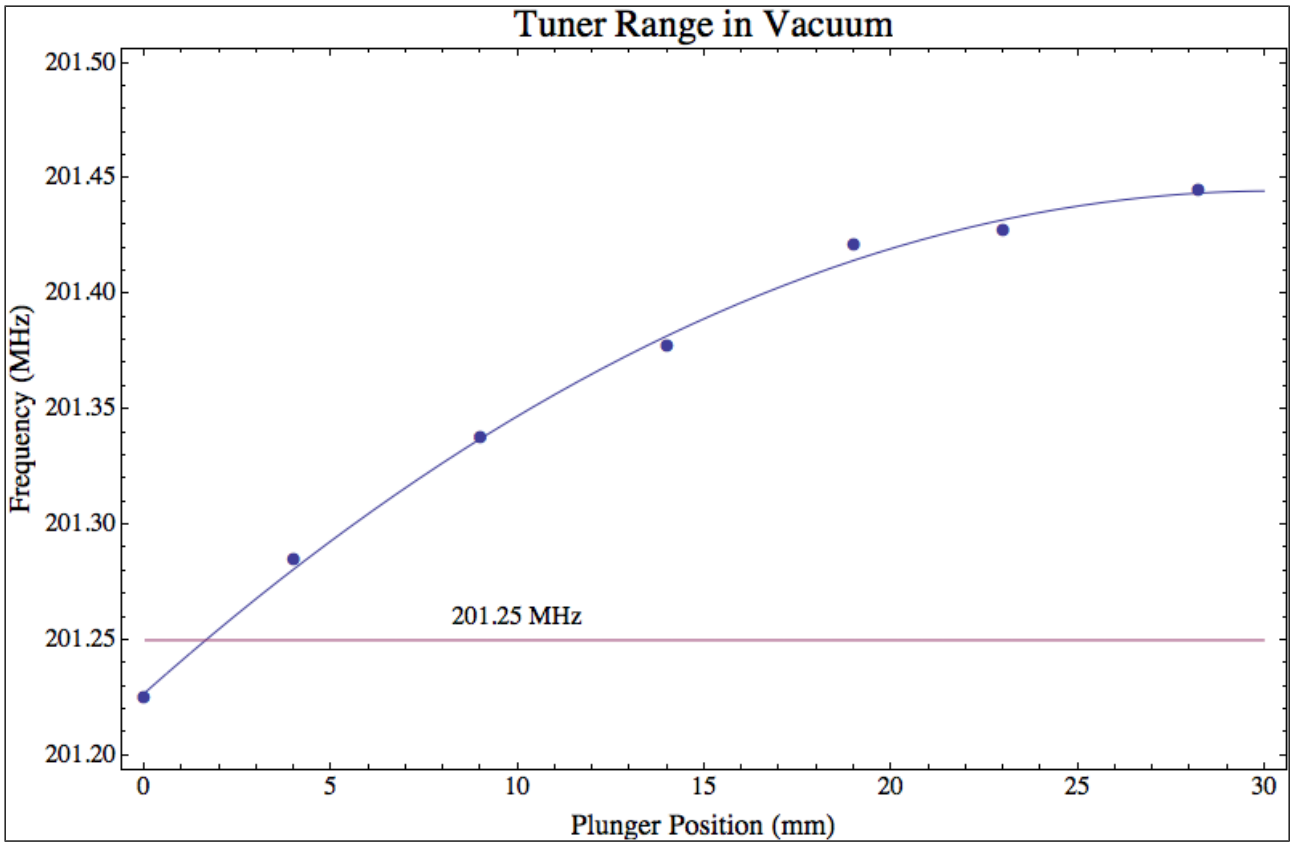

Figure 4.51: *The tuner range under vacuum. The data has been measured with the rods cooled to 60°F. Data was taken on 29 Oct 2012.*

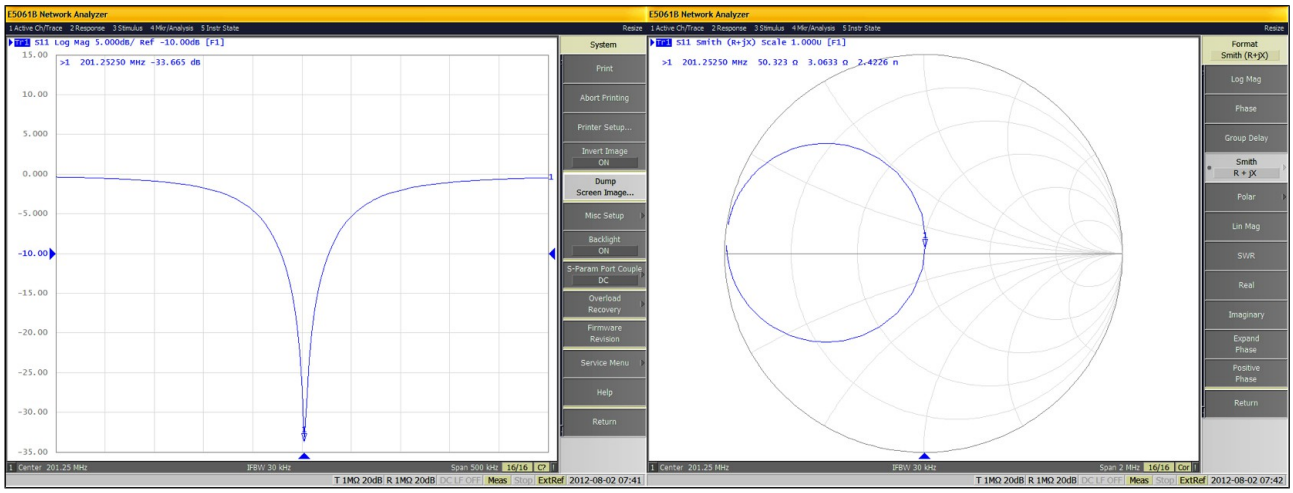

Figure 4.52: The s11 measurements of the power port with the tuner set to the position where the RFQ resonance is at 201.2525 MHz at 60°F. At this position s11 = −34 dB and the impedance is 50Ω.

The s11 measurements of the power port with the tuner set to the resonant frequency 201.25 MHz is shown in Figure 4.52. At this tuner position, $s11 = -34$ dB, and the impedance is 50.32Ω. Note: the definition of s11 in dB is $20\log_{10}[|s11|]$ but it is $10\log_{10}[P_R/P_T]$ where P_R is the

reflected power and P_T is the transmitted power.

4.3.2. Power Coupler

The RFQ power coupler is shown in Figure 4.53. Presently, the coupling beta is

$$\beta = \frac{1+s11}{1-s11} = \frac{1+0.02}{1-0.02} = 1.0 \tag{9}$$

Technically for 60 mA beam, $\beta \geq 1.4$ because [12]

$$\beta = 1 + \frac{P_{\text{beam}}}{P_{\text{cavity}}} \geq 1 + \frac{40[\text{kW}]}{100[\text{kW}]} = 1.4 \tag{10}$$

where P_{beam} is the power required to accelerate 60 mA of beam from 35 keV to 750 keV and P_{cavity} is the power required to maintain the accelerating field in the RFQ when there is no beam. P_{cavity} has been specified by the manufacturer to be < 100 kW. Unfortunately, there is no possible way of rotating the antenna or to enlarge it without the risk of breaking the braze joints. There is some thought that a new RFQ coupler may need to be built so that β is matched to the beam current. But this is not actively pursued at this time.

Figure 4.53: *The power coupler before and after it is inserted into the RFQ. The copper tubing is paired because the coupler was designed to be water cooled. Water cooling is unnecessary in this case.*

4.3.3. Power requirements of thick versus thin rods

A back of the envelope calculation of the power requirements for thick versus thin rods is presented here. The formula (see [13]) that relates the shunt impedance R_p to the perturbation capacitor C_s used in the field flatness measurement (See Figure 4.54) is

$$R_p = \frac{2Q\Delta f}{\pi f_0^2 C_s} \tag{11}$$

where Q is the quality factor, Δf is the frequency shift due to the addition of the perturbation capacitor, f_0 is the resonant frequency of the RFQ.

Using, this formula, the parameters in Table 4.8 for the thick and thin rods are used to calculate R_p and from there, the expected power reduction is shown to be about 30%. The measure that is used to determine whether there is better power efficiency is to measure the power required for bunching. From this experiment, the expected improvement in power efficiency did arise. See sections 4.3.5.c, appendices C.2 and C.3. Bunching using the thin rods occur just above 100 kW while for the thick rods it is above 130 kW. This gives a power reduction of about 23% between thin and thick rods.

	Thick rods		**Thin rods**	
Parameter	**Value**	**Units**	**Value**	**Units**
C_s	1	pF	2	pF
Q	~2500		~2500	
f_0	201.576	MHz	201.000	MHz
Δf	919	kHz	2175	kHz
R_p	36	kΩ	43	kΩ
Ratio of power between thin and thick rods			$\frac{R_p^2 \text{ of thin rods}}{R_p^2 \text{ of thick rods}} = \frac{1/43^2}{1/36^2} = 0.70$	

Table 4.8: *The expected power reduction by going to thin rods compared to thick rods.*

4.3.4. Field flatness

The field flatness is measured by perturbing the capacitance in each *LC* cell of the RFQ with a small capacitor. See Figure 4.54. The field flatness plot after the downstream end plate was removed and the upstream end plate entrance hole was increased to 1.25" is shown in Figure 4.43.

The "relative voltage" that is used for describing the flatness of the E-field comes from the relationship $\sqrt{\Delta f / f_0} \propto E_n$ where Δf is the frequency shift from the RFQ resonant frequency f_0 and E_n is the amplitude of the E-field in the *n*th cell. However, $E_n \propto V_n$, where V_n is the potential in the *n*th cell. If the mean voltage V_{ref} is defined to be the reference voltage, then the relative voltage is

simply V_n / V_{ref} so that at 100%, the voltage is at V_{ref}.

The "field error" that is used to describe the quality of the field flatness is defined to be the (maximum relative voltage) – (minimum relative voltage). In this case, the field error is about 12% and it is actually quite poor because in general, a field error < 5% is the desired goal.

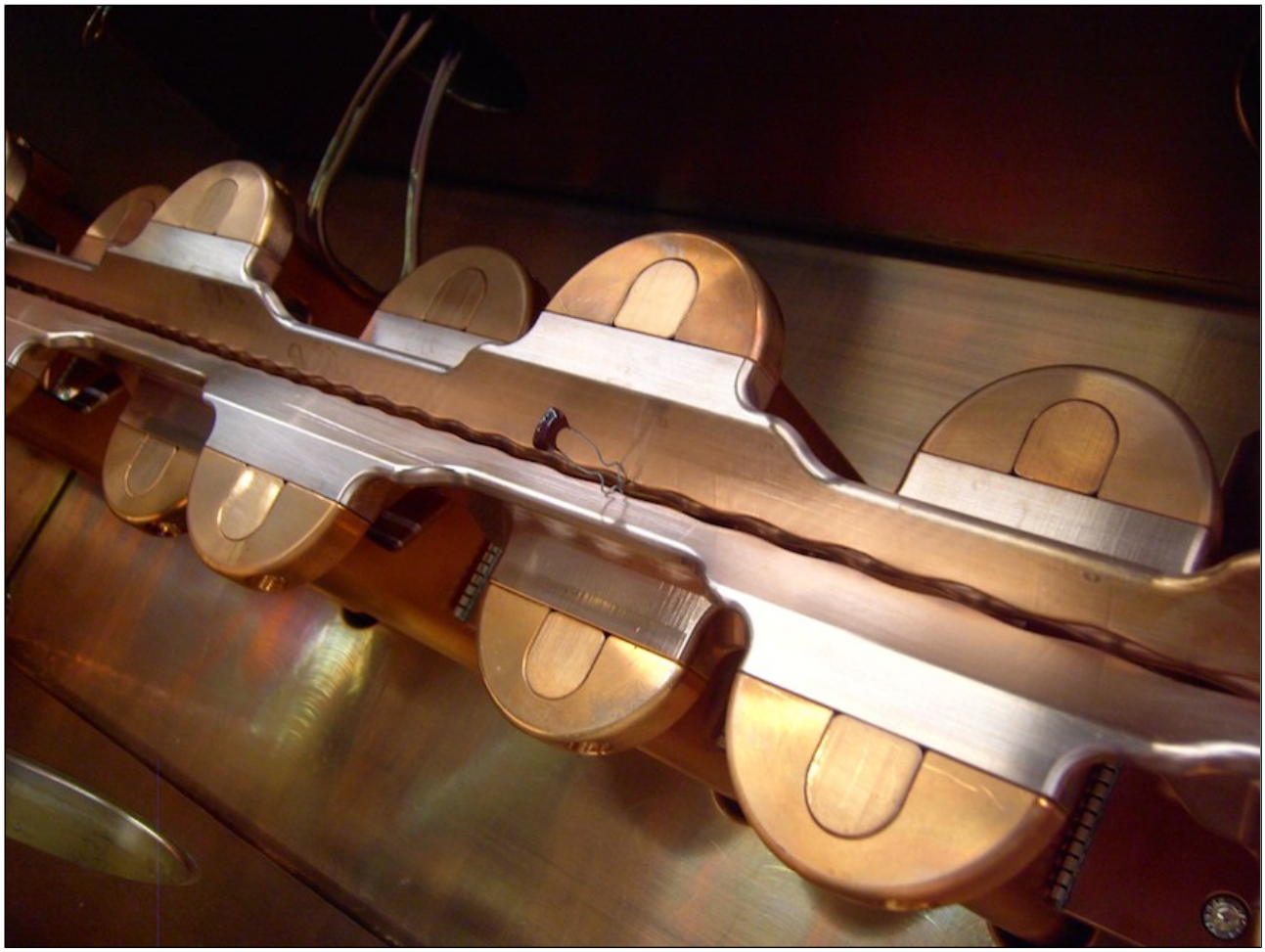

Figure 4.54: *The perturbation of each LC cell is created by inserting a capacitor between the rods in each LC cell. In this case, a 2 pF capacitor is used.*

The reason why the field flatness is poor is because the RFQ was originally tuned with both end plates removed (see Figure C.5 for a picture of the downstream end plate). Unfortunately, without the upstream end plate, enough of the RF escaped from the RFQ that was then picked up by the Einzel lens. The connectors to the Einzel lens acted like antennas that radiated the RF into the outside environment which caused the control system to continuously trip. This meant that the upstream end plate had to be reinstalled. In this present installation, the upstream end plate had its hole enlarged to 1.25" from 20 mm diameter. And because of the boundary condition change, the RFQ had to be retuned by FNAL personnel rather than by the manufacturer and that is the reason why the field quality is not optimal. The previous field flatness measurement when both the upstream and downstream end plates removed is shown in Figure 4.55. In this case, the field error is 6%.

It is interesting that the differences in field flatness between the present tuning plate

configuration and the one with both end plate removed is a small "half moon" in cell 4 and the upstream end plate. These difference result in a dramatic change in field flatness that can be seen in Figure 4.56.

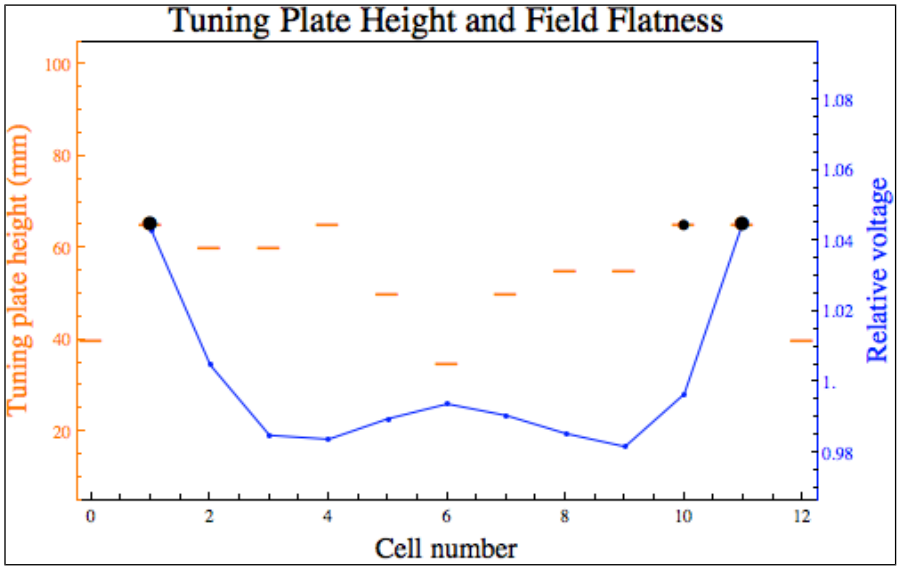

Figure 4.55: *This is the field flatness measured by J.S. Schmidt when both the upstream and downstream end plates are removed. The field error is 6% in this case. The addition of a small "half moon" in cell 4 and the upstream end plate has a dramatic effect on the field flatness. See Figure 4.56 for a comparison.*

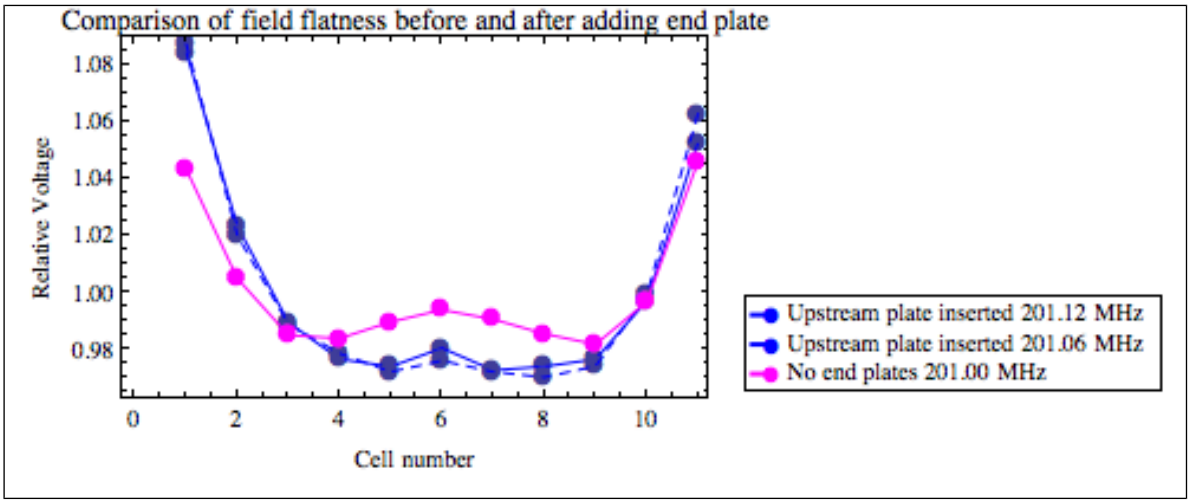

Figure 4.56: *This is the field flatness comparison before and after the upstream end plate is added. It is clear that the addition of a small "half moon" in cell 4 and the end plate changes the field flatness quite drastically.*

4.3.4.a. *Effect of field flatness and capture efficiency*

The effect of field flatness on capture efficiency was studied by S. Kurennoy (LANL) because there is a worry that the poor field flatness of 12% will have a much poorer capture efficiency when compared to 6% field flatness.

Kurennoy found that the capture efficiencies are better correlated to the shape of the field flatness than to the differences between 12% and 6% field flatness, i.e. the shape of the field flatness dominates the capture efficiency. See Figure 4.57 and Table 4.9.

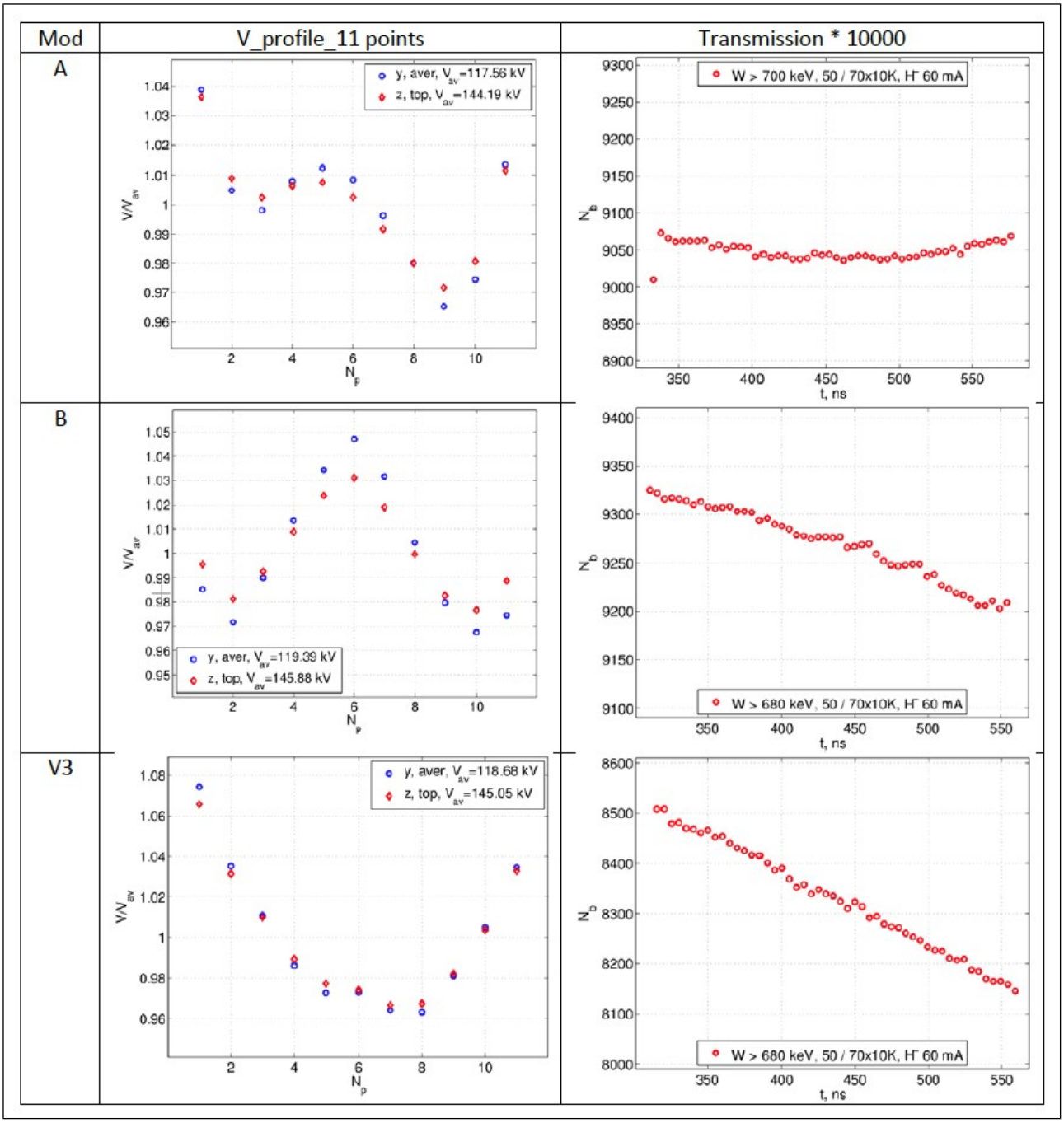

Figure 4.57: *The field profiles of three models show that the with field errors of 8% for A and B and 11% for C. The large difference in capture efficiency between models A, B and model C can only be explained by field shape.*

Model	Field error (%)	Capture efficiency (%)
A	7.5	91
B	8.0	93
V3	11.5	83

Table 4.9: *A comparison of the field flatness and capture efficiencies.*

The results from Kurennoy's CST MICROWAVE STUDIO and PARTICLE STUDIO simulations on capture efficiencies are shown in Table 4.9. From this table and Figure 4.57, the results show that the capture efficiencies are strongly correlated with the shape of the field flatness. In fact, there is a 10% difference in capture between a "∩" shaped curve and a "∪" shaped curve. If the simulations are correct, then this means that the FNAL RFQ capture efficiency can be improved by about 10% if the field flatness can be reshaped to a "∩". However, it must be borne in mind that any change to the field flatness shape also shifts the resonant frequency of the RFQ. And so, care must be taken to ensure that the required resonant frequency of 201.25 MHz is still in the mid-range of the RFQ tuner when it is re-shaped. Work is being done at FNAL and U. Frankfurt to see whether it is indeed possible to change the shape of the field flatness but have the resonant frequency fixed.

4.3.5. Beam tests

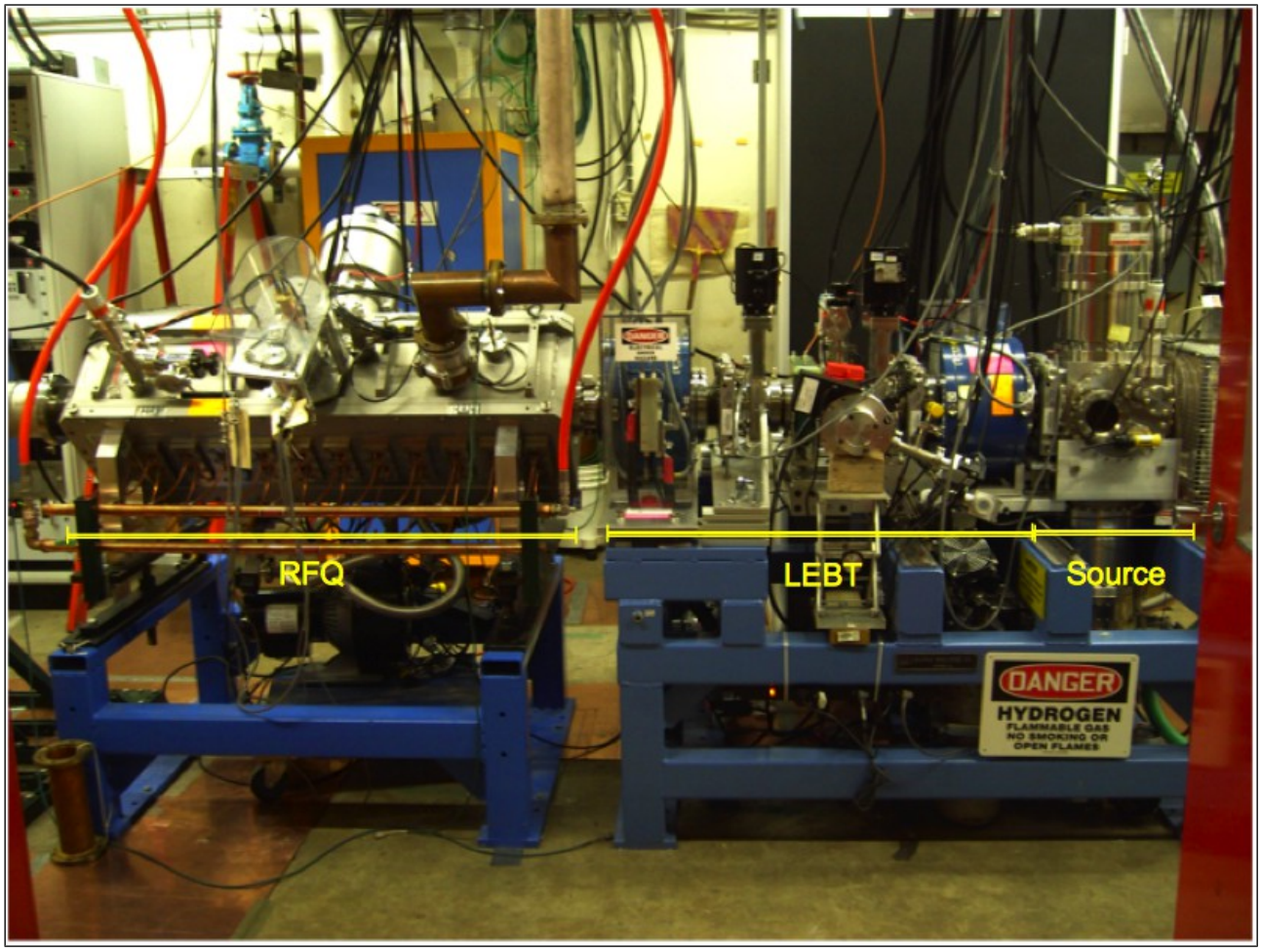

Figure 4.58: *The source, LEBT and RFQ under test.*

The goal of testing the RFQ with beam is to qualify it for operations. The test line is shown in Figure 4.58. The following experiments have been done:

1. Beam capture and bunching efficiency as a function of input power.
2. Output beam energy as a function of input power.
3. Output transverse emittance as a function of position within the bunch train, beam current and input power.

4.3.5.a. *Beam transmission efficiency measurements*

The setup for the beam transmission efficiency measurements consists of a toroid and a beam dump mounted on a 6" beam pipe. Simulations show that beam currents < 60 mA should not hit the wall at this aperture size. Therefore all the beam is measured at the end of the RFQ. Figure 4.59 shows the setup used for these measurements.

The beam from the LEBT is focused into the input of the RFQ using both solenoidal and gas focusing. The timing of the RF is adjusted so that all the beam is within the RF pulse. See Figure 4.60(a). The RF power going into the RFQ is adjusted and the beam at the end of the RFQ is measured. Figure 4.60(b) shows 72 mA in the middle of the LEBT and 46 – 48 mA of beam a the end of the RFQ for an input power of [178 (forward power) – 8.5 (reflected power)] = 169.5 kW

with beam. The power into the RFQ *without* beam is about (169.5 – 30) = 140 kW.[4] The LEBT pressure is 3.2×10^{-6} Torr and extractor voltage is at 38 kV and not the usual 35 kV.

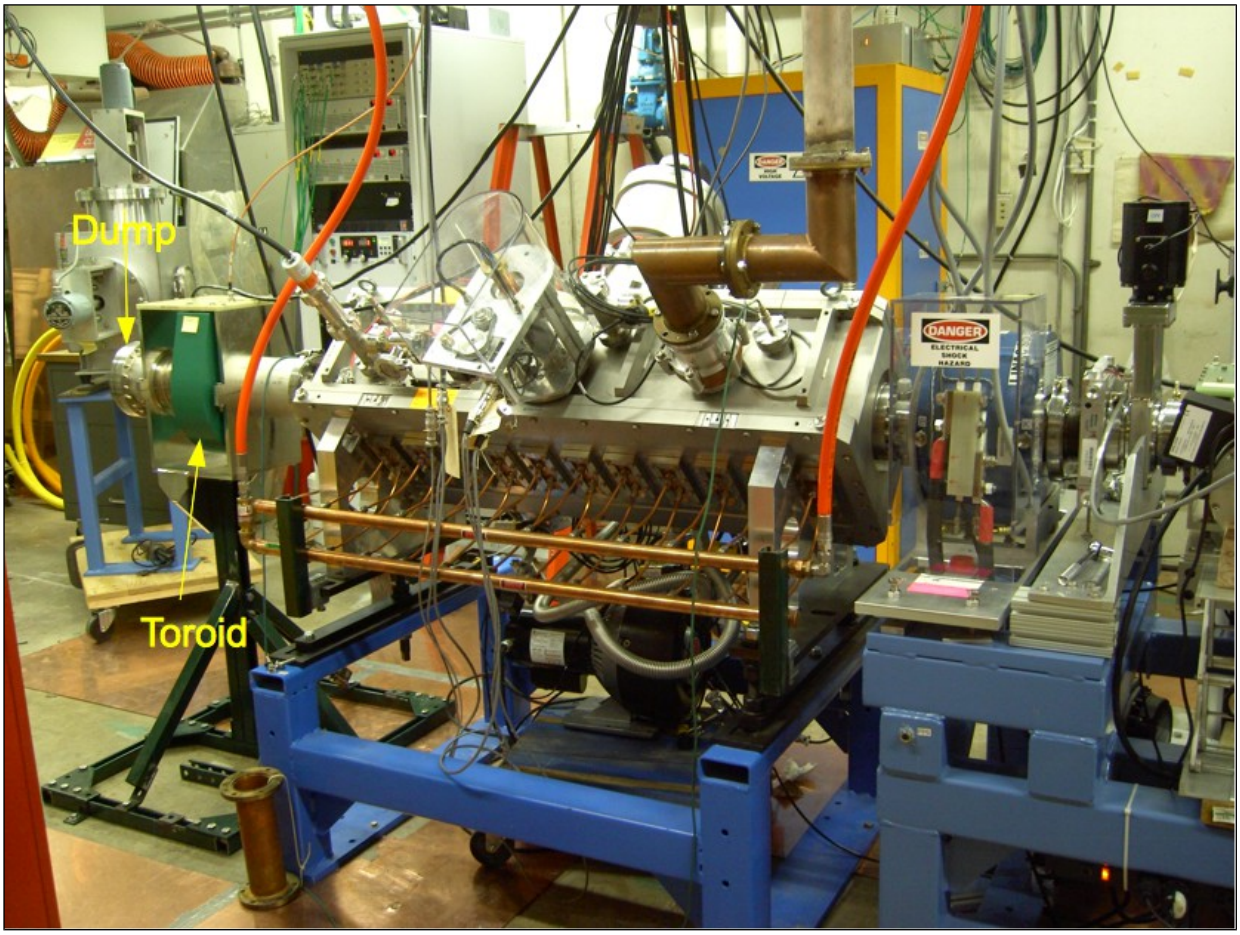

Figure 4.59: *A beam dump and toroid is installed directly at the end of the RFQ for beam capture experiments. A 6″ beam pipe is used to mount these two devices.*

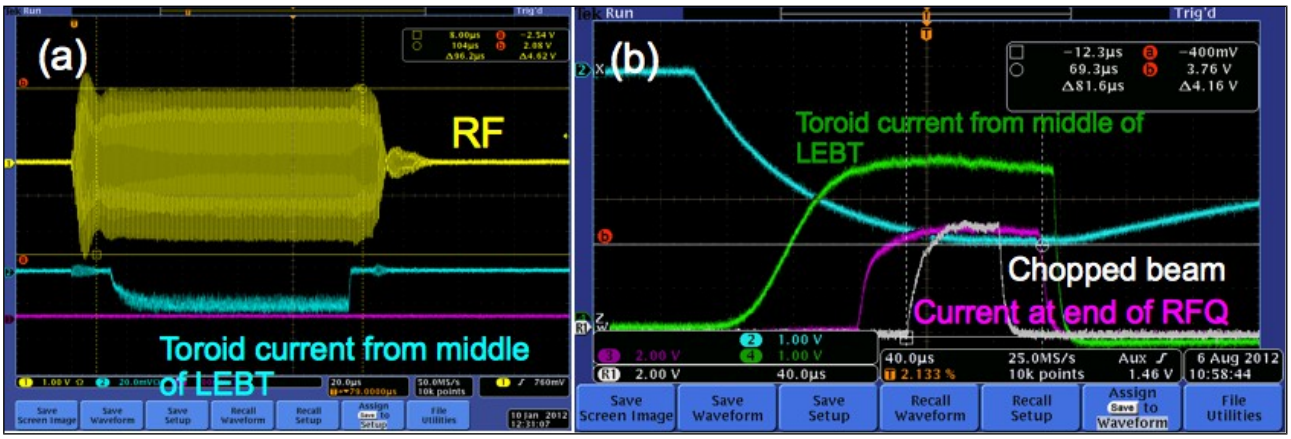

Figure 4.60: *(a) The beam is timed so that it is in the middle of the RF measured at the upstream antenna. (b) 46 mA is measured at the end of the RFQ.*

4 Beam power comes from $(750-35)\ \text{keV}\times(40\ \text{mA})\approx30\ \text{kW}$ for 35 keV input beam.

The transmission efficiency is also strongly correlated to the gas pressure in the LEBT. See Figure 4.61 which shows a clear pressure threshold for high RFQ output current. The plan is to operate the LEBT pressure around 3.6×10^{-6} Torr. The threshold probably comes from insufficient gas focusing below 2×10^{-6} Torr.

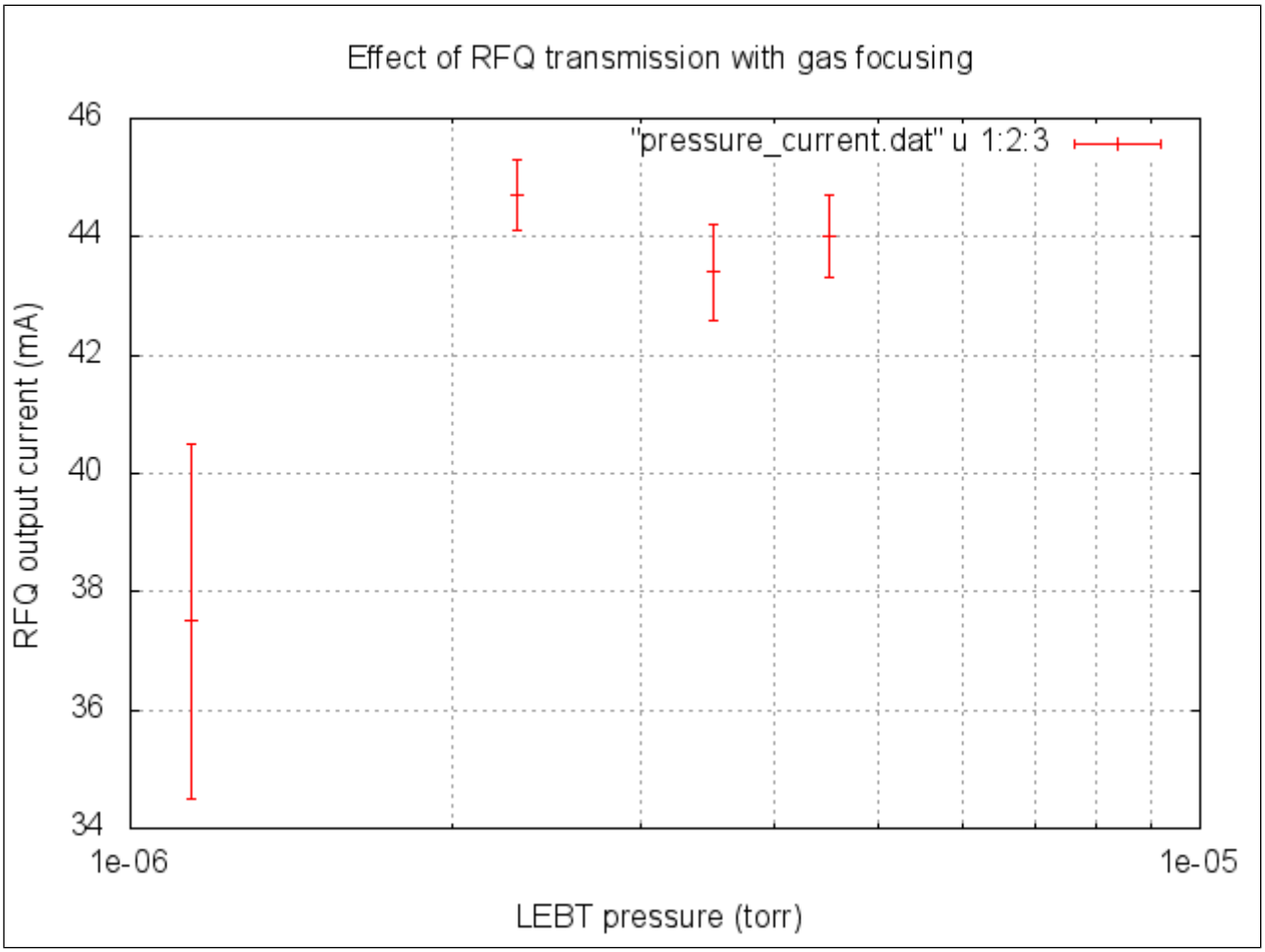

Figure 4.61: *It is clear that the LEBT pressure has to be worse than 2×10^{-6} Torr for good transmission of beam through the RFQ.*

The rise time of the beam when it is within the RF envelope is dominated by the neutralization time from hydrogen in the LEBT. Using Eq.(4), the estimated neutralization time for gas pressure 8×10^{-6} torr from H_2, ionization cross section $\sigma_i=1.8\times10^{-21}$ m^2, $v=0.00864c$ is

$$\tau_N=\frac{1}{\rho\sigma_i v}=\frac{1}{[n_x\times(8\times10^{-6})]\times1.8\times10^{-21}\times0.00864\text{c}}=0.8\ \text{ms}\gg30\ \mu\text{s} \qquad (12)$$

where $n_x=3.3\times10^{22}$ m^{-3}/Torr is the number density of gas per torr at 20°C calculated from Loschmidt's constant. Interestingly, the theoretical value is much longer than the observed value.

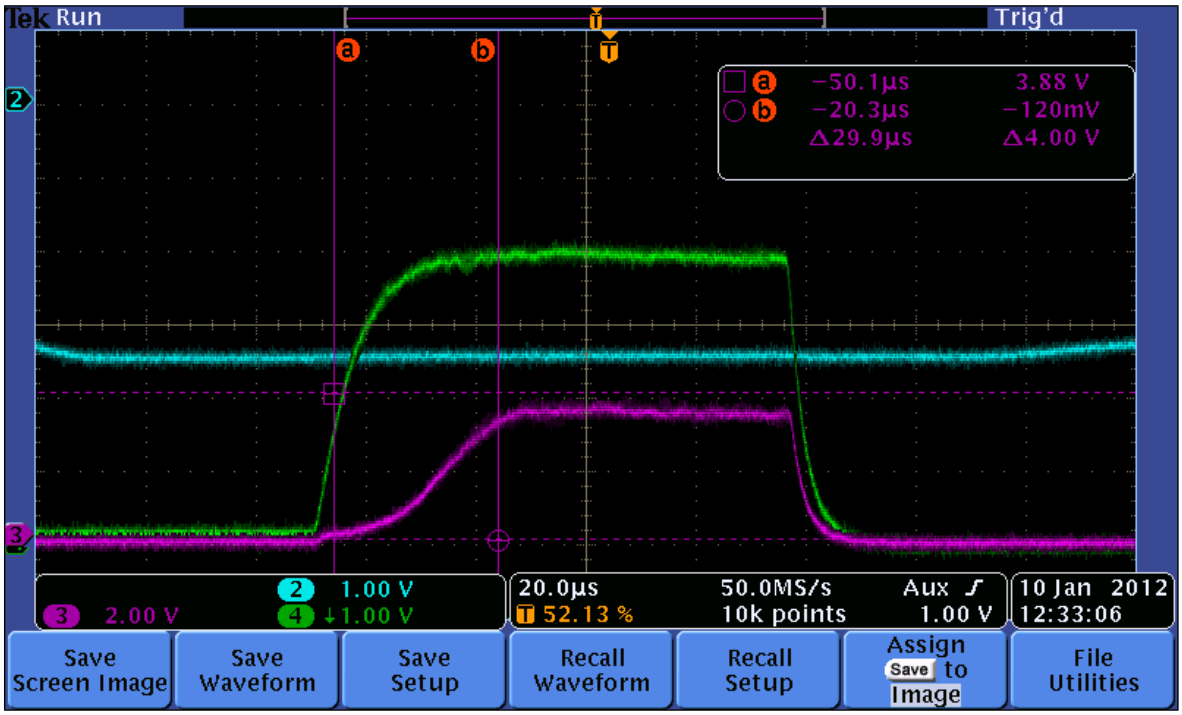

Figure 4.62: *The rise time of the beam at the exit of the RFQ is about 30 µs. This is much faster than the theoretical neutralization time with hydrogen gas at 8 x 10^{-6} Torr. See Eq.(12).*

4.3.5.b. *Beam transmission as function of input power*

The H- beam upstream of the RFQ has been set to 60 mA and the output at the end of the RFQ has been measured. The transmission rolls over at about 180 kW *with beam* and for operations should be set below this level. Figure 4.63 shows the measurement.

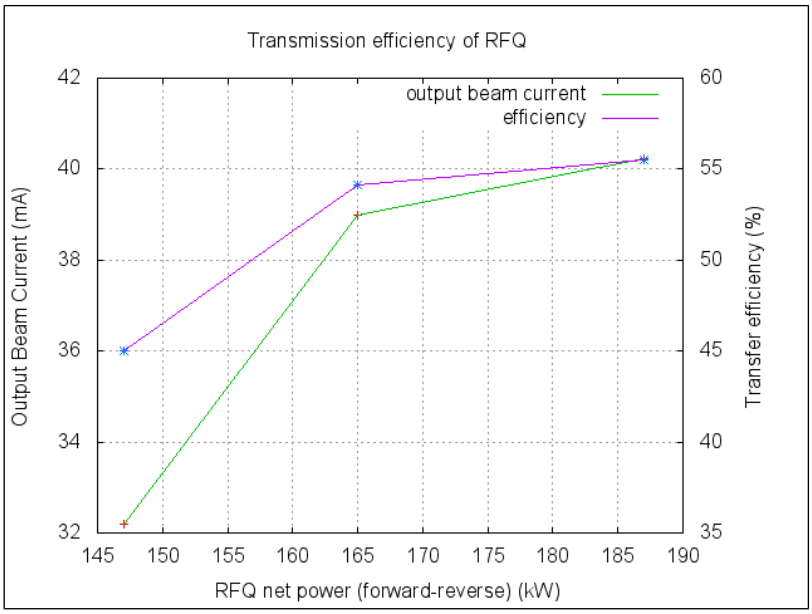

Figure 4.63: *Beam transmission as a function of input power. The amount of beam at the output starts to saturate above 170 kW. Input beam current is 60 mA.*

Although not shown here, the best transmission efficiency that has been achieved is 71% for 60 mA measured in the middle of the LEBT and 43 mA at the exit of the RFQ. Higher currents ~47 mA at the end of the RFQ is achievable with 70 mA of beam, but clearly the transmission efficiency drops to 67%.

4.3.5.c. *Bunching as a function of input power*

A fast Faraday cup [10] is connected downstream of the RFQ. See Figure 4.65. The fast Faraday cup has a bandwidth of 15 – 20 GHz and the signal is connected to a HP oscilloscope with a bandwidth of 6 GHz. See Figure 4.36 for a photograph of the fast Faraday Cup.

When the input power is set to >150 kW, the bunched beam reaches a stable bunch sigma of 0.41 ns. The average bunch sigma is 0.41 ns in this case. See Figure 4.64. The distribution of the bunch length along the beam pulse shows that the bunch length can range from ~0.3 ns to ~0.5 ns. See Figure 4.68.

However when the input power is reduced below 100 kW, the beam is not bunched at all. See Figure 4.67(a).

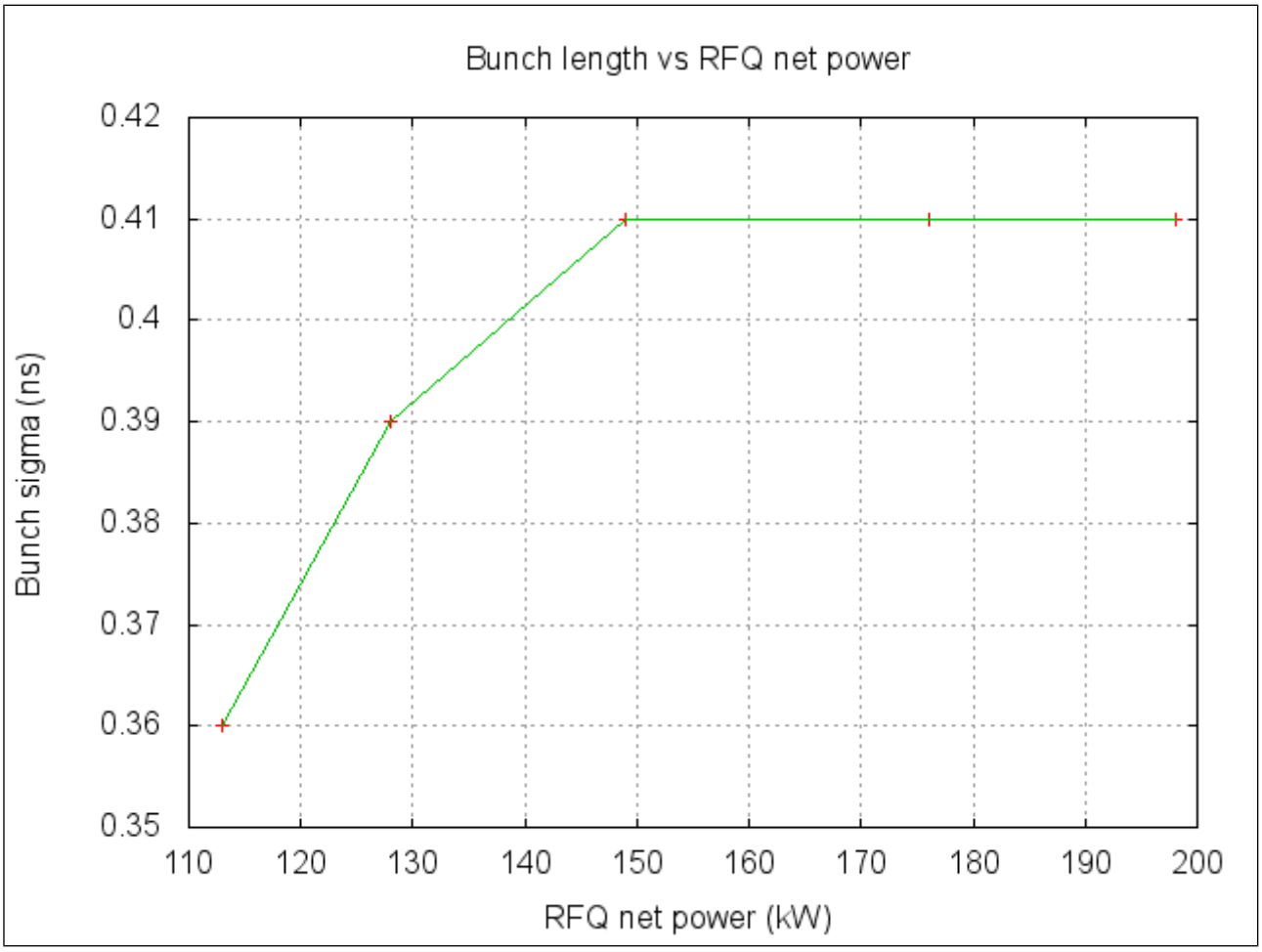

Figure 4.64: *This plot clearly shows that bunching occurs above 150 kW net power (forward – reflected).*

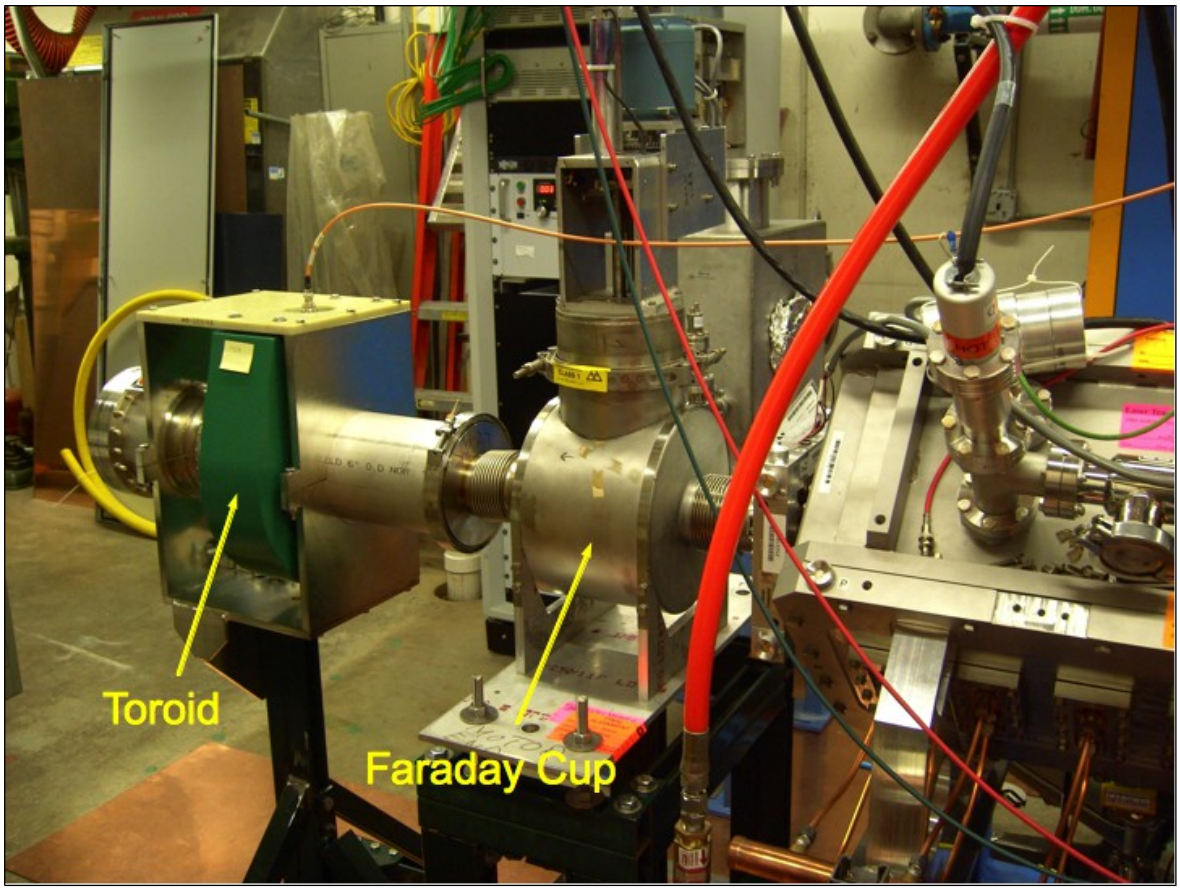

Figure 4.65: *A fast Faraday cup is connected to the RFQ. The distance between the RFQ and the Faraday cup is about 10".*

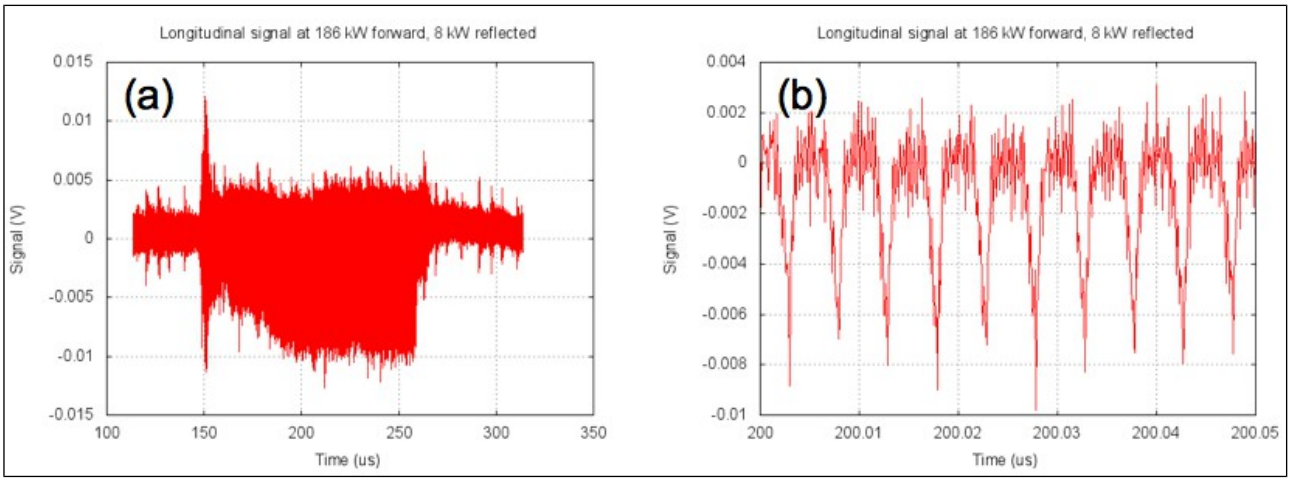

Figure 4.66: *At 178 kW net power, the beam is well bunched. (a) shows the entire bunch train and (b) shows the individual bunches in the train. The average bunch sigma is 0.41 ns.*

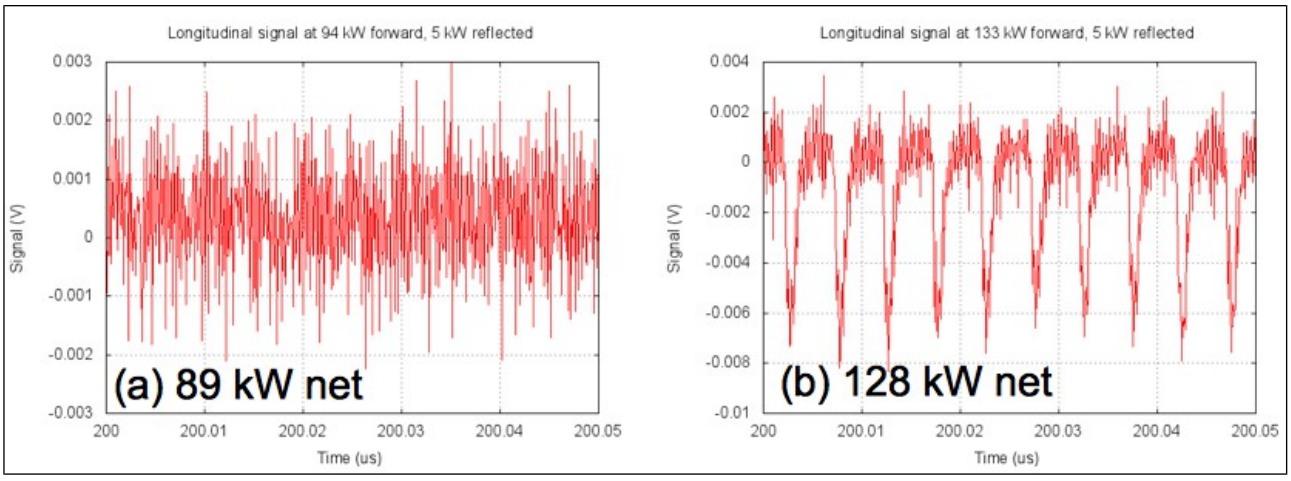

Figure 4.67: *At 128 kW input power, bunching starts and the bunch length sigma is 0.39 ns. Below 100 kW, there is no bunching.*

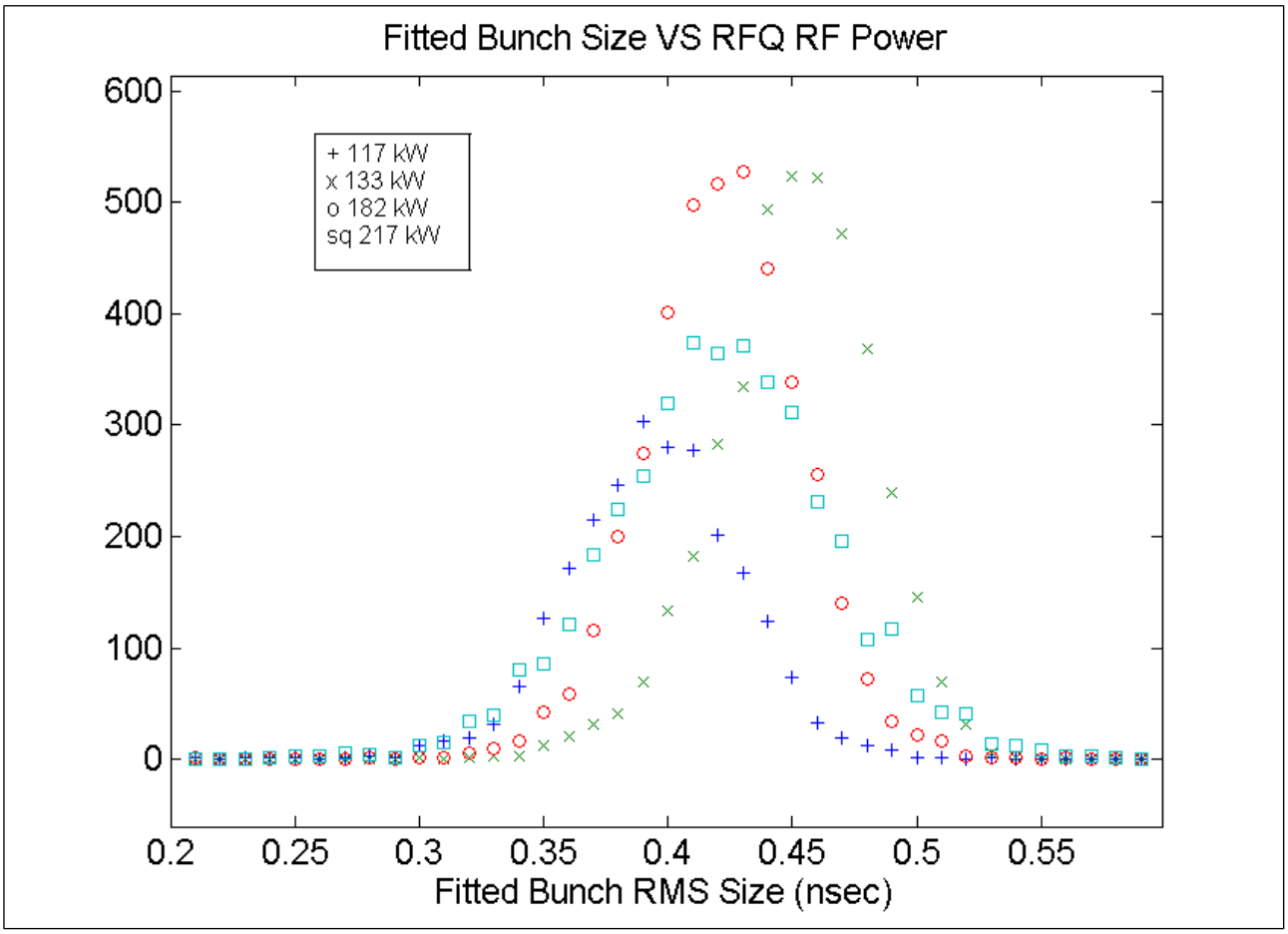

Figure 4.68: *The bunch size distributions for different RFQ forward power.*

4.3.5.d. *Transverse emittance*

The transverse emittance is measured with an emittance probe connected to the end of the RFQ. See Figure 4.69. The emittance probe slits are 8" from the exit flange of the RFQ.

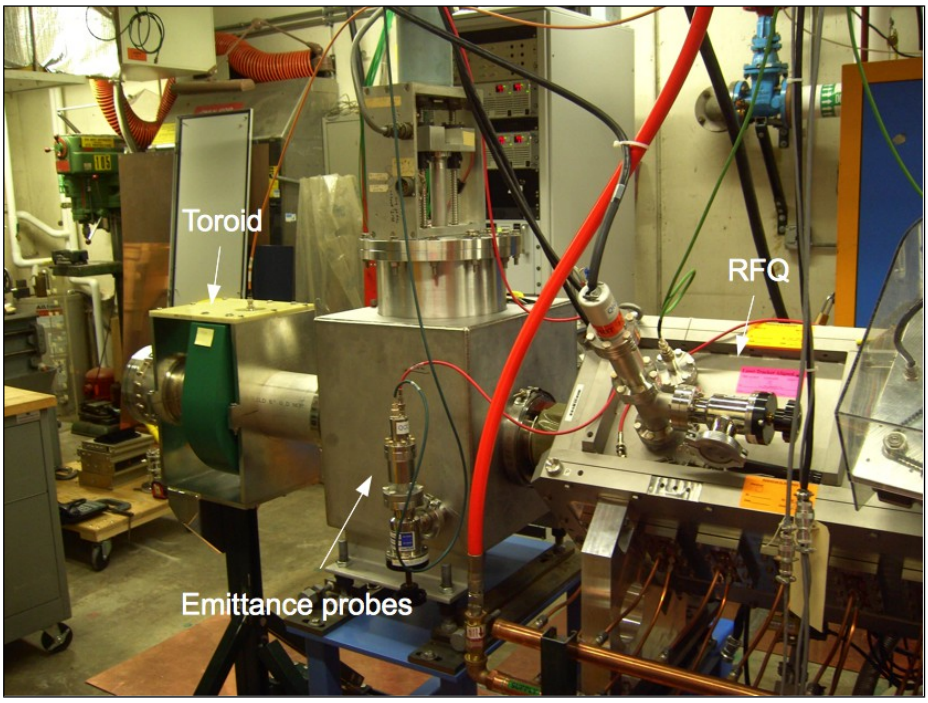

Figure 4.69: *The setup used to measuring the transverse emittance at the end of the RFQ.*

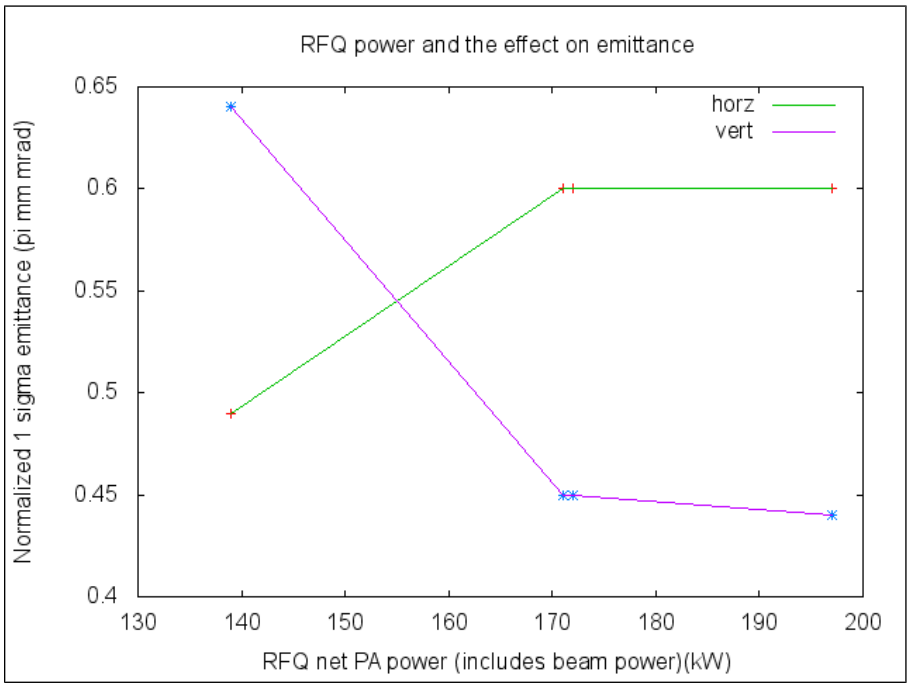

Figure 4.70: *The effect on emittance as a function of RFQ power. The emittances stabilizes above 170 kW.*

The effect of RFQ power on emittance is shown in Figure 4.70. The transverse emittance stabilizes to $\varepsilon_x = 0.6\ \pi$ mm mrad and $\varepsilon_y = 0.5\ \pi$ mm mrad (1× rms normalized) above 170 kW. The input beam current into the RFQ is 65 mA. The output beam current is dependent on beam power and at 168 kW net power, it is 39.5 mA. (Note: the current is lower than expected because the toroid is quite far downstream from the RFQ and so some of the beam is scraped before it is measured). The beam is also asymmetric because the beam coming out of the source is asymmetric. The source of the asymmetry comes from the dipole field in the magnetron source. This assertion is easily proved because when the source rotated by 90° the emittances are exchanged, i.e. ε_x becomes smaller than ε_y. The measured emittances can be compared to the simulated emittance shown in Table 4.6 and it can be seen that the emittances are consistent with the simulation. Note: input emittances do affect the output emittances! See Figure 4.71 to see the measured emittances.

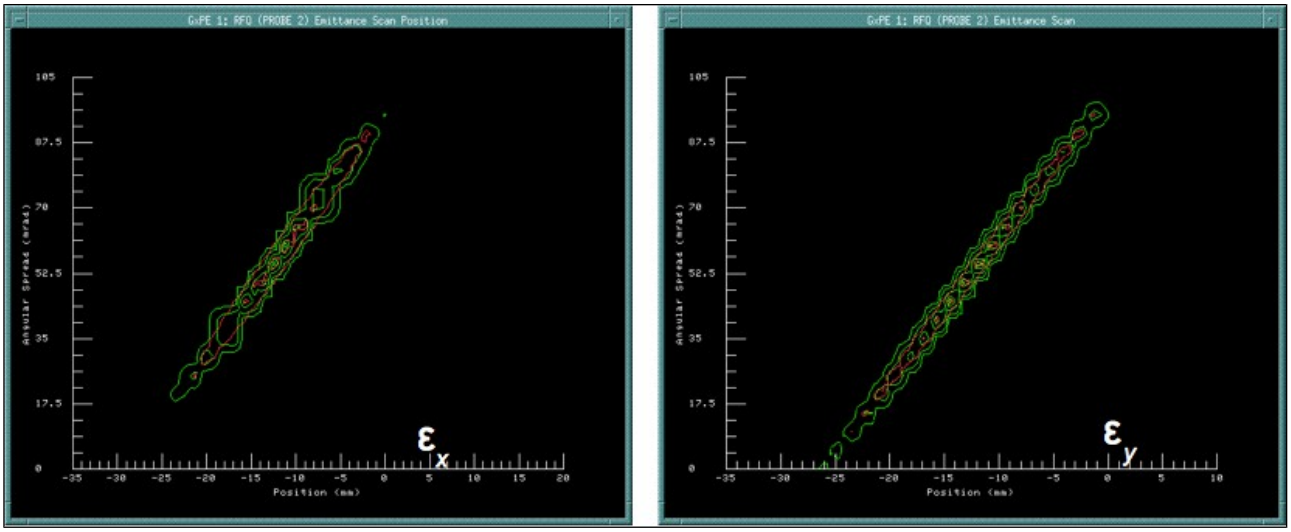

Figure 4.71: *The transverse emittance at the output of the RFQ for 168 kW net power.The $\varepsilon_x = 0.6\ \pi$ mm mrad and $\varepsilon_y = 0.5\ \pi$ mm mrad (1 x rms normalized).*

The emittances shown in Figure 4.71 can be projected back to the exit of the RFQ to calculate the Twiss parameters with TRACE3D and this is shown in Table 4.10. These values should be compared to the simulated values in Table 4.6 which are actually quite different. The TRACE3D results are shown in Figure 4.72.

Twiss Parameter	Horizontal	Vertical
α	–1.5	–2.1
β (cm/rad)	21	17.6
ε (π mm mrad norm., 1× rms)	0.6	0.5

Table 4.10: *The Twiss parameters obtained by back propagating the measured emittances at the emittance probes back to the exit flange of the RFQ. Note: the vertical emittance value is consistent with the value shown in Figure 4.7 at 168 kW.*

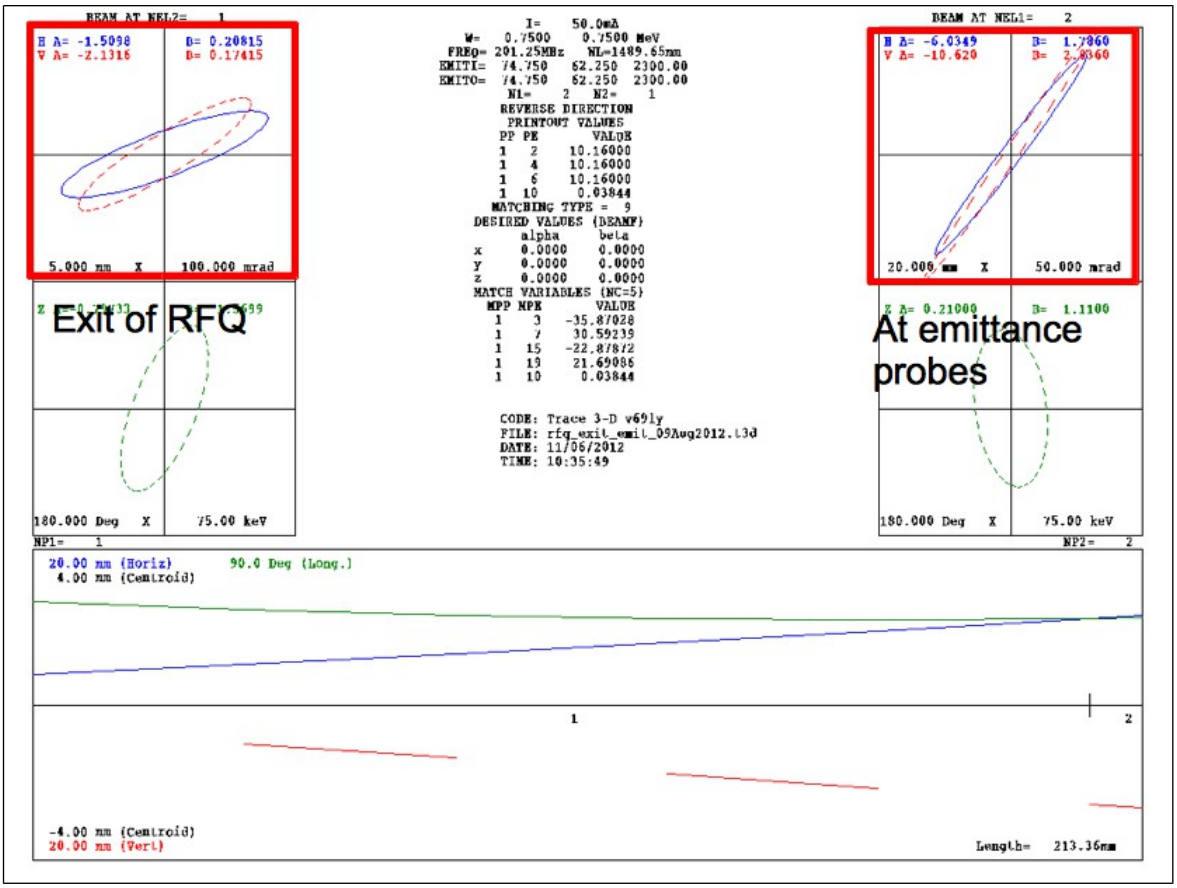

Figure 4.72: *This is the* TRACE3D *calculation that is used to back propagate from the emittance probes to the exit flange of the RFQ.*

4.3.5.e. *Energy*

Three methods can be used to measure the output energy of the RFQ:

- Time of flight (TOF) using buttons.
- Energy spectrometer.
- Single particle calorimeter (SPC).

The TOF method has been discussed in earlier versions of this report and are available in the FNAL document data base. This is the simplest method for measuring beam energy and was the method that showed that the RFQ did not have the correct output energy. (This problem has been fixed and is discussed in Appendix C.1). However, because of time constraints and having had the energy spectrometer already set up, this method was not used after the thick rods were replaced with the thin rods.

The second method is the energy spectrometer. This is the method that will be used to measure the energy. It is a challenging method to set up but once that is done, measurements can be done relatively quickly. It can also measure the energy spread of the beam if the slits are sufficiently narrow.

The final method is the SPC. It is the exotic method that was used at RAL [14] for the energy measurement of their RFQ. However, calibrating the diode detector for single particle energy counts and shielding the diode from X-rays are non-trivial exercises and so this method was not pursued.

4.3.5.e.i. *Energy spectrometer*

The energy spectrometer was built to confirm the TOF measurements (discussed in previous versions of this report. See link). The advantage of the spectrometer is that it can also measure the energy spread of the beam. Although this method is in principle simple, it is a challenge when the absolute energy of the beam needs to be measured. Two important requirements for the success of this method are the accurate measurement of the dipole magnetic field as a function of current and the positions of all the components in the spectrometer. In the setup, the integrated field *Bdl* has been measured to better than 1%, and the positions of the spectrometer components have been surveyed to ±1 mils.

Figure 4.73 shows the spectrometer setup. The two vertical slits (0.8 mm width) at the exit of the RFQ defines the longitudinal axis of the system. The dipole downstream of the RFQ bends the beam to a set of multi-wires (wires are spaced 1 mm apart) that is used to measure the position of the beam. The centre of the multi-wires to the centre of the dipole is 12.12° and for 750 keV beam the required $Bdl \equiv \int \boldsymbol{B} \cdot \boldsymbol{dl}$ is –0.0264 T·m. (The negative sign comes from the negative charge of H-).

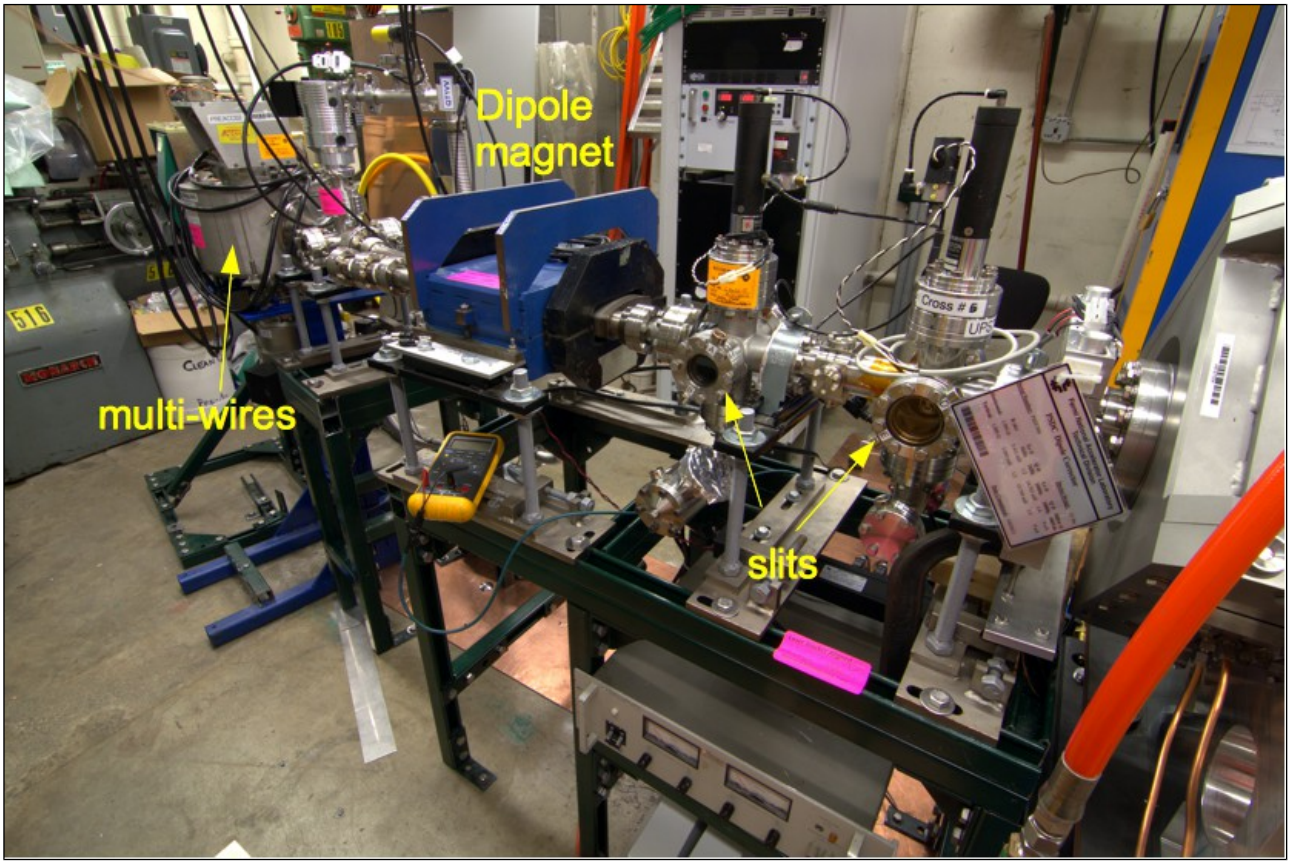

Figure 4.73: *The spectrometer setup. The two slits downstream of the RFQ define the longitudinal axis. The deflected beam is measured on the multi-wires which is 38.655" downstream from the centre of the magnet.*

The relationship between *Bdl* and the deflection angle θ_d of the beam is given by

$$\theta_d = \left(\frac{Bdl}{B\rho}\right) \tag{13}$$

where $B\rho$ is the magnetic rigidity, and for negatively charged beam $B\rho = -p/c$, p is the momentum of H- in units of eV/c, and c is the speed of light in m/s. *Bdl* as a function of current has been measured at Technical Division and is shown in Figure 4.74. The relative error of *Bdl* is 0.7%. This is the systematic error in this experiment.

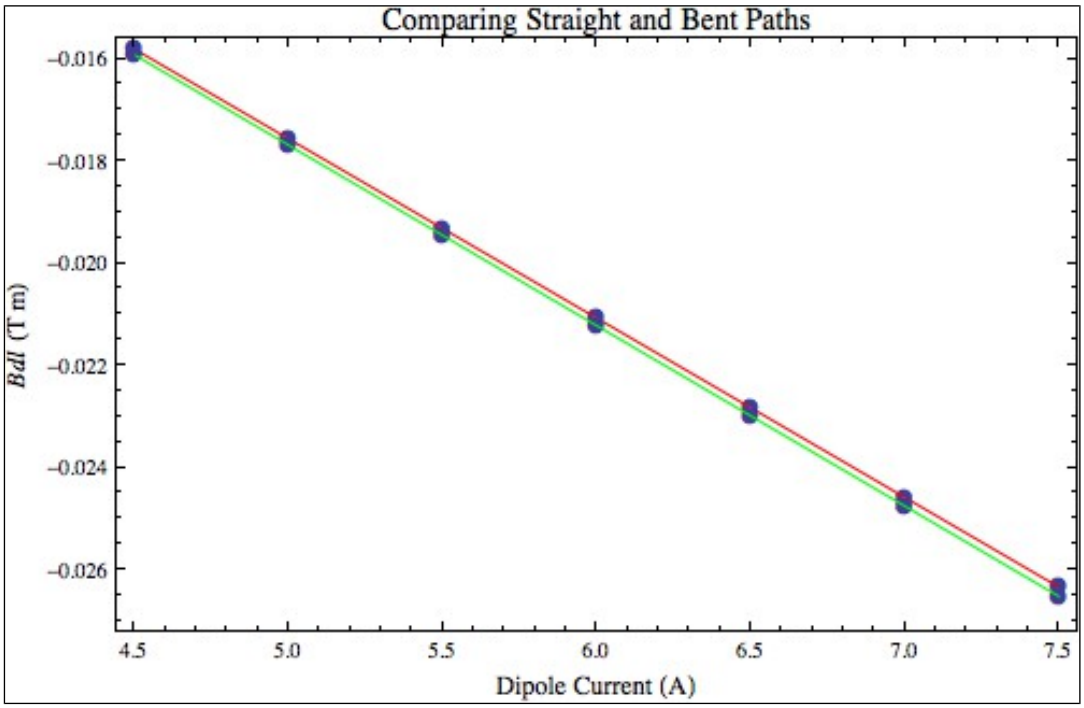

Figure 4.74: *The measured Bdl for the straight ahead (red) and the 12° bent paths (green) through the dipole magnet. The relative difference in Bdl between the two paths is about 0.7%.*

Therefore, by varying *Bdl* (by changing the dipole current) and measuring the deflection angle θ_d, $B\rho$ can be obtained from the *Bdl* versus θ_d plot, and thus the energy of the beam can be found. An example of the application of this method is shown in Figure 4.75 where the mean of the angular distribution shown in Figure 4.76 is tracked as a function of dipole current at 155 kW of RFQ net power. The fitted slope $\langle B\rho \rangle$ is

$$\langle B\rho \rangle = (-0.1257 \pm 0.0001)\ \mathrm{T \cdot m/rad} \tag{14}$$

From Eq. (14), the mean energy of the beam $\langle E \rangle$ is easily calculated and is

$$\langle E \rangle = (756 \pm 1)\ \mathrm{keV} \tag{15}$$

When the systematic error is included, the mean energy of the beam at 155 kW is (756 ± 1 ± 5) keV because the systematic error is dominated by *Bdl* which is 0.7%. In this calculation, the mass of H- is $m_H = (m_p + 2 \times m_e) = (938 + 2 \times 0.511) \times 10^6 = 9.39022 \times 10^8$ eV/c^2, where m_p is the mass of the proton and m_e is the mass of the electron.

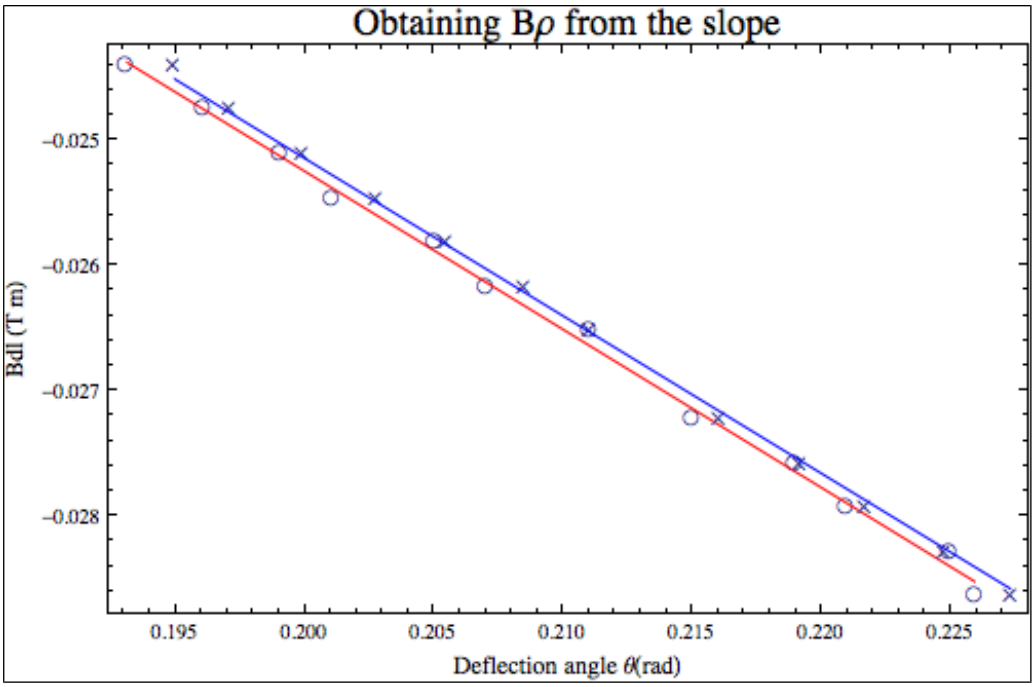

Figure 4.75: *The plots here show the size of Bdl required for the given deflection angle θ_d. The "×" points are when the peak of the the angular distribution shown in Figure 4.76 is tracked, while "o" is when the mean is tracked. The slope of the plot yields Bρ. In this case, tracking either the peak or the mean of the distribution gives the same slope.*

The angular distribution seen on the wires for the RFQ power 155 kW net power is shown in Figures 4.77. The red "■" indicates the expected deflection angle for 750 keV beam. It is clear that at 155 kW, the beam energy is slightly higher than 750 keV which visually confirms the previous calculation.

The mean energy of the beam for different RFQ power settings is shown in Figure 4.77. From this data, it is found that the energy is (758 ± 2) keV using the peak search method and (758 ± 1) keV using the mean position method.

The maximum rms energy spread can be found for several RFQ power settings. The results are seen in Figure 4.78. The result is (15.4 ± 0.4) keV. This can be compared to the simulations shown in section 4.3 where the rms energy spread is ±10 keV for 60 mA beam. Therefore, the measured rms energy spread is 50% larger than simulation results. However, note that this is the maximum energy spread because the transverse contribution is not measured.

4.3.5.f. *Longitudinal Emittance*

The longitudinal emittance can be calculated by using the rms beam size and energy spread if it is assumed that the ellipse is upright. (Technically, it is necessary to back propagate the rms beam size back to the exit of the RFQ taking into account space charge because at this location the ellipse is theoretically upright. However, for simplicity, it will not be done here). The rms bunch size and energy spread are:

- rms bunch length $\Delta t = 0.41$ ns or
  $\Delta\varphi = \omega \Delta t = 2\pi(201.25\times10^{6}\ [\mathrm{Hz}])\times(0.41\times10^{-9}\ [\mathrm{s}]) = 0.5\ \mathrm{rad} = 30^{\circ}$

- rms energy spread $\Delta W = 15.4$ keV.

Using the above two numbers, the unnormalized $1\times$ rms emittance is $\epsilon_L = 0.46$ deg MeV, and the normalized rms emittance is $\epsilon_{L,n} = \epsilon_L[\text{deg MeV}]\frac{c}{360\,mc^2[\text{MeV}]f[\text{Hz}]} = 0.2\times10^{-3}$ cm rad for ~40 mA beam. When this number is compared to Table 4.6, it is $3\times$ larger than the manufacturer's specifications. Note: $c = 2.99792\times10^{10}$ cm s^{-1}, mc^2 = 939 MeV and $f = 201.25\times10^6$ Hz. The definition of normalized rms emittance comes from the PARMILA manual.

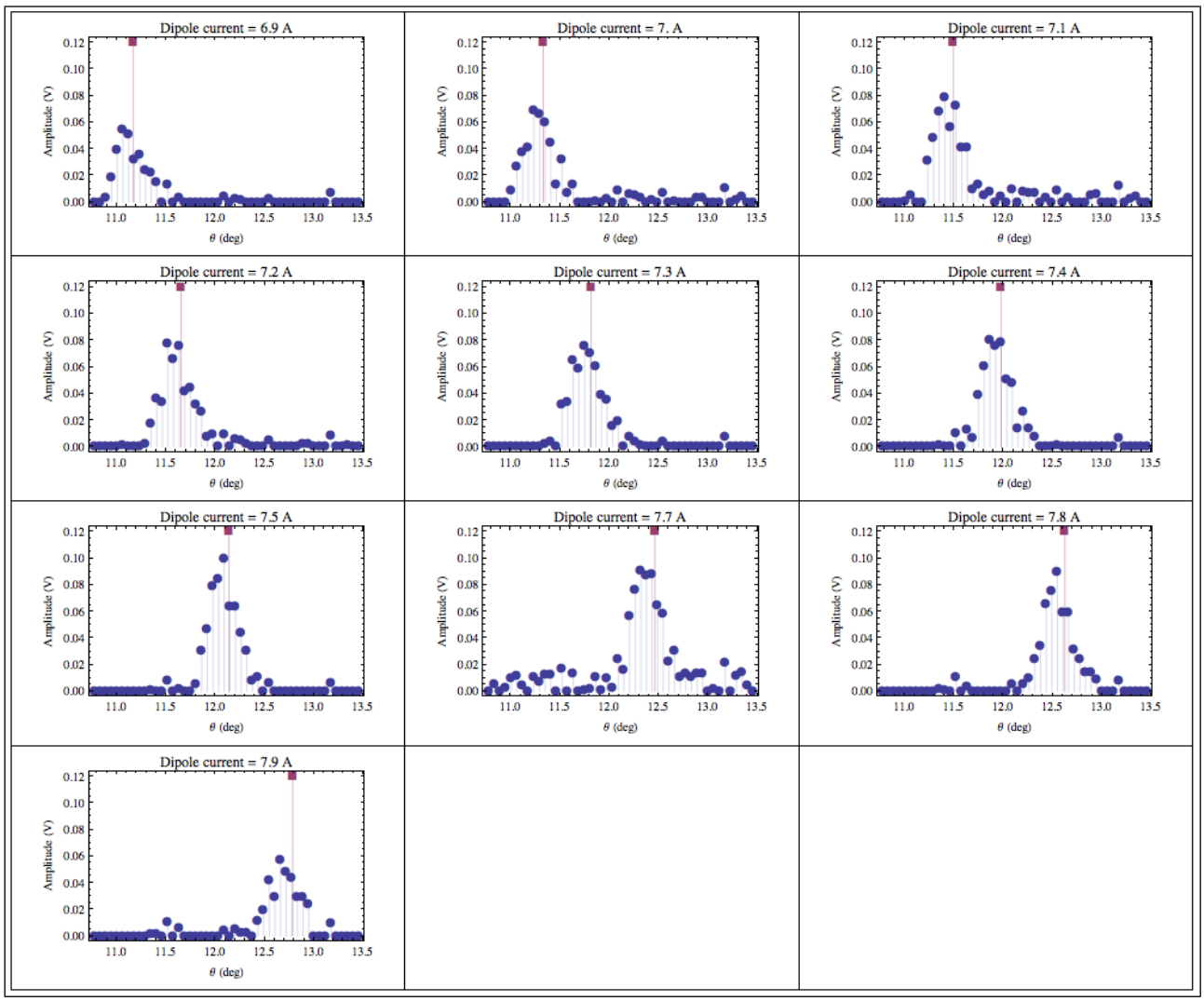

Figure 4.76: *The spectrometer data for the case when the RFQ is set to 155 kW net power. As expected, the entire angular distribution moves when the dipole current is changed. The red "■" indicates the expected deflection for 750 keV beam. The peak of the distributio is clearly above 750 keV and the mean energy is found to be (756 ± 1) keV.*

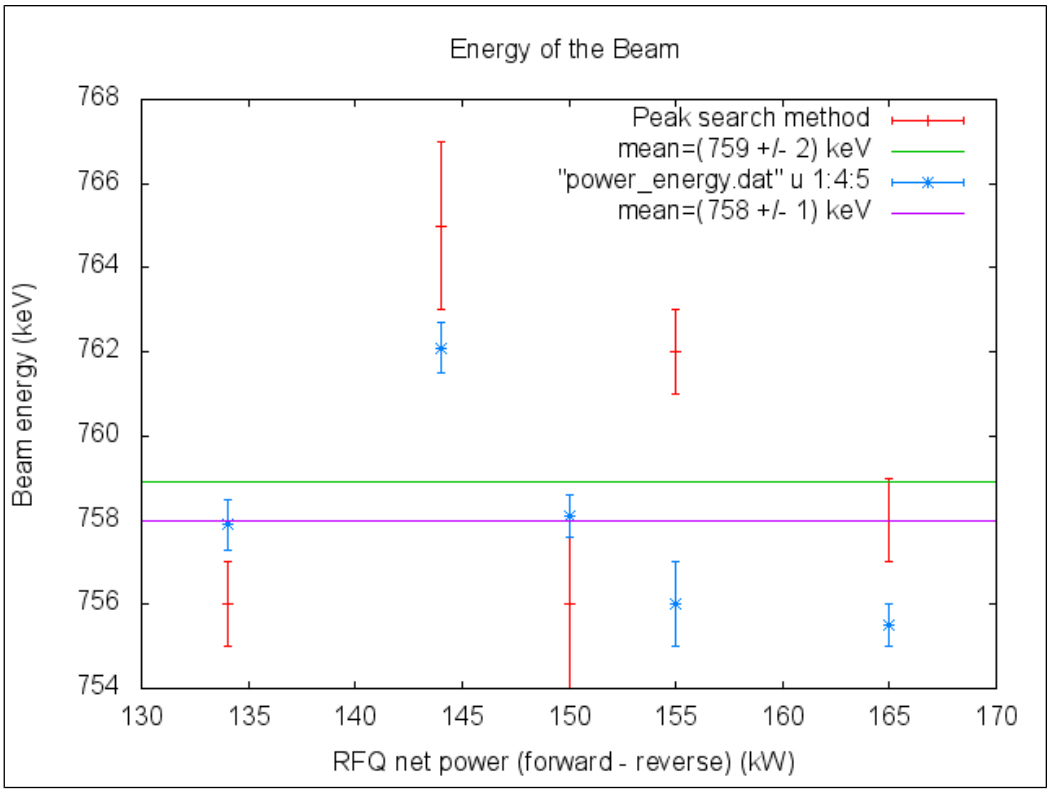

Figure 4.77: *The results of the beam energy calculated by the peak search method and the mean position method.*

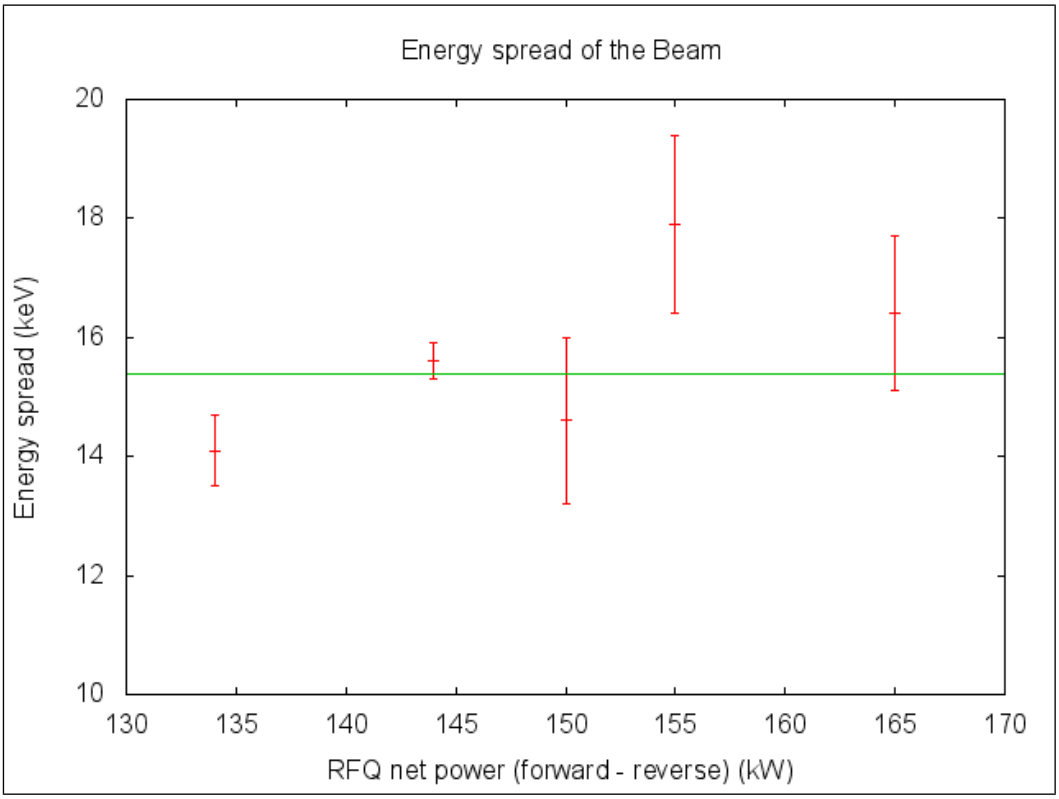

Figure 4.78: *The energy spread of the beam measured with the spectrometer and it is (15.4 ± 0.4) keV.*

4.3.5.g. *LEBT vacuum pressure and its effect on beam capture efficiency and current distribution*

The LEBT vacuum has a very strong effect on the capture efficiency and the current distribution at the exit of the RFQ. The effect of LEBT pressure and the current distribution profile of the chopped beam at the exit of the RFQ is quite dramatic that can be seen in Figure 4.79. When the LEBT pressure is at 1.1×10^{-6} Torr, the chopped beam has a distinct slope and lower current than when the LEBT pressure is 3.5× worse at 3.5×10^{-6} Torr. The effect of vacuum on the capture efficiency is shown in Figure 4.61. From this measurement, the plan is to run the LEBT vacuum pressure at around 3.5×10^{-6} Torr so that there is sufficient gas focusing to get the beam into the RFQ. It is interesting that the LEBT beam current is not noticeably affected by the 3.5× times in gas pressure change.

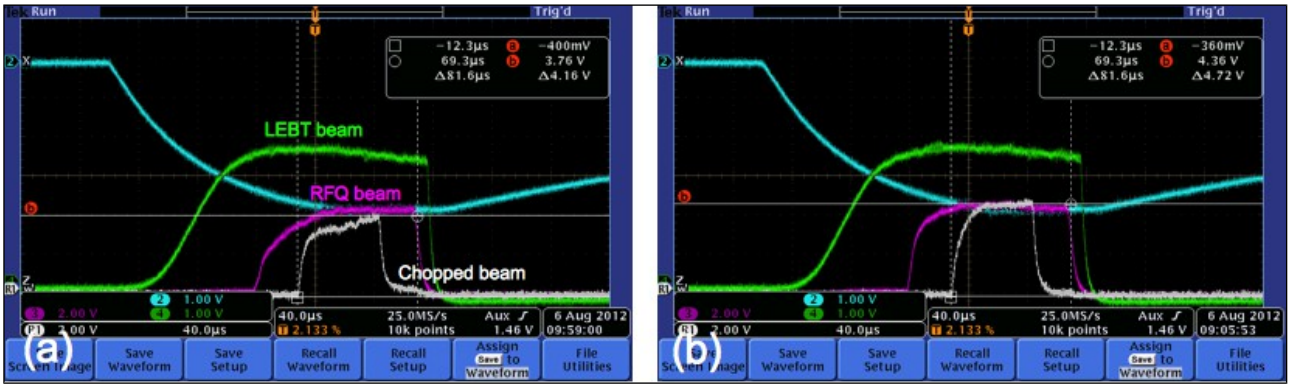

Figure 4.79: These pictures show the effect of gas pressure on the chopped beam measured on a toroid at the exit of the RFQ. (a) is at 1.1 x 10^{-6} Torr and (b) is at 3.5 x 10^{-6} Torr. It is clear that the chopped beam in (a) has a distinct slope and is smaller than (b) which is flatter.

4.4. The MEBT

The design of the MEBT is an amalgam of the BNL MEBT experience and the requirements from the RFQ beam output and DTL 1 input parameters. One important consideration is the length of the MEBT. From the BNL experience, the MEBT must be as short as possible. In fact, the BNL MEBT has been shortened from 7 m to <75 cm, (see Figure B.2) and has correspondingly decreased the losses to essentially zero due to emittance blow ups and debunching of the beam. FNAL has also considered eliminating the MEBT completely and simply mount the exit of the RFQ directly to the entrance of DTL 1. At that time, this option was not selected because of the uncertainty of the RFQ output parameters (which needs to be measured rather than simulated) and the lattice of DTL 1. More concrete numbers are needed before this option can be seriously considered.

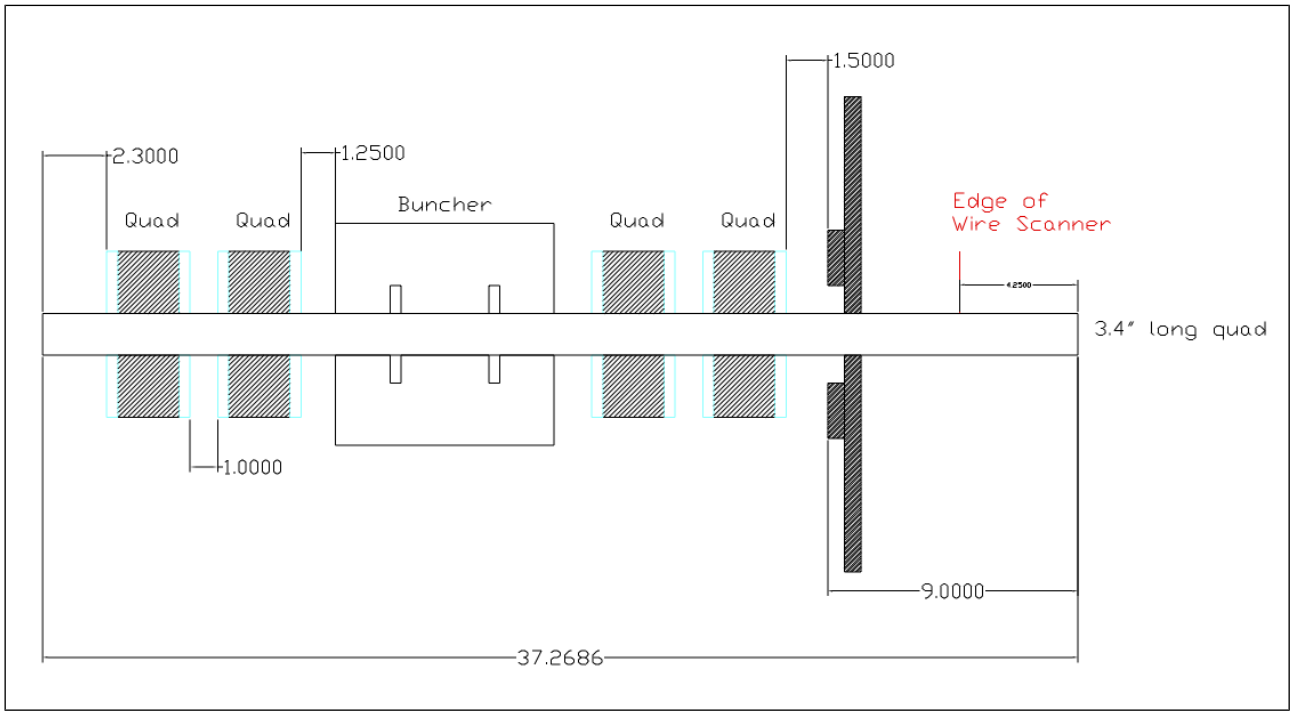

Figure 4.80: *The MEBT. This distances between elements have been selected to minimize the length of the MEBT and yet allow for the addition of bellows and the insertion of bolts.*

The present MEBT design shown in Figure 4.80 contains 1 buncher and 2 sets of doublets for matching, 4 sets of steerers in both planes, and 1 high bandwidth gap monitor at the beginning of Tank 1 for diagnostics. The total length in this design is about 1 m. (This MEBT design is longer than the BNL MEBT because of the extra quadrupole and longer quadrupoles) The choice of doublets for the MEBT comes from the observation that the beam at the output of the RFQ is essentially round. Therefore, a symmetric placement of doublets before and after the buncher should be a good lattice for matching the beam into Tank 1.[5] A photograph of the assembled MEBT before installation is shown in Figure 4.81.

Unlike BNL which uses external dipole correctors for steering the beam, FNAL has decided that the steerings can be built into the quadrupoles. However, this introduces sextupole components

5 Although it is well known that both the RFQ and the DTL lattices are FODO, it is unrealistic to design a FODO matching lattice for the MEBT because $\beta\lambda = 60$ mm and so the spacing is too short to accommodate quadrupoles and bunchers.

which can increase the beam emittance. Fortunately, it is expected that the dipole correctors will not be run very hard and simulations show that if the integrated sextupole field is < 0.5% of the integrated quadrupole field, transverse emittance blow up will be < 1%. See section 4.4.3.d and Figure 4.103.

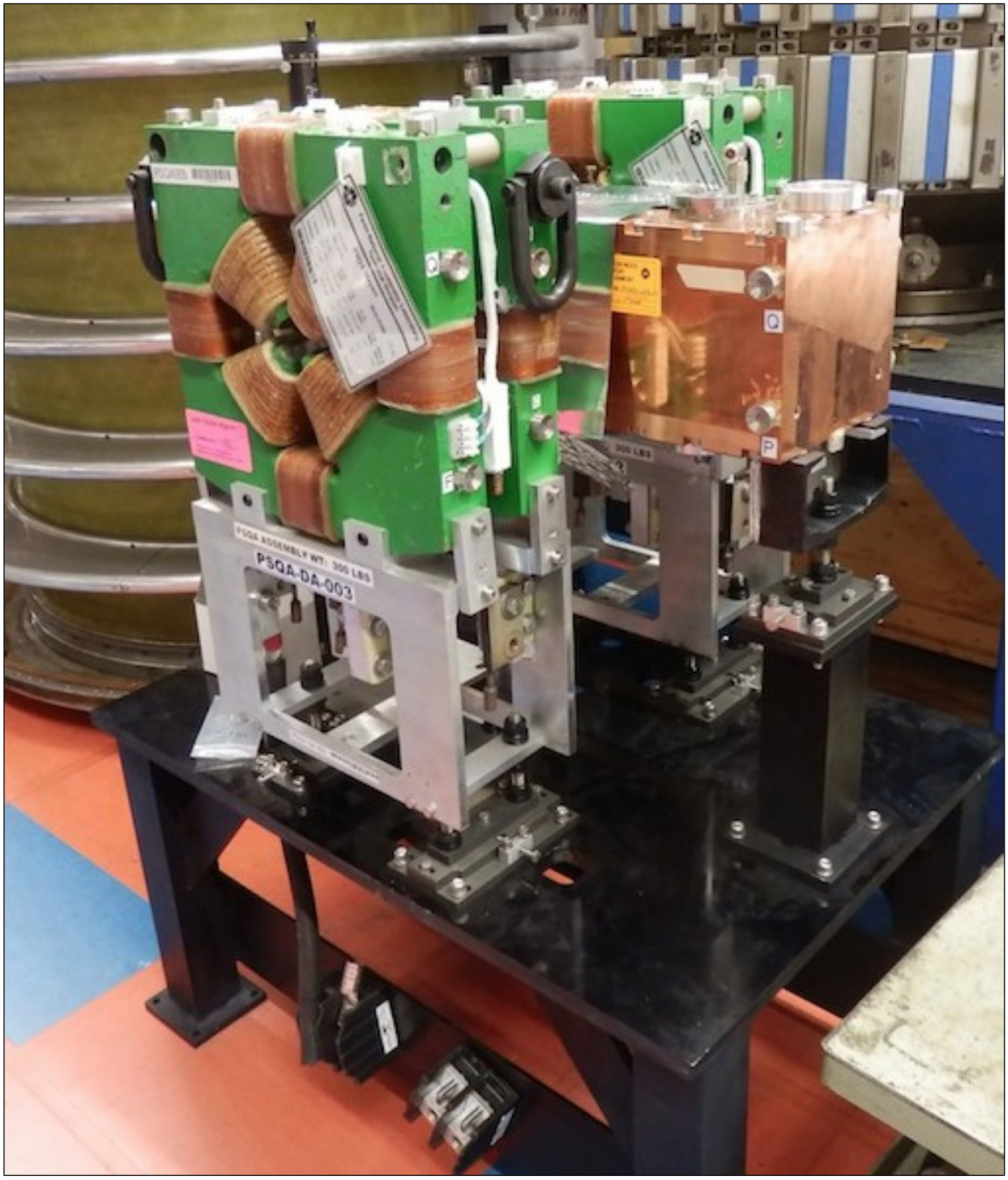

Figure 4.81: *The assembled MEBT (without beam pipes) on its stand before installation.*

The buncher used in the design is the one that BNL has designed and presently used in their beam line. The buncher has been procured and has been delivered. See section 4.4.2

4.4.1. MEBT Lattice

The MEBT lattice is doublet – buncher – doublet because the beam is essentially round at the output of the RFQ. The bunched beam out of the RFQ is space charge dominated and will blow up longitudinally and transversely if the MEBT is too long. Therefore, it is has been designed to be as short as the space requirements of the elements allow. The length requirement has been confirmed at BNL because when their MEBT length was reduced from 7 m to 70 cm in 2009, the transverse emittance was reduced by 3× and capture efficiency at the end of Tank 9 improved from 50% to 70% [15]. Note: The two reasons why the BNL MEBT is about 30 cm shorter than the FNAL MEBT are (a) the BNL MEBT is quadrupole – quadrupole – buncher – quadrupole, i.e. one fewer quadrupole (b) the FNAL quads are ~1.5" longer than the BNL quadrupoles.

Figure 4.80 shows the MEBT from the end of the RFQ to the beginning of Tank 1. The physical length of the MEBT is about 37" (~1 m) and is essentially dominated by the quadrupoles which have a physical length of 3". See section 4.4.3 The spacing between the quadrupoles in each doublet has been determined by the dipole decay field and has been set to 1.8" between the iron cores. (See Figure 4.97 for the quadrupole field gradient as a function of longitudinal position and section 4.4.3.a). The rest of the space are used up by bellows and flanges.

The Trace3D and PARMILA results for 45 mA beam are shown in Figures 4.82 and 4.83 to 4.88. The Trace3D simulation uses 5× rms emittance for tracing the beam envelope and the parameters shown in Table 4.10 and Figure 4.72. It is clear that the beam is large both horizontally and vertically and the beam does not fit vertically in the beam pipe. PARMILA simulations show that about 5% (rms error ~0.1%) of the beam will be lost in the MEBT and that 75% (rms error ~0.2%) of the beam will be transported from the start of the MEBT to the end of Tank 1. *Note: no attempt has been made to vary the quadrupole strengths in the Tank 1 model to improve capture because it is unlikely that the historical model of Tank 1 used here actually corresponds to reality!* Table 4.11 summarizes the rms emittances calculated by PARMILA. The calculated transverse emittances before Tank 1 at the ½ quadrupole are within the measured transverse emittances at the start of Tank 1 shown in Table 7.1 for 46 mA beam. Again, it must be emphasized that the simulation from the start of Tank 1 to the end should be taken as a guide only and probably does not correspond to reality because there is not good model of Tank 1! The initial beam distribution model used in PARMILA is the emit.3sig-gaussian model.

Location	**ϵ_x (norm., rms, π mm·mrad)**	**ϵ_y (norm., rms, π mm·mrad)**	**ϵ_z (norm., rms, deg · MeV)**
Exit of RFQ	0.53	0.44	0.45
Before Tank 1 at ½ quadrupole	0.63	0.77	0.47
Exit of Tank 1	0.85	1.1	0.51

Table 4.11: *RMS emittances calculated by the* PARMILA *simulation for 45 mA beam. The emittances at the start of the RFQ have been derived from Table 4.10 and section 4.3.5.f. Although* PARMILA *claims that the longitudinal emittance is normalized, this is quite dubious given the definition of normalized longitudinal rms emittance discussed in section 4.3.5.f.*

Trace3D Element ID	Element	Gradient (T/m)	Integrated Field (T)	Comments
3	Quadrupole	–32.8	–2.0	Doublet A
7	Quadrupole	27.5	1.5	
15	Quadrupole	–23.4	–1.3	Doublet B
19	Quadrupole	21.6	1.2	
		Gap Voltage (kV)		
15,17	Buncher	31.6 kV		Value is E_0TL. Buncher has two gaps.

Table 4.12 *Summary of the parameters used to match the H- ion beam from the end of the RFQ to the entrance of the DTL. See Figure 4.82 for the* Trace3D *element ID. The integrated field is gradient*yoke length. Yoke length is 55 mm.*

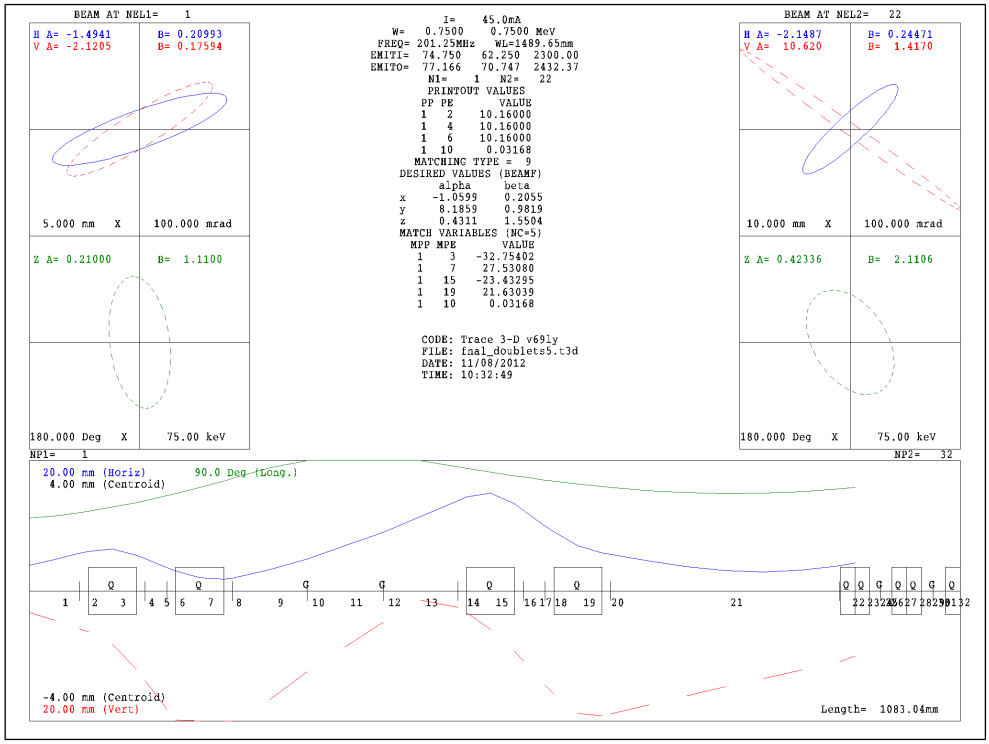

Figure 4.82: *The H- beam is transported from the end of the RFQ to the start of the DTL.* PARMILA *shows that at 45 mA, 95% of the beam is captured and transported to the start of the DTL. See Figure 4.83. Even with this short MEBT, the beam is very large transversely at the second doublet and barely fits in the beam pipe for 5X rms emittances.*

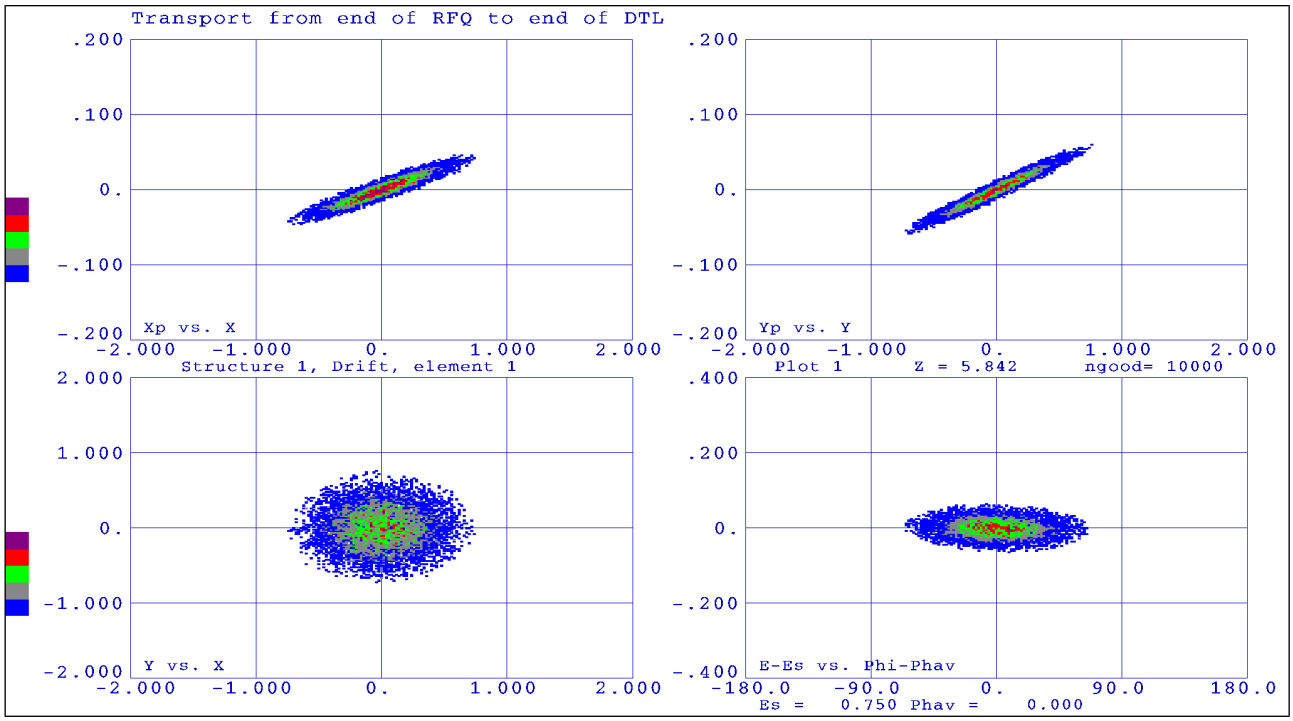

Figure 4.83: *The beam distributions before the first set of doublets. The beam distribution at the beginning of the MEBT (or end of the RFQ) is shown in Figures 4.72 or 4.82.*

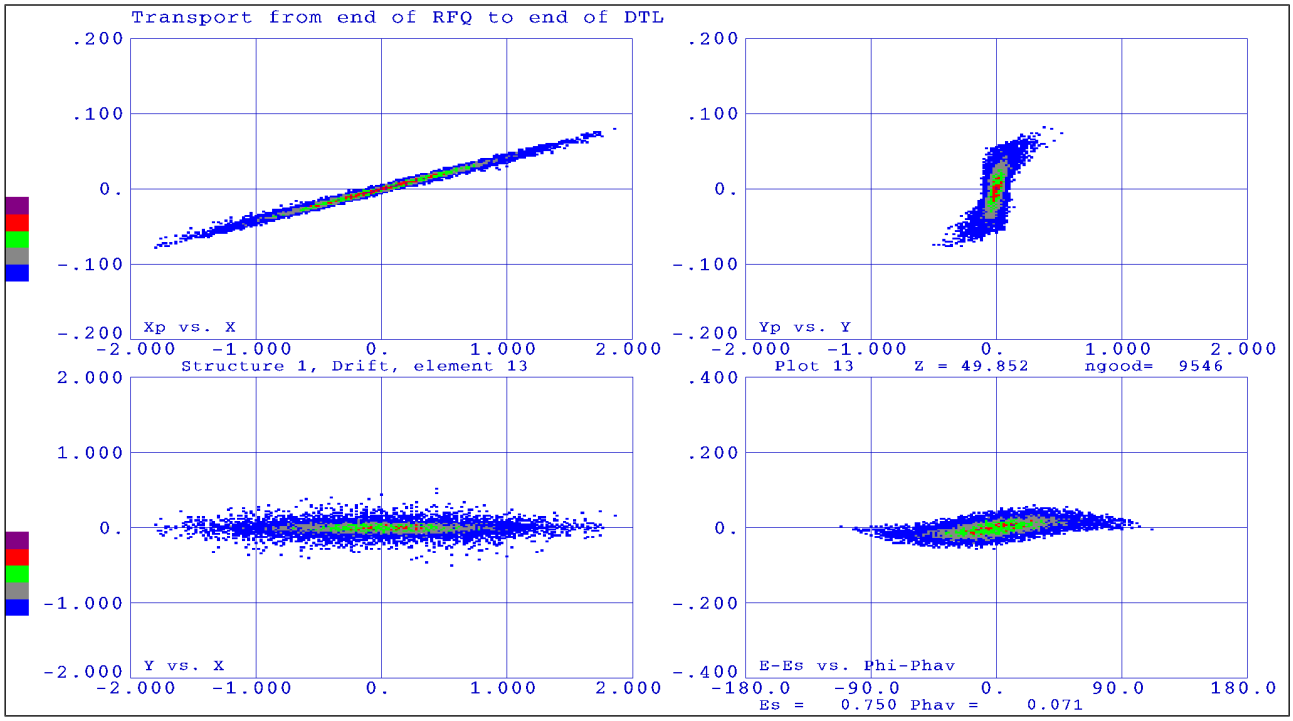

Figure 4.84: *The beam distribution after the buncher. The longitudinal distribution sees the non-linear part of the RF.*

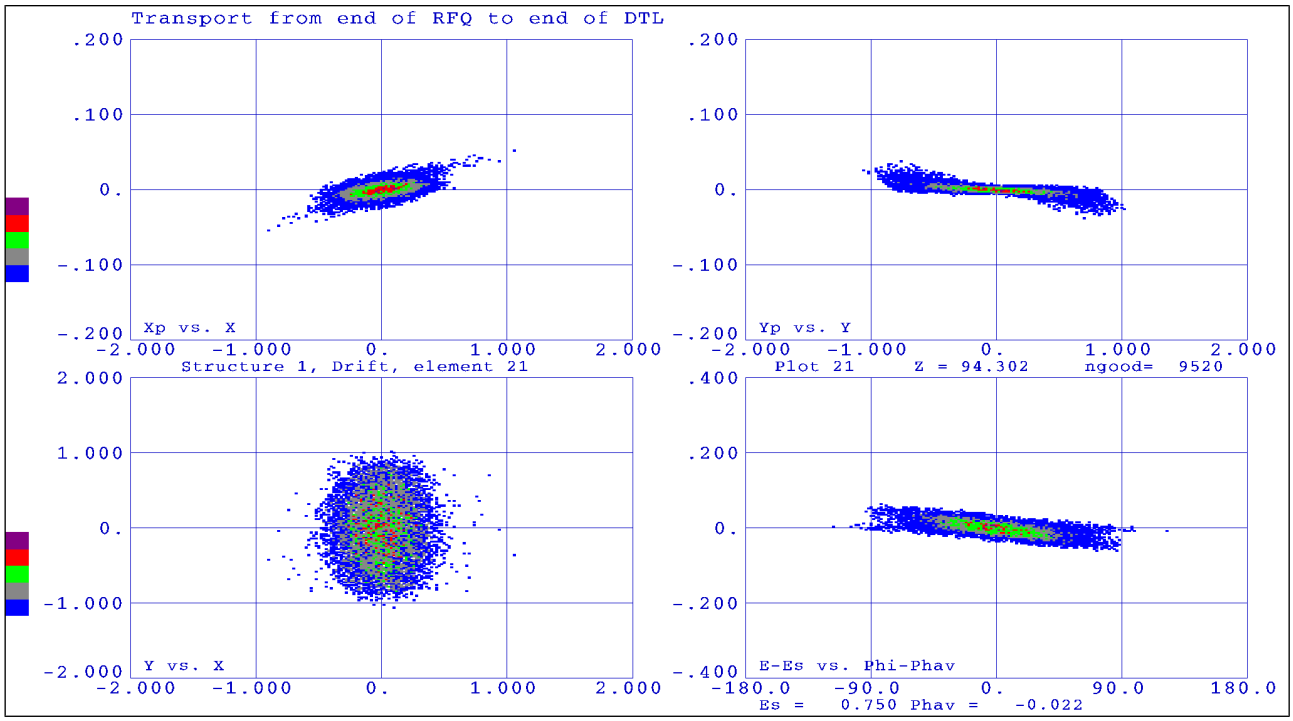

Figure 4.85: *Beam distribution before Tank 1.*

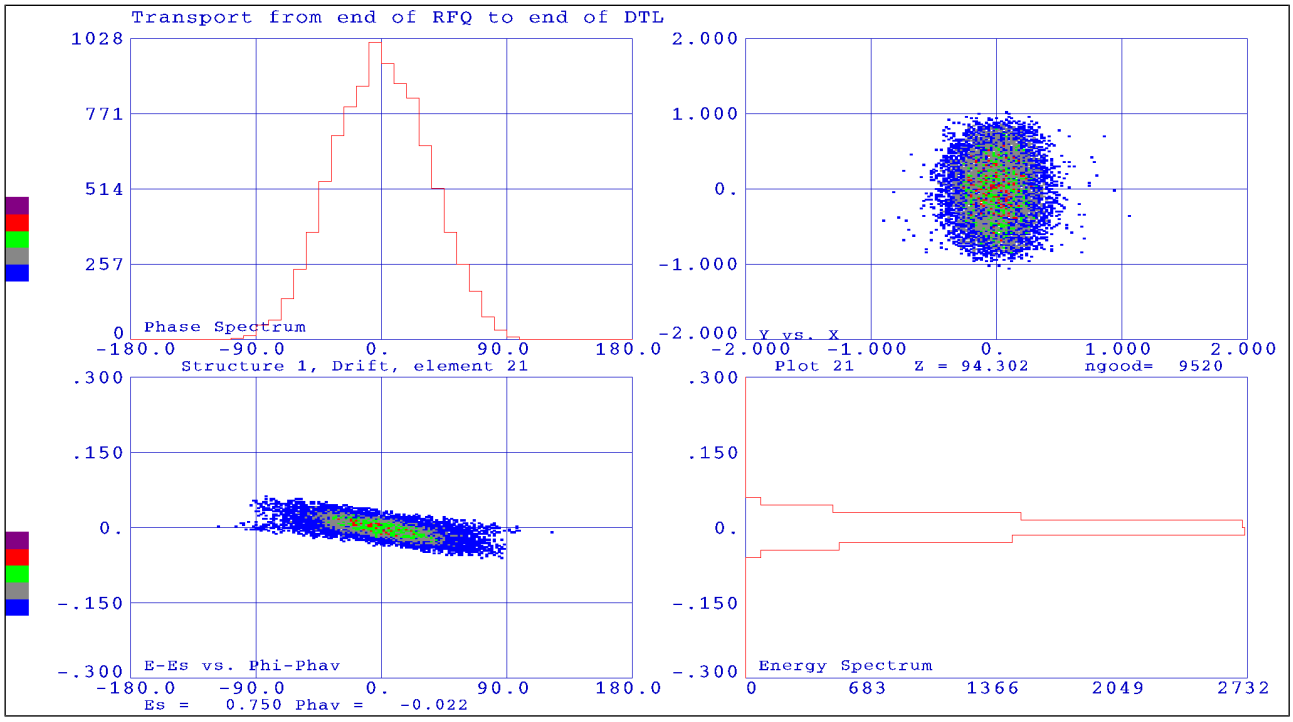

Figure 4.86: *Histograms of the beam distribution before Tank 1.*

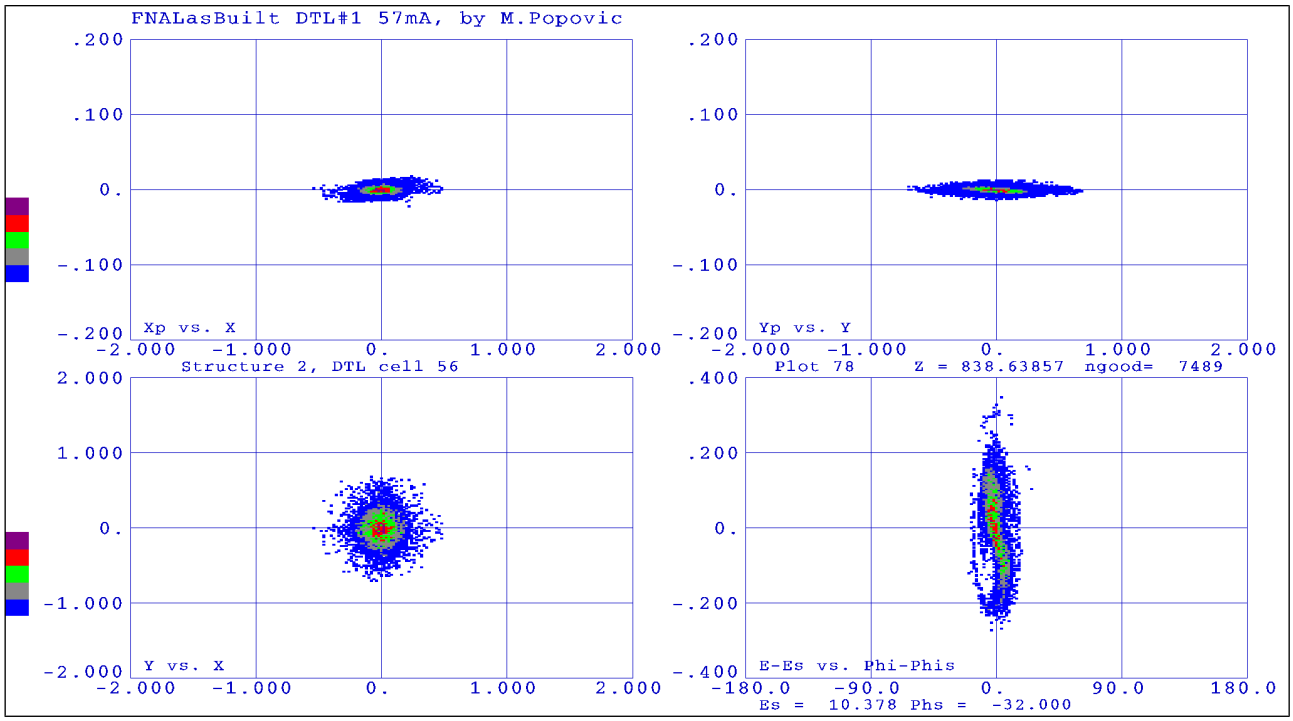

Figure 4.87: *Beam distributions at the end of Tank 1. Note: This is hypothetical because the Tank 1 model used here does not correspond to the actual Tank 1 that is installed.*

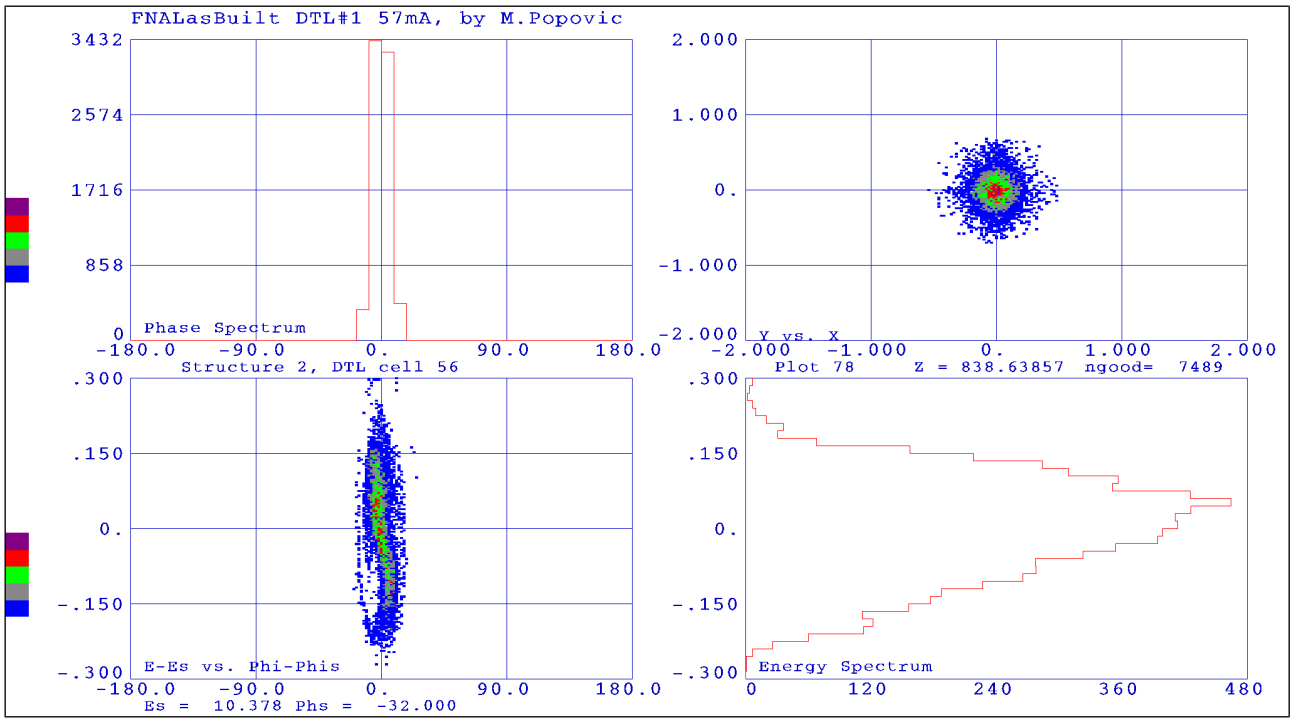

Figure 4.88: *Histograms of the beam distribution at the end of Tank 1. Note: This is hypothetical because the Tank 1 model used here does not correspond to the actual Tank 1 that is installed.*

4.4.2. Buncher

The buncher has been purchased from Time Co., Japan [16] and has been delivered to FNAL on 14 Mar 2011. This buncher is nearly identical to the BNL buncher except that the FNAL buncher is made from copper while the BNL buncher has been made from aluminium. The specifications of the buncher are shown in Table 4.13.

Parameter	Value	Units
Resonant frequency	201.25	MHz @ 20˚C
Resonant type	½ wave length	
Unloaded Q	> 4000	
Min. bore id	32	mm
Max. cavity length	200	mm
Dist. between voltage centers	89.2	mm
Max. input RF power[6]	3	kW
Gap length	10	mm
Induced total gap voltage	> 60	kV

Table 4.13: *The buncher parameters.*

The buncher is a two gap cavity because two single gap cavities cannot fit in 70 cm of space. From Trace3D and PARMILA, the effective buncher gap voltage is $E_0 TL \sim 40\,\mathrm{kV}$ for bunching 60 mA beam. The peak voltage V_g across the gap of the buncher can be calculated by first calculating the peak E-field E_0 with the following formula

$$E_0 = \frac{E_0 TL}{T \times L} \tag{16}$$

where L is the length of the RF gap and T the transit time factor (dimensionless). T is approximately given by the following

$$T = \frac{\sin\left(\frac{\omega_{\mathrm{RF}}}{\beta c}\frac{L}{2}\right)}{\frac{\omega_{\mathrm{RF}}}{\beta c}\frac{L}{2}} \tag{17}$$

where $\omega_{\mathrm{RF}} = 2\pi \times f_{\mathrm{RF}}$, and c is the speed of light. And so for an *effective* RF gap of L = 2 cm (see section 4.4.2.c) and 750 keV H- ions (β = 0.04), the transit time factor is calculated to be T = 0.83. Substituting these values into Eq. (16), E_0 = 2.4 MV/m and thus the peak gap voltage $V_g = E_0 L$ = 48 kV < 60 kV in the buncher specifications.

6 BNL has tested their cavity to 6kW [17].

4.4.2.a. *Buncher drawings and photographs*

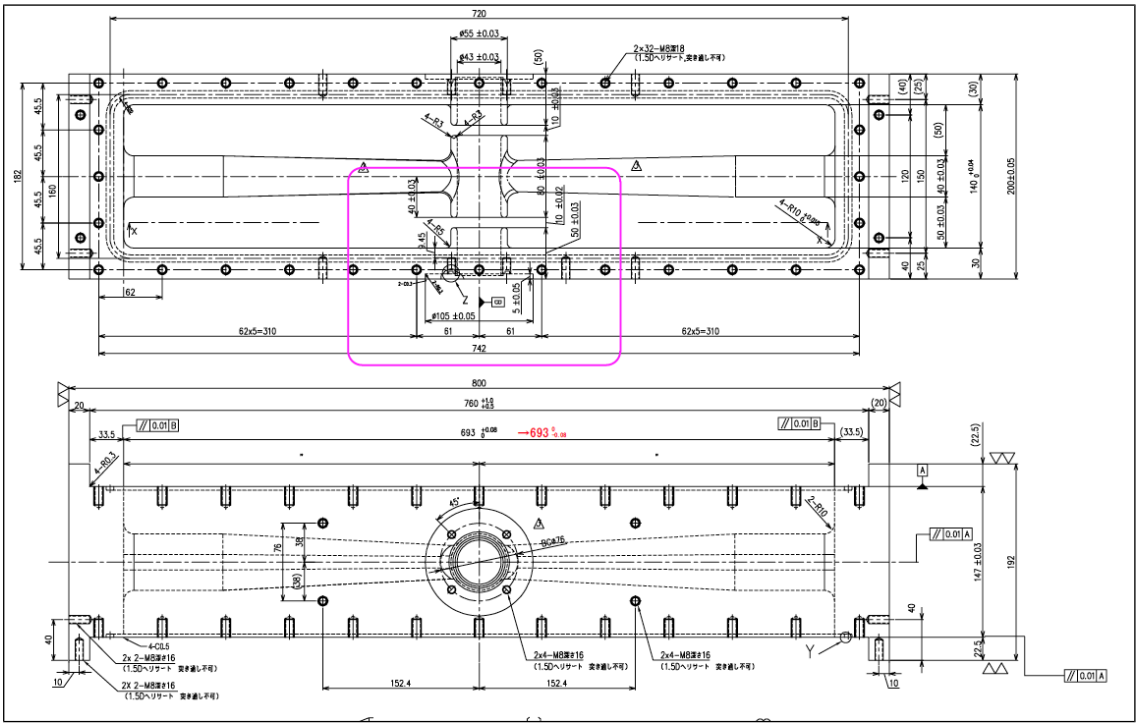

Figure 4.89: *The buncher drawing. All dimensions are in mm.*

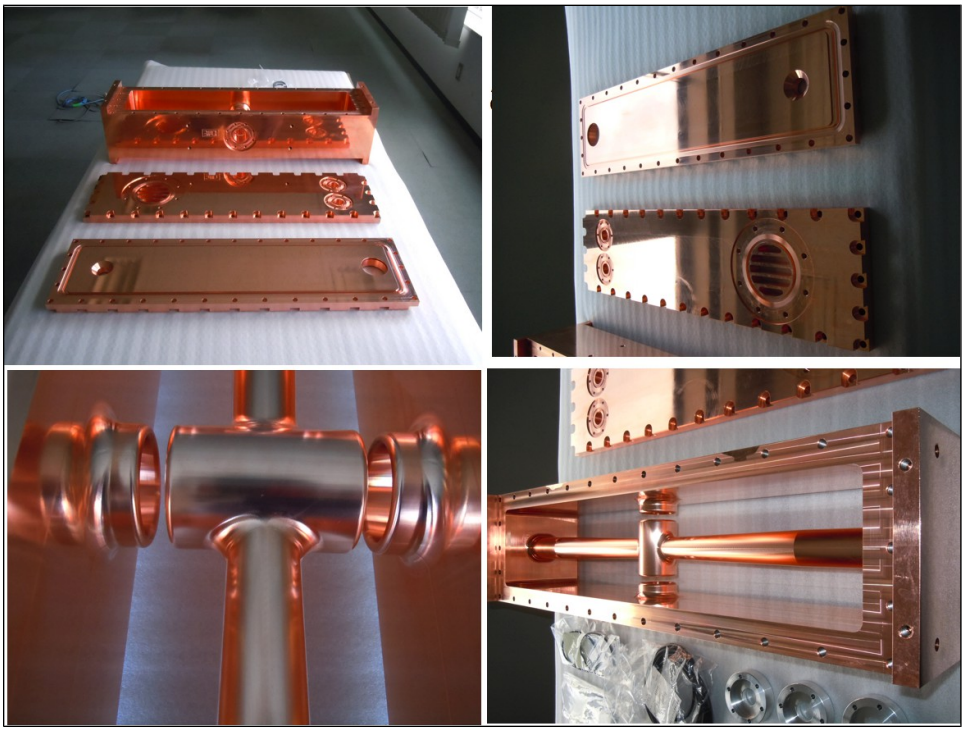

Figure 4.90: *The buncher before assembly.*

The buncher drawing is shown in Figure 4.89 which clearly show the two 1 cm gaps. The total length occupied by the buncher in the beam line is only 20 cm. Its parts before assembly are shown in Figure 4.90.

4.4.2.b. *Correcting transit time factor with grids*

BNL discovered that although the RF characteristics of the buncher are very good, the transit time factor was actually incorrect and needed to be corrected with grids. After this correction was made, the BNL MEBT improved the H- transmission efficiency over the older buncher it replaced (which also had grids)[18]. These grids do cause some beam loss, but the effect is small. The FNAL buncher also has these grids which are shown in Figure 4.91.

The reason why the inserted grid can change the transit time factor is because the grids essentially confine the E-fields to the space within the gaps. Without the grids, the E-fields leak outside the gaps and therefore, the gap length L in Eq. (17) is longer than the physical gap. Using the same equation, it is easy to see that a longer L means a shorter transit time factor T. The confinement of the E-fields due to the grids have been measured with a bead pull. The results are shown in Figure 4.93.

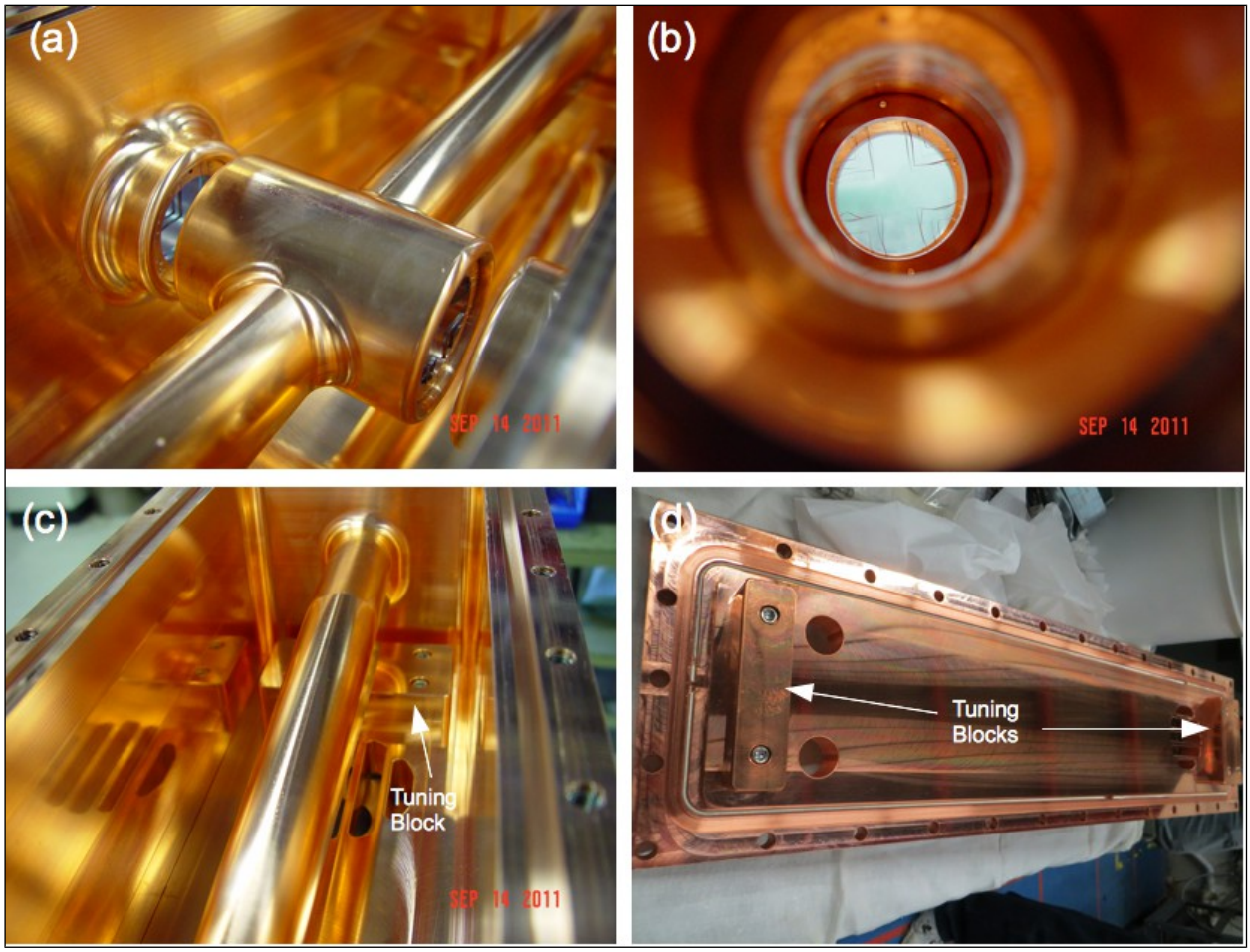

Figure 4.91: *(a) and (b) show the grids that have been inserted into the gaps to confine the E-field to within the gaps. These grids correct the transit time factor. (c) shows one of the tuning blocks used to increase the resonant frequency because the grid inserts lowers it. (d) shows the tuning blocks without the stem blocking the view.*

The capture efficiency measured at BNL by D. Raparia with and without grids are shown in Figure 4.92. It is clear from here that the addition of grids has increased the capture efficiency dramatically. In fact, at 4 kW of buncher power, the efficiency is 1.3× higher at the end of Tank 9 with grids than without grids.

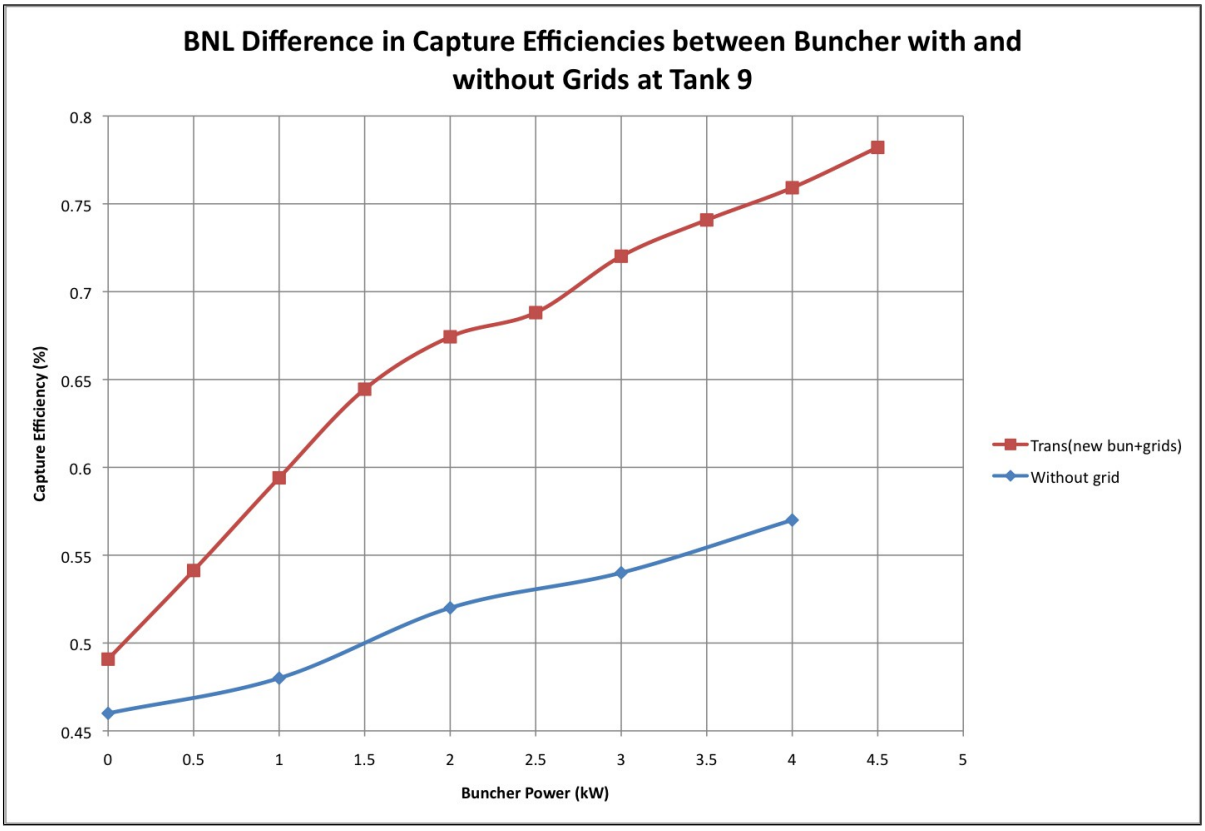

Figure 4.92: *This shows the differences in capture efficiencies at the end of Tank 9 between a buncher with grid and without grid. Clearly, the grids increase the efficiency by 1.3x at 4 kW of buncher power. (Measurements courtesy of D. Raparia).*

4.4.2.c. *Low power RF measurements*

Some low power measurements have been done by the manufacturer Time Co. and by D. Sun at FNAL (see [19] for D. Sun's full report). All the low power RF results are performed by D. Sun. The bead pull results with and without grids are shown in Figure 4.93. There are two peaks in the plot because of the two RF gaps in the buncher. The strength of the electric field E_0 is related to the relative frequency shift $\Delta f / f_0$ by the well-known relation $\Delta f / f_0 \propto E_0^2$ for a perturbation by a very small dielectric bead [20]. As expected, the fields are strongest in the middle of each gap. When the grids are inserted, the effective length of the gap is reduced. The fractional reduction is

$$\frac{L_{\text{with grid}} - L_{\text{no grid}}}{L_{\text{no grid}}} \approx \frac{20 - 32.5}{32.5} \approx -0.4 \tag{18}$$

where $L_{\text{no grid}}$ is the FWHM size of the RF gap without grids, and $L_{\text{with grid}}$ is the FWHM size of the RF gap with grids in Figure 4.93. The transit time factor is correspondingly increased by about 40% with grids than without grids when these values are substituted into Eq. (17). Note: The correct way to calculate the transit time factor is to integrate the measured fields within the gaps shown in Figure 4.93. The s11 and s12 measurement of the buncher with grids inserted are shown in Figure 4.95. The measurements show that the resonance frequency is at 201.25 MHz, unloaded Q = 6820 and s21 between the power an pickup ports at resonance is –23 to –25 dB. Figure 4.94 shows the change in frequency (201.134 – 201.971) MHz when the tuner is inserted to various positions.

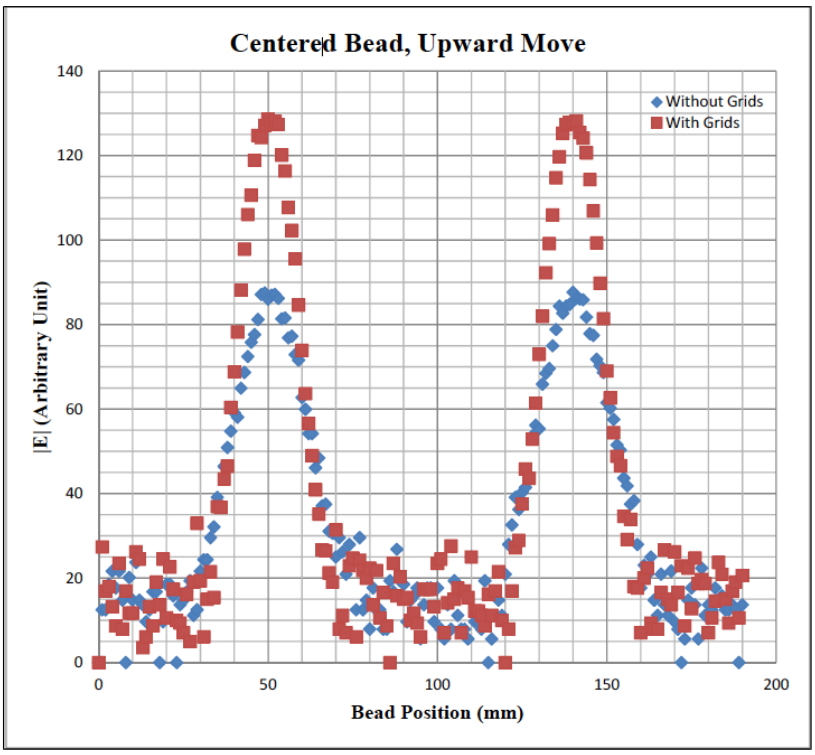

Figure 4.93: *These are the bead pull results for the cases where the grids were absent and present. When the grids are inserted, the fields are better confined in the gaps.*

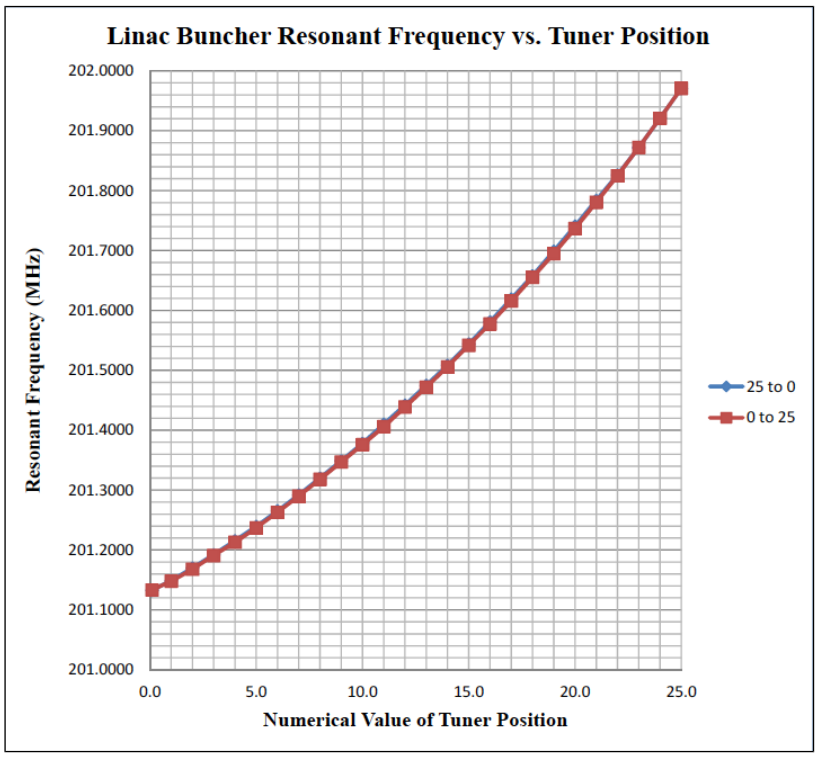

Figure 4.94: *Resonant frequency as a function of tuner position.*

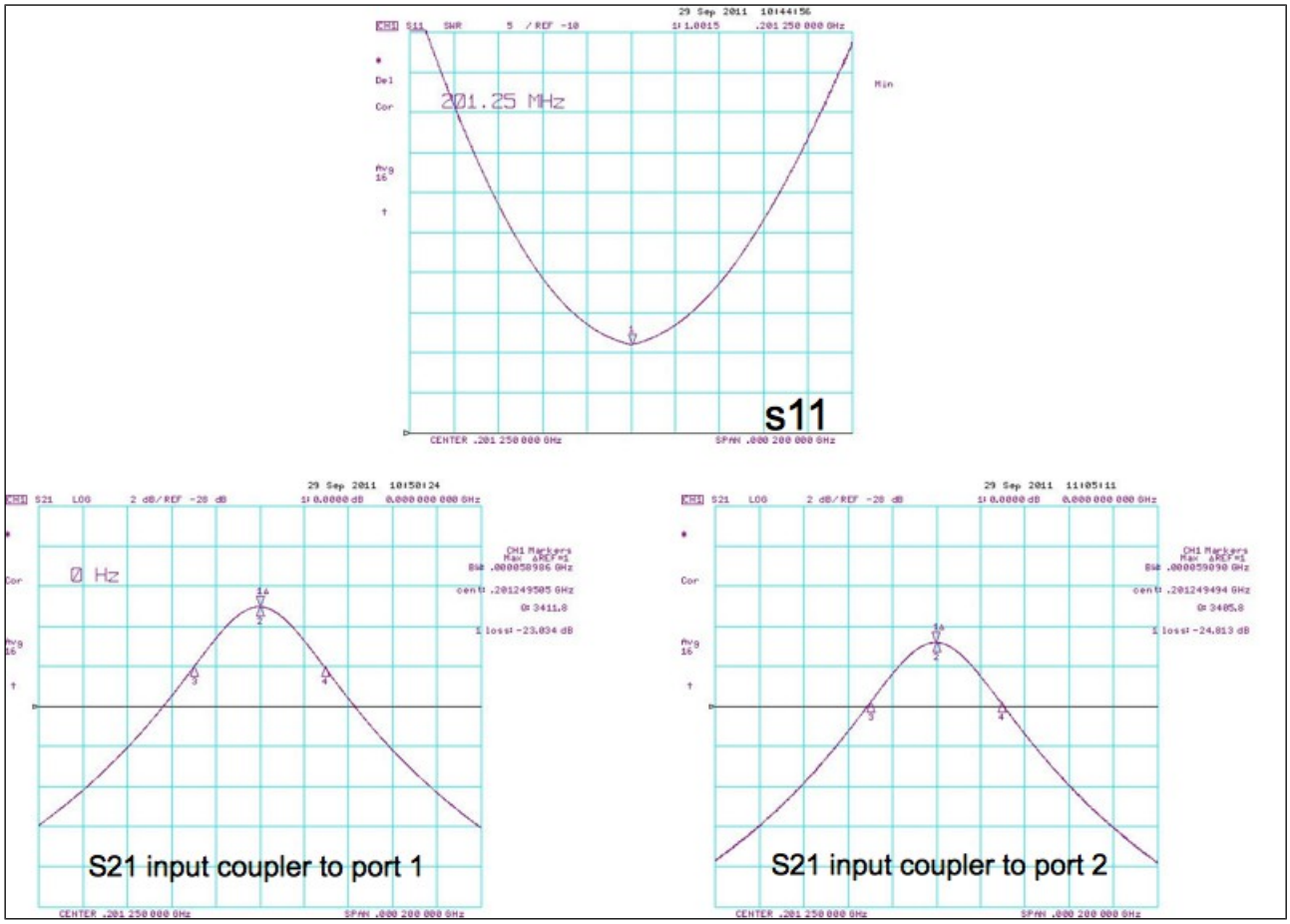

Figure 4.95: *The s-parameters of the buncher. The coupler has been adjusted to critical coupling with VSWR = 1.0015 for tuner position 5.440 mm and temperature 67°F. The s21 from the power port to the pickup #1 is –23.0 dB and pickup #2 is –24.8 dB. The unloaded Q is 6820.*

4.4.3. Quadrupoles with embedded corrector dipoles

To make the MEBT as short as possible, the quadrupoles will have corrector dipoles embedded in them. The challenge in the design is the high integrated gradient of 2 T and its short length. Initially, it was thought that the BNL quadrupole design can be adapted for FNAL use. However, the BNL design only runs at 7.5 Hz compared to 15 Hz at FNAL, and so it is unclear whether the BNL quadrupole will not overheat when ramped at the higher rate. Therefore, it was decided that TD will come up with a design which is compatible with the FNAL requirements. A summary of the requirements and quadrupole parameters is shown in Table 4.14.

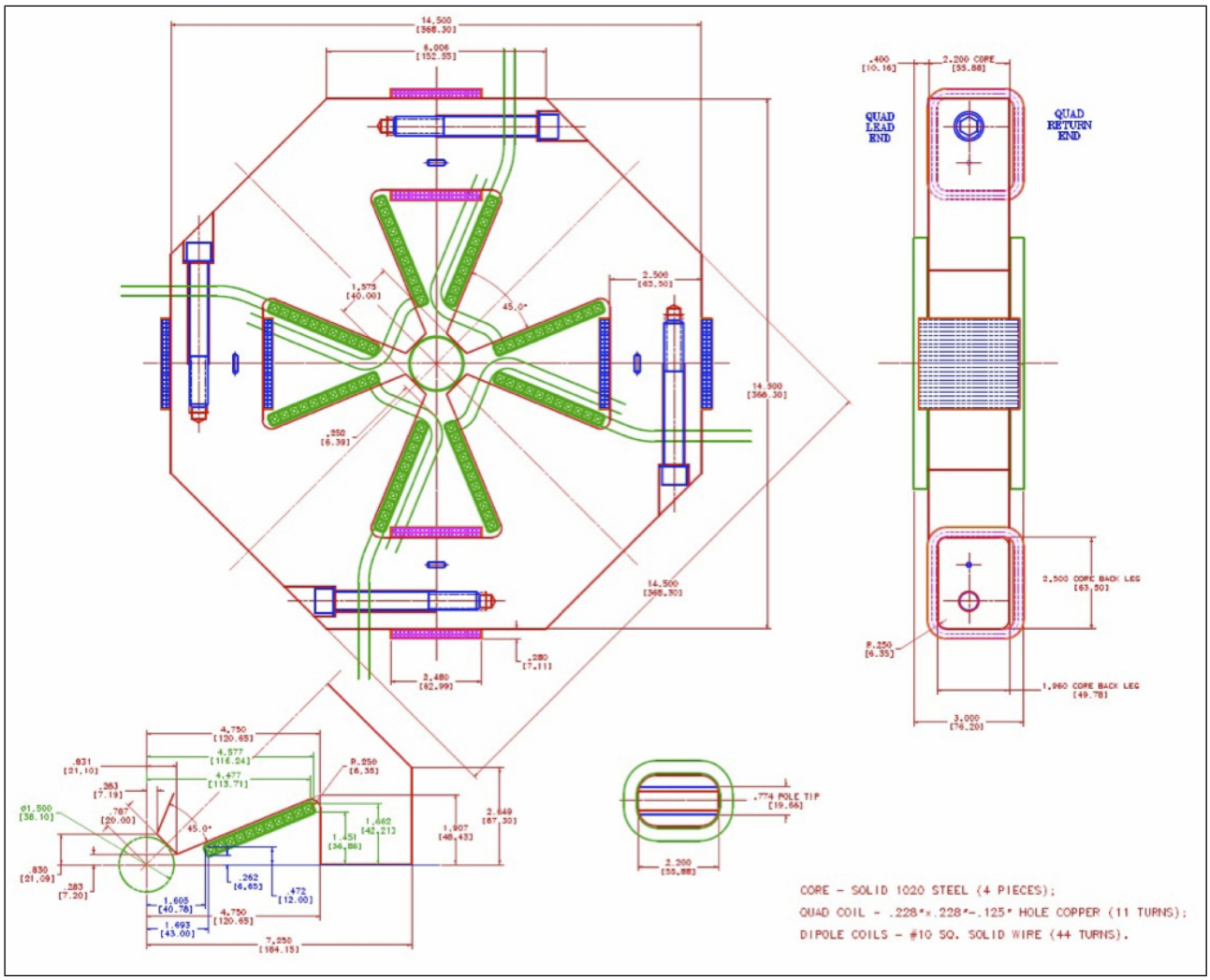

Figure 4.96: *The MEBT quadrupole with embedded dipole correctors. The yoke length is 2.2" and the physical length of the quadrupole is 3". (Designed by V. Kashikhin and A. Makarov)*

TD [21] has come up with a conceptual design shown in Figure 4.96. The quadrupole will run DC and be water cooled. Since it runs DC it can have a solid core rather than a laminated core. A solid core is easier to manufacture and to assemble and will greatly speed up the delivery time. Two sets of doublets, i.e. four quadrupoles have been delivered and installed in the MEBT, and one spare set of doublets are in storage at this time.

Parameter	Value	Units
Required quadrupole integrated gradient Q_{int}	2.2	T
Quadrupole core length L_Q	55.88 (= 2.2")	mm
Quadrupole physical length	76.2 (= 3.0")	mm
Required dipole corrector integrated field *Bdl*	0.45×10^{-3}	T·m
Power loss	1.7	kW
Water flow	3	L/min
Water temperature rise	14	°C

Table 4.14: *The requirements and parameters of the quadrupole and embedded dipole.*

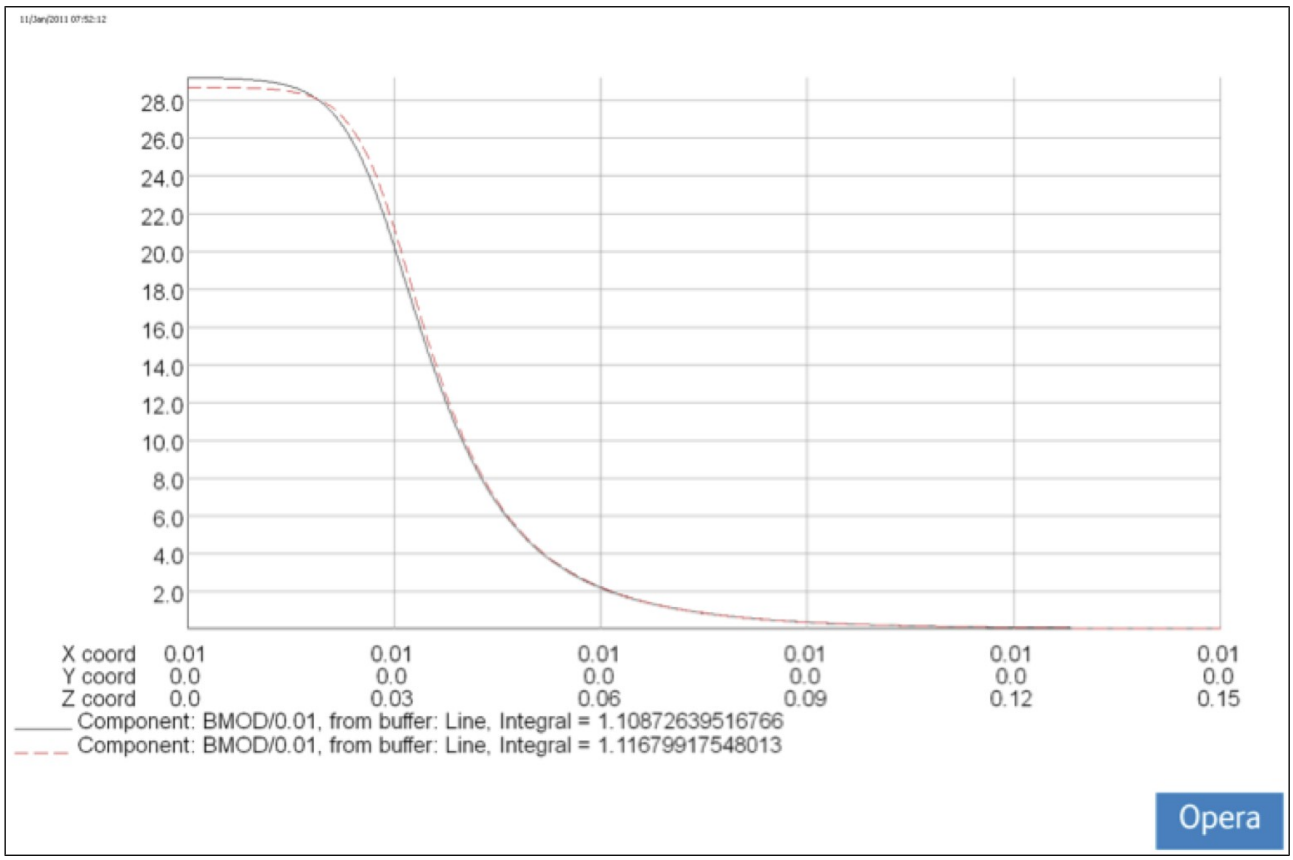

Figure 4.97: *The quadrupole field gradient at 4.4 kA/pole current as a function of longitudinal position z calculated at x=1 cm, y=0 cm. At z=7.4 cm (2.9"), the field gradient is about 3.4% of the gradient at z=0 cm.*

4.4.3.a. *Doublets*

Doublets have to be built from the quadrupoles discussed in section 4.4.3 The distance between the quadrupoles in each doublet has been selected to be 2.9" from the center of the first quadrupole to the closest edge of the core of the second quadrupole. At this distance, the gradient is about 3.4% of the gradient at the center of the quadrupole. See Figure 4.97. At this separation, each quadrupole of the doublet should not perturb the gradient of its partner significantly. See Figure 4.100 and discussion below.

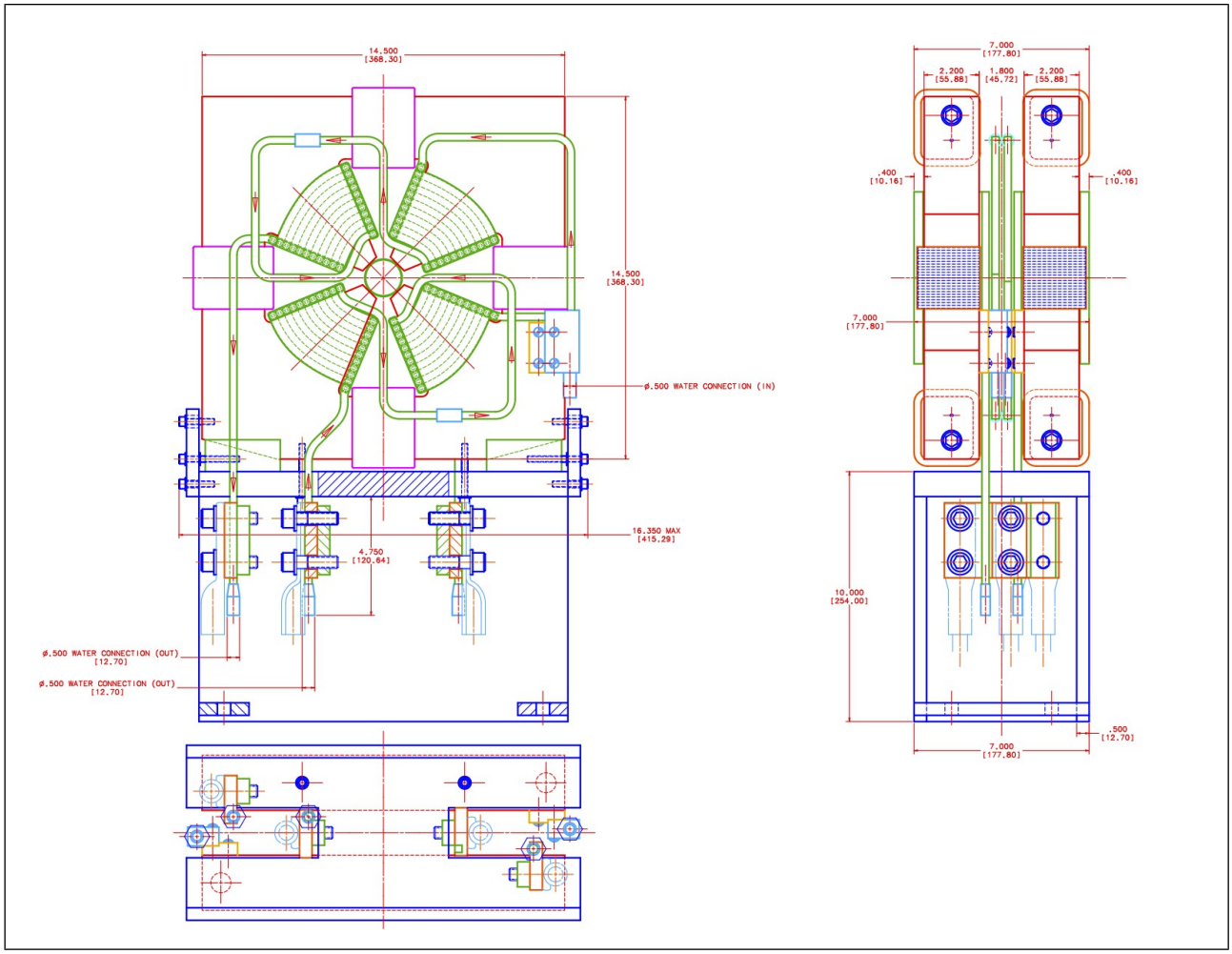

Figure 4.98: *TD will deliver the doublets as a matched pair of quadrupoles.*

Figure 4.98 shows a preliminary drawing of the doublet. The core to core distance (closest edges) is 1.8" (or equivalently 2.9" from the center of the first quadrupole to the closest edge of the second quadrupole). The total physical length of the doublet is 7". TD will deliver the doublets as a matched pair of quadrupoles with the electrical centers aligned and rotations w.r.t. the longitudinal direction corrected to better than 1°. See section 4.4.3.e The assembled doublets are shown in Figure 4.99.

The field gradient of one of the quadrupole of the doublet is shown in Figure 4.100 for the case when one quadrupole is focusing and the other is defocusing at 440 kA/pole at r = 1 cm, 0° and 45° w.r.t. the pole tip. The relative integrated field difference is 1.7% between these two cases.

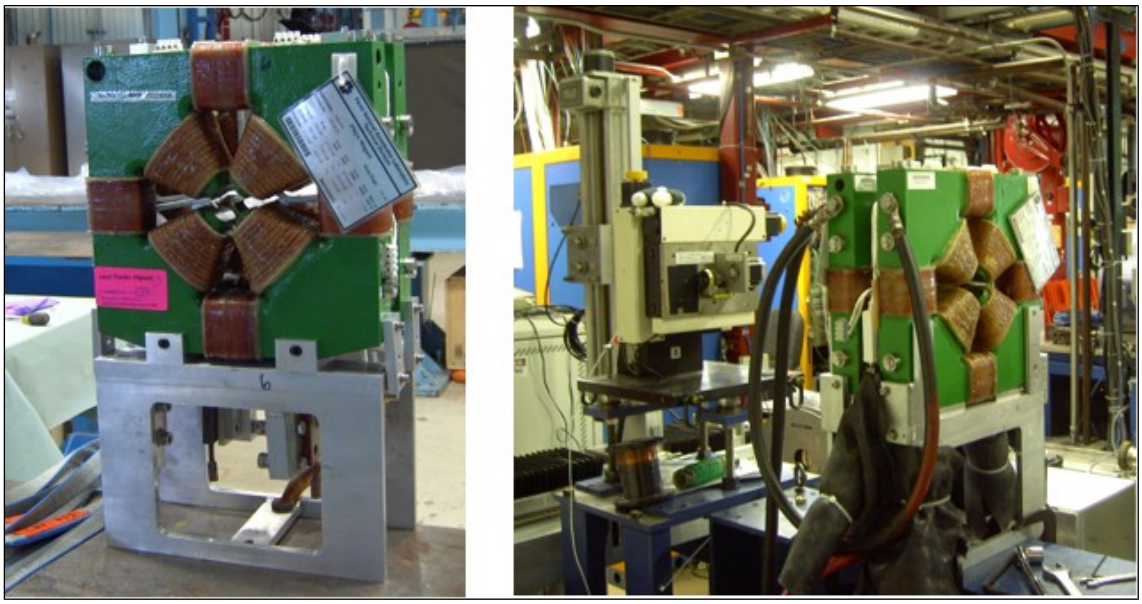

Figure 4.99: *The doublets after assembly and under test.*

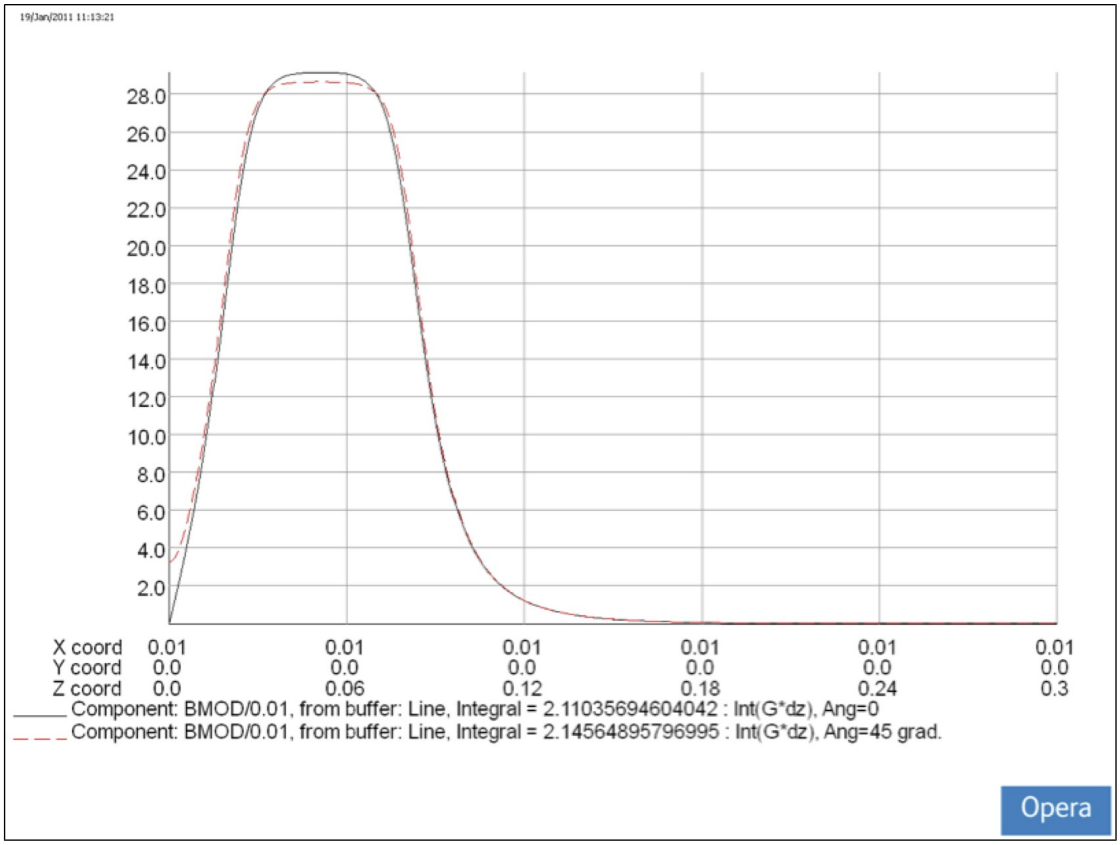

Figure 4.100: *The quadrupole field gradient for the doublet as a function of longitudinal position z calculated at r=1 cm, 0° and 45° w.r.t. the pole tip when the doublet is powered so that one quad is focusing and the other defocusing at 4.4 kA/pole. The relative integrated field difference is 1.7% between these two cases. Note: z=0 is the symmetry plane of the doublet.*

4.4.3.b. *Higher order harmonics*

The B-field of the quadrupoles have higher order harmonics that have to be taken into account. The well-known formula for describing the contribution of higher order harmonics to the B-field is [22]

$$B_y + i B_x = (B_2 \times 10^{-4}) \sum_{n=1}^{\infty} (b_n + i a_n) \left(\frac{x + iy}{r_m} \right)^{n-1} \tag{19}$$

where (B_x, B_y) is the B-field at cartesian coordinates (x, y), B_2 is the quadrupole B-field at r_m, b_n is the normal component and a_n is the skew component of the $2n$'th pole at reference radius r_m. Note that both b_n and a_n are dimensionless and are called "units" in magnet measurement parlance when the numerical factor 10^{-4} is used as a normalization.

In amplitude and phase notation, the n'th higher order harmonic is written as

$$b_n + i a_n = A_n e^{-i n \alpha_n} \tag{20}$$

where $A_n = \sqrt{b_n^2 + a_n^2}$ and $\alpha_n = -\left(\frac{1}{n}\right)\left(\tan^{-1} \frac{a_n}{b_n}\right)$.

However, the amplitude and phase definition given by Eq. (20) is not used by PARMILA. The PARMILA definition [23] of the nth B-field component B_n at radius r is

$$B_n(r) = \mathrm{A_n} G r_m \left(\frac{r}{r_m} \right)^{n-1} \tag{21}$$

where G is the quadrupole gradient, $\mathrm{A}_n G r_m$ is the value of B_n measured at the reference radius r_m. Now the nth component from Eq. (19) measured at (0, r_m) and equated to Eq. (21) is

$$\begin{aligned} B_n(r_m) &= B_2 \times 10^{-4} (b_n + i a_n) i^{n-1} = \mathrm{A_n} G r_m \\ \Rightarrow \mathrm{A_n} &= 10^{-4} (b_n + i a_n) i^{n-1} \end{aligned} \tag{22}$$

because $B_2 = G r_m$. A_n in amplitude phase notation is

$$\mathrm{A_n} = |\mathrm{A_n}| e^{-i n \alpha_n} \tag{23}$$

And $|\mathrm{A_n}|$ and $\alpha_n - (-\pi/4)$ (converted to degrees) are used in the MPOLES arguments of PARMILA. Table 4.15 shows the b_n and a_n values measured at $r_m = 1\,\mathrm{cm}$ for quadrupole named PSQA001. The other quadrupoles have similar b_n and a_n values. The dodecapole harmonic $n = 6$ dominates the modes, and it is this mode which contributes to the greatest transverse emittance growth. See Table 4.15 and Figure 4.101.

However, simulations to the end of Tank 1 show that the emittances remain the same but there a higher loss of < 1% compared to having perfect quadrupoles in the MEBT. Therefore, the dodecapole component is not a big concern.

Harmonic number n	Normal component b_n	Skew component a_n
3	-2.49	1.78
4	0.82	3.62
5	1.84	-0.51
6	39.88	-0.78

Table 4.15: *The measured harmonics of quadrupole PQSA001. The other quadrupoles have similar normal and skew components.*

Harmonic	$\Delta\epsilon_x/\epsilon_x$(ref)	$\Delta\epsilon_y/\epsilon_y$(ref)
From $n=3$ to $n=6$	6%	14%
$n=3$	0.2%	-0.1 %
$n=4$	0.2%	-0.3 %
$n=5$	-0.06 %	-0.06 %
$n=6$	7%	14%

Table 4.16: *Emittance growth from the harmonics is dominated by n=6.*

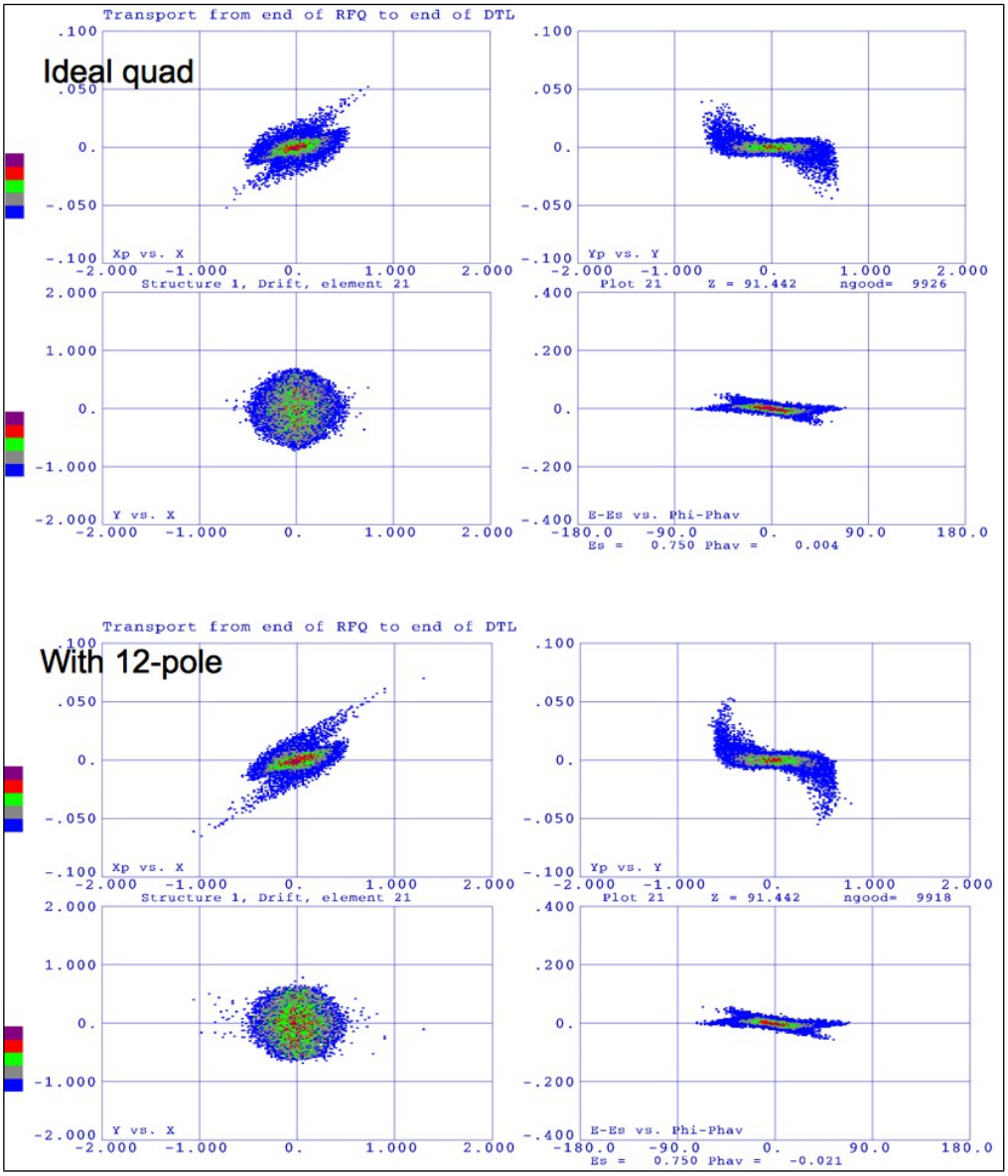

Figure 4.101: *The transverse emittances have larger tails when there is a large dodecapole component.*

4.4.3.c. *Strength of the embedded dipoles*

The strength of the corrector dipole is mainly constrained by the sextupole component that it introduces. See section 4.4.3.d To keep the size of the sextupole component small compared to the quadrupole field, it has been decided that the H- beam can be deflected by a maximum of 1 mm at the entrance of the RFQ by the last dipole. The last dipole has been chosen for this constraint because it has the shortest lever arm, and thus runs the hardest for the same deflection, compared to the other upstream dipoles.

In the present design, the last dipole is about 11" from the entrance of the RFQ. Therefore, for a 1 mm change in position at the entrance, the deflection angle θ is

$$\theta=\frac{1}{11\times 25.4}=3.5 \text{ mrad} \tag{24}$$

Therefore, the integrated dipole strength *Bdl* [Tm] is

$$Bdl[\mathrm{T\cdot m}]=\theta\, p[\mathrm{eV/c}]/c[\mathrm{m/s}] \tag{25}$$

where $p=3.74\times 10^{7}$ eV/c is the momentum of 750 keV H- ions, $c=3\times 10^{8}$ m/s is the speed of light. Substituting these numbers into Eq. (25), $Bdl=0.45\times 10^{-3}$ Tm.

4.4.3.d. *Sextupole components*

The sextupole components which arise from the dipole field can cause emittance blow up if they are too large. Simulations with PARMILA show that if A_3 (the relative amplitude of the sextupole component to the quadrupole field) defined in Eq. (21) above is < 1.2%, the transverse emittance blow up from the sextupole component is < 5%. In fact, for $Bdl=0.45\times 10^{-3}$ Tm, the emittance growth is ~1%.

Using the PARMILA definition of the *n*th B-field component B_n at radius r from Eq. (21), the integrated quadrupole field Q_{int} at r_m over its magnetic length L_Q is

$$Q_{\mathrm{int}}=\int_{-L_Q/2}^{L_Q/2} B_2(r_m)\, dz=G\, r_m\, L_Q \tag{26}$$

because PARMILA uses a hard edge model for the quadrupole and B_2 is a constant inside $z<|L_Q/2|$. Similarly, the integrated sextupole field S_{int} at r_m is

$$S_{\mathrm{int}}=\int_{-L_Q/2}^{L_Q/2} B_3(r_m)\, dz=\mathrm{A}_3\, G\, r_m\, L_Q \tag{27}$$

where the same assumptions have been used as before.

Using Eq. (26), the integrated quadrupole field from the conceptual quadrupole design at $r_m=1$ cm is

$$Q_{\mathrm{int}}=22[\mathrm{T/m}]\times(1\times 10^{-2}[\mathrm{m}])\times(55.88\times 10^{-3}[\mathrm{m}])=0.012[\mathrm{T\cdot m}] \tag{28}$$

where $L_Q=45$ mm and the gradient $G=22$ T/m comes from the last quad in Table 4.12.

From OPERA, $S_{\mathrm{int}}=0.564\times 10^{-4}$ Tm for $Bdl=0.45\times 10^{-3}$ Tm at $x=0$, $y=0$ from Figure 4.102 and section 4.4.3.c Hence, A_3 can be solved by dividing S_{int} by Q_{int}, i.e. using equations (26) and (27), to give

$$\mathrm{A}_3=S_{\mathrm{int}}/Q_{\mathrm{int}}=(0.564\times 10^{-4})/0.012=0.005<0.012 \tag{29}$$

And so the sextupole component is not a concern as long as the corrector strengths are kept below $Bdl=0.45\times 10^{-3}$ Tm. Figure 4.103 shows a plot of emittance blow up versus A_3 applied to the present MEBT design. Clearly, when A_3 is < 0.005, the emittance blow up at the entrance of the DTL1 is < 1%. Note: In the PARMILA simulation, the angle α_3 between the positive pole of the sextupole and the quadrupole has been set to $\pm 45°, 0°$ and $22.5°$. The simulation is the worst case scenario because the same A_3 is used for every quadrupole.

The measured *Bdl* and b_3 of the sextupole field measured at $r_m=1$ cm at 0.52 A for PQSA001 are shown in Table 4.17. The value of the integrated 2*n*'th pole-field at any location is given by the usual formula referenced to the dipole field B_1

$$
\begin{aligned}
B_y + i\,B_x &= (B_1 \times 10^{-4}) \sum_{n=1}^{\infty} (b_n + i\,a_n) \left(\frac{x + iy}{r_m} \right)^{n-1} \\
\Rightarrow \; |B_n\,dl| &= \left| \int B_n\,dz \right| = Bdl \times 10^{-4} \sqrt{b_n^2 + a_n^2} \;\; \text{at} \;\; x = r_m,\, y = 0
\end{aligned}
\tag{30}
$$

where the variables have already been defined in Eq. (19).

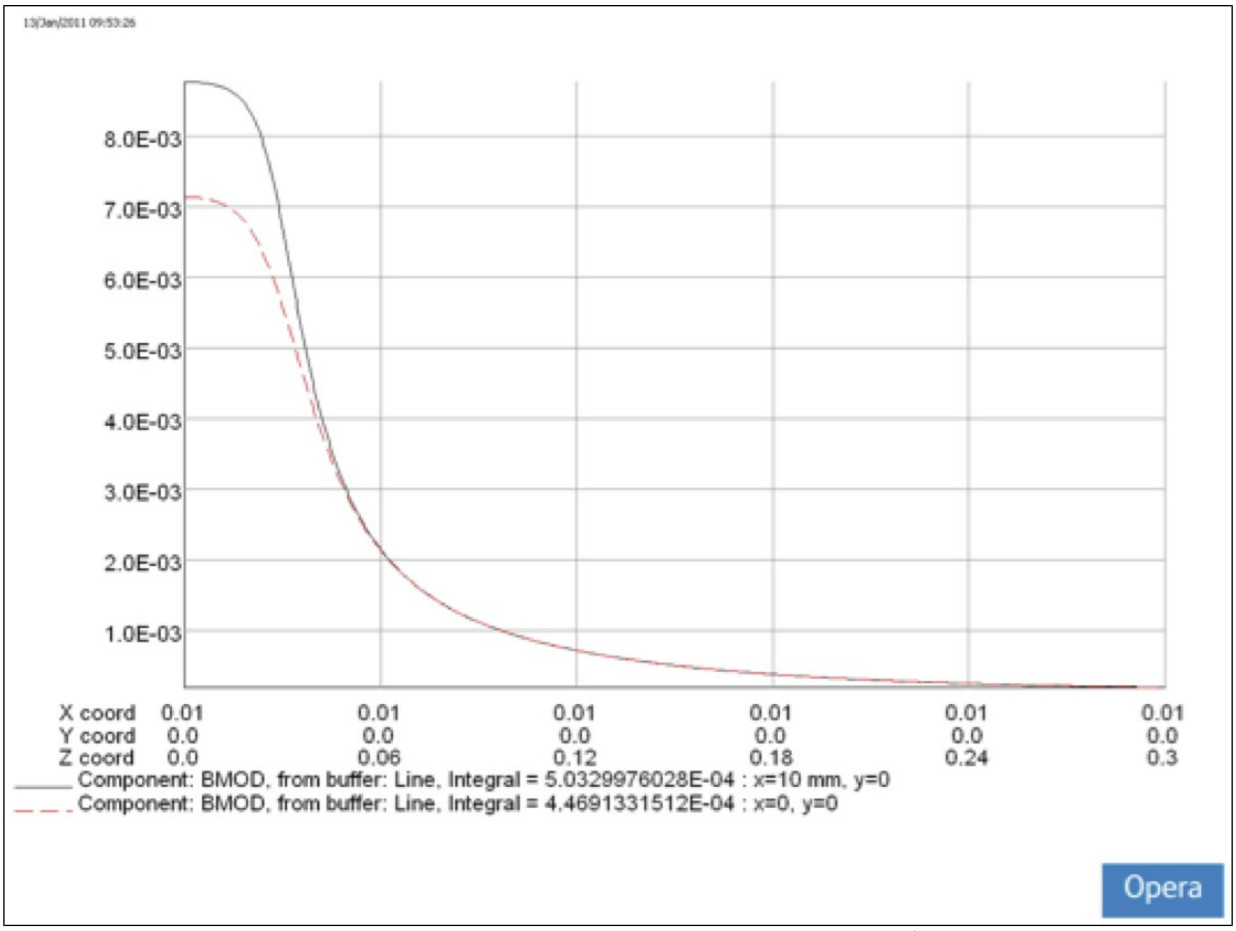

Figure 4.102: *When the embedded dipole is set to* $Bdl = 0.45 \times 10^{-3}$ *T·m at x=0 cm, y=0 cm, Bdl is different at x=1 cm, y=0 cm because of the sextupole contribution. The difference is the integrated sextupole field component* $S_{\text{int}} = 0.564 \times 10^{-4}$ *T·m.*

	Vertical		Horizontal	
Bdl (T·m)	6.40×10^{-4}		6.70×10^{-4}	
	b_3	a_3	b_3	a_3
Sextupole components	1211.41	−41.25	1140.88	137.78

Table 4.17: *The measured Bdl and sextupole components of PQSA001. The strength of the dipole and the sextupole components are very similar to the other quadrupoles.*

The factor required to rescale the measured Bdl to 0.45×10^{-3} T·m is 0.7. Using the measured values for the integrated vertical sextupole component arising from the dipole corrector powered to $(0.52\times0.7=0.36)$ A at $r_m=1$ cm is thus

$$\begin{aligned} S_{\text{int}} &= 0.7\times Bdl\times10^{-4}\sqrt{b_3^2+a_3^2}=0.7\times(6.40\times10^{-4})\times10^{-4}\times\sqrt{1211.41^2+41.25^2} \\ &= 0.54\times10^{-3}[\text{T}\cdot\text{m}] \end{aligned} \tag{31}$$

which is the same value found using OPERA that was discussed above.

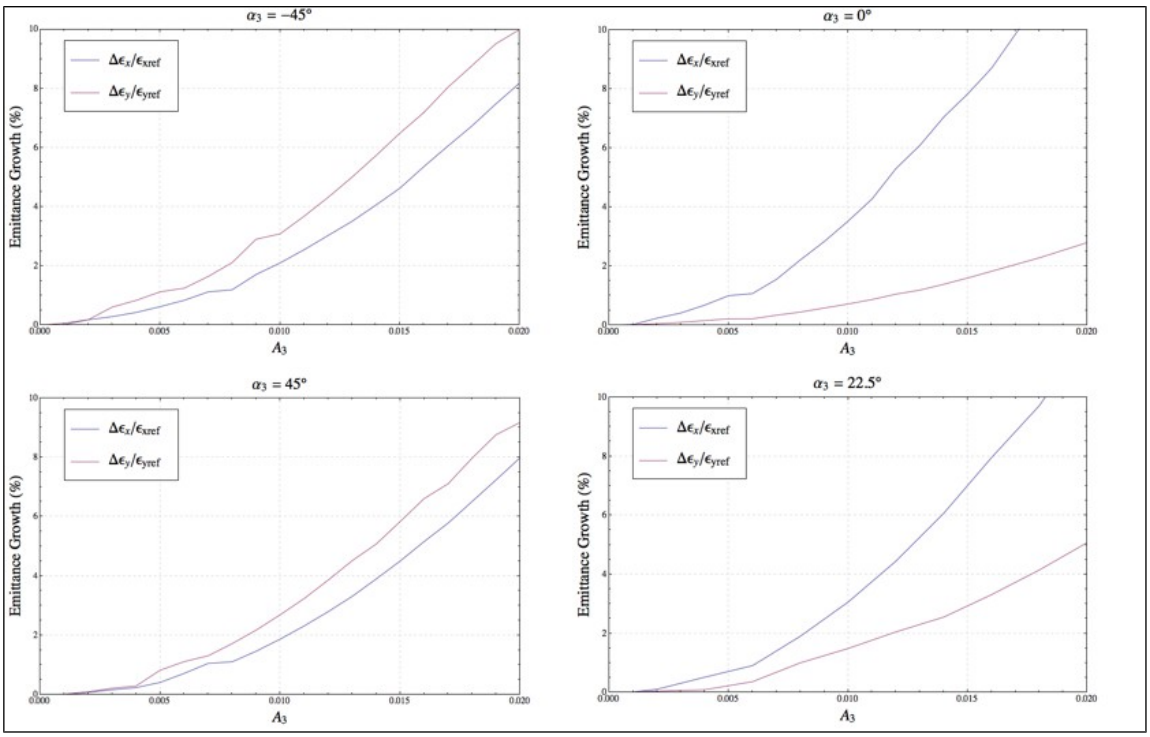

Figure 4.103: *The emittance growth at the entrance of the DTL w.r.t. the emittance when A_3=0. To keep the growth below 1%, A_3 must be < 0.005. In these* PARMILA *simulations, the angle between the positive pole of the sextupole and the quadrupole has been set to ±45°, 0° and 22.5°.*

4.4.3.e. *Coupling*

The quadrupole strengths are very strong in the MEBT and any rotation of the quadrupoles about the longitudinal axis can result in emittance growth from coupling. Therefore, it is necessary to know an acceptable rotation error for the mechanical alignment of these quadrupoles to keep emittance growth to a minimum. Using PARMILA, the beam is propagated through the MEBT with all the quadrupoles randomly rotated within the range $\pm\theta_c$. The emittance at the entrance of the DTL w.r.t. $\theta_c=0$ are shown in Figure 4.104. From these simulations, emittance growth is < 1% if the random roll errors are within $\pm0.5°$.

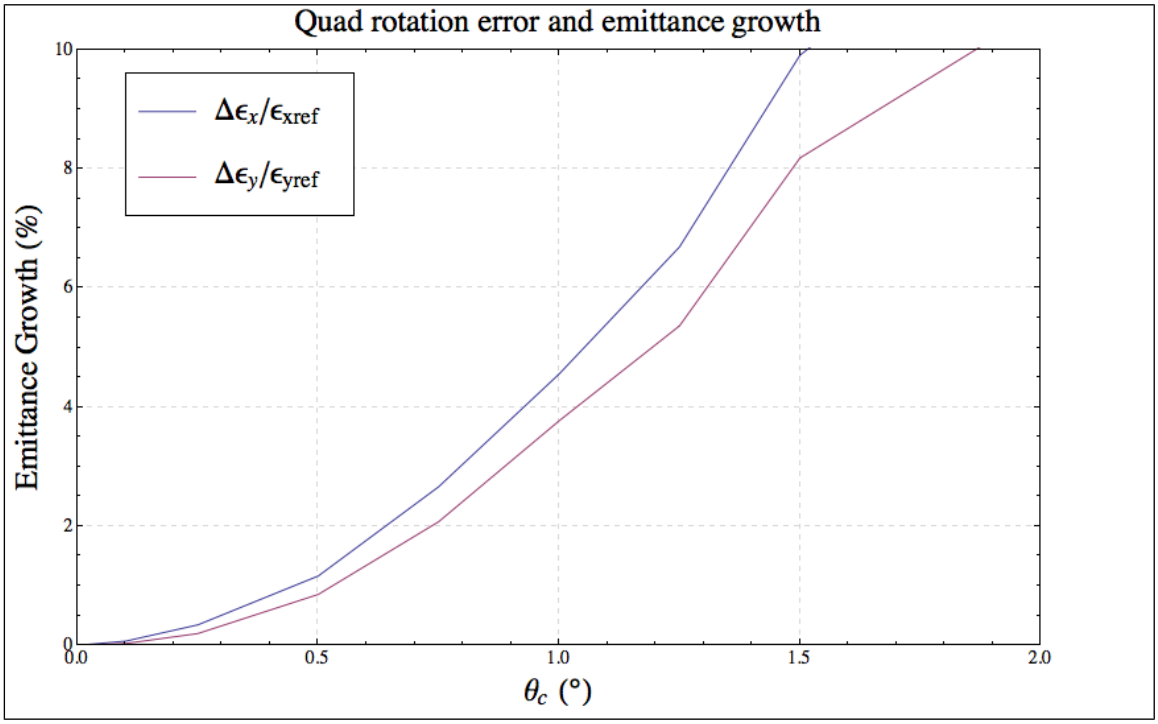

Figure 4.104: *Emittance growth due to random rotation errors in the range* $\pm\theta_c$ *for all the quadrupoles in the MEBT. For < 1% growth, the random errors must in the range* $\pm 0.5°$*.*

4.4.4. Beam measurements

The beam measurements at the entrance of Tank 1 will be discussed in this section. Two sets of measurements have been made. The first is the "flat" beam from the old Cockcroft-Walton system. This measurement can be used to compare the emittance of the "round" beam from the new system.

4.4.4.a. *Emittance of "flat" beam*

The Twiss parameters at the start of Tank 1 from the old Cockcroft-Walton system had been measured just before it was retired from service for two different beam currents. The results are summarized in Table 4.18.

The asymmetries between the horizontal and vertical emittances are apparent for 32 mA of beam current but disappear for 46 mA of current. The measured emittance at the start of Tank 1 is shown in Figure 4.105. Notice, however, that the vertical emittance is not elliptical and the rms emittance is probably not a good measure of it.

For 32 mA of beam current at the entrance of Tank 1		
Parameter	**Horizontal**	**Vertical**
α	3.3	–0.4
β (m)	0.8	0.4
ε (normalized, 1 sigma) (π mm mrad)	0.6	0.8
For 46 mA of beam current at the entrance of Tank 1		
Parameter	**Horizontal**	**Vertical**
α	1.8	0.5
β (m)	0.5	0.3
ε (normalized, 1 sigma) (π mm mrad)	0.9	1.0

Table 4.18: *The Twiss parameters of "flat" beam from the old Cockcroft-Walton system for two different beam currents.*

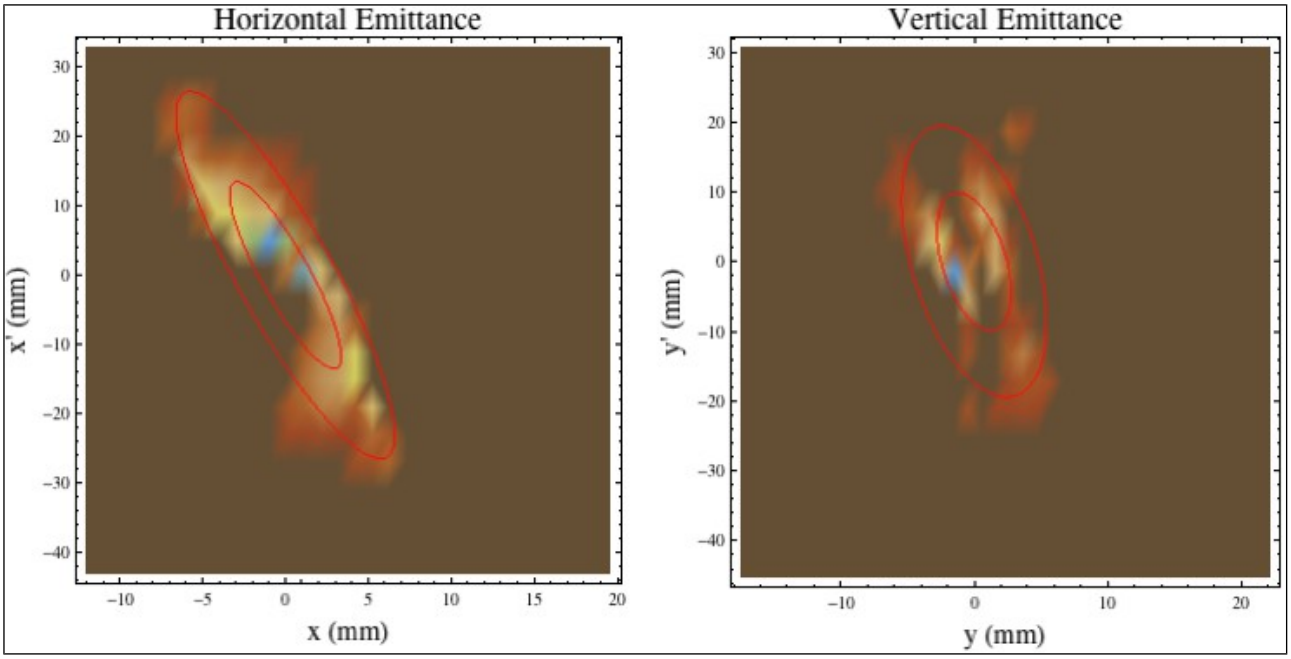

Figure 4.105: The flat beam horizontal and vertical emittances measured on the emittance probes at the beginning of Tank 1 for 46 mA beam. The red ellipses enclose 1σ and 2σ emittances. Notice that the vertical emittance has a very strange non-elliptical shape.

4.4.4.b. *Emittance of "round" beam*

The Twiss parameters from "round" beam in the new RFQ injector system is summarized in Table 5.1 for 46 mA. Notice that these emittances are comparable to the rms emittance of flat beam for 32 mA beam but is ~2× smaller for 46 mA beam using the measurements discussed in section 4.3.5.d.

Parameter	Horizontal	Vertical
α		
β (m)		
ε (normalized, 1 sigma) (π mm mrad)	0.6(?)	0.5(?)

Table 4.19: *The Twiss parameters of "round" beam from the new RFQ injector system for 46 mA beam at the start of Tank 1.*

To be filled in ...

4.5. Layout

The present layout of the H- and I- lines are shown in Figure 4.106. All the elements in the I- line upstream of the DTL will be removed for the installation of the proposed injector. The approximate space required for the proposed injector is drawn in shades of red on the floor plan of the pre-accelerator enclosures shown in Figure 4.107. A new platform will need to be constructed because the new sources will be inside the I- enclosure. Figures 4.109 and 4.110 show the drawings of the new platform. Figure 4.108 shows the completed platform.

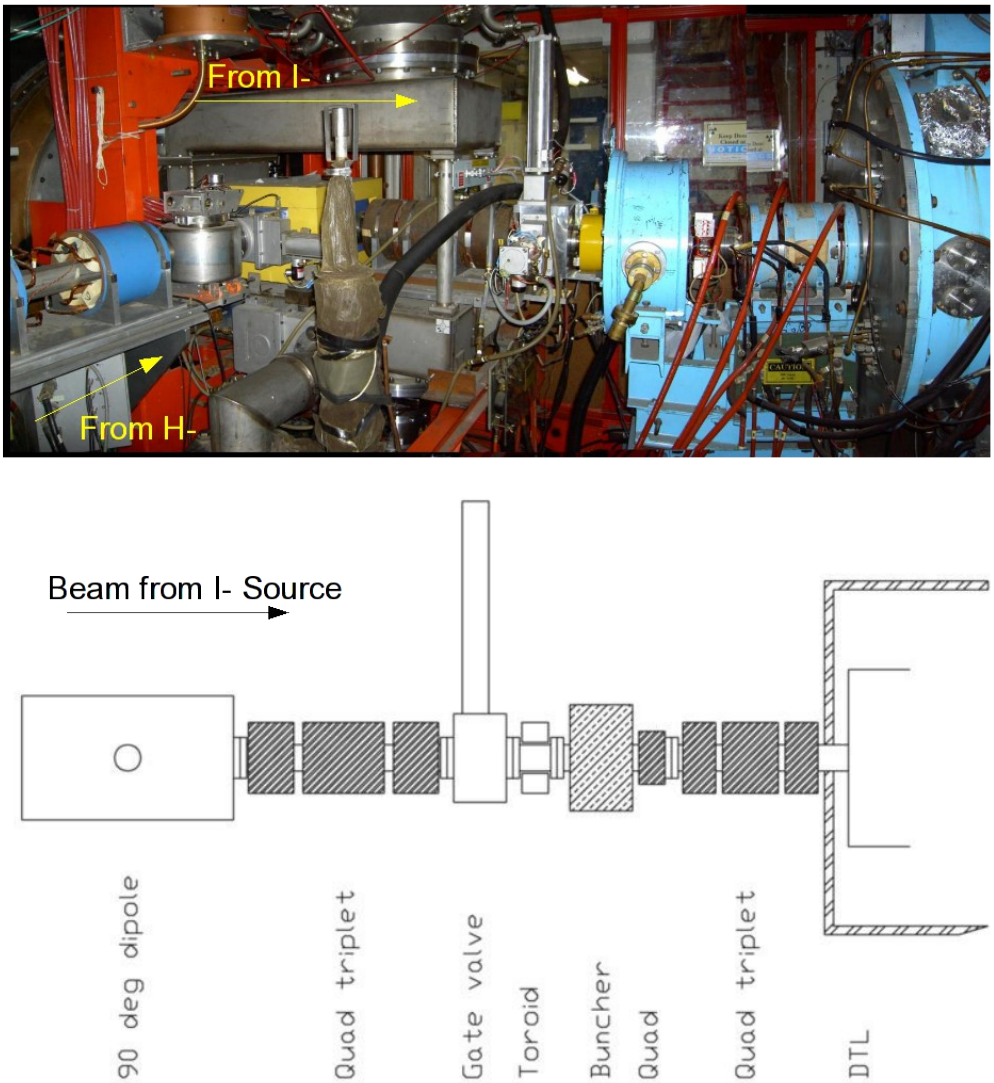

***Figure 4.106**: The photograph (composited from three photographs) in this figure shows the present I- and H- transport lines. The drawing below it shows the elements in the I- line. All the elements upstream of the DTL will be removed for the new injector installation.*

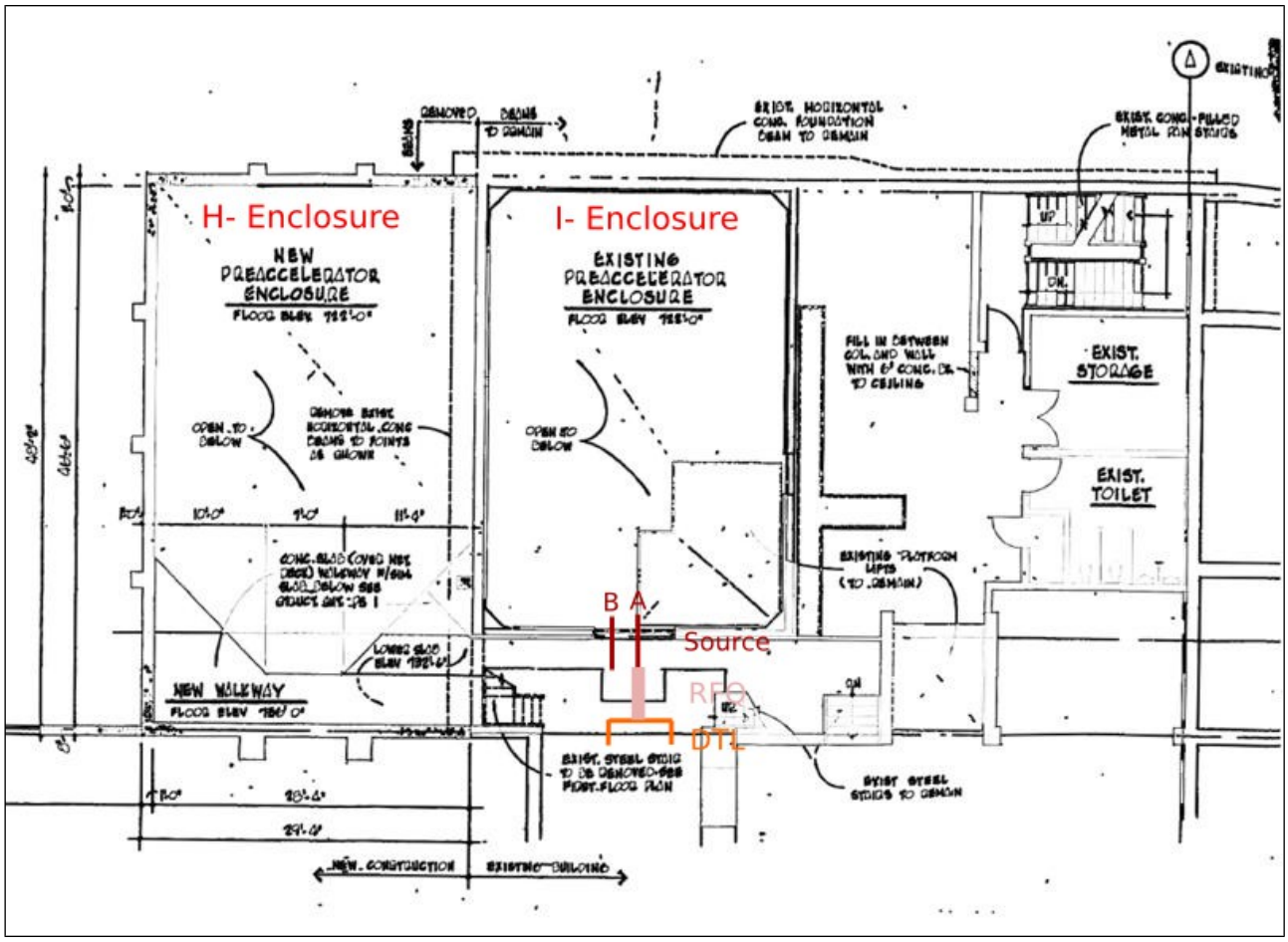

Figure 4.107: *The floor plan of the existing pre-accelerator enclosures which house both the H- and I- sources. A sketch of the new injector is drawn in shades of red in this figure. Note: the length of the sketch is approximately to scale, but the width is not. The new sources will be inside the pit area of the I- enclosure. (c.f. Figure 4.1)*

Figure 4.108: *The completed platform. Left picture was taken on 20 Sep 2012 and the right picture was taken on 15 Oct 2012.*

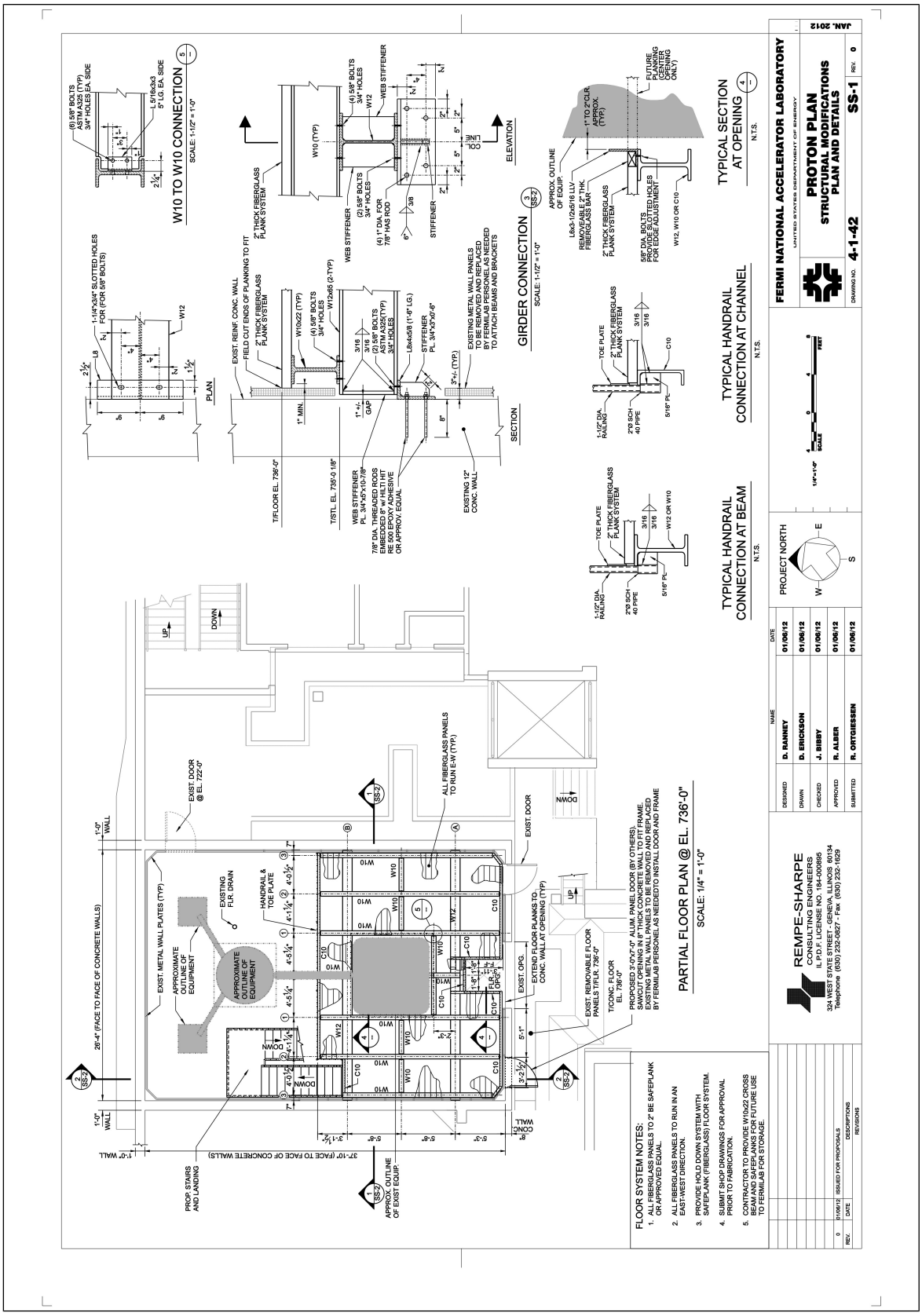

Figure 4.109: *The new platform for housing the injector.*

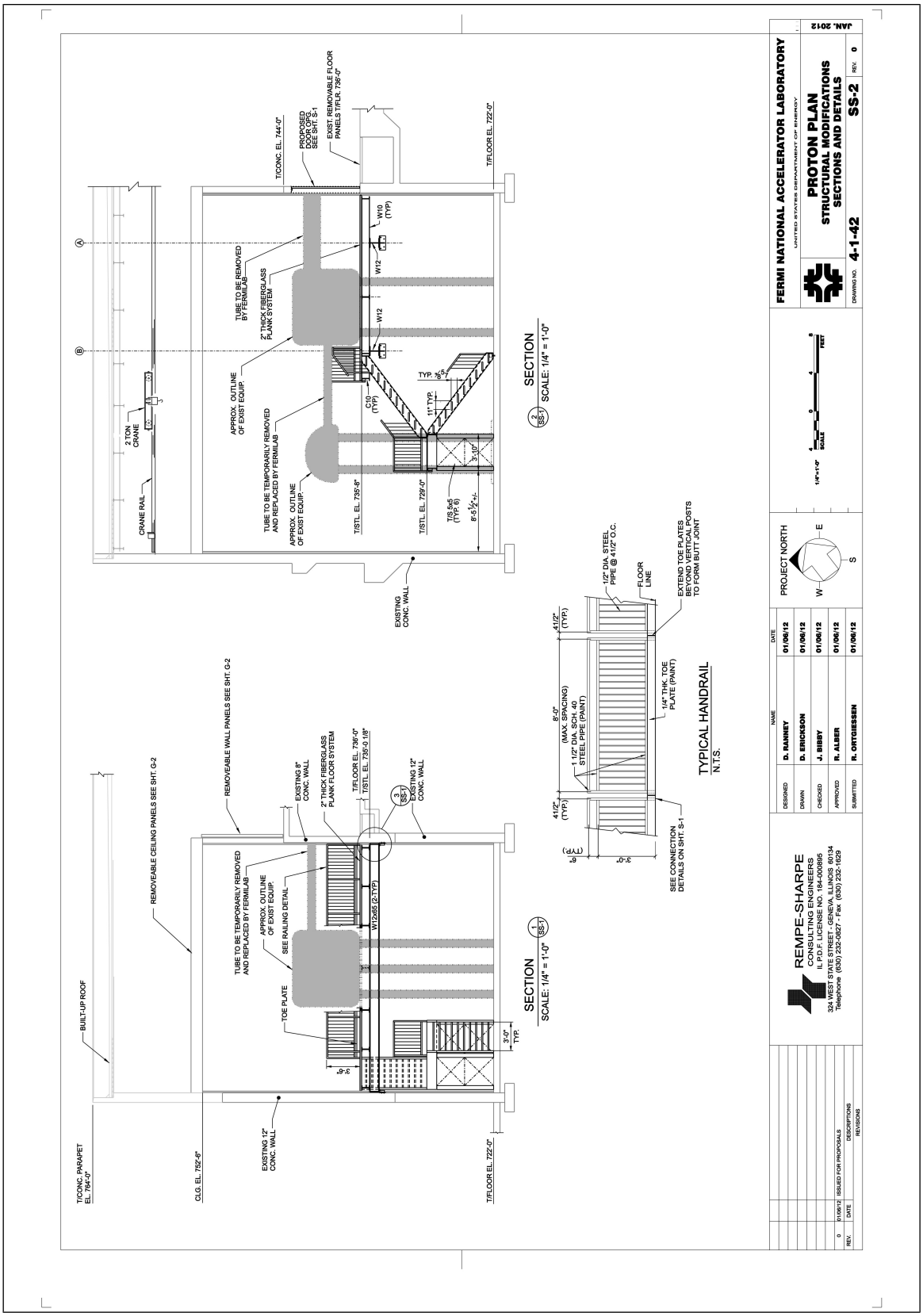

Figure 4.110: *Side view of the platform.*

5. Controls, Interlocks and Safety

5.1. Controls

A combination of various types of I/O hardware will be used to create the controls and interlocks system that will be used for the pre-injector. The main components of the system include: a programmable logic controller (PLC), hot-link rack monitors (HRM), a motor controller device and PC-104 processor cards. A block diagram shown in Figure 5.1 and a description of what each component is used for is provided below. The interlocks and controls system used in the pre-injector line is flexible and allows for expansion of devices as desired.

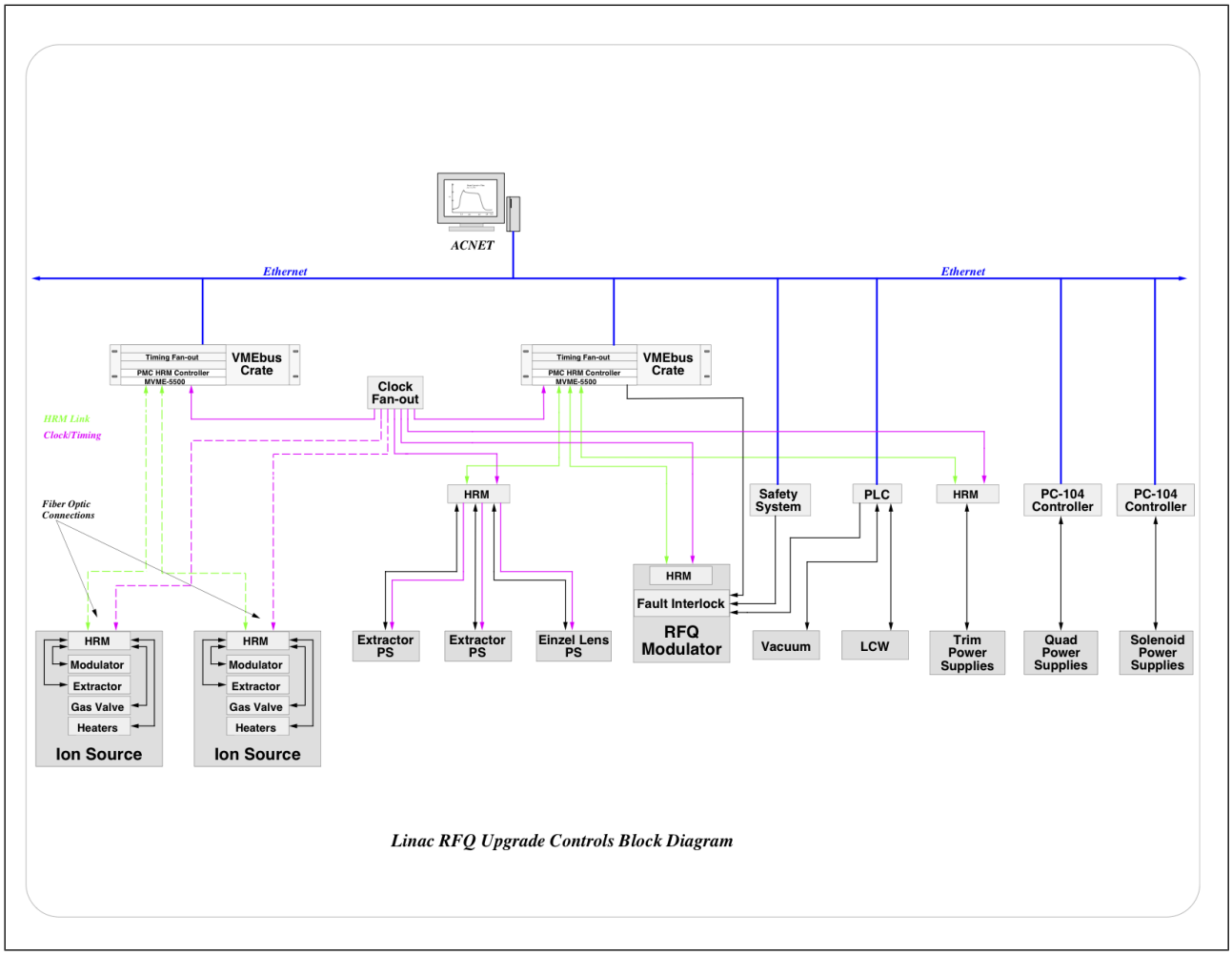

Figure 5.1: *The control system block diagram.*

5.1.1. PLC

The PLC will be used to provide remote operation, interlocks, and monitor signals for all water-cooled and vacuum sensitive devices. The I/O for the flow switches, vacuum valves and vacuum pump and gauge controllers will be fed to the PLC, where combination logic will be used

to create a permit. The permit will then be fed into the Fault Interlock Box inside the RF amplifier rack so that the RF can be inhibited in the event of a vacuum trip or loss of water flow. The PLC will also be used to provide the status and control of the position switch used to determine which of the two Ion Sources will be utilized for operations. All the signals in the PLC will be available via the ACNET parameter pages.

5.1.2. HRM

The HRMs will be used for data acquisition and control of the RFQ modulator, ion source modulators, high voltage power supplies and beam line dipole trim package power supplies. All timing triggers and gates required will be provided by the HRMs or the RFQ frontend VME crate. Data and clock/timing communication with the ion source HV enclosures will be via fiber optic connections. A dedicated RF inhibit control line will be provided to the RF switch. All signals connected to the HRMs will be available as ACNET parameters.

5.1.3. Motor Controls

A motor control system, designed by Al Legan (AD/Controls) will be used to control the RFQ tuner and beamline wire scanner stepping motors.

5.1.4. PC-104

The PC-104 processor cards were designed by EE support and are used to provide control and status of the power supplies for various magnets in the pre-injector. The PC-104 system, which is still under development for the ANU project, will provide for startup operations of the test stand where an analog current regulator and interlock controller will also be needed. The plan is to use one of the NuMI style controllers that have been in operation for the past few years in both NuMI and MTA. This will require a temporary connection to an HRM system for status and control. Each supply will need one digital to analog connection and two analog to digital connections, three control bits (On, Off, Reset TTL) and eight TTL digital status bits (same as H:SOLIUS). For operations, the solenoid power supplies will be controlled and regulated using a PC-104 dedicated controller that can regulate up to four power supplies. This controller will regulate both of the operational solenoid supplies and also have connections to the “hot” spare supply. The plan is to also regulate and control the quadrupole supplies using this system. The PC-104 based controller is a newly developed system for DC power supplies that will provide all PS status, control and regulation over a single E-Net connection. It will provide all the status, control and plotting for up to four supplies connected to it. This controller provides all the controls connections and also has a transient recorder built in for both analog and digital signals. In addition to the PC-104, the power supply system will also have a PLC that manages the 480 VAC contactor and level shifting of signals from 24 VDC to TTL for the system. These signals include doors, ESS, step start, load klixons, cable klixons, 480 VAC contactor rack cooling and independent over-current monitoring.

5.2. Electrical Safety

The electronics cabinet for the proton source in the pre-inector is located inside a large relay rack that is grounded. The front and rear door of this relay rack have magnetic switches interlocked to the HV power supply, and to a ground arm which shuts off the supply and grounds the inner isolated HV part if the doors are moved slightly. The power for the electronics comes from a 60 kV isolation transformer located in a relay rack next to the isolated HV cabinet.

5.3. RFQ Driver PA System Controls

The RFQ PA system controls system is discussed in this section where the specific information includes what signals are monitored via ACNET, which hardware is interlocked, and the Controls system response in the event of a driver PA system trip.

5.3.1. ACNET

5.3.1.a. *Hardware setup*

The ACNET communication portal for the RFQ driver PA system is a standard IRM, node 595, located inside the driver cabinet. For testing and commissioning purposes a local 1 Hz asynchronous reset is generated via a VME GP-IP clock generator card located inside the Pre Acc R&D room. Analog signals in the range of ±10 V are captured using standard S/H module.

5.3.1.b. *ACNET devices*

As of 24 Aug 2011 there are 10 devices for reading back various analog signals, 2 digital devices that indicate the status of the PA system, 1 device for remote control, and 12 devices used to set the delay, width and duration of 4 timing pulses which come out of the IRM.

5.3.1.c. *Analog readbacks*

Directional couplers are used to measure the output RF signal at each stage of amplification. As such there are diode detected signals for the forward and reverse power of each amplifier. A small DC voltage is measured by the IRM and presented to the user after proper scaling.

Amplifier	Power read-back
LLRF	forward
IPA1	forward & reverse
IPA2	forward & reverse
4616	forward & reverse

Table 5.1: *The analog read-back.*

The 3 remaining analog readbacks are used for the 4616 driver anode voltage & current and screen voltage. In the case of the screen voltage, the device is also settable as the 4616 screen regulator card has been modi#ed to accept an IRM DAC output setting for the screen voltage.

5.3.1.d. *Digital status*

Two digital status devices are used to indicate the state of the station ladder logic and present remotely the status of the driver station front panel. When the necessary conditions have been met during the turn-on sequence the digital status bit flips and the turn-on sequence advances accordingly.

The zeroth digital device, see Table 5.2, contains state information at the very top of the

ladder logic. The turn-on sequence will not advance until air and water cooling for the various tubes has been verified. The system does not as of yet have a PLC so the PLC interlock bit has been jumpered. It may be used in the future however.

The first digital device, see Table 5.3, contains state information towards the end of the ladder logic. The DC bias power supplies are on and the system HV is ready to be turned on in anticipation of delivering pulsed RF to the 7651 and subsequently to the 4616. The radiation interlock has been jumpered and may be used in the future.

Description	State
Remote/Local	
Control power	on/off
Air cooling	on/off
Screen water flow	good/bad
Filament water flow	good/bad
Anode water flow	good/bad
7651 filament on	on/off
4616 filament on	on/off
6544 bias	on/off
6544 filament	on/off
7652 bias on	on/off
4616 bias on	on/off
PLC program interlocks	good/bad
Ground stick stowed	yes/no
Anode PS door #1	open/closed
Anode PS door #2	open/closed

Table 5.2: *Digital Device 0.*

Description	State
Rad interlock	ok/trip
Anode PS breaker closed	open/closed
4616 cavity pressure	good/bad
System on	on/off
7651 anode on	on/off
4616 permit	good/bad
7651 screen on	on/off
Crowbar ready	yes/no
4616 screen HV on	on/off
RF amplifier on	on/off
4616 anode off	on/off
Interlock trip	ok/trip
7651 anode overload	ok/trip
4616 anode overload	ok/trip
4616 screen overload	ok/trip
4616 anode crowbar	ok/trip

Table 5.3: *Digitial device 1.*

5.3.1.e. *Controls system response*

The responsibility of the ACNET Controls system will be to provide analog and digital read-backs for monitoring and remote operation. Driver station components and PS's are proteced via ladder logic relays.

5.3.2. Hardware and device protection

The currnent configuration of the driver PA system and its components is similar to that of the PET project. Few modifications to the overall system configuration have been made save for routine maintenance and repairs. The initial output RF power to a matched load is in the range of 120 – 130 kW.

5.3.2.a. *High level block diagram*

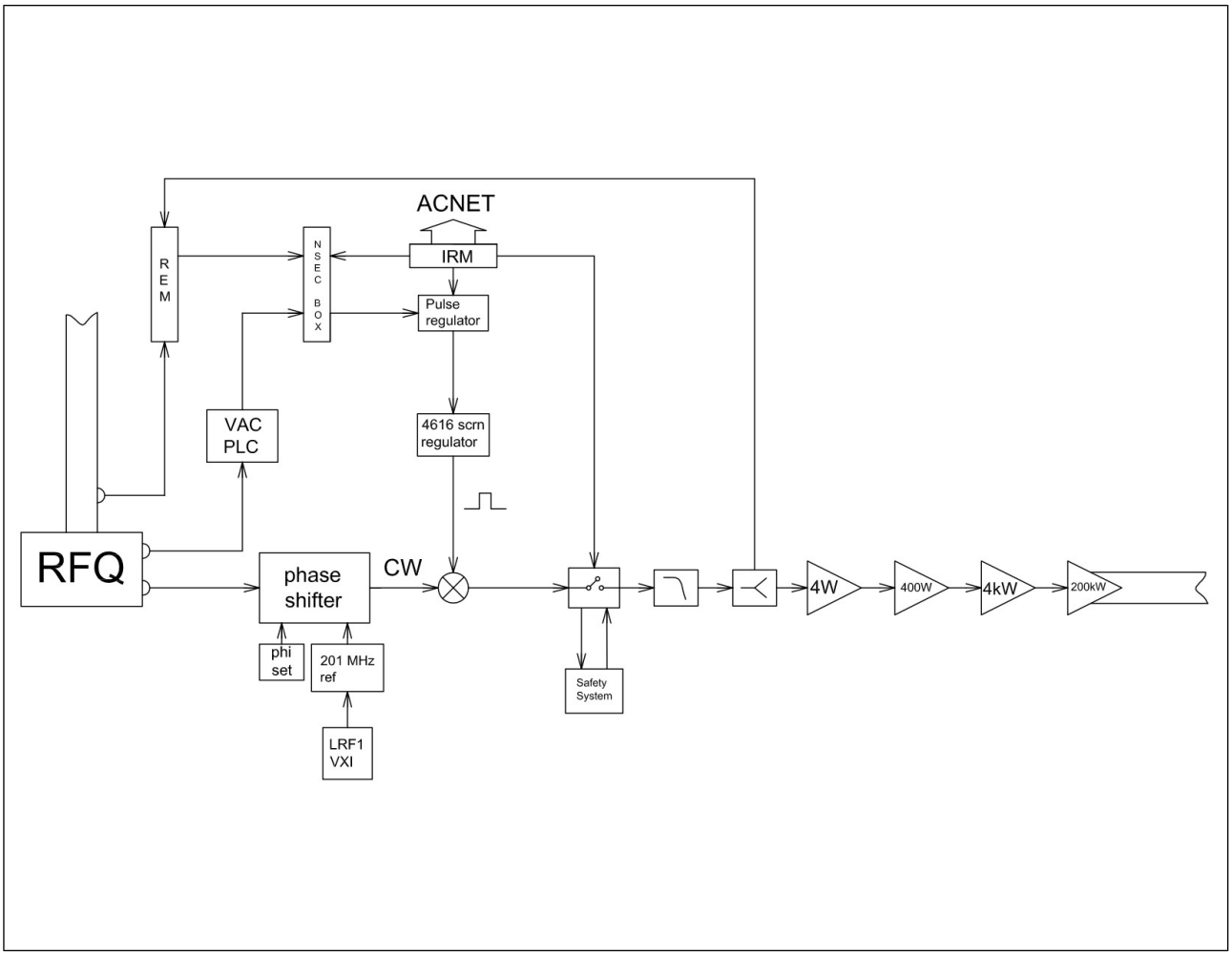

Figure 5.2: *The block diagram of the RFQ magnet and driver station hardware protection scheme.*

5.3.2.b. *Driver PA*

The components inside the driver cabinet proper are interlocked via ladder logic relays. The associated trip conditions will open/close the appropriate relays and return the system state to that point in the ladder logic. As an example, the air cooling and water cooling switches if closed will return the system state to the beginning of the turn-on sequence disabling the appropriate bias and filament PS's. Anode or screen overload trip conditions will disable the appropriate voltage levels requiring a reset and on before re-establishing the proper HV levels for RF output. The associated ON, OFF, and Reset commands are given via a hardware control chassis located in the driver cabinet.

The 4616 driver PA is protected from high levels of reflected power via the reflected energy module and the nano second fault box. The reflected energy module is a window comparator used to determine the associated trip level for the reflected power and the nano second fault box contains the appropriate inputs and logic gates to disable the RF drive signal in a timely fashion. It should be noted that the appropriate tube bias and screen PS regulation pulses shall be disabled with the RF drive signal.

5.3.2.c. *RFQ*

The RFQ cavity will be protected from excessive vacuum levels via PLC hardware which

monitors the cavity vacuum. The response of the driver station due to excessive RFQ cavity vacuum pressure will be to disable the RF drive signal via the nano second fault box until an appropriate level of cavity vacuum has been reached.

The driver station PA will also be used as a secondary failure measure for personnel protection downstream of the RFQ. The fail safe coaxial RF switch at the input to the amplifier chain requires +28 V as supplied by the Rad Safety System in order to pass RF. As such if the primary radiation safety device fails the driver station RF drive signal will be disabled.

5.3.2.d. *Summary*

The ACNET Controls system is primarily used to monitor analog signals and indicate the state of the RFQ driver PA system via digital status devices. The protection of hardware components is provided via sequential ladder logic relays internal to the driver PA cabinet and external modules composed of discrete logic gates.

5.4. Critical Devices

The the Critical Devices and Fail Mode Devices for Linac will be implemented after the RFQ installation. Figure 5.3 shows the critical and fail mode devices and what status that the safety system needs. Both CD1 (Ion Source Extractor Power Supply AC contactor) and CD2 (low level RF amplifier's DC power supply) are permitted when the Linac area is ready for beam. The Fail Mode Device (vacuum gate valve just upstream of the RFQ) is always permitted unless CD1 or CD2 fails to turn off when required.

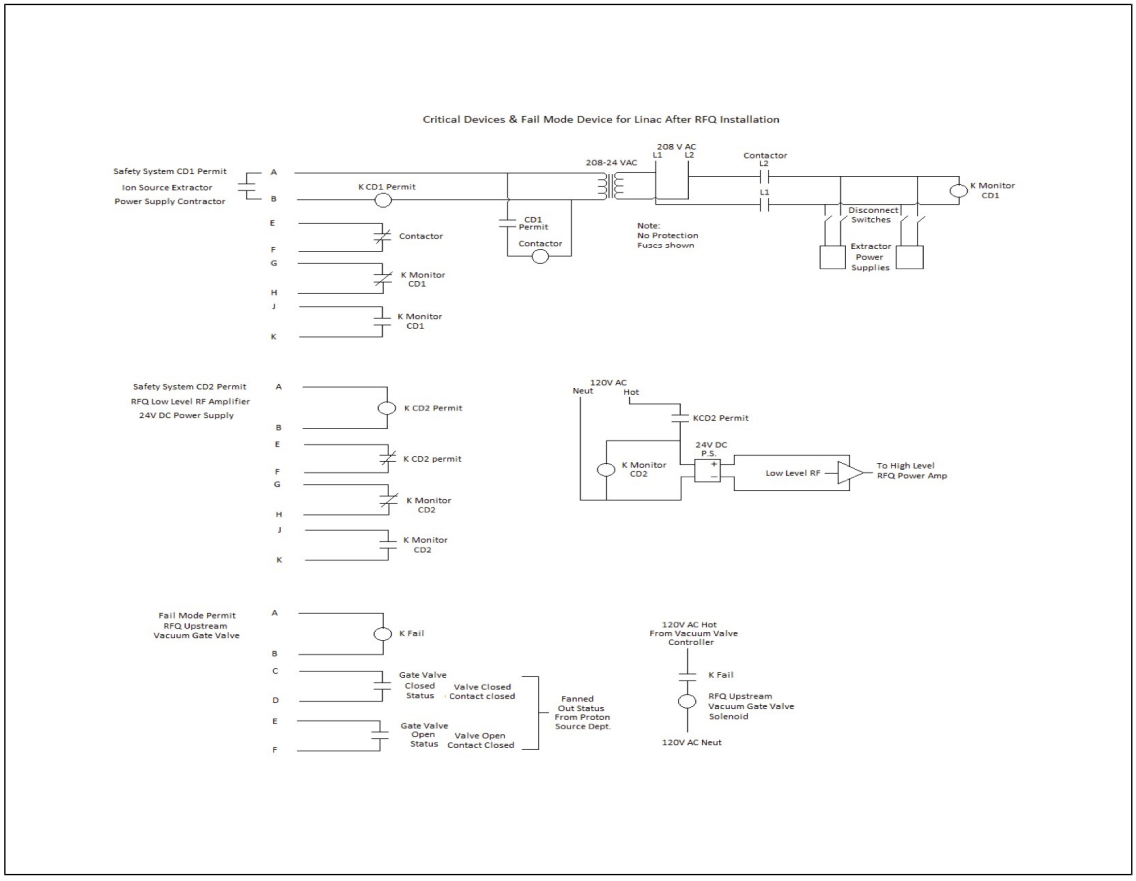

Figure 5.3: *The critical devices.*

6. Vacuum (Deprecated)

The Injector will operate in the high vacuum region and will be achieved primarily with the use of turbo-molecular pumps. The majority of the gas load comes from the hydrogen introduced at the source. See Figure 6.1 for the proposed vacuum system layout. The differential pumping profile is accomplished by sizing the pumps appropriately and taking advantage of different sized apertures and orifices between sections to remove the H_2 gas load and is described in Figure 6.2. Scroll pumps were chosen as the backing pumps for their dry pumping technology that prevents oil back streaming into the system.

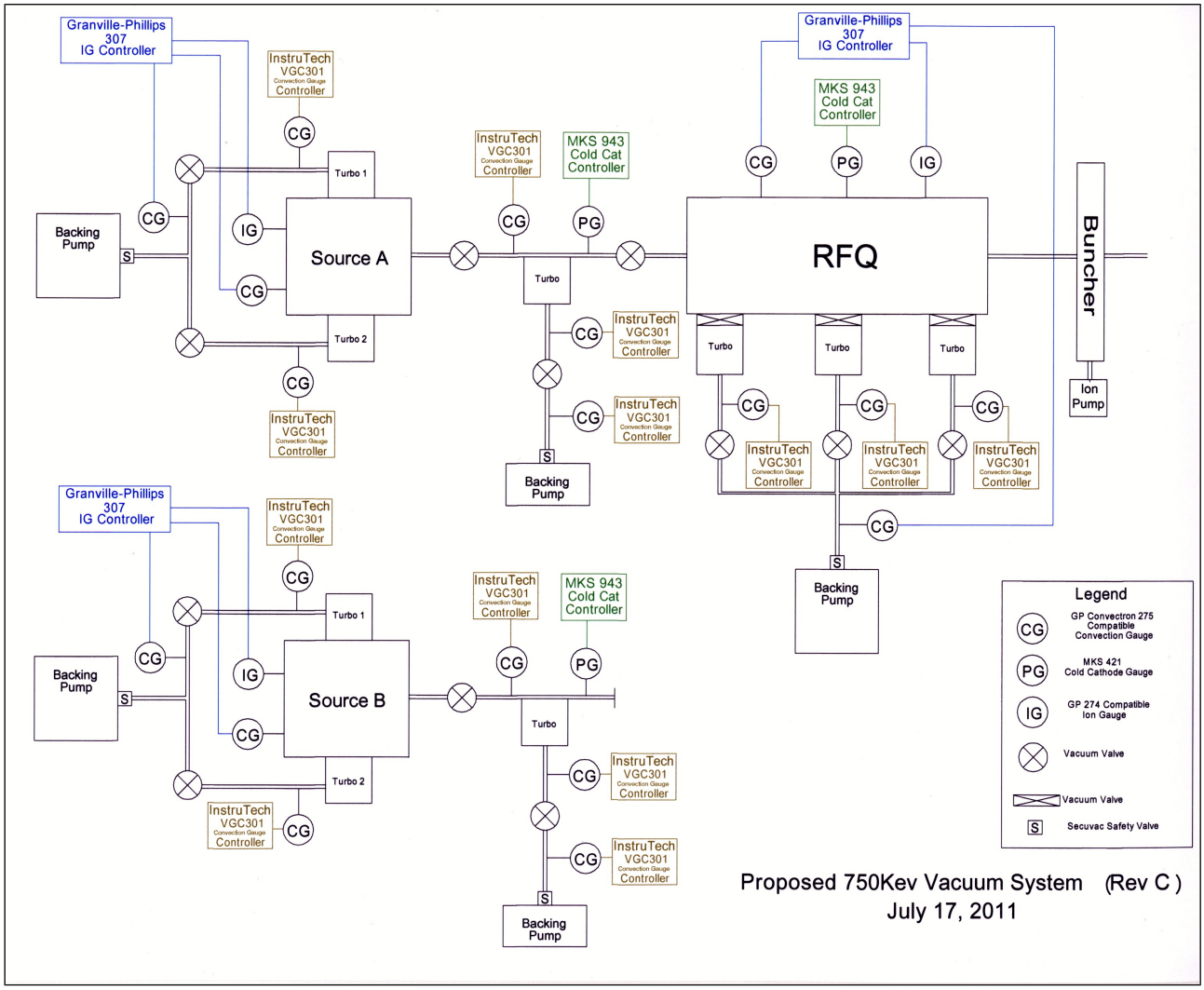

Figure 6.1: *The vacuum system.*

6.1. Source Vacuum

Each source cube will have two Edwards STP-A1603C turbo-molecular magnetically levitated pumps. These pumps were chosen due to their high pumping capacity for the 10" inlet flange diameter and maintenance free feature. The H_2 pumping speed for each of these pumps is 1200 L/s, for a combined H_2 pumping speed of 2400 L/s. The desired source cube vacuum level is approximately 2×10^{-5} Torr. The required pumping speeds were determined using the gas loads

calculated from the current operating sources at FNAL and BNL.

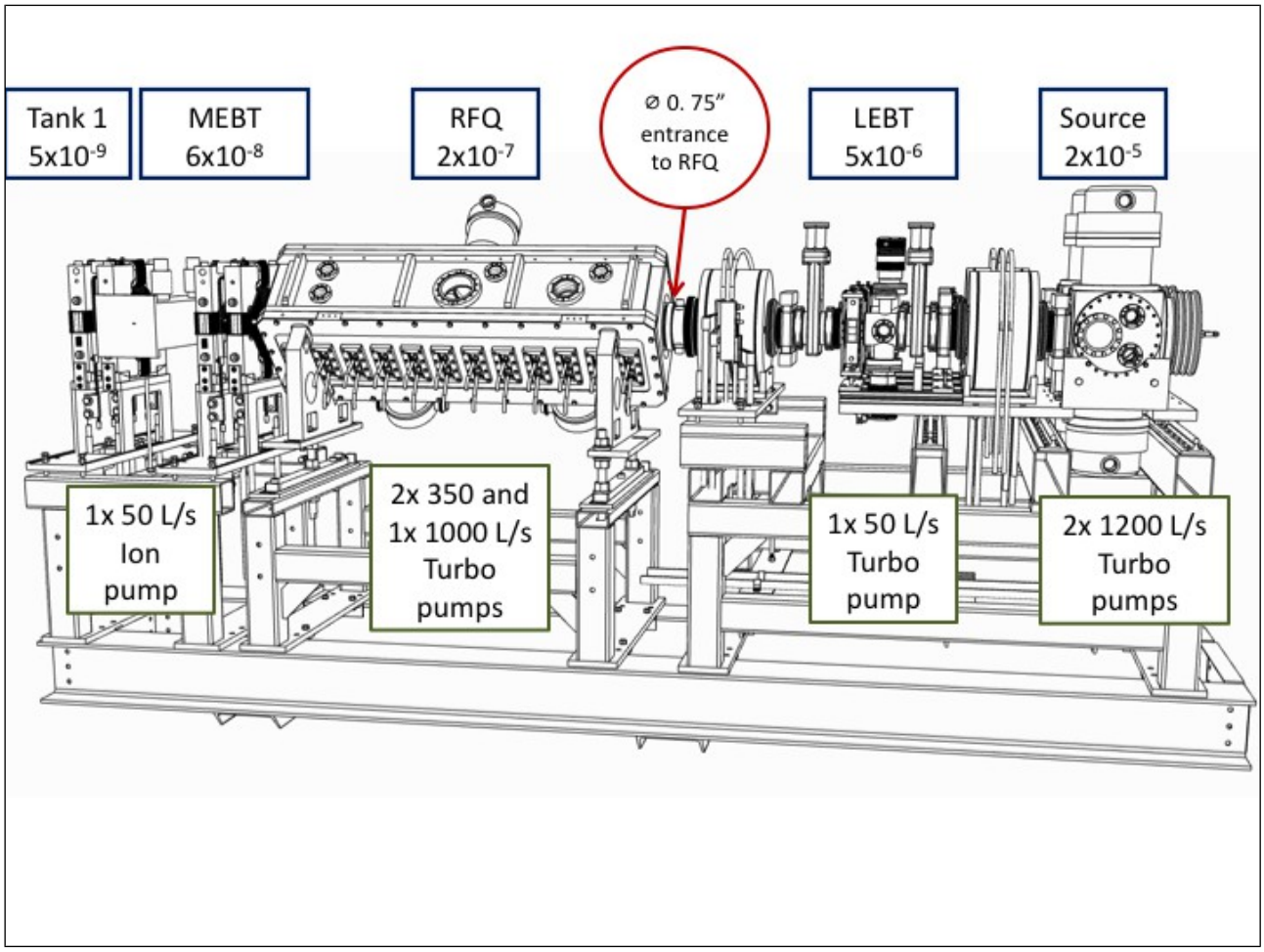

Figure 6.2: *The vacuum levels from the source to DTL 1.*

Each source cube will be fitted with a convection gauge tube and an ion gauge tube. Each turbo exhaust will use a convection gauge tube to monitor the vacuum level before connection to a common backing manifold. The common vacuum manifold will join the turbo exhausts via isolation valves for final backing vacuum. The manifold vacuum pressure will also be monitored by a convection gauge tube.LEBT Vacuum

The dual source design of this injector requires that each source cube have its own upstream LEBT section attached to the source. A smaller turbo pump was chosen for this location with a pumping speed of approximately 50 L/s for H_2. The desired vacuum level for the LEBT section is 5×10^{-6} Torr. This pump is positioned slightly downstream of the Xe gas inlet and will be removing Xe as well as H_2 from the source.

6.1.1. LEBT vacuum gauges

All vacuum gauge tube analog readings will be supplied to the PLC. A set point relay contact from each vacuum gauge controller will also be supplied to the PLC as an additional input for use in monitoring and development of logic for the desired system response. All vacuum valves will be interlocked and offer open/closed states available via the PLC.

6.1.2. LEBT vacuum valves

High vacuum gate valves from MDC will provide isolation of a source from its upstream LEBT section. The downstream LEBT section will contain a second beam valve of the same type.[7] If there is a power loss, these valves will close. Once closed, a lock-in cam-over feature of the valve prevents the valve from floating open should there be a loss of pneumatic drive pressure.

6.2. RFQ Vacuum

The RFQ will have one Oerlikon TurboVac 1000 and two Oerlikon TurboVac 361 turbo pumps. This will provide 1200 liters per second total H_2 pumping speed. The desired RFQ vacuum level is 5×10^{-8} to 1×10^{-7} Torr. The TurboVac 1000 was chosen because these pumps are already in use at the Preacc. The two smaller RFQ vacuum ports required use of two smaller pumps. The TurboVac 361 model was chosen because it may be serviced in house by Mechanical Support personnel who are also equipped to rebuild these pumps. Gate valves will isolate each pump from the RFQ to prevent letting up DTL 1 and 2 when the pumps are removed for maintenance.

6.3. MEBT Vacuum

The MEBT will use a 55 L/s ion pump mounted on the buncher as the final vacuum pump in the injector design. The desired MEBT vacuum is 5×10^{-8} Torr prior to entering DTL 1.

6.4. Vacuum Controls

Figure 6.3 shows the planned arrangement for the vacuum electronics rack layout. An 8" end rack will house the vacuum PLC. It will also provide space for all I/O in and out of the vacuum racks, and mounting space for other needs.n The main rack will be arranged so that controls and gauging for each portion of the vacuum system are conveniently located for ease of local operation.

The existing H- and I- Granville Phillips 307 ion and convection gauge controllers will be re-used. Additional convection gauge monitoring will be provided by Instrutech VGC301 convection gauge controllers, which are completely compatibility with Granville Phillips style tubes. These tubes allow monitoring over the range of 1×10^{-4} Torr to atmosphere. The two LEBT sections and the RFQ will also host an MKS 943 cold cathode style vacuum controller and MKS 421 inverted magnetron gauge tube that provides monitoring over the range 1×10^{-10} to 1×10^{-2} Torr.

---

7 This downstream valve will also serve as a critical device, and will be fitted with additional open/closed status switches to satisfy interlock requirements. Accumulator bottles with one-way valves may be used as a backup to provide positive closing capability should there be a loss of pneumatic drive pressure.

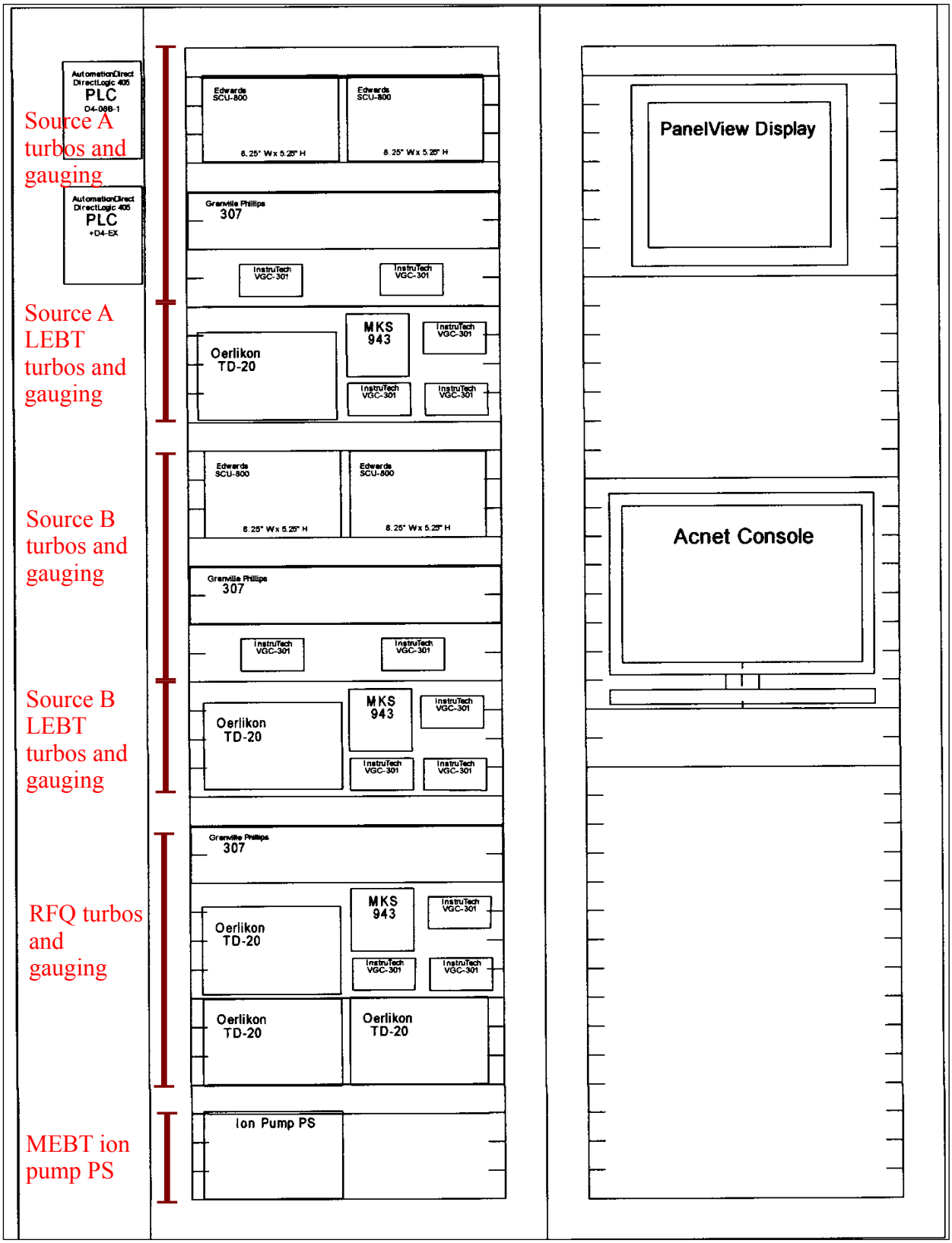

Figure 6.3: *Vacuum controls rack.*

7. Performance Goals

The goal is to have an injector that performs as well as the Cockcroft-Walton system. This means that:

1. The reliability and uptime of the proposed injector must be at least 97%.
2. The beam current at the end of the DTL 2 must be at least 37.5 mA. See Figure 7.1.

Working backwards from 37.5 mA, Table 7.2 shows the minimum beam current requirements at each stage of the proposed injector that will give the same beam current at the end of DTL 2 with the Cockcroft-Walton. Note: The current at the end of DTL 2 is used here because the toroid at the end of DTL 1 is broken.

Current (mA)	**ϵ_x (norm., 1σ, π·mm·mrad)**	**ϵ_y (norm., 1σ, π·mm·mrad)**	**Comments**
46	0.86	0.91	Taken on 3 Jun 2009[8]
~32	0.6	0.8	Taken on 06 Feb 2012. See section 4.4.4.a.
~46	0.9	1.0	Taken on 10 May 2012. See section 4.4.4.a.

Table 7.1 *These are the transverse emittances at the start of DTL 1 when the Cockcroft-Walton system is used. The proposed injector must reproduce or improve upon these numbers.*

Location	**Current[9] (mA)**	**% Transmission from previous location**	**Comments**
Output of H- source	65	–	Source can operate up to 100 mA. See ref. [2].
End of LEBT before RFQ	60	92	See section 4.2.1
End of RFQ	47	70	See section 4.3.5.b
End of DTL 2	37.5	80 – 90	Required.

Table 7.2 *These are minimum beam current requirements for the proposed H- injector which matches the present slit source+Cockcroft-Walton injector.*

8 The way the emittance values were calculated prior to 2012 is incorrect. This is quoted here for historical purposes only. The correct emittance values are in the next two rows.

9 The definition of beam current is discussed in section 7.1.

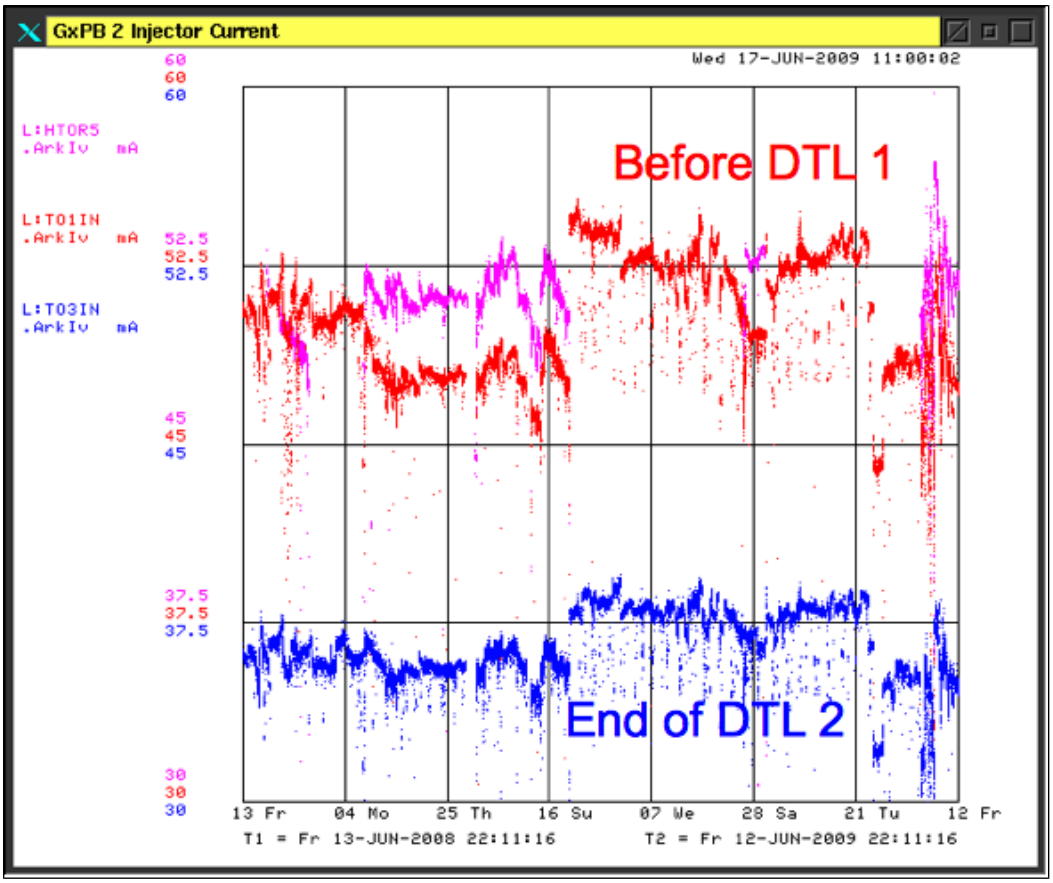

Figure 7.1: *This figure shows the performance of the Cockcroft-Walton injector for 2009. Maximum current at the end of the second DTL is about 37.5mA. The loss of H- by going through both DTLs is about 30% because the beam in the MEBT is essentially DC and the tails are not captured in the DTL.*

7.1. Beam Current Definitions

At the output of the H- source, the beam current I_s is defined to be

$$I_s = Q_s / T_s \tag{32}$$

where Q_s is the total charge at the output of the H- source and $T_s \approx 80\ \mu s$ is the length of the pulse.

In the simulations which use either PARMTEQM[11] or PARMILA [24], the beam current I_{beam} is defined to be:

$$I_{beam} = qNf_{bunch} \tag{33}$$

where q is the charge per particle, N is the number of H- ions, f_{bunch} is the bunch frequency. In the simulations, it is assumed that $f_{bunch} = f_{RF} = 201.25$ MHz because all the adjacent buckets are filled in the ~80 μs macro pulse. This means that if $I_s = I_{beam}$ there are no losses because a uniformly distributed Q_s decreases linearly as the size of the macro pulse is linearly shrunk from T_s to $1/f_{RF}$.

8. Cost Estimate

Initial cost estimates for the RFQ injector project given in FY2009 was approximately $880,000. This cost estimate was a preliminary number based upon similar work done at BNL and FNAL. The estimate did not use escalated dollars, contingency or labor and was unburdened. A revised M&S estimate given in the second quarter of FY10, after an additional engineering review of the project, was $897,000. The latest M&S numbers, given below, are from conception to FY11 third quarter spending. The dollar amounts given are also unburdened. To date the obligated project cost is $891,000. The pie chart shown in Figure 8.1 shows the M&S cost breakdown as a function of task codes.

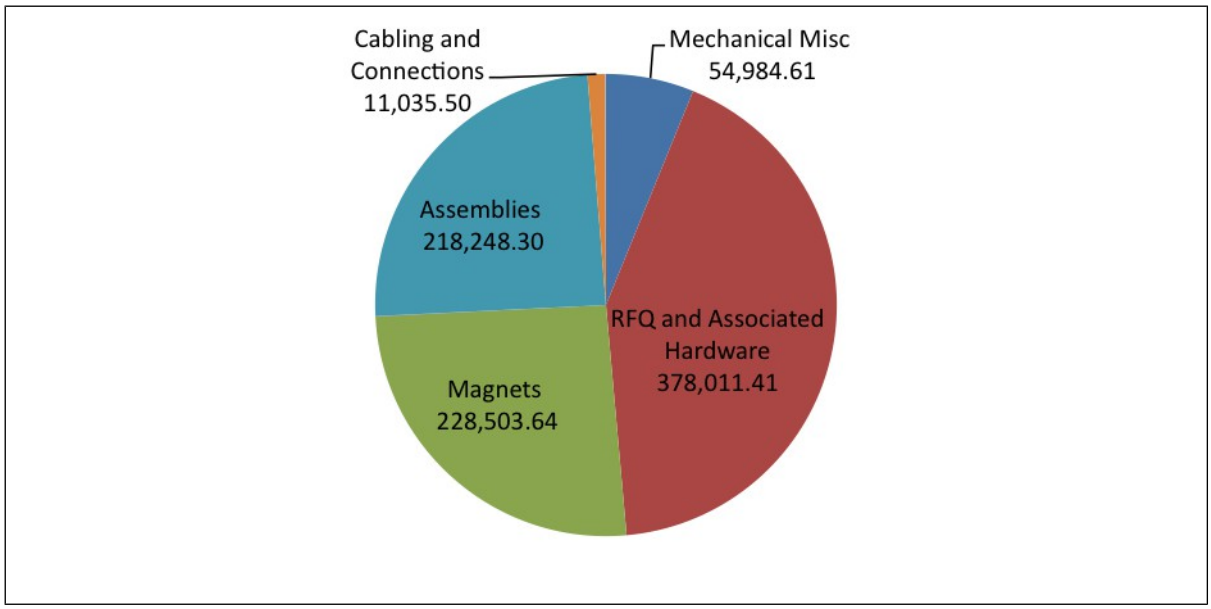

Figure 8.1: *Injector M&S (Q3 FY11)*

The remaining M&S required to complete the project is estimated to be at $87,000. The majority of this M&S will be spent on a platform to be built inside the I- pit area. The platform will be built by outside contractors with an expected cost of $60,000. The remaining $27,000 is allocated for heliax cable and tuner hardware for the RFQ. The final M&S cost will total ~$978,000. The difference of about $87,000 is largely due to the purchase of spare magnets:

1. one set of quadrupole magnets (built in pairs)
2. one solenoid
3. one set of corrector trim magnets (vertical and horizontal window frame dipole)

The cost of the RFQ project was initially estimated accurately and will be completed with an expected overrun of less than 10%. The project had areas that came in under budget (for example, the RFQ) and some were underestimated. The notable cost over-runs were vacuum hardware and power supply hardware. The initial cost estimates assumed a re-use of existing vacuum pumps and controllers. The equipment was later determined not to be reliable enough to install into a new system expected to run for 15+ years.

The labor for the RFQ injector project was not estimated in the original project proposal. The labor to date (FY11 third quarter) is shown in Table 8.1

Long Task Name	INCPTD BUDGET ($)	INCPTD OBL ($)
Engineering and design, mechanical	227,929.25	224,516.76
Simulations and testing	86,008.71	124,543.46
Magnets	5,255.47	4,670.62
Fabrication and assembly	.00	44,043.28
Connections & cabling: mechanical, vacuum, electrical, LCW	.00	20,451.74
Magnets – TD	.00	.00

Table 8.1: *Injector labor cost.*

The final cost of the injector project including labor and M&S is expected to be $1,750,000 unburdened. Labor for commissioning is also not included in this document although effort for planning is this area has been included.

9. Pictures of the installed RFQ injector

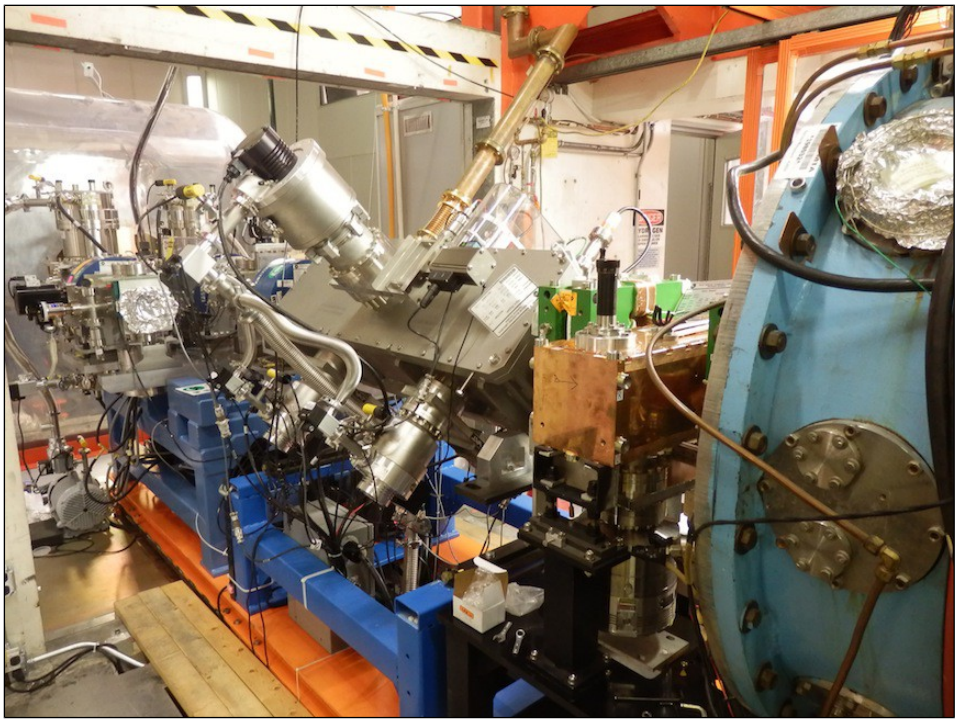

Figure 9.1: *Looking upstream from Tank 1 to the source.*

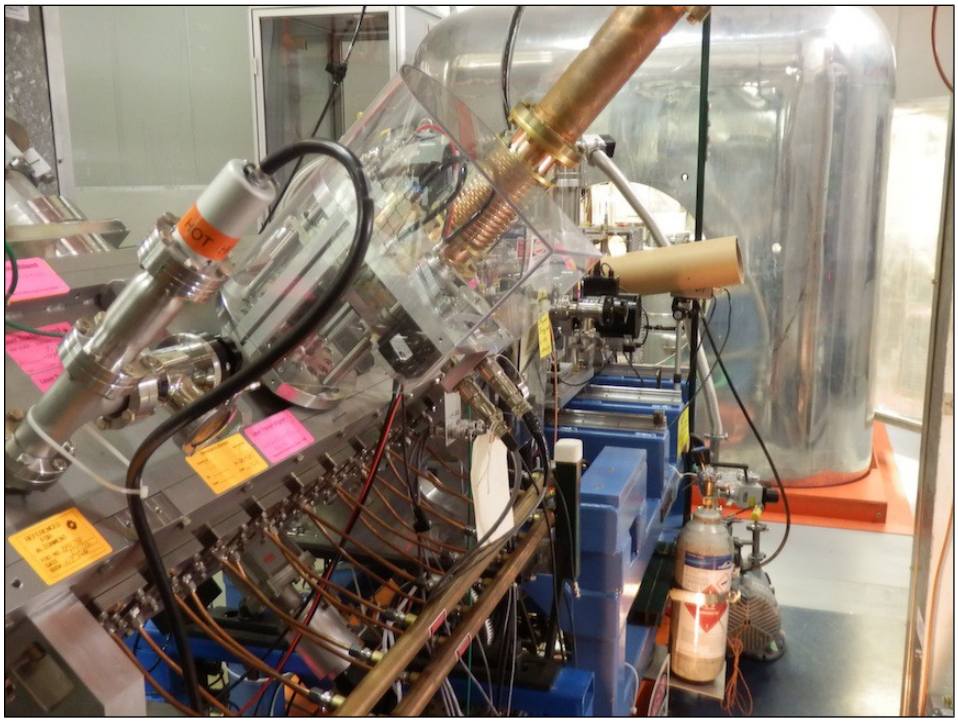

Figure 9.2: *Looking upstream from Tank 1 to source.*

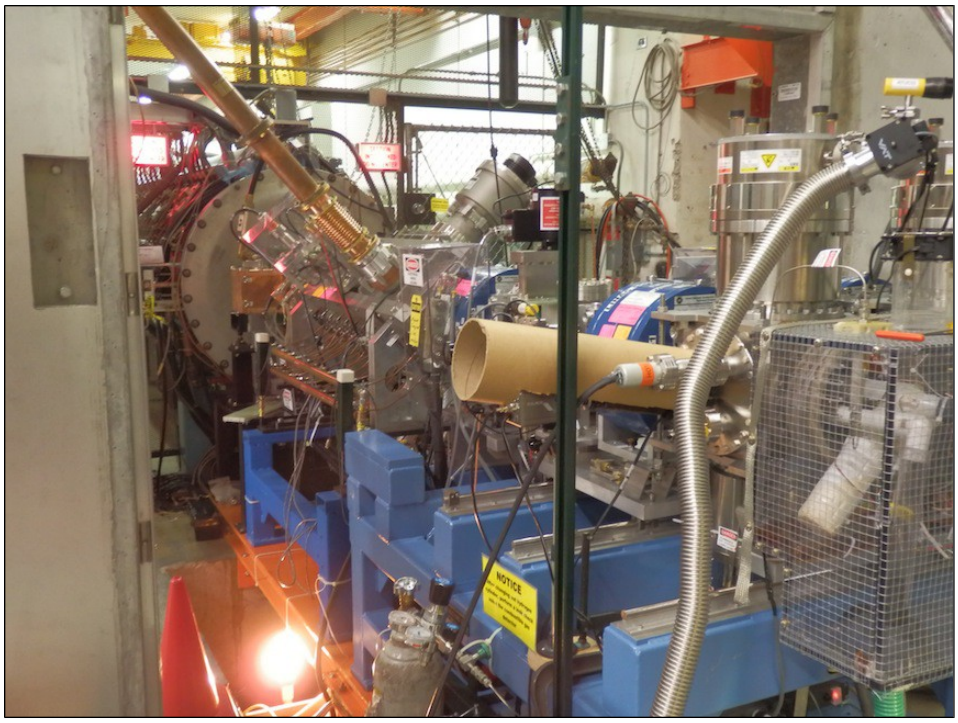

Figure 9.3: *Looking downstream towards Tank 1.*

Figure 9.4: Looking downstream towards Tank 1.

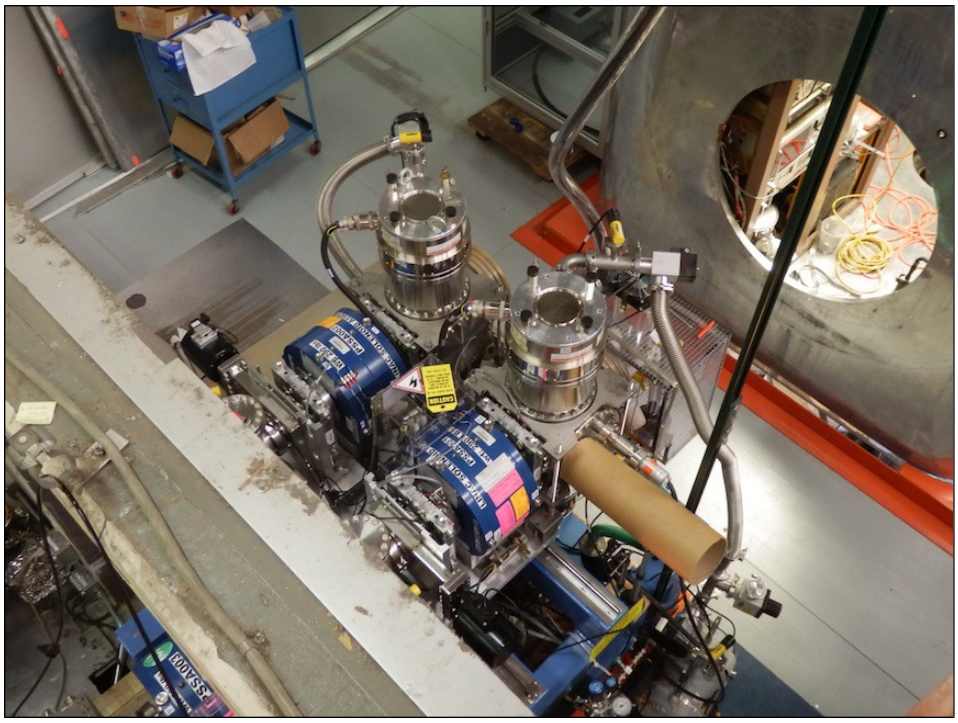

Figure 9.5: *Top view of the twin H- sources.*

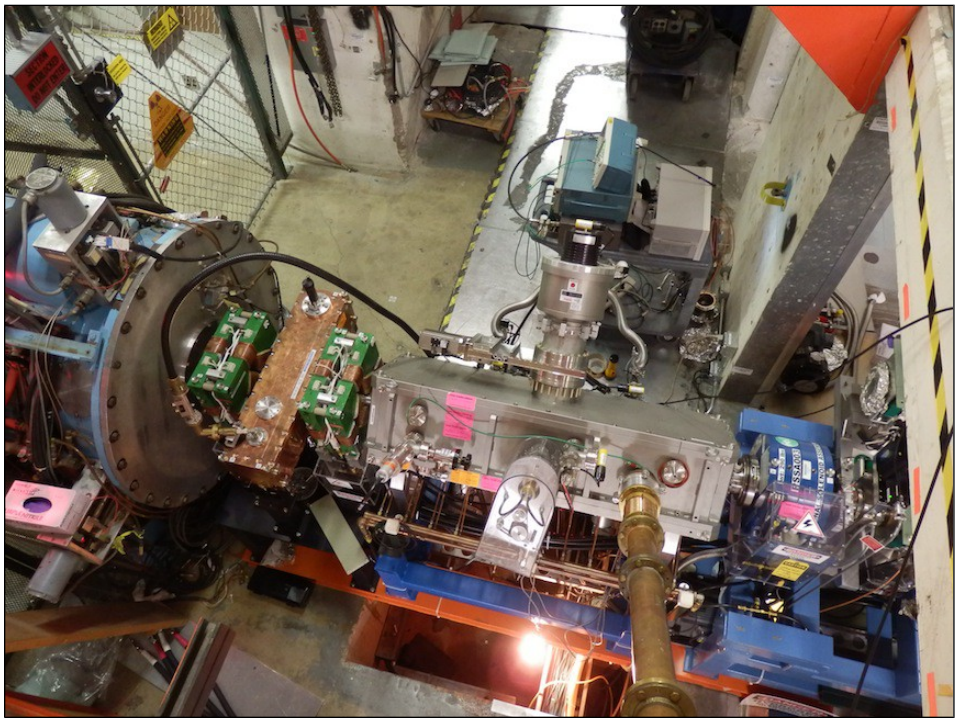

Figure 9.6: *Top view of the RFQ and MEBT.*

10. Conclusion

The injector is over 40 years old. The technology and knowledge required to maintain the systems is being lost either to obsolescence or retirement. The cost of actual parts is relatively small compared to other linac systems but when the cost of downtime and manpower is included the new RFQ injector system will quickly pay for itself. The cost of approximately 40 hours of downtime/year and the labor required to keep the system not only running but up to the required operational beam parameters is estimated to be at $400k/year on average.

This plan will use many of the parts which are already on hand and mature technologies which the lab is familiar with, for example, the H- magnetron source. A new RFQ will need to be built, but its specifications are well within the present technical expertise of industry and should present very little technical risk. Therefore, it is expected that the new injector will work as reliably as the BNL injector.

This plan also assumes that the amount of manpower to maintain the injector will be reduced from the present two senior techs, one junior tech, one tech assistant and one operational specialist mentioned in subsection 3.3 The time and effort required to operate and tune the present H- sources, Linac and the Booster to an acceptable level is difficult to assign a cost value. But this cost is non-negligible because the present system has and will continue to be a major source of instability and downtime. This plan presents a design that will not only pay for itself in a matter of two to three years but will also improve the beam quality for all the downstream users. The implementation of the new system is estimated to take about one year. Installation is expected to occur in the spring of 2012.

11. Acknowledgments

The authors would like to thank:

1. The BNL linac group: J. Alessi, D. Raparia and V. Lodestro who graciously hosted three of the authors (D. Bollinger, C. Schmidt and C.Y. Tan) in the fall of 2008 for a tour of the BNL injector and who gave them much of the information used in this plan.
2. D. Raparia (BNL) who generously supplied the BNL LEBT and MEBT design which served as the base line design in this plan.
3. M. Okamura (BNL) who designed the BNL buncher and fixed the transit time problem and supplied us with the thin quadrupole information used in the BNL MEBT.
4. J.S. Schmidt, B. Koubek and A. Schempp (U. Frankfurt) who worked diligently on tuning and fixing the RFQ.
5. M. Popovic (FNAL) who supplied both the present DTL PARMTEQM model used in the simulations and the data for the cost estimate.
6. W.M. Tam (FNAL) for calculating the required angle for the magnetic kicker in the first version of the plan.
7. B.J. Ogert, J.C. Briney and J.D. Kubinski for dis/assembling the entire RFQ injector many times, installation of instrumentation and vacuum work.
8. K.K. Koch and A.J. Feld for H- source work.

9. G.R. Tassotto and instrumentation technicians.
10. O. Babatunde, C.J. Wilson, and the survey group.

11.1. People

Figure 11.1: *The RFQ injector team. From left to right: B. Schupbach, K. Koch, A. Feld, C.Y. Tan, D. Bollinger, P. Karns.*

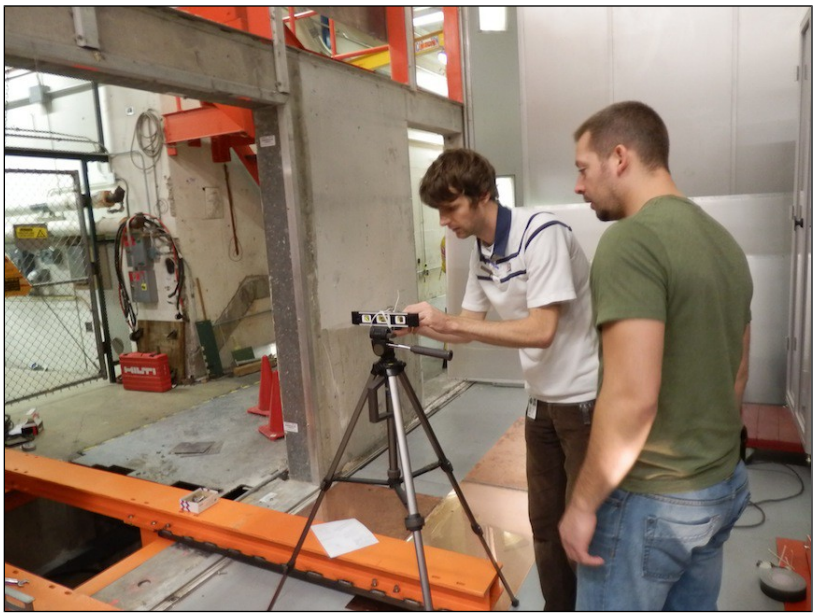

Figure 11.2: *From left to right: K. Duel and A. Feld.*

Figure 11.3: *Mechanical technicians. From left to right: J. Briney, J. Kubinski, B. Ogert.*

Figure 11.4: *A.K. Triplett and J. Larson (to be added)*

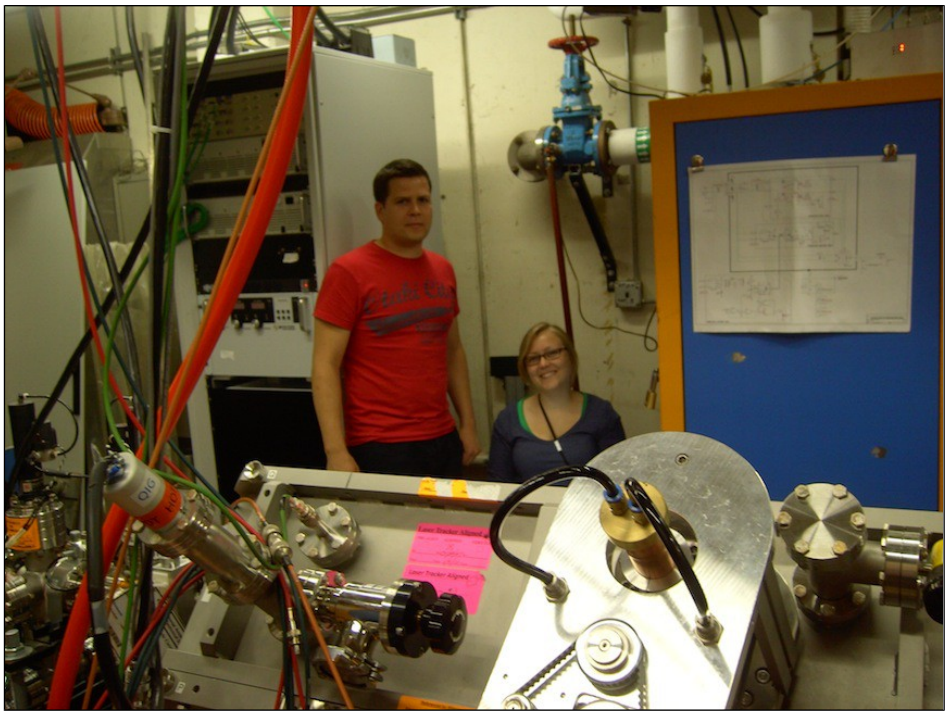

Figure 11.5: *Colleagues from U. Frankfurt. Left to right: B. Koubek and J.S. Schmidt.*

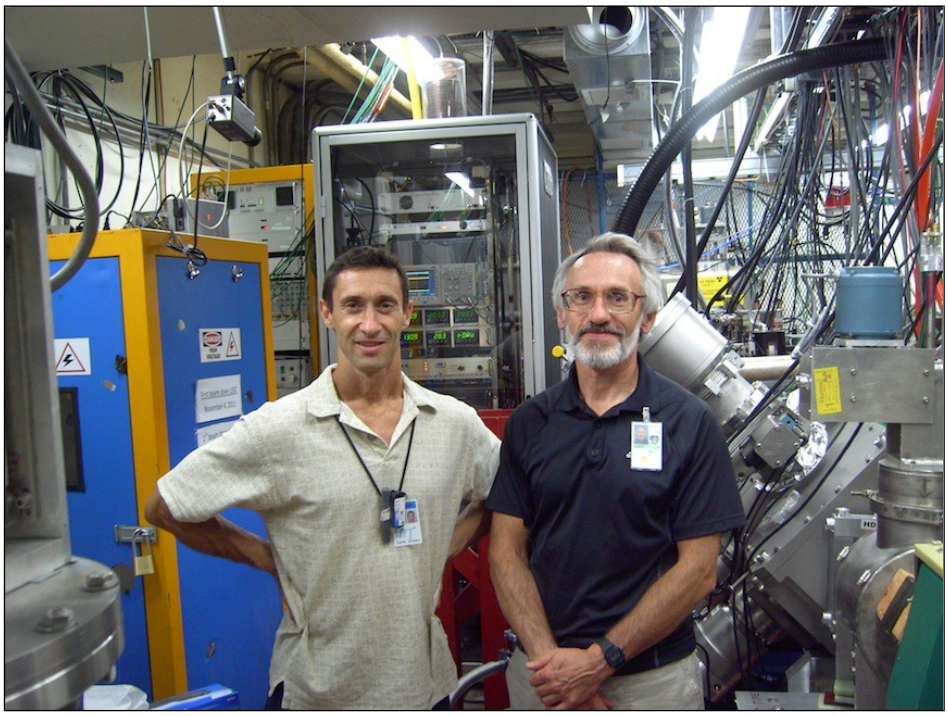

Figure 11.6: *Left to right: B. Pellico (Proton source department head), S. Kurennoy (LANL).*

Plus other photographs to be added!

A. The RFQ.IN4 File

```
run
title
 FNAL, H-, 201.250MHz,i= 60.0mA
trancell 65
linac 1 0.035  201.250  1.00837  1.0
tank 1  0.740 0 0 0 0 0 0 0 0 0 10  0 0 0 0 0 0 0 0 0 0 0 0 0 0
zdata -5    -2.5    0.01    -90 1   0.072
    -1.929  0.356   -90 1   0.072
    -1.286  2.244   -90 1   0.072
    -0.643  5.0 -90 1   0.072
    -0.0001 6.4 -90 1   0.072   4
zdata -5    0   6.8 -90 1   0.072
    1   6.8 -90 1   0.072
    11  8.4 -90 1.03    0.072
    18  10.0    -88 1.075   0.072
    26  11.3    -82 1.16    0.072
    31  11.7    -76 1.24    0.072
    36  11.7    -70 1.3 0.072
    43  11.6    -60 1.39    0.072
    50  11.0    -52 1.48    0.072
    56  10.4    -44     1.58    0.072
    71  9.2 -38 1.76    0.072
    76  8.8 -37 1.8 0.072
    82  8.5 -36.    1.82    0.072
    91  8.3 -36.    1.84    0.072
    110 8.0 -36.    1.92    0.072
    112 8.0 -36.    1.92    0.072   -1
rfqout 0  4 1
rfqout 05
start  1
stop  -1
elimit 0.7281
input -6 -10000  1.5  5.1  0.021  1.5 5.1  0.021 180. 0.
output 3  1 10 00  00 01 1
output 1 -1 10 00  00 01 1
output 2 -1 00 00  00 00 2 300   1
output 2 -1 00 00  00 01 5 300   5
output 4  1 10 05 .01  1 1
optcon  110  6  0.4  1  0.1  2  60  0  0.1  2
```

```
scheff   60.0  0.0250 -0.0321 20 40 5 10  4
;exitffl 1.0
tilt 0.0
vfac 1.1
mpoles 1.0 1.0 1.0 1.0     1.0 1.0 1.0 1.0
image 1.0 1.0
begin
end

15.8    9.4 -89.    1.052   0.072
22.8    10.7    -85 1.114   0.072

64.7    9.8 -39 1.683   0.072
86  8.4 -34.5   1.83    0.072

trancell 65
```

B. The BNL Injector

The BNL injector will be discussed in the following two subsections. The reason for this discussion is because the BNL injector was upgraded from a nearly identical FNAL style slit source and Cockcroft-Walton in the fall of 1988 to a round source+RFQ. The motivation for doing the replacement at BNL came from the expectation of "improved reliability, simpler maintenance, and the added convenience of having the ion source located at nearly ground potential" [25]. These are the same technical reasons for upgrading the FNAL Cockcroft-Walton system to an RFQ system.

The round source+RFQ which has been operational at BNL since then, has operating parameters which are nearly identical to the FNAL requirements and so a direct comparison between the two can be made. The operational experience of the BNL round source+RFQ has been very positive and thus an upgrade of the FNAL injector to this configuration should carry very little technical risk.

B.1 The BNL Injector (1982-1989)

The BNL injector switched to H- operation in 1982 [2]. The 750 keV injector is nearly identical to the present FNAL 750 keV injector except that it has only one slit source+Cockcroft-Walton while FNAL has two slit source+Cockcroft-Waltons. The injector typically runs at a repetition rate of 6.6-7.5 Hz with a pulse width of about 500 μs. The current at the output of the Cockcroft-Walton is about 40-50 mA [26]. The beam is then accelerated and either injected into the Booster or switched into a second beam line for isotope production.

B.2 The BNL Injector (1989-present)

BNL built a round source+RFQ injector which replaced the one slit source+Cockcroft-Walton in 1989. The typical running parameters of the round source are shown in Table B.1. This can be compared to the typical running parameters of the slit source shown in Table 3.3 and it is clear that the BNL round source is operating at about 25% lower power than the FNAL slit source. When operating at this power, the single BNL H- source has been "very reliable, operating continuously for ~6 months, with essentially no parameter adjustments required once the source is stabilized." [2].

There has been a number of reconfigurations of the LEBT and MEBT at BNL. The present configuration [3] is shown in Figure B.1. The length of the LEBT for the unpolarized, high intensity H- source is about 4 m because it is constrained by the position of the polarized H- source. In order to get maximum transmission of the H- beam from the source to the RFQ, Xe gas focusing must be employed. There is a 30% improvement of the transmission of H- beam in the LEBT with Xe gas focusing compared to without gas focusing. However, gas focusing does strip the H- beam and causes a loss of 32% of the beam in the LEBT (gas stripping has been discussed in section 4.2.1).

The LEBT transports the H- beam to the RFQ. The RFQ is about 1.5m long and accelerates the 35 keV beam from the source to 750 keV. The RFQ has not had any problems since its installation [27].

The 750 keV beam is transported to the DTL through the MEBT. The length of the MEBT has been shortened to < 75 cm from the previous configuration of about 7 m. See Figure B.2. The new MEBT has greatly reduced the losses (essentially zero), transmission and emittance of the

beam at the end of the DTL. The improvements are about a factor of 2 smaller in emittance in both planes compared to the previous configuration and a transmission efficiency of between 65 – 70% compared to the previous configuration of 50 – 55% [3].

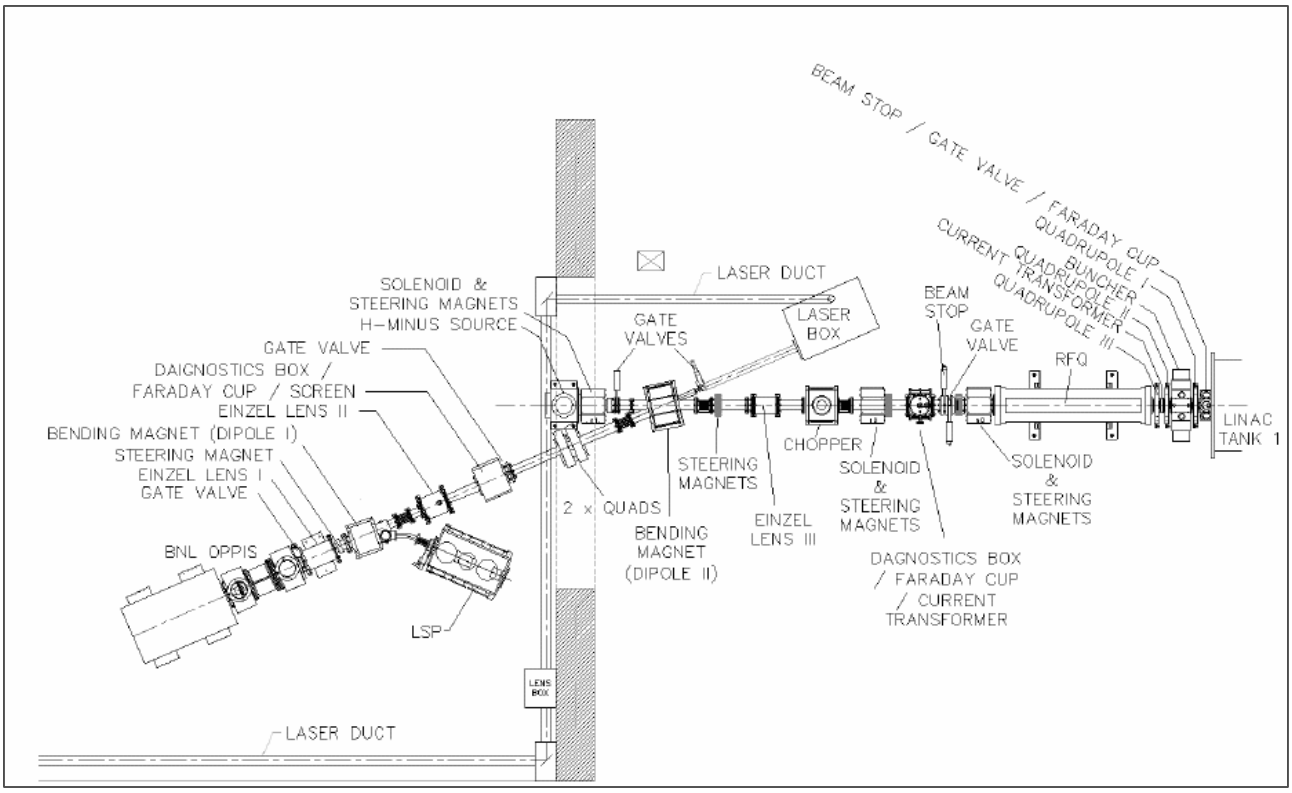

Figure B.1*: This is the BNL injector (as of 2009 [3])which has a H- magnetron source and a polarized H- source. The MEBT, which is after the RFQ and before Linac Tank 1 is only 73.25 cm long, contains 1 buncher, 3 quadrupoles, 2 sets of horizontal and vertical steerers (not shown in drawing), 1 current transformer and 1 beam stop/gate valve/Faraday cup package. Figure B.2 is a picture of the MEBT.(Picture courtesy of D. Raparia)*

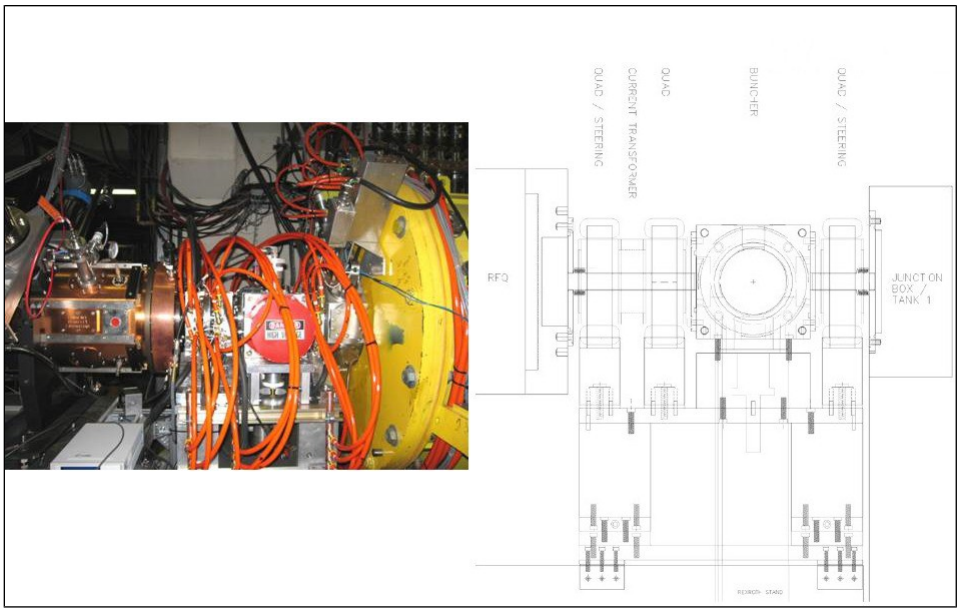

Figure B.2*: This is the BNL MEBT which only occupies 73.25 cm of space between the end of the RFQ and the start of the first DTL.(Pictures courtesy of D. Raparia)*

Parameter	Value	Units
H- current	90 – 100	mA
Current density	1.5	A/cm^2
Extraction voltage	35	kV
Arc voltage	140 – 160	V
Arc current	8 – 18	A
Repetition rate	7.5	Hz
Pulse width	700	μs
Duty factor	0.5	%
rms normalized emittance	~0.4	$\pi \cdot mm \cdot mrad$
Cs consumption	< 0.5	mg/hr
Gas flow	~2	sccm
Average power	$150\,V \times 13\,A \times 5\,Hz \times 600\,\mu s \approx 6$	W

Table B.1 *Some BNL H- round source parameters copied from Ref. [2].*

C. RFQ Problems

The RFQ as delivered on 04 Aug 2011 was plagued with a myriad of problems that had to be fixed in order to meet the FNAL specifications. The problems arranged in order of severity are:

1. **Incorrect energy.** The energy of the RFQ was measured to be at 710 keV rather than 750 keV. The error in energy is the major show stopper for installation. The fix turned out to be rather simple: a copper end plate used for isolating the RFQ RF was removed.
2. **Poor capture efficiency.** The capture efficiency between the beam current measured in the middle of the LEBT to the end of the RFQ is at best 67%. For example, when there is 60 mA of beam current in the LEBT, only ~35 mA at the end of the RFQ at an RFQ power of > 180 kW. In comparison, the BNL injector [4] is able to deliver 45 – 50 mA of beam from 55 mA of LEBT beam.
3. **High power requirements for bunching.** The manufacturer specified that the peak power required for getting to the vane voltage of $V_v = 72$ kV should occur at around 80 – 90 kW (See email message dated 07 Oct 2011 from A. Schempp). However later simulations by J.S. Schmidt showed that the power required is about $V_v^2 / R_p = 72^2 / (36 \times 10^3) = 145$ kW for "thick" rods using the values in Table 4.8. This is in line with the bunching measurements of the beam which showed that bunching is acceptable above 130 kW. In practice, the replacement of "thick" rods with "thin" rods reduced the power required for acceptable bunching by 23% to 100 kW for "thin" rods. See section 4.3.3.
4. **Sensitivity of power coupling.** The s11 of the power port can vary between –16 dB to –30 dB from the placement of the antenna. The coupling is tuned by carefully bending the power antenna either towards or away from the *LC* cell to over-couple it to the *LC* cell. This means that when the RFQ cover is bolted on, the coupling moves towards critical coupling and s11 improves. Unfortunately, the coupler is very sensitive to the physical load that is placed on it because s11 can easily vary by 20 dB because of this load! Care must be taken to not place too much weight on the coupler.
5. **Non straight rods**. The rods bowed out transversely by 0.5 mm at the highest point. This non-straightness turned out to have a negligible effect on the energy of the RFQ, but may have effects on bunching and capture efficiency. Straightening the stands that held the rods fixed the problem.

C.1 Incorrect Energy

This is a major problem that had to be corrected. Energy measurements using the time of flight method and a spectrometer showed that the beam energy is (714 ± 1) keV for a net RF power of $(196 - 17) = 179$ kW. See Figure C.1. Table C.1 summarizes the energy dependence of the beam as function of RF power. In all cases, the energy is always less than the required energy of 750 keV.

C.1.1 Source of the problem

The source of the energy problem was found from a detailed simulation of the RFQ using CST Microwave Studio and Particle Studio. The majority of the simulations were performed by S. Kurennoy (LANL). Supporting simulations were also performed by J.S. Schmidt (U. Frankfurt) and G. Romanov (FNAL). These simulations show that an unexpected bump in the E_z field that has the

wrong phase appearing between the end of the rods and the tank wall when the exit hole is 15 mm in diameter. See Figure C.2. This field reduces the energy of the beam exiting the rods by 20 keV and is the source of the energy problem. Therefore, the solution to the energy problem is to remove the copper end plate. See Figure C.5. Simulations of the E_z field as a function of the exit hole size is shown in Figure C.3. And with the plate removed, the exit energy of the beam calculated with CST Microwave Studio is 753 keV, shown in Figure C.4, and the measured energy is (756.5 ± 0.5) keV shown in Figure C.6.

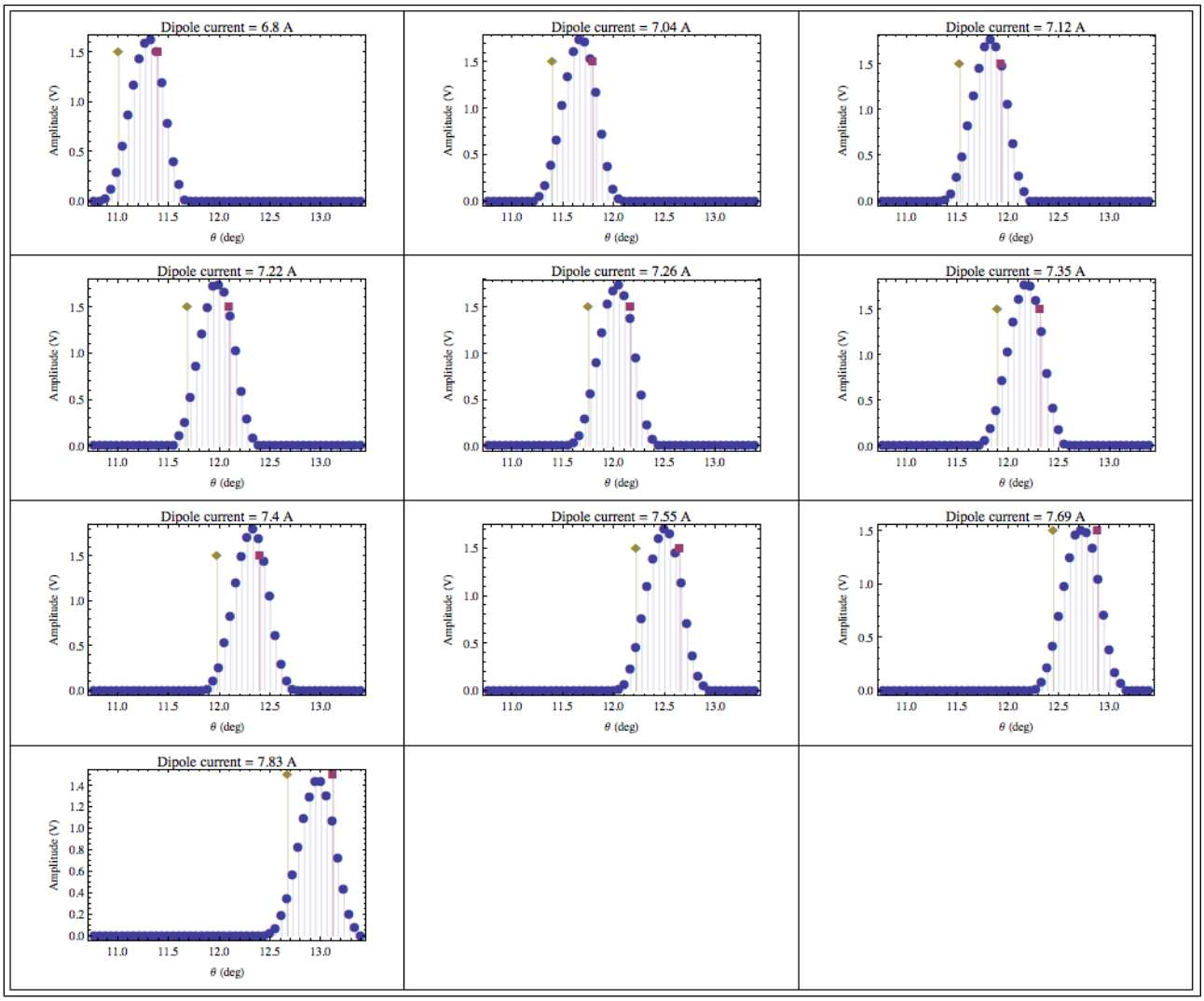

Figure C.1: *The spectrometer data for the case when the RFQ is set to 196 kW (forward power), 17 kW (reflected). As expected, the entire angular distribution moves when the dipole current is changed. The green "♦" indicates the expected deflection angle for 750 keV beam and the red "■" indicates the expected deflection angle for 700 keV beam. The peak of the distribution is clearly above 700 keV and the mean energy is found to be (714 ± 1) keV.*

RFQ Input Power (kW)	RFQ Reflected Power (kW)	Beam Energy (keV)
138	7	683 ± 1
168	12	703 ± 0.6
196	17	715 ± 1

Table C.1: *Summary of the H- energy at the exit of the RFQ as a function of RFQ power. The beam energy error shown here is statistical only. The systematic error is 0.7%.*

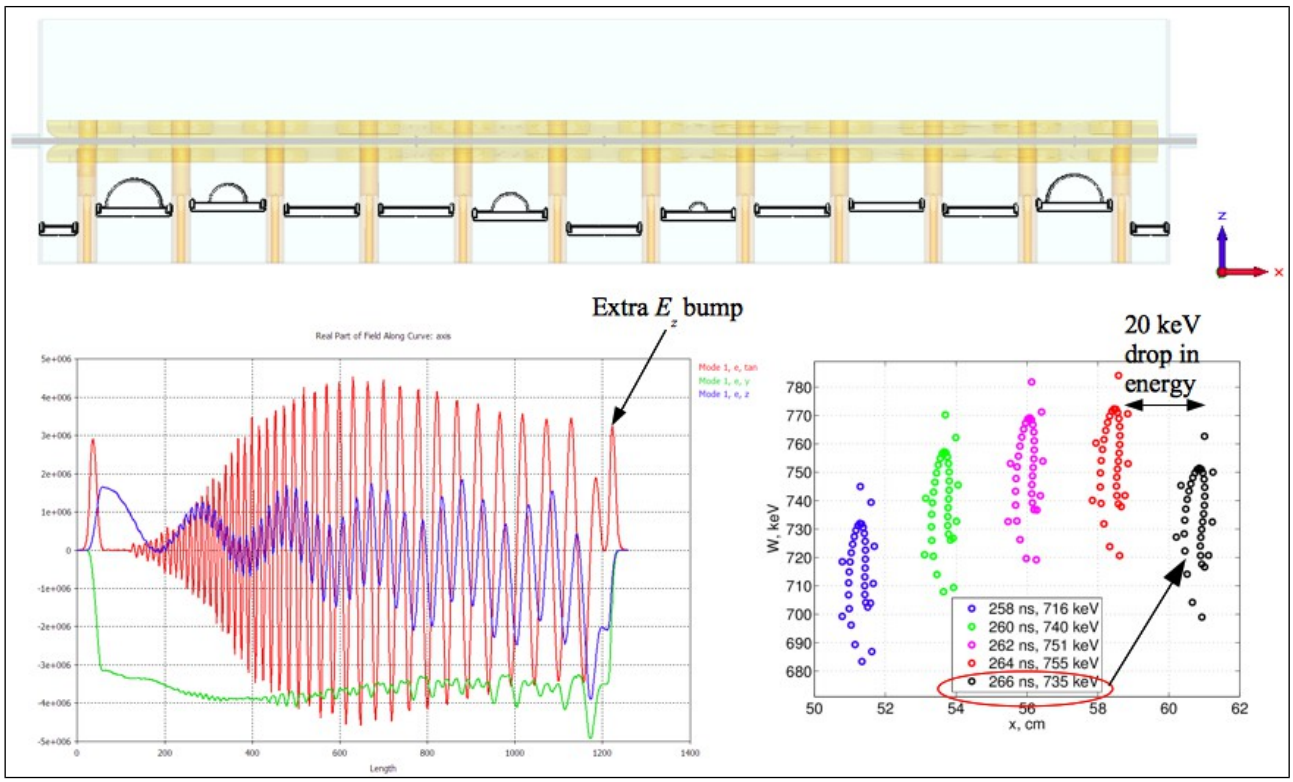

Figure C.2: *Computer simulations of the RFQ with a 15 mm diameter exit hole (Note: the actual hole size is 20 mm). The top picture is the cross section of the model showing the rods and tuning plates. Some of the plates have the addition of half moon inserts.The bottom left picture shows the E-fields along the longitudinal axis of the four rods. The red curve is the E_z field along this axis. The bottom right picture shows the bunched beam near the exit of the RFQ. It is clear from here that there is a 20 keV drop in energy when the beam travels from the end of the rods to the exit. Simulation was performed by S. Kurennoy (LANL).*

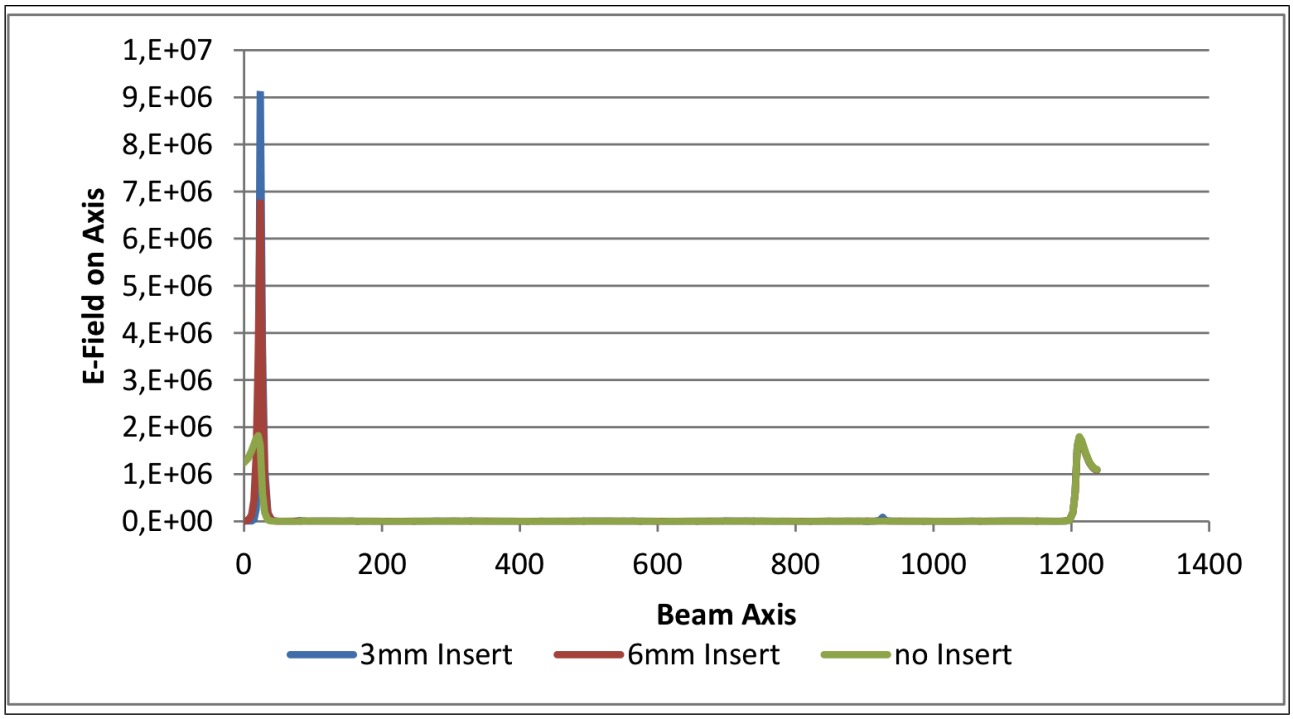

Figure C.3: *This figure shows the effect of hole size and the E-field on axis. The E-field clearly gets smaller as the hole size gets bigger. Simulation was performed by J.S. Schmidt (U. Frankfurt).*

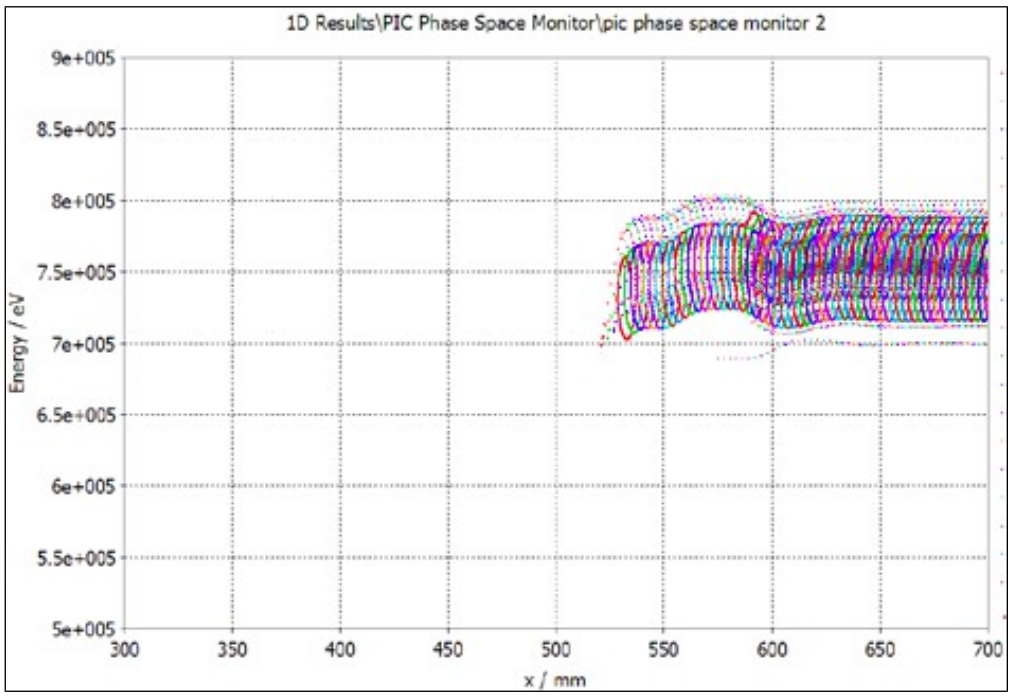

Figure C.4: *This plot shows the phase space evolution for the last few cells and at the exit for the RFQ without the end plate. The mean energy is 753 keV. Simulation was performed by S. Kurennoy (LANL).*

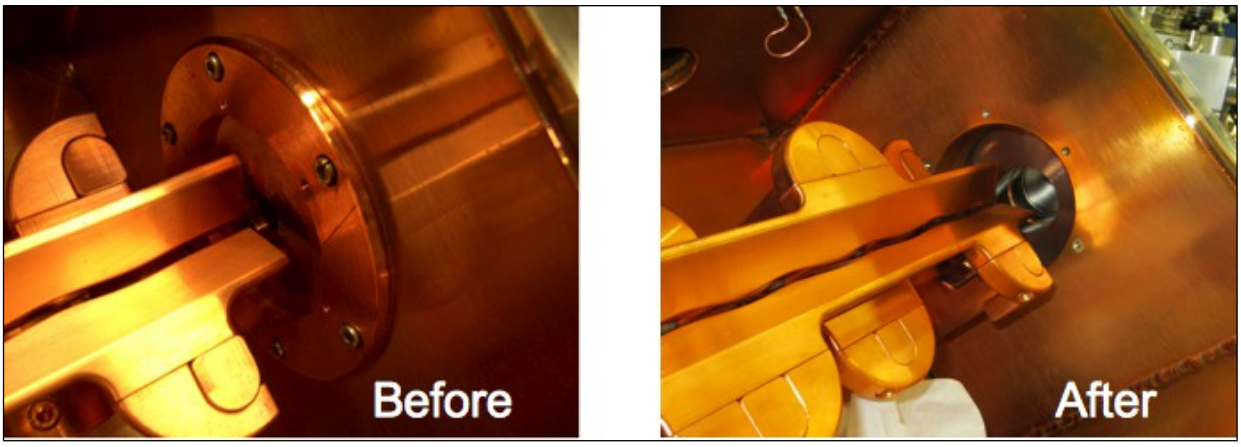

Figure C.5: *The end plate on the downstream end of the RFQ before and after it was removed.*

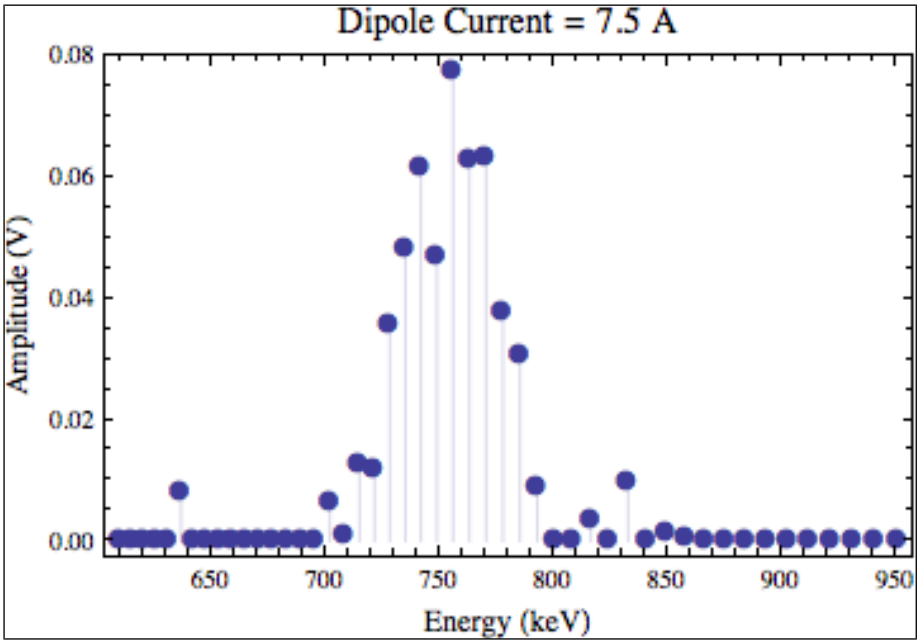

Figure C.6: *With the end plate removed, the energy of the beam is (756.5 ± 0.5) keV.*

C.2 Poor Capture Efficiency and High Power Requirements

The RFQ did not meet the original specifications for capture efficiency of > 90%. The efficiency improved as the power in the RFQ increased. The best efficiency of 67% was attained when the RFQ power was > 180 kW (includes beam power). See Figure C.7. As a comparison, BNL's vane type RFQ has a capture efficiency of > 80% [4]. It is not possible to operate the RFQ with such a high power requirement because the lifetime of the tubes will be greatly lowered.

Another indication that there is a problem is that bunching did not occur until until power into the RFQ is greater than 130 kW. See Figure C.8.

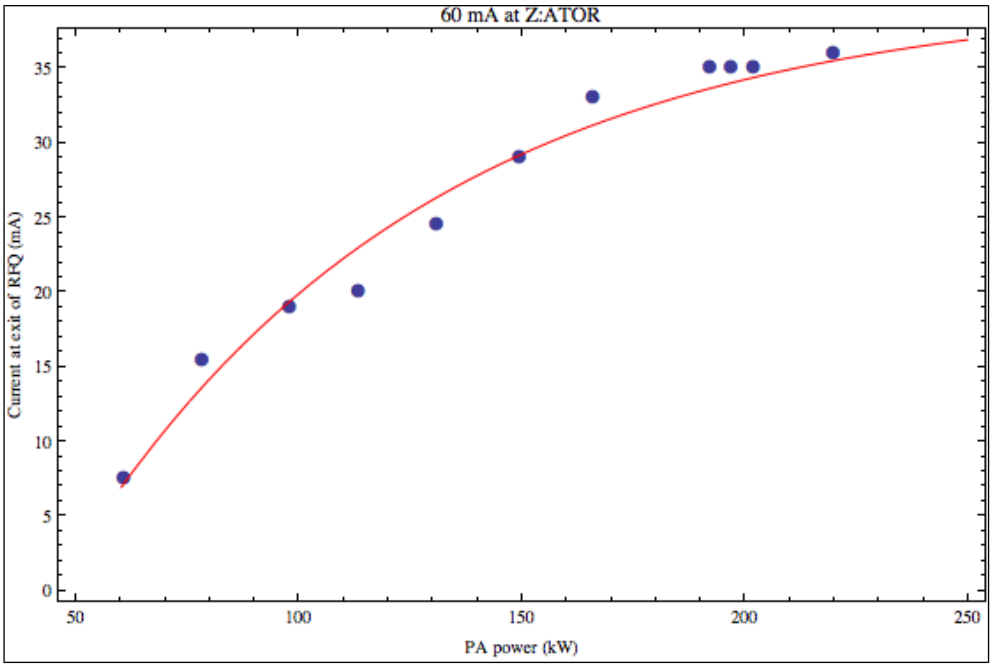

Figure C.7: *The capture efficiency of the RFQ increased as the power into the RFQ increased. Unfortunately, the efficiency is still low despite having > 180 kW into it. The RFQ cannot be powered this way for normal operations.*

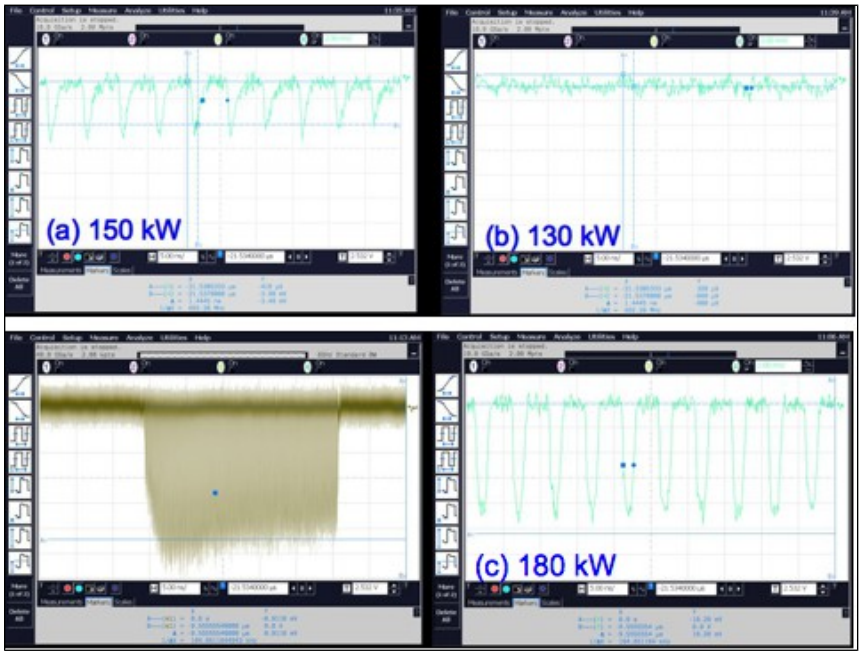

Figure C.8: *Bunching as a function of RFQ power measured with a fast Faraday cup. Bunching starts above 130 kW. There is no bunching at 130 kW.*

C.3 Power Coupler Sensitivity

The power coupler is extremely sensitive to the placement of the external physical load. For example, the transmission line that connects the power amplifier to the coupler, must be carefully placed so that it does not have its entire weight resting on the coupler. When the transmission line is not well supported, s11 can vary by more than 10 dB! See Figure C.9. Note: These pictures were taken on consecutive days. Not shown is the effect of light tapping that will also change the coupling by this amount. The taps cause the s11 to change and then the value stays there until the next tap. The fix that was used in the test line was to mount the transmission line in such a manner as to relieve any pressure on the input coupler. See Figure 4.79.

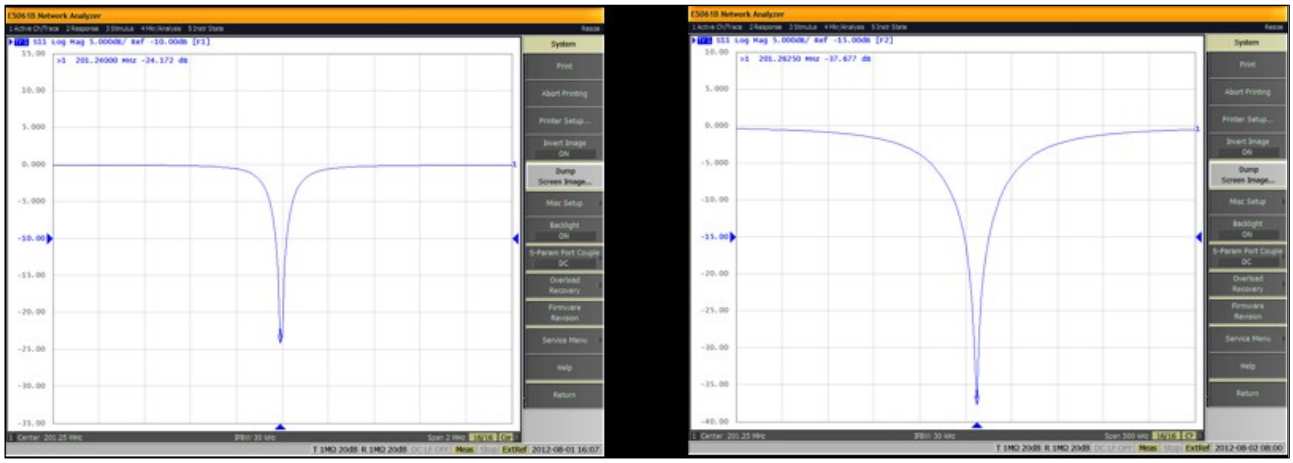

Figure C.9: *These figures show the change in coupler s11 over consecutive days. The change is quite dramatic and indicates that something is not quite right. Light tapping can also change s11 to values that stay until the next tap.*

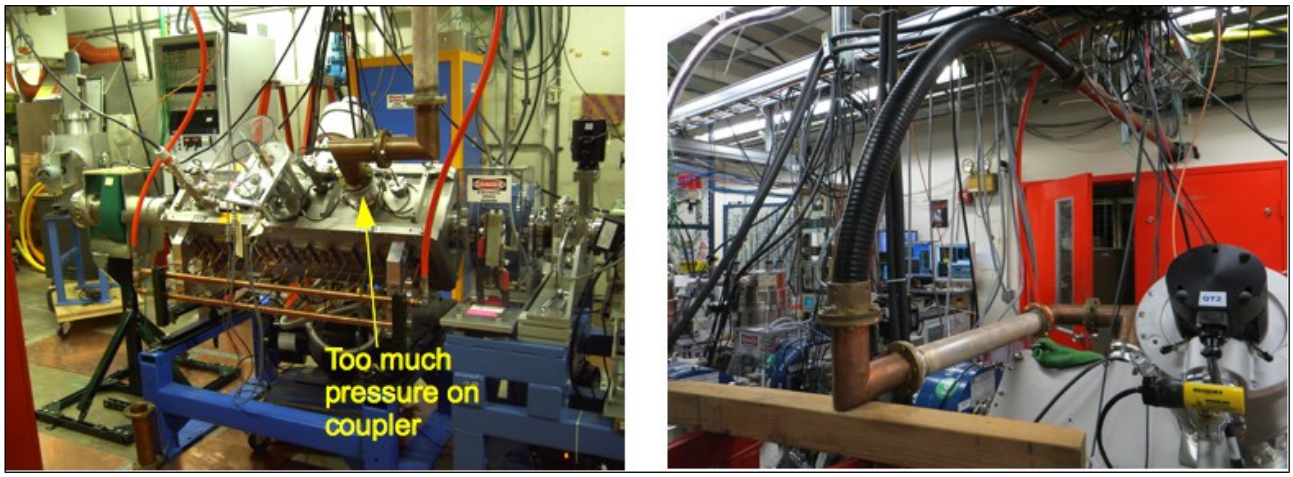

Figure C.10: *The original transmission line was mounted in a manner that put too much pressure on the input coupler which warped it very slightly but enough to cause the s11 to change dramatically. The solution shown in the right picture is to relieve the pressure on the coupler with a piece of wood.*

C.4 Unstraight Rods

The rods in the RFQ are not straight because the mounts that hold them were randomly tilted w.r.t. the base of the RFQ tank. See Figure C.12. It was originally thought that the crooked rods were responsible for the energy error because the gaps are not small ~0.5 mm compared to the RFQ gap size ~5 mm. The reason why the stands were tilted was because the collars holding the stands were not mounted correctly to the base of the RFQ tank. After proper tightening of the bolts, the stands became orthogonal to the base and the rods straightened. See Figure C.13. However, despite this fix, the output energy did not change.

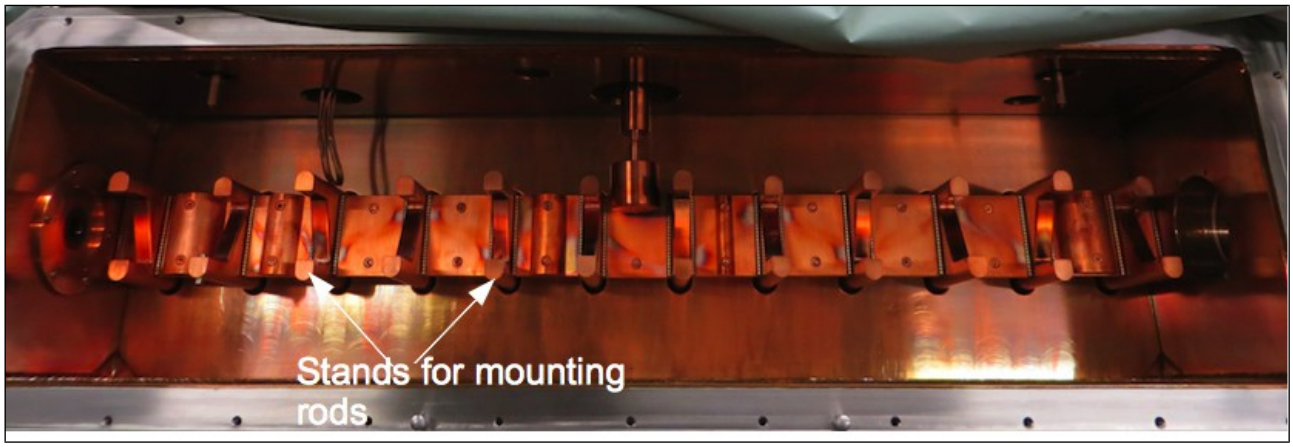

Figure C.11: *This picture shows the stands that mount the rods. Close examination of the stands show that they are not normal to the base of the tank.*

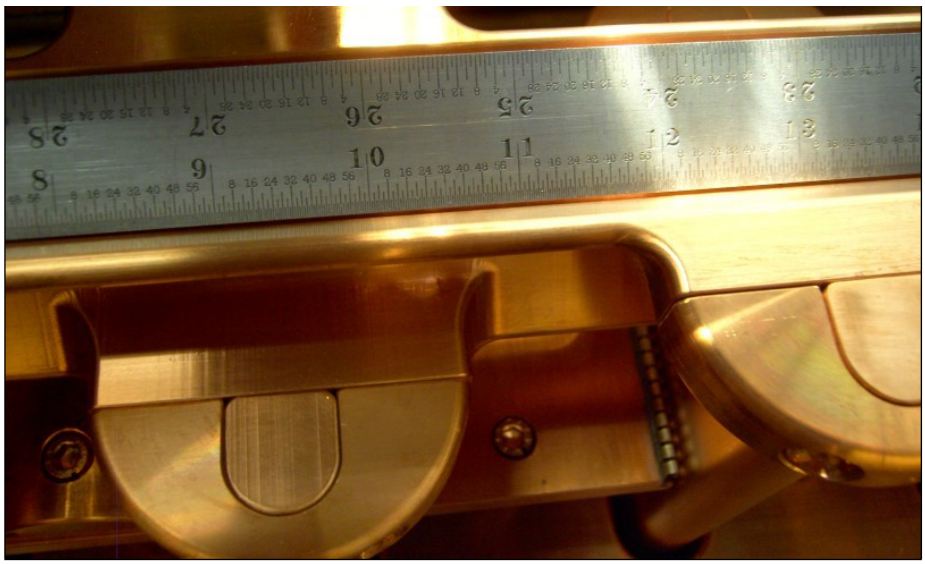

Figure C.12: *This picture shows the straightness of the rod compared to a straight edge. It is clear that there is a gap between them.*

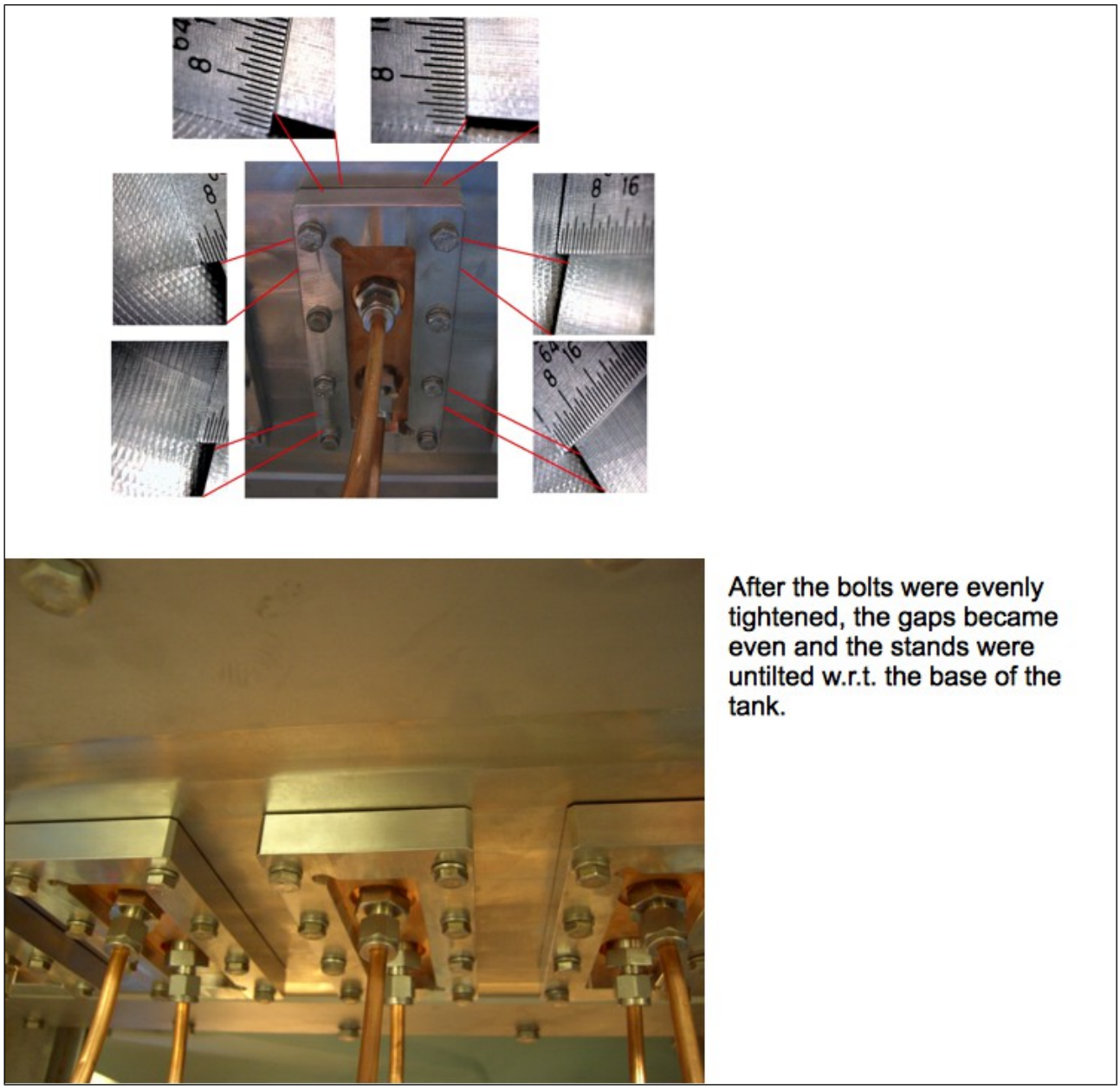

Figure C.13: *The collars that held the stands (that held the rods) were not even with the base of the tank because there are gaps which are clearly visible (top picture). After the bolts of every collar was evenly tightened, the gaps became evenly spaced and the stands became normal to the base.*

References

[1] C.W. Schmidt & C.D. Curtis, "A 50-mA Negative Hydrogen Ion Source", IEEE Proc. Nucl. Sci., NS-26, pg. 4120-4122, 1972.
[2] J.G. Alessi, "Performance of the Magnetron H- Source on the BNL 200MeV Linac", AIP Conf. Proc., Vol. 642, pg. 279-286, 2002.
[3] D. Raparia, et al, "Results of LEBT/MEBT Reconfiguration at BNL 200 MeV Linac", Part. Acc. Conf. Proc., , , 2009.
[4] J.G. Alessi et al, "H- Source and Low Energy Transport for the BNL RFQ Preinjector", AIP Conf. Proc., Vol. 210, pg. 711-716, 1990.
[5] M. Reiser et al, "Theory and Design of Charged Particle Beams", 2nd Ed., pg. 243-254, Wiley-VCH, 2008.
[6] J.P. Carneiro, "H- Stripping Equations and Application to the High Intensity Neutrino Source", Beam docs 2740.
[7] J.F. Williams, "Single and Double Electron Loss Cross Section for 2-50-keV H- Ions Incident upon Hydrogen and the Inert Gases", Phys. Rev., Vol. 154, No. 1, pg. 9-12, 1967.
[8] S.N. Kaplan, et al, "Electron Detachment from 20-MeV D- Ions by a Magnetic Field", Phys. Rev., Vol 131, No. 6, pg. 2574-2577, 1963.
[9] Use of an Einzel lens as chopper was first suggested by D. Raparia (BNL), 2009.
[10] http://www.sns.gov/APGroup/Minutes/ColabMinutes/030211_FastCup.pdf
[11] K.R. Crandall et al, "RFQ Design Codes", 11, LA-UR-96-1836, 2005.
[12] C.Y. Tan, "Back of the Envelope Calculation of the RF coupling β for the FNAL H- Injector RFQ", , Beams-doc-3868-v1, 2011.
[13] J. M. Maus, "Development of RFQ Particle Dynamics Simulation Tools and Validation with Beam Tests", , 101-102, Thesis (U. Frankfurt), 2010.
[14] J.P. Duke et al, "Improved Results from the Gas Scattering Energy Spectrometer on the ISIS RFQ Test Stand", Part. Acc. Conf. Proc., , pg. 2542-2544, 2003.
[15] D. Raparia, "Emittance: Linac and Booster", , BNL Retreat, 2009.
[16] http://www.time-merit.co.jp/index02.htm
[17] V. Lodestro, Private Communication, Aug 2010.
[18] M. Okamura, Private Communication, Dec 2010.
[19] D. Sun et al, "RF Measurement Results of Buncher Cavityfor Linac Pre-injector Upgrade", , Beams-doc-4191-v4, 2012.
[20] A.W. Chao & M. Tigner (Editors), "Handbook of Accelerator Physics and Engineering", 3rd printing, pg. 442 - 444, , 2006.
[21] V. Kashikhin & A. Markarov, "MEBT Quadrupole with Dipole Correctors", , MEBT_Quadrupole+Dipoles_011211c.docx (Unpublished), 2011.
[22] A.K. Jain, "Basic Theory of Magnets", Proc. CERN Accelerator School on Measurement and Alignment of Accelerator and Detector Magnets, , , 1998.
[23] H. Takeda, "Parmila", pg. 107, LA-UR-98-4478, 2005.
[24] H. Takeda, "Parmila", pg. 15, LA-UR-98-4478, 2005.
[25] J.G. Alessi et al, "Performance of the New AGS RFQ Preinjector", Part. Acc. Conf., , pg. 999-1001, 1989.
[26] R.L. Witkover, "Operational Experience with the BNL Magnetron H- Source", AIP Conf. Proc., Vol. 111, pg. 398-409, 1984.
[27] J. Alessi, Private Communication, 2008.